LIDAR REMOTE SENSING AND CO-OPERATIVE OBSERVATIONS: PROCESSING METHODS AND AEROSOL RADIATIVE TRANSFER

PH.D. THESIS DISSERTATION

Submitted in partial fulfilment of the requirements for the degree of

DOCTOR OF PHILOSOPHY

Submitted by

Rubén Barragán Cuesta
Universitat Politècnica de Catalunya (UPC)
Dept. of Signal Theory and Communications (TSC) – Remote Sensing, Antennas, Microwaves and Superconductivity Group (CommSensLab)
Doctorate Program in
Signal Theory and Communications

PhD Thesis Advisors
Dr. Francesc Rocadenbosch Burillo
and
Dr. Michaël Sicard

Universitat Politècnica de Catalunya

Barcelona, April 2019

Lidar Remote Sensing and Co-operative Observations: Processing Methods and Aerosol Radiative Transfer

[1] CommSensLab, Department of Signal Theory and Communications, Universitat Politècnica de Catalunya, E-08034 Barcelona, Spain

[2] Ciències i Tecnologies de l'Espai—Centre de Recerca de l'Aeronàutica i de l'Espai/Institut d'Estudis Espacials de Catalunya (CTE-CRAE / IEEC), Universitat Politècnica de Catalunya, E-08034 Barcelona, Spain

UNIVERSITAT POLITÈCNICA DE CATALUNYA
BARCELONA**TECH**
Escola de Doctorat

Curs acadèmic:

Acta de qualificació de tesi doctoral

Nom i cognoms

Programa de doctorat

Unitat estructural responsable del programa

Resolució del Tribunal

Reunit el Tribunal designat a l'efecte, el doctorand / la doctoranda exposa el tema de la seva tesi doctoral titulada ____ ____.

Acabada la lectura i després de donar resposta a les qüestions formulades pels membres titulars del tribunal, aquest atorga la qualificació:

☐ NO APTE ☐ APROVAT ☐ NOTABLE ☐ EXCEL·LENT

(Nom, cognoms i signatura) President/a	(Nom, cognoms i signatura) Secretari/ària

(Nom, cognoms i signatura) Vocal	(Nom, cognoms i signatura) Vocal	(Nom, cognoms i signatura) Vocal

______________________, _______ d'/de _________________ de _______________

El resultat de l'escrutini dels vots emesos pels membres titulars del tribunal, efectuat per la Comissió Permanent de l'Escola de Doctorat, atorga la MENCIÓ CUM LAUDE:

☐ SÍ ☐ NO

(Nom, cognoms i signatura) President/a de la Comissió Permanent de l'Escola de Doctorat	(Nom, cognoms i signatura) Secretari/ària de la Comissió Permanent de l'Escola de Doctorat

Barcelona, _______ d'/de ____________________ de _________

Menció Internacional en el títol de doctor o doctora

- Com a secretari/ària del tribunal faig constar que part de la tesi doctoral, com a mínim el resum i les conclusions, s'ha redactat i presentat en una de les llengües habituals per a la comunicació científica en el seu camp de coneixement i diferent de les que són oficials a Espanya. Aquesta norma no s'aplica si l'estada, els informes i els experts provenen d'un país de parla hispana.

(Nom, cognoms i signatura) Secretari/ària del Tribunal

“What is a scientist after all?

It is a curious man looking through a keyhole, the keyhole of nature, trying to know what’s going on”

Jacques Yves Cousteau

ACKNOWLEDGMENTS

The following institutions are gratefully acknowledged for their contribution to this work:

- Spanish Ministry of Science, Innovation and Universities (Ministerio de Ciencia, Innovación y Universidades, MICINN) for the doctoral studies grant (BES-2013-066340), held by the author from 01 June 2014 to 31 May 2018 and the mobility grant (EEBB-I-16-11150), held by the author from 01 March 2016 to 31 May 2016 .
- CommSensLab is a Excellence Unit (Unidad de Excelencia María de Maeztu MDM-2016-0600 funded by the Agencia Estatal de Investigación) of the Universitat Politècnica de Catalunya (UPC).
- MICINN and European Regional Development Funds (FEDER) under the projects TEC2012-34575, TEC2015-63832-P, CGL2017-90884-REDT, PGC2018-094132-B-100 (Atmos. Rem. Sens. with cooperative lidar, radar and passive sensors), and UNPC10-4E-442 (UPC Lidar Station).
- Microwave Remote Sensing Laboratory (MIRSL) from the Department of Electrical and Computer Engineering at the University of Massachusetts (UMass), for hosting the author during the research stay carried out in this Ph.D.
- European Commission under the ACTRIS (Aerosols, Clouds, and Trace gases Research InfraStructure Network) FP7 (GA-262254) and under the EU H2020 ACTRIS-2 (GA-654109) and ACTRIS PPP (GA-739530) and EU H2020 GRASP-ACE (GA-778349) projects.
- The Department of Earth and Atmospheric Sciences of the Purdue University and the NOAA National Severe Storms Laboratory for their collaboration and help during this research and for the deployment of some instruments necessary to carry out this thesis.
- Some measurements were acquired in the framework of the ADRIMED and ChArMEx projects. ChArMEx-France is supported through the MISTRALS programme by INSU, ADEME, Météo-France and CEA. ADRIMED project was mainly supported by the French Agence Nationale de la Recherche.
- NOAA Air Resources Laboratory (ARL) for the provision of the HYSPLIT transport and dispersion model; the Barcelona Supercomputing Center for forecasts with the Dust Regional Atmospheric Model (DREAM), the NASA MPLNET data, funded by the NASA Earth Observing System and Radiation Sciences Program, tools used in this Ph.D. thesis.

I would like to express my sincere gratitude to my Ph.D. advisors Dr. Francesc Rocadenbosch and Dr. Michël Sicard for their guidance and support during all these years. Without their wise advices, their help and patience it would have been impossible to finish.

I'm grateful to Dr. Adolfo Comerón, Dr. Constantino Muñoz, Dr. Alejandro Rodríguez and Dr. David García for their help during those days (and nights) working on the lidar and for their support each one of these thousands of days.

Special thanks to Dr. Jordi Tiana, Dr. Umar Saeed and all the staff of the CommSensLab for their advice, help and cooperation.

Finally I would like to express my sincere gratitude also to Dr. Stephen Frasier (Microwave Remote Sensing Laboratory, University of Massachusetts) and the rest of the MIRSL staff members for his kind support and help during the research stay carried out in Amherst, MA.

Llega el momento de plantarte delante de esta hoja en blanco y después de casi 200 páginas escribiendo, no sabes que poner. Como hay que empezar por alguien, nadie mejor que darle las gracias a María José y Nikos por haber sido "mis tutores" en esto, por vuestros consejos, los cafés de una hora, los salseos y las noches largas…ya estoy echándolo de menos.

Raúl, Ary, Alex, Oswi, Marc y Ángel…esa pequeña cosa que hemos montado, no puedo pasar sin nombraros aquí. Este trabajo tiene ruido de motor y olor a gasolina por vuestra culpa, sin vuestro apoyo cada día y la brasa que dais por whatsapp esta tesis nunca hubiera salido adelante.

Tampoco quiero/puedo olvidar darle las gracias a Silvia, Fasu, Carlos, Natalia…a todo ese pequeño ecosistema tossenco que apareció a la mitad del camino para compartir risas y cerveza, pero sobre todo abrazos que llenaban de energía para poder escribir un otra línea más más. Gracias a Laure que ha estado casi desde el día 1, siempre ha sido uno de mis motores en Barcelona (incluso después de meter kilómetros por medio notaba que seguía ahí apoyando). Agradecer también las conversaciones nocturnas en un patio en plena montaña llenas de bromas que tienen más de 10 años…gracias Adri por recordarme que al final con los años solo recordamos las cosas buenas de cada etapa. También quiero dar las gracias a Sam…gracias por cada empujón, por cada palabra de ánimo, por tus consejos optimistas y por confiar ciegamente en que podía llegar aquí. Cómo no agradecerle a Jezabel, que apareció de rebote en todo esto, todo su apoyo y ayuda…aunque llegaba con un delay de 6 horas…gracias por las madrugadas eternas y por todos los momentos de alegría, de tensión, de nervios o de lo que fuera que hemos tenido que soportar. A Sandra, un pilar esencial mientras recorría este laberinto, no sé ni cómo darle las gracias por todo.

Agradecerle a Kike y Mercedes todo lo que han hecho por mí estos años, por ser mi familia en este viaje fuera de mi meseta.

Al resto de buzos –Lore, Cris, Ele y Larry – gracias por acompañarme y compartir conmigo ese mundo en el que no hay jefes, ni problemas, en el que podíamos olvidarnos de todo durante un rato.

Para casi el final me dejo a toda esa gente de Madrid –Javi, Alfredo, Pilar, Noe, Cantero, Laura, Bea, Ángel y Eva – gracias por no fallar cada vez que he recorrido 600 km.

Y ya por último gracias a mi familia por todo el cariño que me han dado, por preocuparse y aconsejarme y por haber hecho posible que haya escrito todo esto. Este trabajo va dedicado a ellos…

ABSTRACT

This Ph.D. thesis focuses on: (i) the design and integration of a polarimetric channel for the multi-spectral Raman lidar station of the Universitat Politècnica de Catalunya (UPC), Remote Sensing, Antennas, Microwaves and Superconductivity Group (CommSensLab), (ii) the study of the temporal and spatial evolution of atmospheric aerosol optical, microphysical and radiative properties by means of active and passive remote sensing in the context of ACTRIS and Spanish National projects, and (iii) rainfall rate retrieval by means of a vertically-pointed ceilometer in the context of the Verification of the Origins of Rotation in Tornadoes Experiment Southeast (VORTEX-SE).

The first goal of this Ph.D., tested on the UPC multi-spectral Raman lidar station, consists of developing a secondary optical receiving chain, installed next to the laser source. The secondary telescope, mounted in the optical chain, allows retrieving the cross-polarized return signal separately from the total-power signal, avoiding the need of a very precise characterization of the crosstalk parameters of the beam-splitters. The first experimental results, corresponding to a collection of atmospheric conditions over the city of Barcelona, are also presented. The second goal of this Ph.D. deals first with the GAME (Global Atmospheric Model) code, necessary to retrieve the aerosol radiative properties. The radiative fluxes estimated in the short-wave and long-wave spectral ranges at the bottom and the top of the atmosphere by GAME are compared to the ones retrieved by a different radiative transfer model, namely Two-Stream, in order to know the importance of the spectral parameterization of a radiative transfer code. Then, GAME code, in both configurations, is fed by means of three different datasets to evaluate the parameterization of the vertically-resolved properties and to assess the uncertainty of GAME when is tuned with input parameters from different sources.

Afterwards, an evaluation of the seasonal variability of the aerosol background optical and radiative properties in the Western Mediterranean Basin (WMB) is performed by means of AERONET (Aerosol Robotic Network) sun-photometers data from two background sites, Ersa (Corsica Island, France) and Palma de Mallorca (Mallorca Island, Spain). In addition, in order to detect possible northeast-southwest gradients in the aerosol properties, a third site located at Abolrán (Alborán Island, Spain) is considered. Finally, during 15-24 June 2013 a moderate Saharan dust multi-intrusion was detected by some EARLINET/ACTRIS (Granada, Barcelona, Naples, Potenza and Serra la Nave (Italy)) and ADRIMED/ChArMEx (Cap d'en Font, (Minorca Island, Spain) and Ersa) stations. This Ph.D. uses this event to study the spatio-temporal evolution of the mineral dust properties, since the lidar stations were supported during the multi-intrusion by collocated AERONET sun-photometers and the Falcon 20 aircraft. Also the GAME code is used to estimate the aerosol radiaite effect during the Saharan dust event. Besides, air- and space-borne lidar measurements, satellite images and back-trajectories are used to confirm the multi-intrusion aspect of the event.

The last goal of this Ph.D. pursues estimation of the rain rate (RR) from ceilometer measurements. In VORTEX-SE, a Vaisala CL-31 ceilometer, a S-band radar, and a disdrometer were deployed in Alabama during March-April 2016. First, rain-extinction coefficients from ceilometer attenuated backscatter measurements are derived by means of a modified form of the well-known slope-method. These coefficients are compared with the RRs measured by a collocated S-band radar and a disdrometer in order to get the RR-to-extinction models. Advanced covariance-weighted techniques are used to best assess and validate the estimated models. These models can be used to estimate the RR from the ceilometer in similar situations without need to have a collocated cooperative instrument permanently deployed

Este Ph.D. se centra en: (i) en el diseño e integración de un canal polarimétrico para la estación lidar multi espectral del grupo de teledetección, antenas, microondas y superconductividad (CommSensLab) de la Universitat Politècnica de Catalunya (UPC), (ii) en el estudio de la evolución temporal y espacial de las propiedades ópticas, microfísicas y radiativas de los aerosoles por medio de teledetección activa y pasiva en el contexto de ACTRIS y proyectos estatales, y (iii) en la recuperación de intensidad de lluvia por medio de un ceilómetro en configuración vertical en el contexto del proyecto Verification of the Origins of Rotation in Tornadoes Experiment Southeast (VORTEX-SE).

El primer objetivo, realizado en la estación lidar de UPC, consiste en el desarrollo de una cadena óptica secundaria instalada junto al láser. El telescopio secundario, montado en la cadena óptica, permite recuperar la componente cross-polarized de la señal total por separado, evitando la necesidad de conocer con precisión los parámetros de los beam-splitters. Se presentan también los primeros resultados obtenidos en Barcelona durante diferentes situaciones atmosféricas. El segundo objetivo de este Ph.D. se centra en el código GAME (Global Atmospheric Model), necesario para recuperar las propiedades radiativas de los aerosoles. Los flujos radiativos estimados tanto en onda larga como en onda corta en la base y en la parte superior de la atmósfera son comparados con los estimados por otro código de transferencia radiativa, Two-Stream, para conocer la importancia de la parametrización espectral. Después, el código GAME es alimentado con 3 bases de datos diferentes para evaluar la parametrización de las propiedades resueltas en altura y conocer la incertidumbre de GAME cuando es alimentado con parámetros con diferentes orígenes.

Por otro lado, se presenta una evaluación de la variabilidad estacional de las propiedades ópticas y radiativas del aerosol de fondo en la cuenca oeste mediterránea (WMB) realizada con datos de fotómetros solares de la red AERONET (Aerosol Robotic Network) situados en dos puntos considerados libres de contaminación: Ersa (isla de Córcega, Francia) y Palma de Mallorca. Además, para detectar posibles gradientes noreste-suroeste en las propiedades delos aerosoles, se considera un tercer punto ubicado en la isla de Alborán. Por último, en este Ph.D. se aprovecha una multi intrusión moderada de polvo sahariano, detectada entre los días 15 y 24 de junio de 2013 por algunas estaciones EARLINET/ACTRIS (Granada, Barcelona, Nápoles, Potenza y Serra la Nave (Italia)) y ADRIMED/ChArMEx (Cap d'en Font (Menorca) y Ersa), para estudiar la evolución espacio-temporal de las propiedades del polvo mineral, ya que las estaciones lidar estaban apoyadas durante el evento por fotómetros solares pertenecientes a la red AERONET, situados junto a las estaciones lidar, y por vuelos del Falcon 20. GAME es usado para obtener también el efecto radiativo de los aerosoles durante el evento de polvo sahariano. Para confirmar el aspecto de multi intrusión se utilizan medidas lidar tomadas a bordo de aviones y satélites, imágenes satelitales y retro trayectorias.

El último objetivo del Ph.D. persigue la estimación de la RR utilizando medidas de un ceilómetro. En VORTEX-SE, se desplegaron (Alabama, marzo-abril 2016) un ceilómetro Vaisala CL-31, un radar de banda S y un disdrómetro. Se han estimado los coeficientes de extinción debida a la lluvia a partir del retorno atenuado medido por el ceilómetro, utilizando una versión modificada del método de la pendiente. Estos coeficientes se comparan con las intensidades de lluvia (RR) estimadas con el radar y el disdrómetro para obtener modelos de RR-extinción. Para validarlos se utilizan técnicas avanzadas de covarianza ponderada. Dichos modelos pueden usarse para estimar la RR con un ceilómetro, en situaciones similares, sin necesidad de tener desplegado permanentemente un instrumento cooperativo.

LIST OF CONTENTS

LIST OF FIGURES

LIST OF TABLES

LIST OF SYMBOLS

Roman Symbols

$\boldsymbol{a}$	Aerosol radius (m)
AER	Super-index term for AERONET origin (·)
AAE	Absorption Ångström exponent (·)
AAOD	Aerosol absorption optical depth (·)
AE	Ångström exponent (·)
$\boldsymbol{AOD}$	Aerosol optical depth (·)
ARE	Aerosol Radiative Effect ($W \cdot m^{-2}$)
$\mathbf{A_r}$	Effective telescope receiving area (m^2)
$\boldsymbol{abs}$	Sub -index term for absorption (·)
$\boldsymbol{aer}$	Sub/super-index term for aerosol (·)
alb	Surface albedo (·)
$\boldsymbol{BOA/TOA}$	Sub -index term for bottom and top of the atmosphere respectively (·)
CNR	Carrier-to-Noise ratio (dB)
$\boldsymbol{C_c^v}, \boldsymbol{C_f^v}$	Coarse, fine mode median volume concentration ($\mu m^3 \mu m^{-2}$)
$\boldsymbol{c}$	Speed of light in vacuum ($2.998 \cdot 10^8$ ($m \cdot s^{-1}$))
$\boldsymbol{ceilo}$	Super-index term for ceilometer (·)
$\boldsymbol{D}$	Diameter of the scatter (mm)
$\boldsymbol{DN}$	Super-index term for downward (·)
$\boldsymbol{dAE/d\lambda}$	Ångström exponent curvature (·)
$\boldsymbol{disdro}$	Super-index term for disdrometer (·)
$\mathbf{E}$	Energy pulse (J)
$\boldsymbol{e}$	Partial pressure of water vapour (hPa)
$\boldsymbol{FE}$	Forcing efficiency ($W \cdot m^{-2}\ \mathrm{AOD}_{550}^{-1}$)
$\boldsymbol{F}$	Fluxes with aerosol ($W \cdot m^{-2}$)
$\boldsymbol{F^0}$	Fluxes without aerosol ($W \cdot m^{-2}$)
$\boldsymbol{f}$	Fine mode fraction (·)
$\boldsymbol{f_0}$	Carrier frequency (Hz)
$\boldsymbol{f_b}$	Beat frequency (Hz)
$\boldsymbol{f_b^+}$	Maximum value of f_b (Hz)
$\boldsymbol{f_b^-}$	Minimum value of f_b (Hz)
$\boldsymbol{f_{br}}$	Beat frequency moving target (Hz)
$\boldsymbol{f_d}$	Doppler frequency shift (Hz)
$\boldsymbol{f_e}$	Emission frequency (Hz)
$\boldsymbol{f_n}$	Discrete frequency (Hz)
$\boldsymbol{f_m}$	Modulation frequency (Hz)
$\boldsymbol{f_r}$	Reception frequency (Hz)
$\boldsymbol{f_s}$	Sampling frequency (Hz)
$\boldsymbol{\dot{f}}$	Rate of frequency change or chirp rate (Hz/s)
$\boldsymbol{G_t}, \boldsymbol{G_r}$	Transmitter and receiver antenna gain (·)
$\boldsymbol{g}$	Asymmetry parameter (·)
$\mathbf{h_{bottom}}, \mathbf{h_{top}}, \mathbf{h_{CM}}$	Bottom, top and centre of mass heights (m)
$\boldsymbol{i}$	Sample index
$\boldsymbol{j}$	Sample index
$\mathbf{K}$	System constan ($W \cdot m^3$)
$\boldsymbol{k}$	Imaginary part of the refractive index (·)
LST	Land-surface temperature (K)
$\boldsymbol{LWF}$	Long-wave irradiances ($W \cdot m^{-2}$)
$\mathbf{MD}$	Super-index term for mineral dust
$\mathbf{m}$	Complex refractive index (·)
$\boldsymbol{mol}$	Sub/super-index term for molecular (·)

$\boldsymbol{N}$ Radioelectric refractivity $(\cdot)$

$\boldsymbol{NetF}$ Net flux $(W \cdot m^{-2})$

$\boldsymbol{N(D)}$ Particle size distribution $(m^{-3} \cdot mm^{-1})$

$\boldsymbol{N_{aer}}$, $\boldsymbol{N_g}, \boldsymbol{N_R}$ Aerosol, Gas, Nitrogen molecule number concentration (m^{-3})

$\boldsymbol{n}$ Real part of the refractive index $(\cdot)$

$\boldsymbol{no\_rain}$ Sub/Super-index term for "no-rain" condition $(\cdot)$

$\mathbf{P}$ Backscattered power (W)

$\boldsymbol{P(R)}$ Range-corrected power (W)

PSD Particle size distribution $(g \cdot cm^{-3})$

$\boldsymbol{p}$ Atmospheric pressure (hPa)

$\boldsymbol{P_r}$ Received power (W)

$\boldsymbol{P_t}$ Transmitted power (W)

$\boldsymbol{P_{Tot}}$ Total power (W)

$\boldsymbol{P_{\perp}}$ Cross-polarized power (W)

$\boldsymbol{P_{\parallel}}$ Co-polarized power (W)

$\boldsymbol{Q_{ext}}, \boldsymbol{Q_{sca}}, \boldsymbol{Q_{abs}}, \boldsymbol{Q_{back}}$ Extinction, scattering, absorption and backscatter efficiency $(\cdot)$

$\boldsymbol{R}, \boldsymbol{R_0}$ Observation, specific range (m)

$\boldsymbol{R_1}, \boldsymbol{R_2}$ Start and end ranges heights of the slope-method (km)

$\boldsymbol{RH}$ Relative humidity (%)

$\boldsymbol{RMSE}$ Relative root-mean-square error (a.u.)

$\boldsymbol{RR}$ Rainfall rate $(mm \cdot h^{-1})$

$\boldsymbol{rain}$ Sub/Super-index term indicating "rain" $(\cdot)$

$\boldsymbol{r_c}$, $\boldsymbol{r_f}$ Coarse and fine mode radii (μm)

$\boldsymbol{r_{eff,c}}$, $\boldsymbol{r_{eff,f}}$ Coarse and fine mode effective radii (μm)

$\boldsymbol{r_c^v}, \boldsymbol{r_f^v}$ Coarse and fine-mode volume median radius (μm)

$\boldsymbol{SSA}$ Single scattering albedo $(\cdot)$

$\boldsymbol{SSAc}$ Critical single scattering albedo value $(\cdot)$

$\boldsymbol{SZA}$ Solar zenith angle $(^{\text{o}})$

$\boldsymbol{sca}$ Sub -index term for scattering $(\cdot)$

$\boldsymbol{S_{Tot}}, \boldsymbol{S_{Dep}}$ Total power, depolarization channel voltage (V)

$\mathbf{T}$ Time delay (s)

$\boldsymbol{T}$ Temperature (K)

$\boldsymbol{T(\lambda, R)}$ Atmospheric transmittance $(\cdot)$

$\boldsymbol{T_S}$ **S**kin surface temperature (K)

$\boldsymbol{T_v}$ Transmission function of the atmospheric gases $(\cdot)$

$\boldsymbol{U(R)}$ Log-range-corrected signal (a.u.)

$\boldsymbol{UP}$ Super-index term form upward $(\cdot)$

$\boldsymbol{V_{sca}}$ Scattering volume (m^3)

$\boldsymbol{V_{Tot}}, \boldsymbol{V_{Dep}}$ Total power, depolarization channel responsivity (V/W)

$\boldsymbol{V^*}$ Depolarization channel system function $(\cdot)$

$\boldsymbol{x}$ Particle size parameter $(\cdot)$

$\boldsymbol{Z}$ Radar reflectivity factor (dBZ)

$\boldsymbol{Z_e}$ Equivalent radar reflectivity factor (dBZ)

Greek Symbols

$\boldsymbol{\alpha}$ Atmospheric extinction coefficient (m^{-1})

$\boldsymbol{\beta}, \boldsymbol{\beta_p}$ Backscatter and particle backscatter coefficient $(m^{-1} \cdot sr^{-1})$

$\Delta \boldsymbol{f}$ Bandwidth (frequency deviation) (Hz)

$\Delta \boldsymbol{R}$ Radar spatial resolution (m)

$\Delta \mathbf{R}'$ Effective spatial pulse length (m)

$\Delta \boldsymbol{S}$ Antenna projected-reading area (m^2)

$\Delta \boldsymbol{T}$ Smoothed temporal resolution (s)

$\Delta \boldsymbol{T_{master}}$ Master-time resolution (s)

$\Delta\boldsymbol{v}$ Side-band frequency (Hz)

$\boldsymbol{\delta}$ Lidar particle depolarization ratio

$\boldsymbol{\delta\alpha}$ Ångström exponent difference ($\cdot$)

$\boldsymbol{\delta^P}$ Particle depolarization ratio ($\cdot$)

$\boldsymbol{\delta^V}$ Volume depolarization ($\cdot$)

$\boldsymbol{\delta^*}$ Depolarization channel system function ($\cdot$)

$\boldsymbol{\delta_{mol}}$ Molecular volume depolarization ratio ($\cdot$)

$\boldsymbol{\varepsilon}$ Surface LW emissivity ($\cdot$)

$\boldsymbol{\eta_{RAW}}, \boldsymbol{\eta}$ Raw volume reflectivity, reflectivity density ($m^2 \cdot m^{-3}$)

$\boldsymbol{k}$ Wavelength shift associated to the molecular species of interest (Hz)

$\boldsymbol{\lambda}, \boldsymbol{\lambda_0}, \boldsymbol{\lambda_R}$ Wavelength, elastic wavelength and Raman wavelength (nm)

$\boldsymbol{v}$ Terminal/radial velocity ($m \cdot s^{-1}$)

v_n Doppler velocity ($m \cdot s^{-1}$)

$\boldsymbol{v_0}$ Incident frequency (Hz)

$\boldsymbol{v_R}$ Frquency shift (Hz)

$\boldsymbol{\xi}$ Optical transmissivity ($\cdot$)

$\boldsymbol{\rho}$ Backscatter ratio ($\cdot$)

$\boldsymbol{\varrho}$ Backscattering cross-section (m^2)

$\boldsymbol{\sigma}$ Standard deviation

$\boldsymbol{\tau_d}$ Detection time (s)

$\boldsymbol{\tau_l}$ Pulse duration (s)

$\boldsymbol{\vartheta}$ Stefan-Boltzmann's constant

LIST OF ACRONYMS

1-D One-Dimensional

ABL Atmospheric Boundary Layer

AGL Above Ground Level

ACE-Asia Aerosol Characterization Experiment-Asia

ACTRIS Aerosol, Clouds and Trace Gases Research Infrastructure

ADRIMED Aerosol Direct Radiative Impact on the Regional Climate in the Mediterranean Region

AERONET Aerosol Robotic Network

AFGL Air Force Geophysics Laboratory

AL Alabama

APD Avalanche Photo-Diode

BOA Bottom of the Atmosphere

BSC-DREAM Barcelona Supercomputing Center Dust Regional Atmospheric Model

CALIOP Cloud-Aerosol Lidar with Orthogonal Polarization

CALIPSO Cloud-Aerosol Lidar and Infrared Pathfinder Satellite Observation

CAPS Cavity Attenuated Phase Shift

CERES Clouds and the Earth's Radiant Energy System

ChArMEx Chemistry-Aerosol Mediterranean Experiment

CLAMPS Collaborative Lower Atmospheric Mobile Profiling System

CommSensLab Remote Sensing, Antennas, Microwaves and Superconductivity Group

CW Continuous Wave Radar

DISORT Discrete Ordinates Method

DOM Discrete Ordinate Method

DS Dataset

DSD Drop Size Distribution

EARLINET European Aerosol Research lidar Network

FIR Finite Impulse Response Digital Filter

FMCW Frequency-Modulated Continuous Wave

FOV Field of View

FT Free Troposphere

GALION GAW Atmospheric LIdar Observation Network

GAME Global Atmospheric Model

GAW Global Atmosphere Watch

GDAS Global Data Assimilation System

GEOSS Global Earth Observation System of Systems

GFAT-UGR Atmospheric Physics Group of the University of Granada

GRASP Generalized Retrieval of Aerosol and Surface Properties

HF High Frequency

HITRAN High-resolution transmission molecular absorption database

HPBW Half Power Band-Width

HSRL High Spectral Resolution Lidars

HYSPLIT Hybrid Single Particle Lagrangian Integrated Trajectory

IF Interference filter

IFT Institute for Tropospheric Research

IISTA-CEAMA Andalusian Institute for Earth System Research

IOP Intensive Observation Period

libRadTran Library for Radiative Transfer

Lidar Light Detection and Ranging

LOA Laboratorie d’Optique Atmosphérique

LOS Line-Of-Sight

LOWTRAN Low resolution Transmission model

LPDR Lidar Particle Depolarization Ratio

LR Lidar ratio

LW Long-wave

LWC Liquid Water Clouds

MD Mineral Dust

METEK Meteorologische Messtechnik GmbH

MIRSL Microwave Remote Sensing Laboratory

MODIS Moderate Resolution Imaging Spectroradiometer

MODTRAN Moderate Resolution Atmospheric Transmission

MP Marshall-Palmer

MPL Micro Pulse Lidar

MPLNET Micro Pulse Lidar Network

MSG/SEVIRI Meteosat Second Generation/Spinning Enhanced Visible and Infrared Imager

MULHACEN Multi-wavelength Aerosol Raman Lidar

Nd:YAG Neodymium-doped Yttirum Alominium Garnet

NDACC Network for the Detection of Atmospheric Composition Change

NIR Near InfraRed

NOAA National Oceanic and Atmospheric Administration

O-TS Optimized Two-Stream Model

OPAC Optical Properties of Aerosol and Cloud Model

OVF Overlap Function

OWV Optimized Water Vapor Absorption Spectrum

P Polarizer

PBL Planetary Boundary Layer

PIPS Portable In situ Precipitation Station

PLASMA Photomètre Léger Aéroporté pour la Surveillance des Masses d’A

PMT PhotoMultiplier Tube

PR Pulse Radar

PRF Pulse Repetition Frequency

PRIDE Puerto Rico Dust Experiment

Radar Radio Detection and Ranging

RASS Radio Acoustic Sounding System

RF Radio Frequency

RR Rainfall Rate

RTM Radiative Transfer Model

SBDART Santa Barbara DISORT Atmospheric Radiative Transfer

SMPS Scanning Mobility Particle Sizer

SNR Signal-to-Noise Ratio

SPALINET Spanish and Portuguese Advanced Lidar Network

SSF Single Scanner Footprint

SW Short-wave

TOA Top of the Atmosphere

TRP Tropical Model

TS Two-Stream Model

UHF Ultra High Frequency

UHSAS Ultra-High Sensitivity Aerosol Spectrometer

UMASS University of Massachusetts

UNILE University of Lecce

UTC Coordinate Universal Time

UPC Universitat Politècnica de Catalunya

UV Ultraviolet

VHF Very High Frequency

VIS Visible

VORTEX-SE Verification of the Origins of Rotation in Tornadoes Experiment-Southeast

WMB Western Mediterranean Basin

WSR Weather Surveillance Radar

CHAPTER 1

Introduction to the Ph.D. Thesis

This Chapter gives an overview of the UPC multi-spectral lidar system and UMass S-band profiler radar and ceilometer in the context of atmospheric aerosol and rain remote sensing. Next, it proceeds to present the motivation, objectives and organization of this Ph.D. thesis.

1.1 INTERNATIONAL CONTEXT

1.1.1 GALION & EARLINET

In the context of the ground-based lidar networks, the GAW (Global Atmosphere Watch) programme of observation of aerosols, since its inception in the year 2000, has a strategic goal (2008-2015) [Bösenberg et al., 2007] "the determination of the spatio-temporal distribution of properties of atmospheric aerosols related with climate change and air quality in multi-decade time scales" [Bösenberg and Hoff , 2007; Hoff et al., 2008]. More specifically, the objective of GALION. (GAW Atmospheric Lidar Observation Network) is to provide the vertical component of aerosol distribution by means of advanced lidar systems organized into a network of cooperative networks [Hoff et al., 2008] (see Fig. 1.1). The international context of these initiatives is, ultimately, GEOSS (Global Earth Observation System of Systems), which aims to achieve global coordinated multi-sensor observation of the Earth.

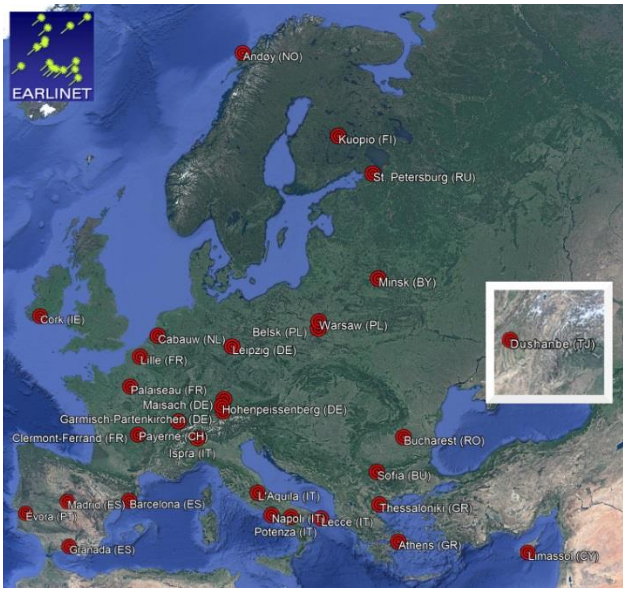

Fig. 1.1. ACTRIS research infrastructure as of December 2017 (PI UPC partner, Prof. A. Comerón) (Adapted from EARLINET [2017]).

The Micro Pulse Lidar Network (MPLNET) [Welton et al., 2001] is a global network of low-power lidars providing long-term observations of aerosol and cloud properties. Most MPLNET stations are collocated with AERONET (Aerosol Robotic Network) [Holben et al., 1998] sites that provide column-integrated properties of aerosols and clouds. Also, the Network for the Detection of Atmospheric Composition Change (NDACC) is composed of more than 70 remote sensing research stations with observational capabilities which include lidars, spectrometers, microwave radiometers and ozone and aerosol sondes. At present, the CommSensLab

(Remote Sensing, Antennas, Microwaves and Superconductivity) Group, Universitat Politècnica de Catalunya (UPC) of which the lidar group is part) also hosts one MPLNET lidar system.

At the continental scale, the EARLINET (European Aerosol Research Lidar Network) [Böckmann et al., 2004; Pappalardo et al., 2004b], established in 2000, is the first coordinated ground-based aerosol lidar network whose key aim is the provision of a comprehensive, quantitative, and statistically significant database on the spatial and temporal aerosol distribution on a continental scale [Bösenberg and Matthias, 2003]. EARLINET represents the most advanced coordinated effort in GALION, SPALINET (the Spanish and Portuguese Advanced Lidar Network) [Sicard et al., 2009; SPALINET, 2007] being the co-operative extension of EARLINET in Spain [Sicard et al., 2007]. At present (2018), the network includes 31 stations distributed over Europe. The CommSensLab lidar group of the UPC is part of the EARLINET, which is also one of the leading components of GAW. Lidar observations within EARLINET are performed on a regular schedule since May 2000, allowing for the collection of long-term data sets for climatological studies [Matthias et al., 2004]. In addition to coordinated routine measurements, further observations are devoted to the monitoring of special events such as Saharan dust outbreaks [Ansmann et al., 2003; Mona et al., 2006; Papayannis et al., 2008], forest fires [Müller et al., 2007] and volcanic eruptions [Pappalardo et al., 2004a, 2013; Wang et al., 2008; Mattis et al., 2010; Sawamura et al., 2012; Sicard et al., 2012b].

1.1.2 UPC 3+2+1 MULTI-SPECTRAL ELASTIC/RAMAN/DEPOLARIZATION LIDAR SYSTEM

The multi-spectral elastic/Raman lidar station of the CommSensLab, (Figs. 1.2 and 1.3) has currently set-up a 7-channel atmospheric lidar system including 3+2 elastic/Raman aerosol channels, one water-vapour channel [Kumar et al., 2011] and a depolarization auxiliary channel [Rodríguez-Gómez et al., 2017]. The lidar system uses a Q-switched Nd:YAG laser at 1064, 532 (2nd harmonic) and 355 nm (3rd harmonic) wavelengths. The return signal is collected by a 40 cm aperture telescope. A fiber bundle conveys the light return from the telescope focal plane to a polychromator, the spectrally selective unit in reception, designed with a view to minimize optical losses and physical dimensions. The reception field of view, which is limited by the fiber bundle characteristics, is virtually the same for all wavelengths. The backscattered received optical power is separated into the 355, 532, and 1064 nm elastic wavelengths as well as the 386.7 and 607.4 nm N2 Raman-shifted wavelengths, and the 407.5 nm water-vapour Raman-shifted wavelength (Table 1.1). Signal detection is achieved by using an Avalanche Photo-Diode (APD) at 1064 nm and PhotoMultiplier Tubes (PMTs) at all other wavelengths. A simultaneous analog/photon-counting acquisition unit is used. All the engineering details can be found in Kumar et al. [2006]. The depolarization auxiliary channel uses a 70 mm aperture, 300 mm focal distance TAIR-3S telephoto lens as secondary. This is because aerosol depolarization-ratio measurements require the comparison of the signals recovered by two channels in the system: one proportional to the total power and another proportional to the cross-polar component of the collected light [Sassen, 2005; Comerón et al., 2015]. These two channels operate at 532 nm. In parallel with these hardware activities, the CommSensLab lidar group has also carried out an important research activity in the field of data processing and inversion since 1993 [Rocadenbosch, 1996]. The assessment of system performance has been presented in terms of range-corrected power returns, Signal-to-Noise ratio (SNR) and maximum system range, and in Lange et al. [2012], the measured backscattered elastic-lidar power returns against the link-budget theoretical ones [Kumar et al., 2012].

Fig. 1.2. Local and international context. The UPC automated lidar station (scientific and technological research infrastructure, UNPC10-4E-442, PI Prof. F. Rocadenbosch) housing the multi-spectral lidar system.

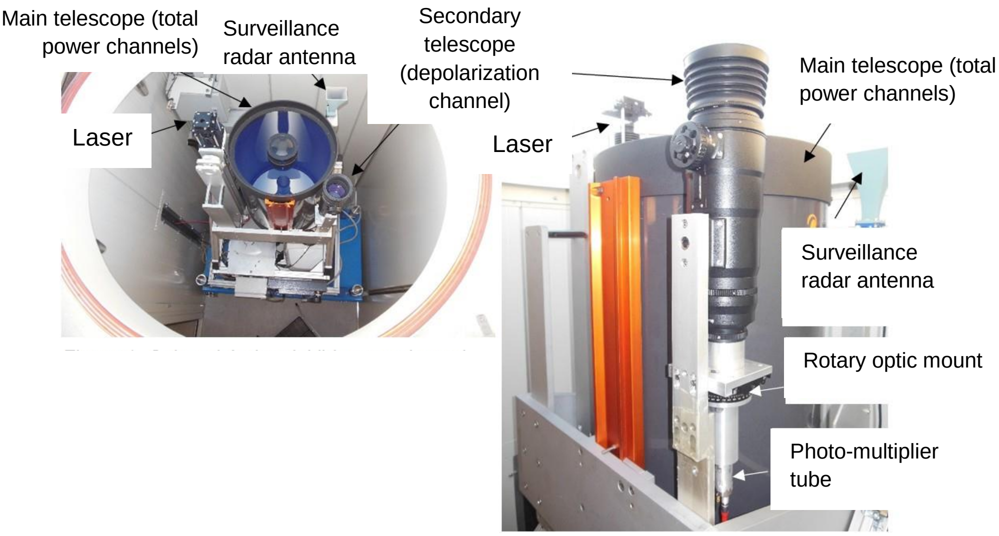

Fig. 1.3. The CommSensLab multi-spectral lidar system optical head with the depolarization channel. Left: top view. Right: side view with the optical head of the depolarization channel in the foreground.

Table 1.1: Main specifications of the CommSensLab multi-spectral lidar system.

Emitter							
Laser	Model	Quantel Brilliant					
	Output (nm)	Nd: YAG	355/532/1064				
	Pulse Energy total (J)		0.060/0.160/0.350				
	Pulse repetitio rate (Hz)	20					
	Pulse length [ns]	3.6					
	Laser beam diameter (mm)	6					
Receiver							
Telescope	Model	Celestron, Classic 8, 1989					
	Type	Schmidt-Cassegrain, primary spherical					
	Aperture diameter (mm)	203.2					
	Obscuration diameter (mm)	69.85					
	Focal length (m)	2.032					
	Field of view (mrad)	1.48					
Secondary telescope	Model	TAIR - 3S, BelOMO					
	Type	Telephoto lens					
	Aperture diameter (mm)	70					
	Focal length (m)	0.3					
Optical fiber	Type	Bundle					
	Numerical aperture	0.12					
	Telescope-laser axes distance (m)	0.18					
	Collimation system type	Double – convex lens					
	Collimation focal length (mm)	27					
Detection channels							
Central wavelength (nm)	532.1	532.1 desp.	607.4	1064	407.5	386.7	354.7
Scattering mechanism	Elastic	Elastic	Rot. Raman N_2	Elastic	Rot. Raman H_2O	Rot. Raman N_2	Elastic
Detector type	PMT	PMT	PMT	APD	PMT	PMT	PMT
Daytime capability	yes	yes	no	yes	yes	yes	yes
Spectral bandwidth, Δλ (nm)	1	1	1	1	1	1	1
Detector NEP ($fW \cdot Hz^{-1/2}$)	0.192	0.192	0.296	36.6	0.892	0.0407	0.0444
Channel NEP ($fW \cdot Hz^{-1/2}$)	7.7		3.0	925	26.2	6.4	7.7

1.2 MOBILITY CONTEXT: THE UMASS MICROWAVE REMOTE SENSING LABORATORY

The Microwave Remote Sensing Laboratory (MIRSL) is the largest research laboratory of the Department of Electrical and Computer Engineering at the University of Massachusetts (UMASS), Amherst. Co-directed by Professors Stephen Frasier and Paul Siqueira, the MIRSL laboratory includes 11 graduate students, three faculty, and two staff (January, 2017). The laboratory occupies over 9000 square feet of space in the Knowles Engineering Building and is well outfitted with modern Radio Frequency (RF) and microwave test equipment. MIRSL researchers specialize in the conception, design, implementation, and evaluation of novel microwave and optical remote sensing instruments and methods. These are used to study aspects of the geophysical environment including the oceans (winds, waves, and currents) [İnce et al., 2003; Contreras and Frasier, 2008; Frasier et al., 2008], atmosphere (severe storms, atmospheric boundary layer) [Contreras and Frasier, 2008; Pollard et al., 2000], and land (topography, ice, carbon, biomass) [Ahmed et al., 2013]. Over the last twenty years, the MIRSL has developed over a dozen new instruments and methods [İnce et al., 2003; Pollard et al., 2000; Trabal et al., 2013; Bioucas-Dias et al., 2012]. In addition to its own graduate students, MIRSL has hosted several students from foreign universities (primarily from Germany and Spain) as visiting scholars pursuing projects for their MS or Diploma degrees. *R. Barragan has been hosted for a Ph.D. stay from Feb., 2016 to July. 2016.*

MIRSL has developed a fleet of novel atmospheric remote sensing systems. These mobile systems participate in field experiments to better understand the dynamics of the lower atmosphere, and in particular, the atmospheric boundary layer. Some active remote sensing examples are meteorological radars operating at microwave frequencies (Fig. 1.3) [Frasier et al., 2008] and wind profilers operating at VHF and UHF frequencies [İnce et al., 2003].

1.2.1 THE MIRSL FMCW RADAR AND CEILOMETER SYSTEMS

The MIRSL systems of concern for this Ph.D. are an S-band (2-4 GHz [Mahafza and Elsherbeni, 2004]) FMCW (Frequency-Modulated Continuous-Wave) radar and a Vaisala CL-31 532-nm lidar ceilometer (Fig. 1.4). A lidar ceilometer is a low-cost simple backscatter lidar originally devoted to cloud height and extent monitoring. Modern ceilometers such as the Vaisala CL-31 also enable to profile the aerosol structure within the low troposphere [Vaisala, 2014]. A FMCW radar usually uses a frequency-modulated instantaneous frequency to retrieve both the range and Doppler shift from a moving target. In the context of atmospheric remote sensing and S-band radar the "moving target" is basically Rayleigh scattering from hydrometeors and interferent targets (e.g., insects and birds) and Bragg scattering from refractive index turbulence (Sect. 2.3).

Fig. 1.4. The S-band, FMCW atmospheric radar profiler from the Microwave and Remote Sensing Lab. (MIRSL, Univ. Massachusetts). It employs separate antennas for transmitting and receiving. A ceilometer is also housed in the truck as indicated. Source: MIRSL (2014).

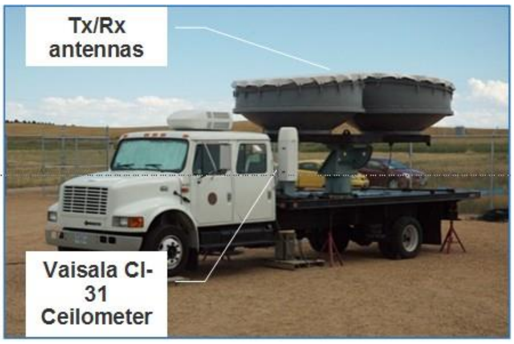

A 6-month stay to UMASS was carried out from February 29 to August 5, 2016

1.3 MOTIVATIONS OF THE STUDY

The following motivation topics have been identified from the state-of-art, and the international context:

- *Exploitation of the UPC CommSensLab multi-spectral Raman lidar system.*- The importance of aerosol tropospheric profiling in a coordinated basis at continental level (EARLINET) has already been outlined previously.
- *Aerosol radiative forcing estimation*.- Aerosol radiative effect estimates obtained with one-dimensional (1-D) radiative transfer models (RTMs) have commonly been used to constrain and/or validate regional climate models. Many 1-D RTMs have been reported in the literature, and some of them are available online as open-source codes. SBDART [Ricchiazzi et al., 1998], Streamer [Key and Schweiger, 1998], MODTRAN [Berk et al., 2006], and libRadtran [Mayer and Kylling, 2005] represent some of the online available RTMs, widely accepted and used by the scientific community. The 1-D RTMs are also often used to locally estimate the aerosol radiative effect under clear-sky or cloudy conditions. Most of the aerosol optical properties required in RTMs can be retrieved from experimental measurements in the short-wave (SW) spectral range. On the contrary, the aerosol optical properties in the long-wave (LW) spectral range have to be taken from look-up tables or calculated by using light scattering codes [Sicard et al., 2014a], since the current remote sensing technologies do not allow retrieving them. The atmospheric parameters not related to the aerosols (e.g., concentration of absorbing gases, relative humidity profile, surface albedo, and temperature) also may significantly influence the estimation of the radiative fluxes in the SW and in the LW spectral range, respectively. Therefore, many sources of uncertainty can affect the determination of the aerosol direct radiative forcing. SW and LW fluxes simulated by RTMs are commonly compared with the corresponding ones measured at the bottom of the atmosphere (BOA) and at the top of the atmosphere (TOA) to test the performance of RTMs and estimate the accuracy of the calculated aerosol direct radiative effect [e.g., Romano et al., 2016].
- *Development of a 532-nm depolarization channel.- S*ince the 1970s the use of the lidar depolarization technique has proven to be a valuable tool for atmospheric sciences (Schotland et al. [1971], Pal and Carswell [1973] among others). Regarding aerosol characterization, the depolarization information has been widely used for aerosol typing when combined with additional optical properties (e.g., [Winker and Osborn, 1992; Groß et al., 2011b]). In this sense, it can also be very useful in the retrieval of the atmospheric boundary layer (ABL) height since it allows discriminating between the aerosol within this layer and different aerosol types coupled to the ABL height based on aerosol data [Bravo-Aranda et al., 2017]. In Wandinger et al. [2008] it is shown how the depolarization data combined with the color ratio allow for discriminating among different kinds of aerosols and clouds, so depolarization information can be added to the set of parameters to be considered in aerosol classification [Wandinger et al., 2008; Burton et al., 2012]. Besides aerosol typing, the depolarization technique also provides relevant information for the retrieval of aerosol microphysical properties. Due to the particle shape information associated to lidar depolarization, the detection of non-spherical particles can be highly improve (see for instance [Burton et al., 2015; Chaikovski et al., 2016]). The majority of the currently working systems [Tesche et al., 2009; Althausen et al., 2000; Esselborn et al., 2009] use a single telescope and either a polarizing beam-splitter that separate the parallel and perpendicular polarization components of the light collected by the telescope or a non-polarizing beamsplitter in one of whose outputs a polarizer is inserted. These approaches present the issue of needing a very precise characterization of the crosstalk parameters of the beam-splitters. The system implemented in the CommSensLab lidar uses an additional telescope (a telephoto lens) to measure the cross-polarized return signal (and thus, the un-polarized component of this signal), without altering the original system.

- *Ceilometer-based Rainfall Rate (RR) estimation:* Disdrometers and radars [Rogers, 1984; Krajewski and Smith 2002] have successfully been used to study the variability of rain and Liquid Water Content (LWC). These instruments are, however, not exempt of limitations: On one hand, disdrometers cannot provide, in a direct way, information about the vertical behavior of the rain. In addition, measurements can be skewed in situations with exceptionally small raindrops (less than 1 mm diameter) during intervals with a small number of raindrops [Krajewski et al. 2006]. On the other hand, vertically pointing radars have difficulty providing reliable information of the vertical distribution of rain close to ground level because of near-field and/or parallax effects.

  Ceilometers offer attractive possibilities for RR measurement: Thus, mono-axial ceilometers typically have a much lower height of the laser-telescope cross-over function (typ. below 100 m) and keep a good SNR in light rain or even in the absence of rain. As with weather radars, the ceilometer return signal is affected by the number and type of raindrops. [Lewandowski et al., 2009] did a first empirical effort to observe the small-scale spatial and temporal evolution of precipitation over a sampling area (1-2 km measurement line) by using a ceilometer in horizontal configuration and different rain gauges. They successfully correlated the disdrometer-measured RR with the ceilometer-measured optical extinction (RR-relationship) along a 1-km horizontal path.

1.4 OBJECTIVES

This Ph.D. thesis deals with Lidar and S-band radar profiling of the atmosphere: Lidar remote sensing and co-operative observations: Processing methods, aerosol radiative transfer and rainfall rate retrieval. Tentative goals are:

- *Obj.1 (block "HANDS ON LAB.") Design and integration of polarimetric channels for the multi-spectral LIDAR station of the UPC.* This objective was carried out by the lidar research group as a team and comprises system exploitation in the EARLINET context and in support of international cal/val satellite missions, as well as a gluing-data method for dynamic range enhancement elastic lidar signals. Key result has been the implementation of a 532-nm depolarization channel in the CommSensLab lidar system.

- *Obj. 2. Radiative forcing: Characterization of the radiative, optical and microphysical properties of the Mediterranean aerosol.* The Ph.D. is to deal with the GAME code. Key result has been the semi-automation of the code to compute one-dimensional aerosol radiative forcing, and its further application and comparison to a different one-dimensional radiative forcing code.

- *Obj. 3. Combined lidar/radar techniques for atmospheric observation: Ceilometer-based rainfall-rate estimation.-* It is proposed to address ceilometer RR measurements in vertical configuration without need of a co-operative radar/rain-gauge permanently deployed. The ground of this hypothesis is to use as a proxy of calibration co-operative measurements from collocated S-band radar or a disdrometer in similar measurement scenarios as with the ceilometer alone. This objective will also address the topic of RR estimation using radar profilers (UMASS).

OBJ. 1. Design and integration of polarimetric channels for the multi-spectral LIDAR station of the UPC.

The multi-spectral elastic/Raman lidar station of the CommSensLab has currently seven channels (355, 387, 407, 532, 532 depol., 607 and 1064 nm wavelength) in reception. In 2010 the lidar station started regular operation within EARLINET. This system permits calibrated multi-spectral range-resolved measurement of the extinction and backscatter opto-atmospheric parameters in the UV (ultraviolet, channels at 355- and 387-nm), VIS (visible, 532 and 607nm), and NIR (near-infrared, 1064 nm) as well as measurement of water-vapor content (407 nm) and depolarization information (532 nm). Retrieval of the atmospheric extinction and backscatter coefficients in the VIS and UV, which is always semi-quantitative using elastic techniques, becomes quantitative thanks to the incorporation of the respective Raman channels (i.e., the Raman return due to the atmospheric nitrogen, the most abundant atmospheric molecular species, is used to calibrate the associated elastic channel).

The first goal of the PhD is to implement a new channel sensitive to the depolarization produced by the aerosols (and the clouds) of the emitted power linearly polarized at 532 nm. Besides, this effort is transversally oriented at exploiting the CommSensLab lidar measurements in terms of data interpretation. This includes transport and aerosol source analysis, and aerosol layers aloft, and synergies with sun-photometers, among others. The latter is of application to the intercomparison of lidar instruments. The scope of lidar measurements in support of this Ph.D. objective comprises:

- Regular coordinated measurements within EARLINET network (3 per week, February 2000 - February 2018).
- CALIPSO measurements (June 2006 - February 2018): 2 to 3 measurements every 16 days (diurnal and nocturnal) in coincidence with overpasses of the CALIPSO satellite.
- Monitoring of special events/alerts: Saharan dust, volcanic eruptions, and fire plume outbreaks, measurements of diurnal cycle, cloud height, etc.
- Calibration/validation of CommSensLab lidar data products, in particular, optical properties of aerosols, cloud height and vertical distribution. This includes the pre-processing of the lidar signals (“raw data” to “clean data”) and the inversion and categorization of data

In parallel to the implementation of the depolarization channel, the calibration procedure following the EARLINET rules [Freudenthaler et al., 2008] is also performed.

A preliminary design of the depolarization channel has been made in the Master Thesis (PFC) of Eric Vidal [Vidal, 2013]. The design concept of the depolarization channel is the same as the one of the Polly system used at the IFT (Institute for Tropospheric Research, Leipzig) lidar station [Heese et al., 2002] (Fig. 1.5). A significant difference is that our design is conceived around a double telescope configuration (Fig. 1.3) so that the collected powers are the total power (P_{Tot}) and the cross-polarized power ($P_{\perp}$). The proposed design offers two advantages: 1) the initial 6-channel design of the UPC multi-spectral lidar system is not modified, and 2) the total and cross-polarized powers are measured simultaneously by two independent telescopes.

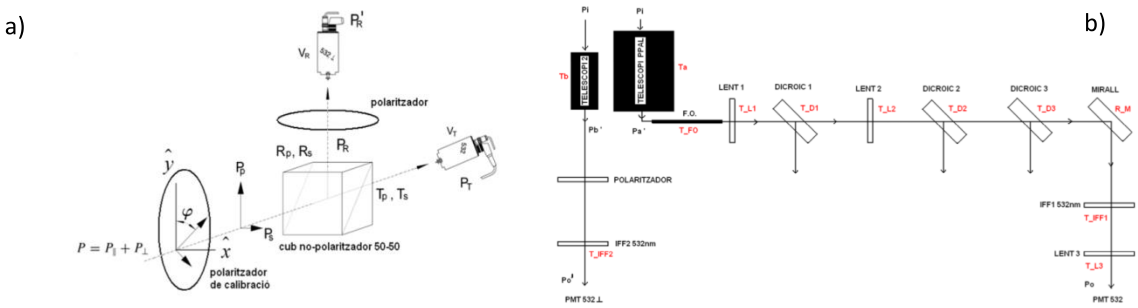

Fig. 1.5. Optical polarizer layout. (a) Scheme of the IFT LIDAR station (Polly system). (b) Scheme of the double telescope system.

OBJ. 2. Radiative forcing: Characterization of the radiative, optival and microphysical properties of the Mediterranean aerosol.

The following sections compose the development of this objective:

- Semi-automation of a radiative transfer code both in SW and in LW,
- Comparison with another radiative transfer model and validation with flux measurements (pyrgeometers and pyranometers).
- Application to a dust event detected during the ChArMEx (Chemistry-Aerosol Mediterranean Experiment, http://charmex.lsce.ipsl.fr/)/ADRIMED field campaign [Dulac et al., 2012] to obtain the aerosol direct 1-D radiative forcing with a unique radiative transfer code and uniform input data at several sites in the western and central Mediterranean Basin.

The GAME radiative transfer code allows to model SW (0.2 – 4 µm) and LW (4 – 40 µm) down- and upward fluxes assuming stratified plane and homogenous layers using the Discrete Ordinate Method (DOM) [Dubuisson et al., 1996]. The aerosol direct radiative effect (ARE) at the bottom and the top of the atmosphere is obtained through two computations, with (w) and without (0) aerosols: $DRF = (F^{DN,w} - F^{UP,w}) - (F^{DN.0} - F^{UP.0})$ where F^{DN} and F^{UP} are the down- and upward fluxes, respectively. The input parameters of a radiative transfer code include (i) the thermodynamic state of the atmosphere (such as pressure and temperature), (ii) the Earth's surface properties (albedo), and (iii) the aerosol properties in the atmospheric column (AERONET retrievals).

The *semi-automation of GAME* consists in the automated production of the input parameters files required by the model. By a Matlab® script the AERONET retrievals, the pressure and temperature from radiosoundings and the lidar backscatter measurements are transformed into the GAME input files and interpolated to the spectral and/or spatial resolutions of GAME. The proposed script allows performing much faster simulations and allows working with data from different stations, also lidar stations that do not meet EARLINET standards.

The aim is to compare the GAME code and the two-stream radiative transfer code, the latter is widely described in Tafuro et al., [2007]; Perrone and Bergamo, [2011] and Perrone et al. [2012]. The stay of PhD student S. Romano at CommSensLab will be used to compare the AREs provided by both models, previously parameterized using the same input sources (AERONET retrievals, lidar measurements and radiosoundings). It is planned to validate the modelled radiative fluxes for both models with radiometers data and after that, to study the temporal evolution of the radiative properties of a dust plume after mixing with marine aerosols [Meloni et al., 2003] and the deposition of the coarse fraction [Osada et al., 2014]. Fig. 1.6 shows the temporal evolution of the short-wave radiative effect at the surface between 20 and 24 June 2013.

Seasonal analysis of aerosol microphysical, optical and radiative properties based on AERONET-only data prior the calculations of aerosol DRFs, will be used to understand the background situation in the Western Mediterranean Basin (WMB) [Sicard et al., 2014b; 2016a] and how the results provided by GAME code and two-stream radiative transfer code let us know how the intrusion of a Saharan dust plume affect the atmosphere.

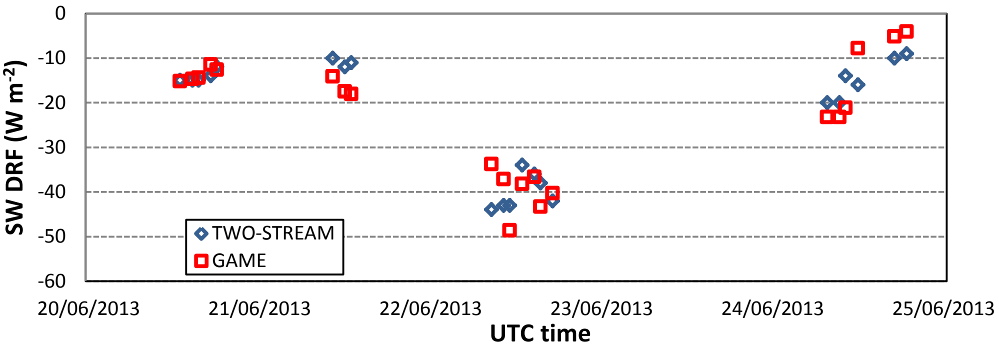

Fig. 1.6. Temporal evolution of the short-wave direct radiative effect at the surface, estimated by GAME (red squares) and two-stream (blue diamonds) during the period 20-24 June, 2013.

Obj. 3: Combined lidar/radar techniques for atmospheric observation: Ceilometer-based rainfall rate estimation.

Objective carried out in collaboration with the Dep. of Computer and Electrical Eng. of the University of Massachusetts (UMASS) as part of the 6-month stay of the candidate.

We plan to address RR estimation from vertical-configuration ceilometer measurements (Vaisala CL-31) and its limitations in comparison with collocated S-band FMCW radar and disdrometer RR measurements. The well-known slope-method and/or different variants of it [Kunz and de Leeuw, 1993; Rocadenbosch et al., 2000] will be considered to derive the rain optical extinction coefficient from the backscattered lidar signal. The methodological part will address the foundations of the RR retrieval procedures from both for both the ceilometer-radar and ceilometer-disdrometer combinations. Besides, derivation of suitable RR-to-extinction models that would allow us to estimate the RR from ceilometer measurements without need to permanently deploy the radar or the disdrometer in similar scenarios will also be considered. Emphasis will be given to the signal processing retrieval procedure for both the ceilometer and the radar. Because of the complexity of the radar system, retrieval of the radar reflectivity factor and radar RR using spectral estimation of the radar return will also be a goal. Verification of the ceilometer RR-to-extinction correlation hyphotesis will be carried out in the context of the VORTEX-SE [Rasmussen and Koch, 2016], as part of the Intensive Observation Period (IOP) carried out during spring 2016 in Huntsville, AL environs [Tanamachi et al. 2016], Fig. 1.7. The UMASS and Purdue University deployed the mobile S-band FMCW radar, collocated Vaisala CL-31 ceilometer (Fig. 1.4), and portable disdrometers. The NOAA National Severe Storms Laboratory deployed a Doppler lidar among other instruments.

Fig 1.7 illustrates the evolution of a rain event which took place near Belle Mina (Alabama, USA) during the first hours of 30 April 2016. First (ceilometer) and second (radar) strips show colorplot similarities in the vertical distribution of rain and its temporal evolution, all of which is in support of the correlation hypothesis proposed above and that will be further developed in this Ph.D.

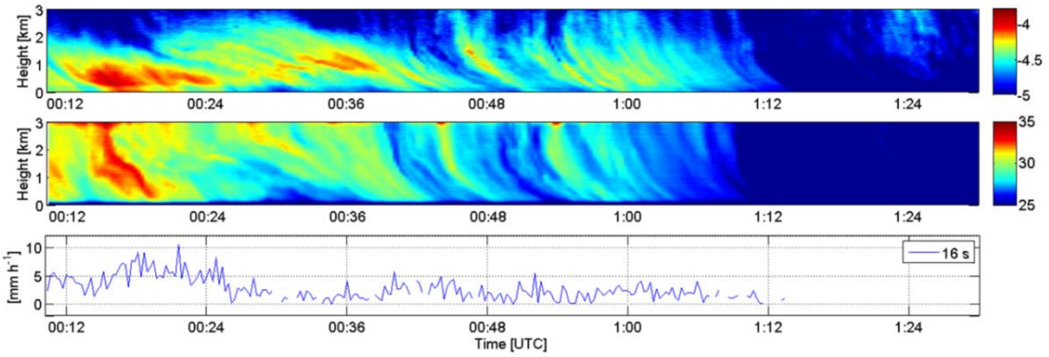

Fig. 1.7. Overview of 30 April 2016 rain episode (VORTEX-SE campaign, Bellemina, AL, environs). (a) Ceilometer range-corrected lidar signal (arbitrary units, (a.u.)) versus time. (b) Radar reflectivity factor (dBZ). (c) RR ($mm \cdot h^{-1}$) time series measured by the disdrometer.

1.5 ORGANIZATION OF THE PH.D. THESIS

This Ph.D. thesis is organized as follows:

Chapter 1 focuses on the motivation and main objectives of this Ph.D. and in relation to the CommSensLab multi-wavelength elastic/Raman lidar system and to the FMCW weather radar and ceilometer instruments from UMASS MIRSL.

Chapter 2 reviews lidar and radar atmospheric remote-sensing foundations of these instruments and presents the new CommSensLab 532-nm polarization channel. The latter is to enlarge the capabilities of the UPC lidar station (Fig. X) and to allow the retrieval of new optical and microphysical information from the atmospheric aerosols (Obj. 1).

Chapter 3 presents the importance of a correct parameterization and evaluation of the GAME Radiative Transfer Model, widely used in the CommSensLab Lidar group, by comparing the obtained fluxes and radiative effects to the ones obtained by a different radiative transfer model and by comparing the fluxes obtained feeding GAME with data from three different sources.

Chapter 4 gives a perspective of the evolution of the aerosol optical and radiative properties in the Mediterranean Basin, where CommSensLab Lidar Group is located, putting into practice the GAME code characterized in Chapter 3 and the acquired knowledge in lidar products, including depolarization information. This Chapter, together with Chapter 3, is in response to Obj. 2.

Chapter 5 follows with the radar- and ceilometer-based active remote sensing of the rainfall by taking advantage of the instrumentation deployed by the UMASS MIRSL, the University of Purdue, and the NOAA National Severe Storms Lab in the framework of VORTEX-SE field campaign., This Chapter is directly related to Obj. 3.

Chapter 6 gives concluding remarks along with future recommendations.

CHAPTER 2

Atmospheric Remote Sensing: Lidar, Radar and Radiative Transfer

This Chapter introduces the basic concepts and principles of lidar and radar remote sensing with focus on elastic lidar and FMCW clear-air weather radar as well as a description of the polarization channel developed for the CommSensLab multi-spectral lidar system and an overview of the concept of the Aerosol Radiative Transfer and related state-of-the art methods for Aerosol Radiative Transfer estimation.

2.1 INTRODUCTION

Nowadays, remote sensing techniques are a key component of the atmospheric research. Specifically, lidar and radar systems are the backbones when atmospheric and, more specifically, tropospheric profiling is needed. In both cases, the interaction of the emitted radiation (from natural or artificial sources) with the atmospheric constituents like aerosols, trace gases and clouds can be used to determine physical and environmental variables of interest like, temperature and humidity and to characterize atmospheric processes. The importance of tropospheric profiling is due to the fact that the troposphere, which is the lower layer of the atmosphere, contains approximately 80% in mass of the atmospheric constituents (aerosol/particles and molecules/gases aloft) and 99% of its water vapour and aerosols and is the place where most of human activities take place. Remote sensing technologies such as lidars, radar wind profilers, and Radio Acoustic Sounding System (RASS) [Seibert et al., 2000; Emeis et al., 2008] provide range-resolved profiles simultaneously for the whole observation range, which greatly improves the temporal resolution of ground instruments to enable a true monitoring of the lower part of the atmosphere compared to radiosounding methods [Sugiyama, G. and Nasstrom, J. S., 1999].

For ground-based remote sensing of the lower atmosphere, backscatter lidars are widely used as a key range-resolved atmospheric remote-sensing instrument to monitor the atmospheric constituents because it enables spatial resolution of a few meters and time resolution of a tens of seconds to a couple of minutes. These systems have been used since 1960's when it was first introduced by Fiocco and Smullin [1963] to measure the turbid layers of the atmosphere. Besides, lidars are the closest optical counterparts, of much better spatial and temporal resolution, of conventional microwave radars as they take advantage of the relatively strong interaction of laser light with the atmospheric constituents.

Within EARLINET, lidar systems have evolved from the basic elastic backscatter lidar to the more advanced multi-spectral elastic/Raman lidar with polarization capabilities (3+2+1 architectures and above). These systems play an essential role in ground truth calibration/validation in support of space missions such as CALIPSO [Winker et al., 2006]. Besides, co-operation between terrestrial lidar networks and satellite-borne lidars requires of quality-assured procedures both at system and algorithm level. When multi-spectral lidar data is considered, aerosol micro-physical properties inversion (size distribution) can also be achieved [Böckmann et al., 2008]. Also, independent inversion of the opto-atmospheric parameters of interest, namely, aerosol extinction, aerosol backscatter, and lidar ratio, has been tackled by combining at least one elastic and one inelastic Raman channel [Ansmann et al., 1992], multiple zenith-angle elastic signals (assumption of a horizontally stratified atmosphere) [Sicard et al., 2002], High Spectral Resolution Lidars (HSRL), and backscatter lidar measurements combined with sun-photometer measurements [Reba et al., 2010]. [Rocadenbosch et al., 2010a, 2012] presented an analytical formulation to compute the backscatter range-dependent error bounds for the one- and two-component elastic lidar inversion algorithm.

In the field of lidar signal processing the advances made - although sufficient from the operative point of view of the atmospheric observation stations - have comparatively been more modest than those achieved in radar. Fundamentally, because the bridge between the lidar remote sensing and signal processing disciplines (as inherited from the telecommunications area) is still immature.

Considering the radar, since the early 1960s, different type of radars have been developed in the VHF, UHF, and lower microwave frequency ranges, so they can measure the backscattered power from refractive index variations in the clear atmosphere and its morphology [Gossard, 1990]. FMCW clear-air radars were first introduced in the late 1960s to study the atmospheric boundary layer and lower troposphere. Since then, several such systems have been developed [Richter, 1969; Eaton et al., 1995], and virtually all of these radars operate at S - band, near 3 GHz. This frequency enables maximum azimuthal resolution (narrowest beam width) for a given antenna size while still retaining sensitivity to clear-air scattering from refractive index fluctuations with high resolution in height and time [Ince et al., 2003].

Finally, an important part in the research described here is the direct aerosol radiative forcing which assesses the effect of the atmospheric aerosols in the atmospheric radiative budget. For instance, the Mediterranean region, where CommSensLab lidar system is located, is one of the most sensitive regions to global warming according to recent climate projections [Giorgi, 2006]. Also, this region is often affected by mineral dust, one of the aerosols with the highest influence on the radiative budget [Forster et al, 2007; Mallet et al, 2016]. Mineral dust interaction with the atmospheric processes is one of the unknowns in the estimation of the Earth’s energy balance [IPCC, 2013]. The impact of the atmospheric aerosols, and especially mineral dust, radiative forcing on the climate of the western and central Mediterranean basin is of great concern [Mallet at al., 2016]. This topic is explored within ACTRIS (https://www.actris.net) and, especially, within ChArMEx projects. ChArMEx is a French initiative with nowadays a strong international participation.

This Chapter is organized as follows: In Sect. 2.2, lidar remote sensing fundamentals are detailed. Included in this Section, in Sect. 2.2.6, a complete description of the 532-nm polarization channel developed for the CommSensLab multi-spectral lidar is provided. Sect. 2.3 presents the radar fundamentals. Finally, in Sect. 2.4, an overview of the concept of the Aerosol Radiative Transfer and an overview of the GAME Radiative Transfer Model are presented.

2.2 LIDAR REMOTE SENSING

This type of sensors is the counterpart of radar sensors working in the optical wavelength spectral range. In this spectral range the interactions between electromagnetic radiation and atmospheric constituents are strong, allowing to detect the presence and concentration of aerosols and trace gases [Collis and Russell, 1976] and to measure the speed of wind [Huffaker and Hardesty, 1996] with high spatial resolution. Lidar principles were introduced in the 1930 decade, when first attempts to measure air density profiles were made by determining the scattering intensity from searchlight beams [Wandinger, 2005]. First atmospheric observations were published by Fiocco and Smullin [1963] using a ruby laser. Over the last four decades the lidar technique has proved to be an efficient tool for evaluating the stratification of aerosols, i.e., the vertical structure of the aerosol layers (base, top and thickness) and in particular of the planetary boundary layer (PBL). The retrieval of structural and optical properties which requires simple systems (one or two channels) exists since the 1960 and 1970 decades, while the retrieval of microphysical properties, which requires advanced systems, is much more recent (~year 2000)

Basically, a lidar system consists in general of collocated transmitter and receiver stages (Fig. 2.1) with fast photodetectors and acquisitions electronics. For aerosol remote sensing the transmitter is usually a pulsed laser, which emits light pulses to the atmosphere along the Line-Of-Sight (LOS) of the instrument and the receiver is an optical assembly with a telescope which acts as a collector of the backscattered radiation. The short pulse length produced by the laser source (approximately, 20 ns) and receiver detectors and electronics with sufficient bandwidth allow for highly-resolved ranging measurements with high SNR and pulse repetitions that range from a few to several thousand shots per second [McCormick and Leavor, 2013].

The optical signal is filtered to reduce the background radiation induced noise, converted into an electric signal by means of a fast photodetector, amplified, digitized and recorded. The time resolution of the optical signal is meaningless, since lidar signals are averaged over time intervals of a few seconds to minutes. Nowadays, the estimation of the particle extinction is the main design requirement; therefore the emitted laser beam wavelength must lie between the spectral transmission windows of the atmosphere in order to reduce the atmospheric attenuation. The most useful transparent spectral bands are the Visible (VIS) (0.4 - 0.7 m), the Near InfraRed (NIR) (0.7 - 1.5 m), and the windows between 3-5 m and 9-13 m. Since the 1980s, high-power excimer and Nd:YAG (Neodymium-doped: Yttrium Aluminum Garnet) lasers are widely used as a laser source. While excimer lasers produce UltraViolet (UV) radiation, Nd:YAG lasers emit in NIR spectral region at 1064 nm.

A common setup used along the Nd:YAG lasers is frequency doubling and tripling with nonlinear crystals to convert the primary 1064 nm radiation to 532 and 355 nm, respectively (this is the selected setup for the CommSensLab multi-spectral lidar system) resulting in effective three-frequency sources with wavelengths conveniently located in the spectral transmission windows of the atmosphere and the near ultraviolet. On the receiver side, besides a telescope used as an optical antenna, the combination of sensitive, compact and reliable photodetectors (avalanche photodiodes and photomultiplier tubes), interference filters and of fast and flexible acquisition systems allows for sensitive detection and storage of the faint returns from the atmosphere.

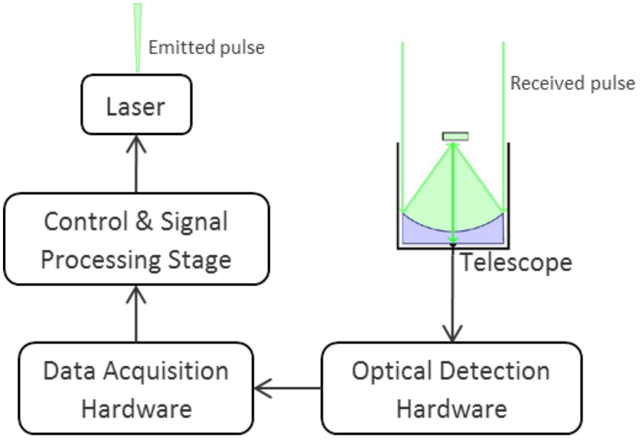

Fig. 2.1. Block diagram of a basic lidar setup. Transmitter (left) part: laser source or optical transmitter “antenna”, including perhaps an output beam expander to ensure eye-safety considerations or a silica plate to protect the laser aperture. Receiver (right) part: telescope or optical receiver “antenna” and the optical detection hardware. The latter includes spectrally selective equipment in order to detect the signal in all the desire wavelengths (an interference filter or a polychromator) depending on the type of lidar configuration and opto-electronic receiver/s, based on APD or PMT detectors. Finally, the optical laser return signal is recorded and processed in the control and signal processing stage.

In the case of the optical antenna, the Field-Of-View (FOV) is defined as the angle through which a detector is sensitive to electromagnetic radiation- It must be chosen as low as a few hundred μrad because laser beams are highly collimated and their divergence is often further reduced [Wandinger, 2005]. Cassegrain telescopes are typically chosen because their design provides moderate f-numbers (the ratio of the focal length of a lens or a lens system to the effective diameter of its aperture). The FOV is usually determined by a field stop in the focal plane of the receiver optics.

Following Fig. 2.1, laser radiation coming from the laser source is attenuated along the radiation path in the atmosphere and part of this radiation is scattered back towards the receiving optics by atmospheric constituents. Photons scattered back (i.e., the optical echo) to the receiver are collected by the telescope and then directed to a detector whose signal is analog-to-digitally recorded or counted as a function of altitude or range. The strength of the return signal is related to the physical and optical properties of the scatterers [McCormick and Leavor, 2013]. Elastic (emission and reception are done at the same wavelength) and Raman (the reception wavelength is shifted relative to that emitted by the Raman effect) lidar systems allow the measurement of optical properties such as the backscatter and extinction coefficients. Advanced lidar systems (at least three elastic channels and two Raman channels) also provide information on the aerosol microphysical properties (effective radius, single scattering albedo, modal volume concentration, complex refractive index).

2.2.1 ATMOSPHERIC EXTINCTION

The atmospheric extinction results from absorption as well as scattering from the constituents of the atmosphere According to the Beer-Bouguer's exponential extinction law, the spectral intensity of a laser pulse propagating along the range direction between distances $r = 0$ and $r = R$ in an inhomogeneous medium is given by [Beer, 1852; Collis and Russell , 1976] (see Fig. 2.2b)

$$\frac{I(\lambda,R)}{I_0} = T(\lambda,R) = \exp\left(-\int_0^R \alpha(\lambda,R)dr\right), \qquad [2.1]$$

where I_0 is the initial intensity at $r = 0$, I is the intensity $(W \cdot m^{-2})$ at $r = R$, λ is the operation wavelength (m), α is the total atmospheric extinction coefficient (m^{-1}) within the transmission range $[0, R]$ and $T(\lambda, R)$ $(\cdot)$ is the transmittance. Strictly speaking, Eq. 2.1 applies only to monochromatic radiation. However, it can also be applied to narrow wavelength intervals over which the intensity and the extinction vary slowly, as is the case of laser radiation for scattering (both molecular and aerosol), aerosol absorption, and ozone absorption, but not for gaseous line absorption [Lenoble et al., 2013]. The α is the sum of three simultaneous attenuation mechanisms: molecular (Rayleigh) scattering, aerosol (Mie) scattering, and absorption, since both molecules and aerosols absorb (radiative energy is transformed into another form of energy) and scatter (a part of the incident light changes its direction of propagation) radiation. That is

$$\alpha = \alpha_{aer,sca} + \alpha_{aer,abs} + \alpha_{mol,sca} + \alpha_{mol,abs} \quad (m^{-1}), \qquad [2.2]$$

where the subscripts aer, mol, abs, and sca stand for “aerosol” and “molecular” constituents, and “absorption” and “scattering” mechanisms, respectively [Rocadenbosch, 2003b]. Scattering is a function of the physical properties (e.g., refractive index, cross section, radii distribution) of the atmospheric constituents. Scattering of photons by the aerosols and the molecules can be defined in terms of their relative size with respect to the wavelength of the incident light. On the one hand, scattering by the aerosols, $\alpha_{aer,sca}$, is defined by Mie’s scattering, in which the size of scatterers is comparable to that of the incident wavelength. On the other hand, the molecular scattering, $\alpha_{mol,sca}$, is defined by the Rayleigh scattering mechanism since the size of the molecules is generally much smaller than the wavelength of the incident light. The aerosol extinction term, $\alpha_{aer} = \alpha_{aer,sca} + \alpha_{aer,abs}$, is computed from Mie's scattering models based on homogeneous dielectric spheres with a given radius distribution. Thus, the volumetric aerosol extinction coefficient can be written as

$$\alpha_{aer}(\lambda) = \alpha_{Mie}(\lambda) = \int_0^\infty \pi a^2 Q_{ext}(x,m) N_{aer}(a) da \quad (m^{-1}), \tag{2.3}$$

where a is the aerosol radius, Q_{ext} is the extinction efficiency (where $Q_{ext} = Q_{sca} + Q_{abs}$ with Q_{sca} and Q_{abs} the scattering and absorption efficiencies, respectively) $(\cdot)$, x is the particle size parameter defined as $x = 2\pi a/\lambda$ $(\cdot)$, m is complex refractive index $(\cdot)$, and $N_{aer}(a)$ is the aerosol number density per unit radius interval (m^{-3}). The term $\pi a^2 Q_{ext}(x,m)$ directly represents the extinction cross-section (m^2) for such a particle of radius a.

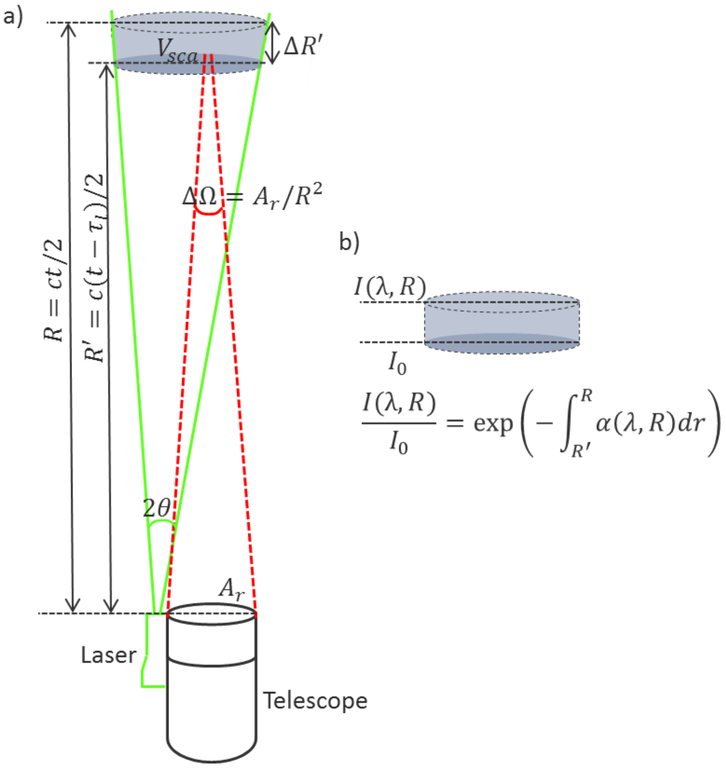

Fig. 2.2. Monostatic pulsed lidar setup geometry using a laser-telescope biaxial arrangement. (a) Transmitter and receiver parts, with V_{sca}, the scattering volume (or resolution cell), 2θ, the full-angle laser divergence (green solid lines), $\Delta\Omega$, the telescope solid angle subtended to the scattering volume (red dashed lines), A_r, the telescope effective area, $\Delta R = R - R' = c\tau_l/2$, the spatial difference between the leading edge and the trailing edge of the laser pulse, τ_l, and R, the range. (b) Sketch of the Beer-Bouguer's exponential extinction law. (Light blue volume), the scattering volume, (green fading away arrow) Incident/absorbed/scattered light intensity before/inside/after the scattering volume (light blue volume) (Adapted from Comerón et al. [2005]).

On the other hand, Rayleigh scattering coefficient is proportional to λ^{-4} (Rayleigh's spectral law) and is given in terms of the number density of gas molecules $(no.of\ molecules/m^3)$, N_g, and the Rayleigh's scattering cross-section $(m^2/molecule)$, $\varrho_{Ray}(\lambda)$, as follows the Rayleigh scattering extinction can be defined as

$$\alpha_{mol,sca} = \alpha_{Ray} = N_g \varrho_{Ray}(\lambda) \quad (m^{-1}), \tag{2.4}$$

According to Collis and Russell [1976], the dominant component of the total extinction, α, is the molecular absorption term, $\alpha_{mol,abs}$, which becomes a significant component of the total extinction only when the laser wavelength is tuned-in in an absorption band of the atmospheric molecule (or gas species) of interest, most frequently in the UV ($\lambda < 300\,nm$) and in the IR ($\lambda > 900\,nm$) regions of the spectrum, where the effective range of the lidar can be severely limited (Fig. 2.3).

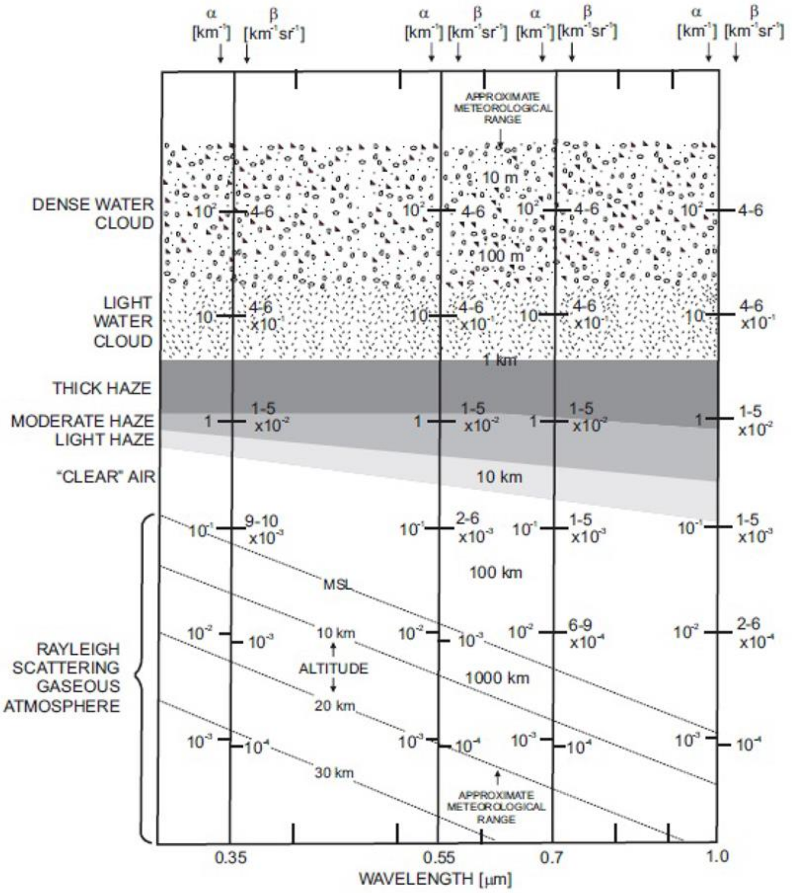

Fig. 2.3. Variation of extinction, α, and backscatter coefficients, β, with UV, VIS and NIR wavelength and atmospheric condition. Source: Fig. 4.8 in Collis and Russell [1976].

2.2.2 ATMOSPHERIC BACKSCATTER

While the total extinction, α, gives information about losses (absorption and scattering) in the emitted radiation flux, the total backscatter coefficient, β, describes how much light is scattered backwards 180 degrees to the incident light pulse, towards the lidar receiver, including contribution from molecular and aerosol scattering. It is the atmospheric parameter that determines the strength of the lidar signal return. It is defined as the volume scattering coefficient for a scattering angle $\theta = \pi$ (i.e. towards the telescope) [Wandinger, 2005]. As explained in the previous Section, the total backscatter coefficient, β, is defined as the a sum of contributions from both molecules, β_{mol}, and aerosols β_{aer}, as

$$\beta = \beta_{mol} + \beta_{aer} \quad (m^{-1}sr^{-1}), \tag{2.5}$$

In the atmosphere, light scattering properties of particles are difficult to be precisely described, because of their natural variability in shape, composition, and size [Collis and Russell , 1976; Lenoble et al., 2013]. Nevertheless, the total backscatter coefficient is directly related to the amount of light intensity received at the telescope of the lidar. The individual contributions from the molecular backscatter, β_{mol}, and the aerosol backscatter, β_{aer}, can be formulated on the similar lines as the total molecular scattering, $\beta_{mol,sca}$ (Eq. 2.4), and aerosol scattering, $\beta_{aer,sca}$ (Eq. 2.3). Consequently, as in Eq. 2.4, the molecular backscatter coefficient, β_{mol} due to atmospheric gases is described by Rayleigh scattering theory as

$$\beta_{mol}(\lambda) = \beta_{Ray}(\lambda) = N_g \frac{d\sigma_{Ray}(\pi,\lambda)}{d\Omega} \quad (m^{-1}sr^{-1}), \tag{2.6}$$

where $d\sigma_{Ray}(\pi,\lambda)/d\Omega$ (m^2sr^{-1}) is the differential Rayleigh's scattering cross section per solid angle unit in the backward direction. It is characterized by a λ^{-4} wavelength dependency [Andrews, 2004] and thus, the molecular backscatter, β_{mol}, in Eq. 2.6 above is insignificant at NIR wavelengths [Rocadenbosch, 2003b; Wandinger, 2005].

The aerosol backscatter coefficient, β_{aer} can be formulated analogously to Eq. 2.3 as [Deirmendjian, 1964, 1969]

$$\beta_{aer}(\lambda) = \beta_{Mie}(\lambda) = \int_0^{\infty} \pi a^2 Q_{back}(x,m) N_{aer}(a) da \quad (m^{-1}sr^{-1}) , \qquad [2.7]$$

where the term $Q_{back}(x,m)$ is the backscatter efficiency. The rest of the variables have been already defined in Eq. 2.3.

2.2.3 THE ELASTIC LIDAR EQUATION

Finally, the relationship between the measured lidar backscattered signal and the total backscatter coefficient is described by the, so called, elastic-backscatter single-scattering lidar equation. The elastic lidar equation joins extinction and backscatter parameters with the inherent lidar system parameters, refers to systems emitting at a single wavelength and designed to detect only the elastic return, i.e., the one in which the energy of the incident photons is conserved. The elastic lidar equation takes the form

$$\mathrm{P}(\lambda_0,\mathrm{R}) = \mathrm{K}\frac{\mathrm{O(R)}}{\mathrm{R}^2}[\beta_{aer}(\lambda_0,\mathrm{R}) + \beta_{mol}(\lambda_0,\mathrm{R})]\exp\left\{-2\int_0^{\mathrm{R}}[\alpha_{aer}(\lambda_0,\mathrm{r}) + \alpha_{mol}(\lambda_0,\mathrm{r})]\mathrm{dr}\right\} \quad (\mathrm{W}), \qquad [2.8]$$

where $\mathrm{P}(\lambda_0,\mathrm{R})$ is the backscattered laser power at wavelength λ_0 from the height R. K is the range-independent system constant and $O(\mathrm{R})$ is the overlap function (OVF). The range-independent system constant is defined as

$$\mathrm{K} = \frac{\mathrm{E}(\lambda_0)\xi(\lambda_0)\,\mathrm{A_r c}}{2} \quad (\mathrm{W}\cdot\mathrm{m}^3), \qquad [2.9]$$

where $\mathrm{E}(\lambda_0)$ is the pulse energy (J) at wavelength λ_0, $\mathrm{A_r}$ is the effective telescope receiving area (m^2) and $\xi(\lambda_0)$ the optics net transmission of the system $(\cdot)$ The OVF, inherent to any lidar, accounts whether the completeness of the laser-illuminated volume can be imaged on the detector (i.e., falls into the FOV of the telescope) [Measures, 1992c; McCormick and Leavor, 2013] and for a well aligned lidar system the OVF is unity from the range of full overlap (e.g., typically 200-1000 m depending on the system geometry) onwards (see Fig. 2.2). It depends on many different optical and geometrical parameters of the system, such as the geometrical separation between the laser and the telescope axes, the effective radius of the telescope aperture, laser aperture radius, field of view, imaging properties and laser divergence; as well as on the laser intensity distribution (irradiance) of the beam. [Halldórsson and Langerholc, 1978; Stelmaszczyk et al., 2005; Comeron et al., 2011; Kumar and Rocadenbosch, 2013].

Eq. 2.8 describes the operational capabilities of the lidar system, containing the laser-telescope OVF, $O(\mathrm{R})$ [Measures, 1992b], and excluding receiving optics losses such as those associated to lenses or interference filters. Assuming that the molecular terms in the lidar equation can be calculated by means of standard atmosphere conditions or an atmospheric density profile from radiosondes launched nearby lidar station, $\beta_{aer}(\lambda_0,R)$ and $\alpha_{aer}(\lambda_0,R)$ are the two height-dependent unknowns which must be retrieved from a single observable, $\mathrm{P}(\lambda_0,\mathrm{R})$. Therefore, two inputs are necessary from the user's side to solve the lidar equation: (i) a boundary calibration, usually in the form of a far-end backscatter-coefficient calibration; and (ii) an extinction-to-backscatter relation. This relation, a priori unknown, between aerosol backscatter and extinction coefficients is the extinction-to-backscatter ratio or lidar ratio (LR) of the scattering particles with

$$LR_{aer}(\lambda_0,R) = \frac{\alpha_{aer}(\lambda_0,R)}{\beta_{aer}(\lambda_0,R)} \qquad [2.10]$$

Under this assumption, the retrieval of the aerosol backscatter coefficient at λ_0, Eq. 2.5, can be solved by following the Klett-Fernald-Sasano algorithm [Fernald et al., 1972; Klett, 1981; Fernald, 1984; Sasano and Nakane, 1984; Klett, 1985]:

$$\beta_{aer}(R) + \beta_{mol}(R) = \frac{U(R) exp\left\{-2\int_{R_0}^{R}[LR_{aer}(r) - LR_{mol}]\beta_{mol}(r)dr\right\}}{\frac{U(R_0)}{\beta_{aer}(R)+\beta_{mol}(R)} - 2\int_{R_0}^{R} LR_{aer}(r) RCS(r) T(r,R_0) dr} \qquad [2.11]$$

where $U(R)$ is the range-corrected lidar return power, $U(R) = R^2P(R)$, LR_{mol} is the molecular LR, $LR_{mol} = \frac{\alpha_{mol}(\lambda_0,R)}{\beta_{mol}(\lambda_0,R)} = \frac{8\pi}{3}$. The exponential term is the transmission term (also called atmospheric transmissivity).

$$T(r, R_0) = \ exp\left\{-2\int_{R_0}^{r}[LR_{aer}(r') - LR_{mol}]\beta_{mol}(r')dr'\right\} \qquad [2.12]$$

In order to determine the aerosol backscatter coefficient, $\beta_{aer}(R)$, from Eqs. 2.11 and 2.12, the first user input require to solve the lidar equation, it has to be estimated at a specific reference height, $R_0(\beta_{aer}(R_0)$. This reference height is usually chosen such that at R_0 the aerosol backscatter coefficient is negligible compared to the known molecular backscatter value.

Fig. 2.2a shows a monostatic pulsed lidar setup geometry using a laser-telescope biaxial arrangement. Considering that the emitted laser pulses have to travel forth and back from the atmosphere, the range information is determined from the two-way-path time of flight of the emitted laser pulses to the scattering target (i.e., aerosols and/or molecules) as

$$\mathrm{R} = \frac{\mathrm{ct}}{2}, \qquad [2.13]$$

where, t is the time delay (s), and c is the velocity of light ($m \cdot s^{-1}$). The factor 2 is a consequence of the go-and-return path from the lidar instrument to the atmospheric scattering target.

Assuming that the transmitted laser pulse has a rectangular temporal shape and finite time duration, τ_l, the lidar signal is detected at an instant time t_0 (unlimited reception bandwidth or equivalently, nil detection time) after the leading edge of the laser pulse is emitted, the backscattered light produced by this leading edge arrives from a distance R (Eq. 2.13). At the same time, the trailing edge of the pulse produces backscattered light that comes from a distance $\mathrm{R}' = \mathrm{c}(\mathrm{t} - \tau_l)/2$. Therefore, the length of the scattering volume from which backscattered light arrives at any instant time t is

$$\Delta\mathrm{R}' = \mathrm{R} - \mathrm{R}' = \frac{\mathrm{c}\tau_l}{2} \quad (\mathrm{m}), \qquad [2.14]$$

where $\Delta\mathrm{R}'$ is known as the effective spatial pulse length (km) [Wandinger, 2005]. In practice, the detection time, τ_d, is not nil (because of a finite receiver bandwidth) and then the detected lidar signal at each time bin of the transient recorder (e.g., an analog acquisition card, photon-counter, or mixed unit) corresponds to the time interval $[\mathrm{t}, \mathrm{t} + \tau_d]$ rather than to the instant time t. As a consequence, the length of the observation volume contributing backscattered light into a given time bin becomes

$$\Delta\mathrm{R}' = \frac{\mathrm{c}(\tau_l + \tau_d)}{2} \approx \frac{\mathrm{c}\tau_d}{2}, \tau_l \ll \tau_d, \qquad [2.15]$$

Often, the duration of the emission laser pulses is comparatively much shorter than the detection time of the signal acquisition unit ($\tau_l \ll \tau_d$) so the effective spatial pulse length reduces to $\Delta\mathrm{R}' \approx \mathrm{c}\tau_d/2$, (Eq. 2.15). If the transient recorder unit operates in analog mode by sampling at a frequency $\mathrm{f_s}$, then the detection period becomes $\tau_d = 1/\mathrm{f_s}$ [Measures, 1992c].

As explained before, the laser emits a short pulse of time duration τ_l with a full-angle divergence 2θ and an operating wavelength λ_0, so that the laser beam actually illuminates a slightly divergent conical volume of space, V_{sca} (grey blue volume in Fig. 2.2a and Fig. 2.2b), whose length and cross section are $\Delta R'$ and πr^2 ($r = R\theta$), respectively. This beam propagates through the atmposphere, causing light to scatter isotropically [Kovalev, 2004; McCormick and Leavor, 2013]. Under practical approximation, the scattering volume can be considered cylindrical in shape ($V_{sca} = \pi r^2 \Delta R'$) [Skolnik, 2001], with R the mean distance.

A particular case are ceilometers, characterized by emitting in the near infrared (usually between 900 and 1100 nm) using inexpensive pulsed laser diodes with a high pulse repetition frequency and a low pulse energy in order to operate in eye-safe mode [Wiegner et al., 2014]. This type of lidars was originally designed for cloud-base height detection, but their use is rapidly growing due to their simplicity, small size, low cost and commercial availability. For instance, several national weather services have set networks of ceilometers operating in quasi continuous-unattended regime and providing near real-time data. Nowadays, the capability of the ceilometers to retrieve aerosol properties is constrained by technological limitations and suffer from significantly poorer SNR than more advanced lidar systems, but the use of this system is spreading out throughout the scientific community as complement of the existing networks of advanced lidar stations, with the aim of increasing both the spatial density of available aerosol data and the temporal continuity of observations [Wiegner et al., 2014, Madonna et al., 2015].

The detection of the molecular return at aerosol-free altitudes, required for the backscatter calibration at a reference height, becomes problematic and makes it difficult a correct quantitative retrieval of aerosol optical properties. Their current use is thus focused on the detection of cloud base heights and, regarding aerosol information, on vertical-structure profiling, which in turn allows determining meteorological parameters like the mixing layer height using the aerosols as a proxy [Coulter, 1979]. The basic functional scheme of a typical commercial ceilometer is formed by a pulsed laser diode as light source (typically 5–10 kHz PRF and 1–10 mJ pulse energy), an optical assembly to collect the backscattered radiation (100–200 mm diameter), a photodetector, commonly an avalanche photo diode (APD), and a digitizer board. Common performance parameters result in typical time and range resolutions of 5 min and 15 m and maximum range of 7.5 km.

2.2.4 THE RAMAN LIDAR EQUATION

As mentioned in Sect. 2.1, common lidar configurations, as is the case of the CommSensLab multi-spectral lidar system, include elastic and Raman channels. Difference between elastic and Raman interaction is depicted in Fig. 2.4a, 2.4b, 2.4c and 2.4d. In contrast to elastic scattering, the Raman scattering process involves an internal energy transition of the molecular species of interest (atoms and molecules in the atmosphere) and introduces a series of side-band frequencies, Δv, around the incident frequency, v_0 (Hz), in which the amount of shifting is equivalent to the vibrational-rotational frequencies of the molecules being irradiated. This frequency shift can be formulated as [Inaba, 1976]

$$v_R = v_0 \pm \Delta v \quad (Hz), \qquad [2.16]$$

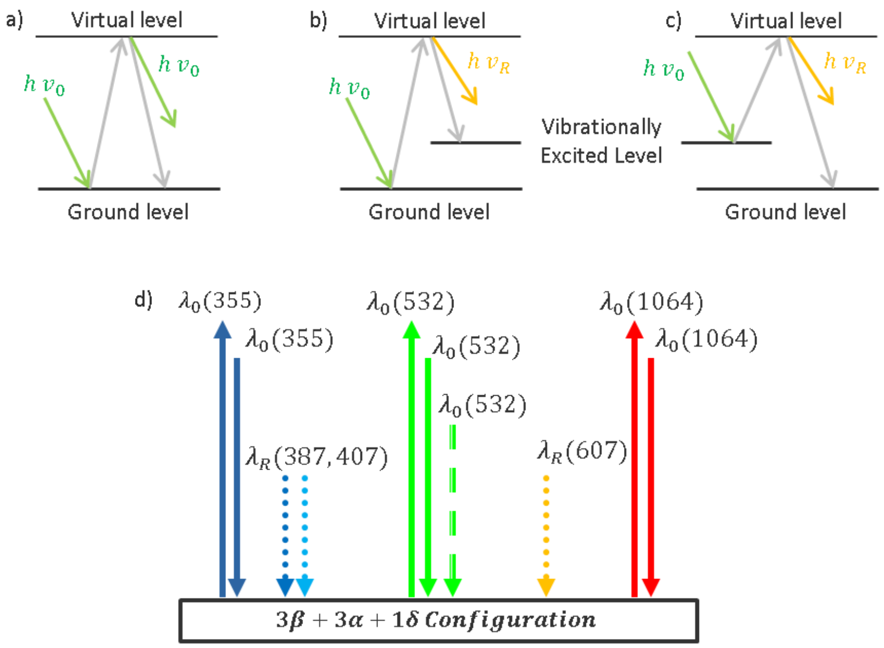

Fig. 2.4. Elastic/Raman interaction and 3+3+1 elastic/Raman configuration. (a) Sketch of the elastic scattering for a single photon (green arrow). (b) Same as (a) for vibrational Raman scattering, where h stands for the Plank constant, v_0, the incident (and also the scattered in (a)) frequency, and v_R, the Raman frequency. (c) Same as (b) in the case of anti-Stoke Raman interaction. (d) The 3+3 elastic/Raman configuration. Elastic interaction (emission and reception wavelength coincide) is depicted in solid arrows. Raman interaction is depicted in dotted lines and close to the corresponding elastic wavelengths. Up arrows indicate emission, down arrows indicate reception. (Adapted from Measures, 1992a; Comerón et al., 2005).

The frequencies shifted down ($\Delta v = -1$) are called Stokes lines while those shifted up ($\Delta v = +1$) are called anti-Stokes lines. The Raman scatterer molecule absorbs energy by being excited to a higher energy level while the frequency of the scattered photon decreases. The wavelength of the scattered photon is shifted towards higher values; this process is known as Stoke Raman scattering. In the case of anti-Stoke lines, the frequency of scattered light, v_R, compared to the frequency of incident light, v_0, is shifted by Δv. However the scattering molecule might also loose energy to the scattered photon and decrease its energy level. The frequency of the scattered photon is now increased (shifted up) and the wavelength is shifted towards lower levels. A pure rotational band ($\Delta v = 0$) is centered on the incident frequency. The Raman lidar principle lies in that, for a purely molecular atmosphere, the law followed by the molecule-specific Raman-shifted radiation collected by the lidar receiver is known, as it only depends (assuming it does not fall in the absorbing spectrum of an atmospheric gas) on the species number concentration and the molecular scattering. In comparison with the elastic-backscatter lidar equation, in which both the optical emission path (i.e., from the laser source to the atmosphere) and return path (i.e., from the atmosphere back to the telescope) were operating at the same wavelength, if λ_0 is the laser emission wavelength and $k = 1/\lambda\ (m^{-1})$ is the wavelength shift associated to the molecular species of interest producing the Raman scattering then the Raman return wavelength, λ_R, can be computed as

$$\lambda_R = \frac{\lambda_0}{1-\lambda_0 k} \quad (m). \qquad [2.17]$$

As Raman molecular scattering cross-sections are 3-to-4 orders of magnitude weaker than elastic ones, thus, leading to vary faint returns, aerosol-monitoring Raman lidars resort to any abundant atmospheric species such as nitrogen, oxygen or water vapor to interact with. Also, Raman lidar require highly energetic laser pulses, larger telescopes, sensitive detectors (PMTs), longer integration times, and are usually limited to night-time operation [Rocadenbosch, 2003a; Kumar et al., 2012].

Usually the Raman channels are spectrally tuned to receive backscattered radiation from atmospheric nitrogen molecules. Nitrogen is nearly always the chosen species, because it is the most atmospheric abundant constituent (78 % volume concentration) and with a very well-known Raman cross-section. The setup of a cooperative N_2 Raman channel for atmospheric aerosol lidar sensing is of advantage to calibrate the elastic channel and hence, to obtain independent retrievals of both extinction and backscatter atmospheric optical components [Ansmann et al., 1992]. In the case of the CommSensLab multi-wavelength lidar system emitting at $\lambda_0 = 355$ (UV), 532 (VIS) and 1064 nm (NIR) wavelengths, the 3+3+1 elastic/Raman receiving wavelengths are plotted in Fig. 2.4d.

As mentioned above, the Raman return wavelength is different than the laser emission wavelength; therefore the transmittance in this case is a two-way path transmittance ($T_0(\lambda_0, R)T_R(\lambda_R, R)$) in contrast to the two-way elastic transmittance given by $T(\lambda_0, R)^2$,

$$T_0(\lambda_0, R)T_R(\lambda_R, R); \quad T(\lambda_i, R) = exp\left\{-\int_0^R [\alpha_{aer}(\lambda_i, r) + \alpha_{mol}(\lambda_i, r)]dr\right\}. \qquad [2.18]$$

In addition, since the Raman-reception channel is specifically tuned to receive backscattered radiation from the atmospheric N_2 molecules at the Raman shifted wavelength ($\lambda_R = 607.4$ nm for an emission wavelength $\lambda_0 = 532.1$, Eq.(2.17)), the Raman backscatter coefficient is computed as

$$\beta_{\lambda_R}(R) = N_R(R)\frac{d\sigma_{\lambda_R}(\pi)}{d\Omega} \quad (m^{-1}sr^{-1}), \qquad [2.19]$$

where $N_R(R)$ is the nitrogen molecule number density at λ_R and $\frac{d\sigma_{\lambda_R}(\pi)}{d\Omega}$ is the range-independent nitrogen Raman backscatter cross-section per solid angle unit. Accordingly, the Raman lidar equation can be written as

$$\mathrm{P}(\lambda_R, R) = \frac{K}{R^2}\left[N_R(R)\frac{d\sigma_{\lambda_R}(\pi)}{d\Omega}\right] exp\left\{-\int_0^R [\alpha_{aer}(\lambda_0, r) + \alpha_{mol}(\lambda_0, r) + \alpha_{aer}(\lambda_R, r) + \alpha_{mol}(\lambda_R, r)]\right\}\xi(\lambda_R, R), \qquad [2.20]$$

where atmospheric absorption effects have been neglected. In order to compute Eq. 2.20, $N_R(R)$ and $\alpha_{mol}(\lambda_0; \lambda_R, r)$ profiles are approximated from a US-standard atmosphere model along with temperature/ pressure ground-level conditions or from temperature/pressure radiosounding measurements [Bodhaine et al., 1999].

2.2.5 DEPOLARIZATION RATIO

In order to get advanced aerosol micro-physical properties, some lidar systems can present polarimetric capabilities, based on a depolarization channel, as mentioned in Sect. 2.1. Due to the particle shape information associated to lidar depolarization, the detection of non-spherical particles can be highly improved (see for instance [Olmo et al., 2008; Müller et al., 2013; Burton et al., 2015; Veselovskii et al., 2016; Chaikovsky et al., 2016]). Besides, the depolarization information, combined with additional optical properties, retrieved by means of the methods explained above; is widely used for aerosol typing (e.g., [Winker, 1992;,Murayama et al., 2004; Tafuro et al., 2006; Tesche et al., 2009; Groß et al., 2011a; Groß et al., 2011b]). Since the 1970s the use of the lidar depolarization technique, has proven to be a valuable tool for atmospheric sciences [Schotland et al., 1971; Pal and Carswell, 1973], for instance, depolarization capabilities are very useful in the retrieval of the atmospheric boundary layer (ABL) height since these capabilities allow to discriminate between the aerosol within this layer and different aerosol types coupled to the ABL height based on aerosol data [Wandinger et al., 2008]. Also depolarization capabilities have proven their utility, combined with the color ratio, discriminating among different kinds of aerosols and clouds [Wandinger et al., 2008; Burton et al., 2012].

Next, it is introduced how a depolarization channel works and how the particle depolarization ratio (δ^P) and the molecular volume depolarization ratio (δ_{mol}) are obtained from the received power. Thus, the voltage signal obtained at the total-power PMT output can be written as:

$$S_{Tot}(R) = V_{Tot}(R) \cdot P_{Tot}(R), \qquad [2.21]$$

where $V_{Tot}(R)$ is the total-power 532-nm channel responsivity including the effect of the partial overlap and $P_{Tot}(R)$ stands for the backscattered light collected, in power units, at 532 nm by the main telescope of the system. The voltage signal obtained at the depolarization channel PMT output can be estimated as the total voltage in Eq. 2.21,

$$S_{Dep}\left(90^{\circ}, R\right) = V_{Dep}(R) \cdot P_{\perp}(R), \qquad [2.22]$$

where $V_{Dep}(R)$ is the depolarization channel responsivity including the effect of the partial overlap, and $P_{\perp}(R)$ is the cross-polar fraction power of the depolarized backscattered light.

The depolarization channel system function is defined as:

$$V^{*}(R) = \frac{V_{Dep}(R)}{V_{Tot}(R)}, \qquad [2.23]$$

While is very difficult to determine $V_{Dep}(R)$ and $V_{Tot}(R)$ in a separate way, it is possible to determine $V^{*}(R)$ by means of a calibration process that compares the output signals of the total-power channel and the depolarization channel, when the polarizer is set successively at + and −45° from its nominal position [Freundethaler et al., 2009]. By setting the polarizer in these calibration positions (45° from its nominal position), the optical path of the depolarization channel is proportional to the total power:

$$V^{*}(R) = 2\sqrt{\frac{S_{Dep}(90^{\circ}-45^{\circ},R)}{S_{Tot}(R)} \cdot \frac{S_{Dep}(90^{\circ}+45^{\circ},R)}{S_{Tot}(R)}}, \qquad [2.24]$$

The factor 2 in Eq. 2.24 above, takes into account that, at the calibration positions, the depolarization channel is detecting half of the total backscattered power.

Furthermore, the volume depolarization is defined as [Freudenthaler et al., 2009]:

$$\delta^{V}(R) = \frac{P_{\perp}(R)}{P_{\parallel}(R)}, \qquad [2.25]$$

Assuming that $P_{Tot}(R) = P_{\parallel}(R) + P_{\perp}(R)$, the volume depolarization can be estimated by means of the depolarization channel system function [Vidal, 2017] as:

$$\delta^{V}(R) = \frac{\delta^{*}(90^{\circ},R)}{V^{*}(R) - \delta^{*}(90^{\circ},R)}, \qquad [2.26]$$

where

$$\delta^{*}\left(90^{\circ}, R\right) = \frac{S_{Dep}(90^{\circ},R)}{S_{Tot}(R)}, \qquad [2.27]$$

Finally, the particle depolarization ratio can be computed by combining the volume ratio with the molecular and aerosol backscattering profiles [Freudenthaler et al., 2009]:

$$\delta^P(R) = \frac{[1+\delta_{mol}]\cdot\delta^V(R)\cdot\rho(R)-[1+\delta^V(R)]\cdot\delta_{mol}}{[1+\delta_{mol}]\cdot\rho(R)-[1+\delta^V(R)]}, \qquad [2.28]$$

where

$$\rho(R) = \frac{\beta_{mol}(\mathrm{R})+\beta_{aer}(\mathrm{R})}{\beta_{mol}(\mathrm{R})}, \qquad [2.29]$$

where $\beta_{mol}(\mathrm{R})$ and $\beta_{aer}(\mathrm{R})$ stand for the molecular and aerosol backscattering profiles, retrieved by means of a Klett–Fernald [Klett, 1981; ,Fernald, 1984] or Raman [Ansmann et al., 1990; Ansmann et al., 1992] inversion performed over the signal of the total-power channel.

Finally, the molecular volume depolarization ratio:

$$\delta_{mol} = \frac{\beta_{\mathrm{mol},\perp}}{\beta_{\mathrm{mol},\parallel}}, \qquad [2.30]$$

computed according to Behrendt and Nakamura [2002], has an approximately constant value of 3.8 × 10^{-3} for a receiver with a spectral width of 0.5 nm, as the one installed in the CommSensLab multi-spectral lidar system.

2.2.6 COMMSENSLAB 532-NM POLARIZATION CHANNEL

In this section, is discussed the implementation of a polarization channel in the CommSensLab multi-spectral lidar system.

This paper was published in Sensors. The paper can be found at the following URL on the Sensors website: https://www.mdpi.com/1424-8220/17/12/2957. Systematic or multiple reproduction or distribution to multiple locations via electronic or other means is prohibited and is subject to penalties under law.

2.2.6.1 SYSTEM ARCHITECTURE

Because of the importance of depolarization measurements for aerosol science, a new depolarization measurement channel has been developed and implemented for the CommSensLab multi-spectral lidar system. As mentioned in Sect. 2.1, some of the lidar systems present now polarization capabilities and most of these lidar systems [Althausen et al, 2000; Tesche et al, 2009; Freudenthaler et al, 2009; Esselborn et al, 2009; De Tomasi and Perrone, 2014; Engelmann et al, 2016; Freudenthaler, 2016] use a single telescope and a polarizing beam-splitter that separate the parallel and perpendicular polarization components of the light collected by the telescope or a non-polarizing beamsplitter in one of whose outputs a polarizer is inserted. In the case of the CommSensLab multi-spectral lidar system (see Fig. 2.4d), it is installed an additional telescope, next to the original one, to measure the cross-polarized return signal. Therefore, in order to perform aerosol depolarization ratio measurements it is necessary a comparison between the signals recovered by two different channels that operate at 532 nm: one proportional to the total power and another proportional to the cross-polar component of the collected light [Sassen, 2005; Comeron et al., 2015].

The axe of the telescope sensitive to the cross-polar component is parallel with the axe of the laser beam, separated by 40 cm, causing the partial overlap between the part of the atmosphere illuminated by the laser beams and that “seen” by the receivers that affects to the amount of light collected from short distances [Halldórsson and Langerholc, 1978, Stelmaszczyk et al., 2005; Comerón et al., 2011; Kumar and Rocadenbosch, 2013; Engelmann et al., 2016; Freudenthaler, 2016 Rodríguez-Gómez et al., 2017]. The original telescope, used by the channel proportional to the total power, sends the collected backscattered light to a wavelength separation unit, which splits the light to the different channels, by means of a custom-made 3 m long fiber bundle. The polarization performance of the fiber bundle has been tested [Vidal, 2017], finding that, for a linearly polarized input, the power values measured at the output of a polarization analyzer show a standard deviation of less than 1%. Therefore, it can be considered that the light coming out of the fiber bundle shows a nearly total effective depolarization. This fact permits to consider that the 6 channels of the CommSensLab multi-spectral lidar system are basically sensitive to the total collected power, without any polarization discrimination, even though the wavelength separation unit includes several beam-splitters that could cause di-attenuation. The overall calculated transmission of the fiber bundle and the wavelength separation unit at the 532 nm output is 6.18% [Kumar et al., 2011].

Fig. 2.5 shows the optical path of the depolarization channel. The basic elements (Fig. 2.5a) are a separate secondary telescope (70 mm aperture, 300 mm focal distance TAIR-3S telephoto lens, BelOMO, Minsk, Belarus) and a polarization analyzer, from now on polarizer, (P), located in the focal plane of the secondary telescope. The rest of the optical arrangement, sketched in Fig. 2.5b, includes a field-of-view stop iris (D), an eye-piece lens (L4) and an interference filter (IF). The polarization analyzer consists on a linear polarizer mounted on the goniometric mount that can be seen in Fig. 2.5a. The characteristic of this optical path are summarized in Table 2.1.

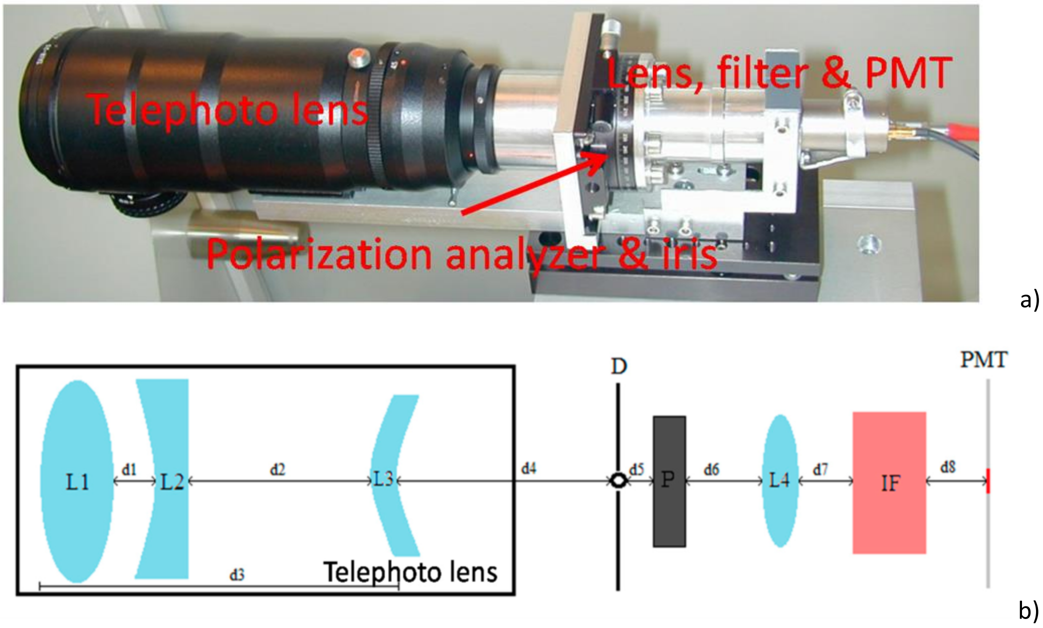

Fig. 2.5. (a) Optical mount of the secondary depolarization channel. Most relevant elements labelled in red. Source: Fig. 2 in Rodríguez-Gómez et al. [2017]. (b) Depolarization channel optical configuration; L1 to L3 are the lenses included in the telephoto lens; L4 works as an eye-piece lens that produces an image of the telephoto lens input aperture on the PMT active surface; P is a polarizing analyzer; IF is an interference filter centered at 532 nm; distances d4 to d8 are listed in Table 2.1.

Some of the parameters provided in Table 2.1 have been determined experimentally and adjusted for an optimal performance of the depolarization channel. Every component (except for the telephoto lens) has a diameter of 2.54 mm. The distances between the lenses included in the telephoto lens (d1 to d3) are not provided by the manufacturer, while distance d4 has been estimated as a function of its overall performance.

The nominal position, the position in which the measurements should be performed, of the polarizer is 90° from the transmitted beam polarization plane; making the channel sensitive to the cross-polar component of the light backscattered by the atmospheric constituents.

Table 2.1: Parameters of the different optical elements of the depolarization channel.

Parameter	Value
d4	138.9 mm (estimated)
d5	1 mm
d6	39.4 mm
d7	5 mm
d8	23 mm
Telephoto lens focal length	300 mm
Eye-piece lens focal length	38 mm
FOV stop iris diameter	1 mm
Interference filter	BARR 532-0.5 nm (custom made)
Center wavelength	531.9 nm
Spectral width	0.5 nm
Thicknes	11 mm

2.2.6.2 CALIBRATIONS

The determination of the depolarization channel system function is made by means of a calibration procedure that compares the outputs of the depolarization and the total power channels [Althausen et al, 2000; Kokkalis, 2017; Vidal, 2017]; during the calibration the polarization analyzer of the depolarization channel is set first at +45°, and second at −45° from the nominal position. The outputs of the depolarization and total power channels are divided and then a geometrical average is computed (as indicated in Eq. 2.24) between the system profiles obtained at the two positions. Finally, the values obtained for heights over ~10 km are discarded due to noise effects, being the value obtained at 10 km the one used for greater heights.

Several calibrations have been performed since the implementation of the depolarization channel, and the history is presented in Fig. 2.6. The color sequence shows the time evolution of the estimated system functions. As the colder colors point out, the early functions are affected by mechanical instability in the mutual alignment between the laser and the depolarization channel receiving telescope. The most recent calibrations are stabilized to a medium-height above ground level (AGL) value around 4, showing a deviation lower than 10%, while the deviation of the early functions is greater than 30%.

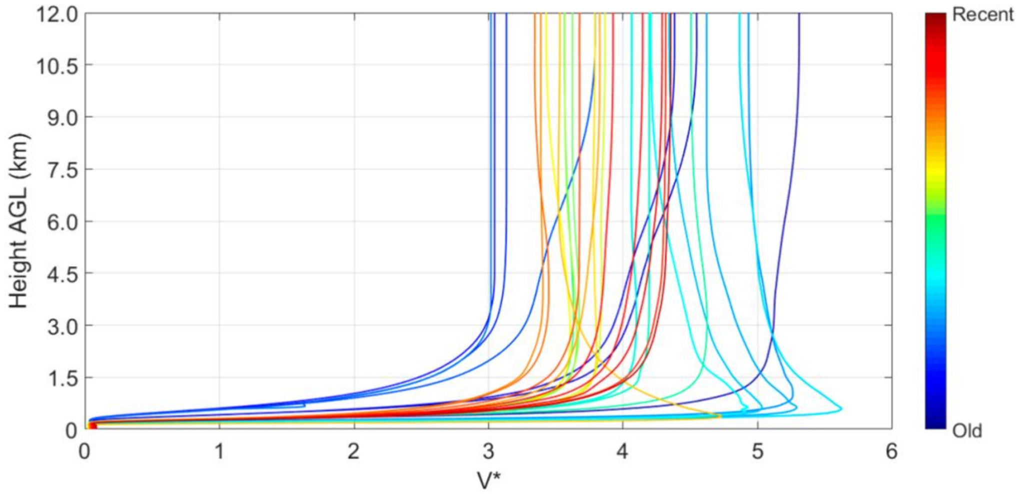

Fig. 2.6. History of the calibrations of the depolarization channel system function obtained from March 2016 to June 2017. The colder colors refer to early calibrations while the warmer ones to the recent ones.

The system function includes the effect of the different overlap functions [Halldórsson and Langerholc, 1978; Wandinger, 2005; Stelmaszczyk et al., 2005; Kokkalis, 2017; Comeron et al., 2011; Kumar and Rocadenbosch, 2013] of the two channels; it also draws attention on the fact that, even though the ratio of the main telescope and the telephoto lens collecting surfaces is approximately 25, the depolarization channel optics has a higher transmission.

2.2.6.3 DEPOLARIZATION RATIO MEASUREMENTS

Fig. 2.7 shows some the retrieval of volume and particle depolarization for different aerosol loads, dust (Fig. 2.7a) and fire smoke (Fig. 2.7b). The measurements are compared with those from a collocated SigmaSpace MPL-4B-IDS Series micro-pulse lidar (SigmaSpace Corporation, Lanham, MD, USA) [SigmaSpace, 2012]. The volume depolarization ratio is retrieved from both total power and depolarization signals and the calibration depolarization channel system function, V*(R), following equations above. The particle depolarization ratio is then retrieved with Eq. 2.28 from the volume depolarization ratio and the particle backscatter coefficient, β_p [Belegante et al., 2016]. β_p has been retrieved with the Klett–Fernald [Fernald et al., 1972; Fernald, 1984; Klett, 1981; 1985] method and a constant lidar ratio of 50 srad. Every profile of the molecule backscatter coefficient, β_{mol}, is calculated with the closest (in time) radio-sounding either at 12 or 00 UTC. The error bars are calculated following the well-known technique of the error propagation [Goodman, 1960; Ku, 1966]. For the sake of clarity, the points of the profiles of the particle depolarization ratio for which the error bar is larger than 50% are not represented.

Fig. 2.7a shows typical values of depolarization for mineral dust. The mineral dust intrusion observed here present AOD values about 2 [Costa et al., 2017]. Above 1 km, δ^V is in the range 0.17–0.24 and δ^P in the range 0.23–0.28. The small differences between δ^V and δ^P are due to the high values of the particle backscatter coefficient (~15 $Mm^{-1}sr^{-1}$) inside the dust layer. According to Sassen and Hsueh [1998], the values of δ^P are in the upper range of desert dust mixtures (0.14–0.28) and below the values of pure desert dust (0.30–0.35). The agreement with the MPL measurements only takes place at height over 1 km, once again probably because of the MPL sensitivity to the overlap function correction in weak aerosol loads.

The example shown in Fig. 2.7b illustrates the transport of aged smoke from Canadian fires to the Iberian Peninsula on 24 May 2016, at 15 UTC. The aged smoke layers were first detected on the evening of 22 May and lasted until the evening of 24 May. In Fig. 2.7b the fire smoke layer can be seen at 2 km, under a dust layer above 3.5 km. In the fire smoke plume δ^P ranges between 0.05–0.10, in agreement with Groß et al. [2013] which found values of δ^P for pure biomass burning measured in several places around the world in the range 0.02–0.08, being values of fresh smoke slightly lower than for aged smoke.

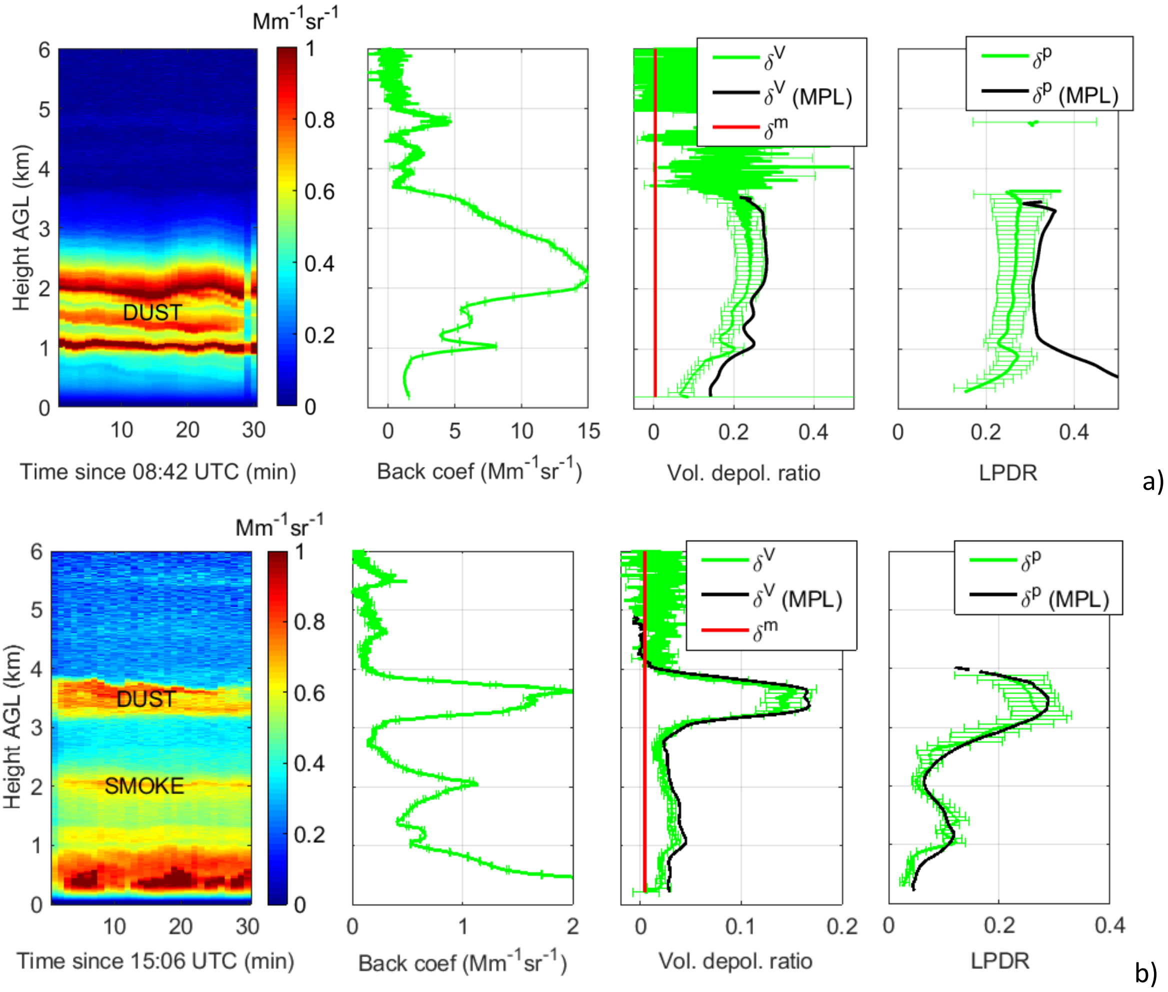

Fig. 2.7. Some examples of volume and particle depolarization ratio retrievals showing (left) time-height plots of range-square corrected signals in arbitrary units, (center) particle backscatter coefficient at 532 nm, (right) volume and particle depolarization ratios at 532 nm for (a) dust and (b) dust and fire smoke. The points of the particle depolarization ratio profiles for which the associated error is larger than 50% are not represented.

2.3 RADAR FUNDAMENTALS

Propagation of electromagnetic radiation in the atmosphere depends directly on the atmospheric physical properties. The most common radar applications try to avoid or minimize the atmospheric effects, but, in the weather-radar case, those effects are maximized for observing the atmosphere behavior, and the solid targets are treated as noise. In what follows, the radar concepts given in Chapter 1 and Sect. 3.4 of Mahafza [2005], are summarized.

The study of the scattering of electromagnetic waves by turbulent media has been approached by many authors, among them stands out Tatarski'i [1961]. This research presents general view of the theoretical results that served as a basis for interpreting a variety of experimental studies. In Ottersten [1969] can be found a summary of these theoretical basis, allowing to define the relationship between the concepts used to describe an atmospheric phenomena and the measurable quantities which characterize the atmospheric turbulence.

Radar systems can be classified following two different criteria: (i) by the type of waveforms or (ii) by their operating frequency (see Table 2.2). In the first case, radars can be Pulsed (PR) or Continuous Wave (CW) radars. PR radars transmit and receive a train of modulated pulses, and range information is extracted from the two-way time delay between a transmitted and received pulse. On the other hand, CW radars continuously emit electromagnetic energy, the transmitted signal is constant in amplitude and frequency, and use separate transmit and receive antennas (or a single Tx/Rx antenna and a circulator), that allows to receive and process permanently the echo signal. The CW radars without modulation can accurately measure target radial velocity (due to Doppler shift) and angular position, however to extract range information it is necessary some form of modulation because of the lack of pulses [Mahafza and Elsherbeni, 2004]. But, thanks to frequency shifting methods, this CW disadvantage can be corrected. Thus, in order to detect stationary targets, a signal that constantly changes in frequency around a fixed reference frequency is used. When an echo signal is received the frequencies are examined and compared to the original frequency emitted. This principle permits a range calculation similar to using a train of pulses. This specific type of radar is known as Frequency-Modulated Continuous Wave radar, which use a smoothly varying ramp of frequencies up and down instead of random frequencies.

Table 2.2: Radar frequency band classification [Mahafza and Elsherbeni, 2004].

Letter Designation	Frequency Range (GHz)
HF (High Frequency)	0.003 – 0.03
VHF (Very High Frequency)	0.03 – 0.3
UHF (Ultra High Frequency)	0.3 – 1.0
L-band	1.0 – 2.0
S-band	2.0 – 4.0
C-band	4.0 – 8.0
X-band	8.0 – 12.5
Ku-band	12.5 – 18.0
K-band	18.0 – 26.5
Ka-band	26.5 – 40.0
MWF	> 34.0

Focusing on weather-radar systems, historically, while rain precipitation were detected using radars since the early beginning of the radar technology, and the first meteorological observations exploiting radar were made in 1941, it was not until the early 1970s when Doppler radar started to provide meteorological research with full efficiency [Sauvageot, 1992b]. Also in the early 1970s, thanks to the VHF and UHF radar systems (Table 2.2) appeared the first clear-air detection techniques, allowing a continuous observation of the atmosphere, and not only when rain precipitation was present. Nowadays, most weather radar systems use either S-band or C-band [Mahafza and Elsherbeni, 2004]. Weather-radar systems are remote sensing systems that detect variations of the refractive index of the atmosphere that are in the same order as the wavelength of the sensor [Stull, 1988a].

In clear-air radar, two different types of scattering are present. First, the refractive index gradients give rise to Bragg scattering [Contreras and Frasier, 2008], which is the signal component. On the other hand, hydrometeors and hydrometeors-like scatterers as insects and birds produce Rayleigh scattering and are considered the noise component in addition to usual thermal noise. To remove the contribution of such scatterers, different techniques have been developed: for instance, Angevine et al. [1993]; Angevine [1997] have based their method on the elimination of the spatial samples or “outliers” characterized by a SNR, speed or spectral width exceeding a predetermined standard-deviation threshold (usually 2-3 σ) computed over 1-h measurements. Out-of-threshold signal levels are discarded as outliers hence preserving information on the measured turbulence intensity from the radar signal. Merritt [1995], in his behalf, has proposed a statistical averaging technique in which, in contrast to classic Doppler-radar spectral estimators, signals from different objects are identified and separated before the average spectral estimate is made.

2.3.1 RADAR EQUATION AND ATMOSPHERIC RADAR REFLECTIVITY

According to the antenna configuration, radar systems can be classified as monostatic and biestatic radars. The first type uses the same antenna for both transmission and reception stages, while biestatic radars use one antenna for each stage, and both antennas are usually located in different places. Although CW and FMCW radars use separate transmit and receive antennas (biestatic radars), they are considered as monostatic, unless the distance between the antennas is considerable [Mahafza and Elsherbeni, 2004].

The monostatic radar equation (i.e., with collocated emitter and receiver antennas or with a single emitter/receiver antenna) can be expressed as

$$P_r = \frac{P_t}{4\pi R^2} G_t \frac{1}{4\pi R^2} \eta V \left(\frac{\lambda^2}{4\pi} G_r\right), \tag{2.33}$$

where $P_r(W)$ is the received power, $P_t(W)$ is the transmitted power, $R\ (m)$ is the range, $G_t\ (\cdot)$ and $G_r\ (\cdot)$ are the transmitter and receiver antenna gains respectively, $\lambda\ (m)$ is the radar wavelength, and $\eta\ (m^{-1})$ is the volume reflectivity within the observation volume V. The observation volume is expressed as $V\ = \Delta R \Delta S (m^3)$, where ΔR is the radar spatial resolution and ΔS is the antenna "beam area" at range, R, $\Delta S = R^2 \Delta\theta \Delta\varphi$, with $\Delta\theta$ and $\Delta\varphi$ the angular E- and H-plane HPBW (Half Power BandWidth) of the antenna pattern, respectively. Fig. 2.8 shows the radar geometry used to describe the monostatic radar equation.

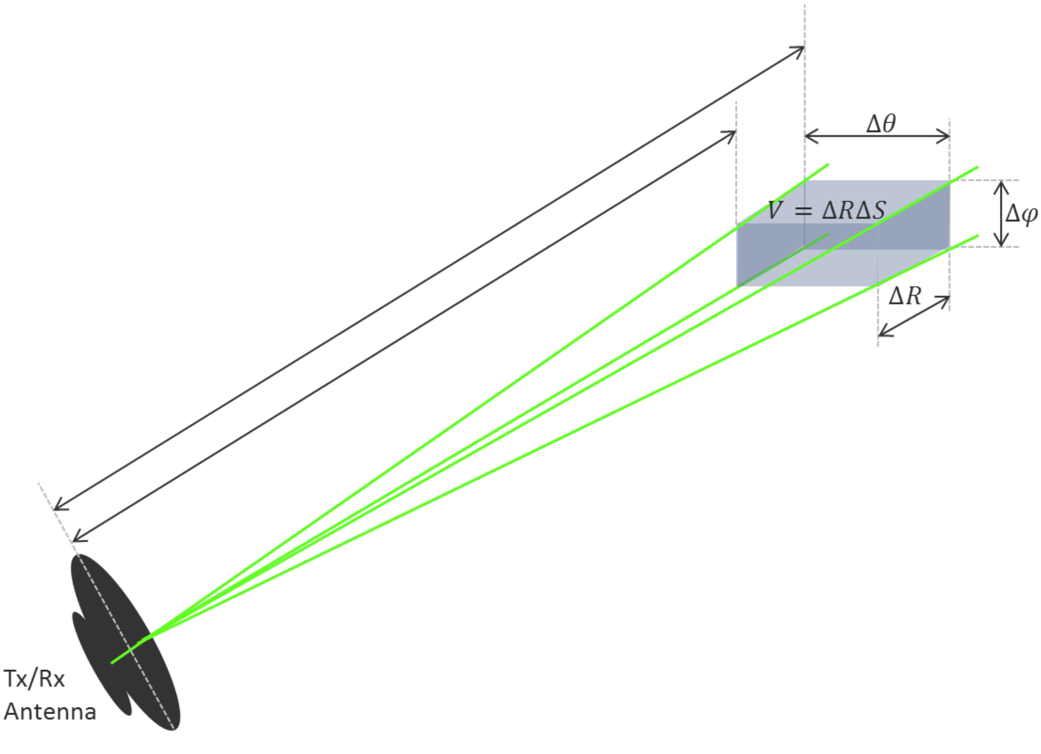

Fig. 2.8. Monostatic radar setup geometry used to derive the radar equation. Transmitter and receiver parts, V is the scattering volume or resolution cell, $\Delta\theta$ and $\Delta\varphi$ are the angular resolution of the antenna beam along the direction R from the radiation source (equivalently, the E- and H- plane Half Power Bandwidth (HPBW) of the Tx/Rx antenna pattern respectively), R is the range, and ΔR is the radar spatial resolution. Green solid lines mark off the idealized antenna beam pattern (same in transmission and reception).

The terms in Eq. 2.33 are explained next for physical significance: (i) the term $\left(\frac{P_t}{4\pi R^2}\right)$ is the power density (W/m^2) incident on the target observation volume at the range R, assuming an isotropic antenna; (ii) the term $\left(\frac{P_t}{4\pi R^2} G_t\right)$ is the power density incident at the range R, including the transmission antenna gain, G; (iii) the term $\left(\frac{P_t}{4\pi R^2}G_t\eta V\right)$ is the collected power (W) in the observation volume V; (iv) the term $\left(\frac{P_t}{4\pi R^2}G_t\frac{1}{4\pi R^2}\eta V\right)$ is the backscattered power density from the observation volume, V, and received at the radar location; and (v) the term $\left(\frac{\lambda^2}{4\pi}G_r\right)$ is the effective area (m^2) of the antenna in reception according to the antenna reciprocity theorem assuming an ideal antenna [Balanis, 2005]. Therefore, the product of terms (iv) and (v) gives the radar received power $P_r(W)$. As radars have a limited spatial resolution, the observation volume, V can be though as filled with a homogeneous distribution of targets (or meteorological scatterers) with randomly distributed phases [Sauvageot, 1992a]. As a result, the product ηV in Eq. 2.33 can be interpreted as the sum of the RCSs (i.e., the Radar backscattering Cross Section) of all these scatterers inside the observation volume,

$$\varrho = \sum_V \varrho_i = V\left(\frac{\sum_V \varrho_i}{V}\right) = V\eta, \tag{2.34}$$

where $\left(\eta = \frac{\sum_V \varrho_i}{V}\right)$ $(m^2\ m^{-3})$ is the average backscattering cross section of the scatterers per unit volume, and is called the volume radar reflectivity, $\eta\ m^{-1}$. In what follows it will be addressed as the “reflectivity” and will be computed in decibels $(\eta(dB) = 10\log\eta)$.

Because the size of a hydrometeor (e.g., a raindrop) is much smaller than the radar wavelength (i.e., diameter $D_i \leq \lambda/16$), the dominant scattering mechanism is Rayleigh scattering and the backscattering cross section of the individual scatterers is well approximated by that of a spherical raindrop, which is proportional to the reciprocal of the fourth power of the wavelength and to the sixth power of the scatterers' diameter [Sauvageot, 1992a],

$$\varrho_i = \frac{\pi^5}{\lambda^4}|K_m|^2 D_i^6, \tag{2.35}$$

where, $|K_m|^2$ is a factor depending on the refractive index of the scattering medium, $K_m = (m^2-1)/(m^2+2)$ with m the complex refractive index. For instance, in the case of water at 0^oC and 2.94-GHz operating frequency, $|K_w|^2 \approx 0.92$.

When, as is the case in practice, a particle size distribution is considered, η can be written as

$$\eta = \frac{\pi^5}{\lambda^4}|K_m|^2\int_0^\infty N(D)D^6 dD = \frac{\pi^5}{\lambda^4}|K_m|^2 Z, \tag{2.36}$$

where D stands for the diameter of the scatter, $N(D)$ is the particle size distribution (particles per unit volume with diameter between D and $D + dD$) and Z is the radar reflectivity dactor defined as the sixth power of the raindrop diameter summed over all the size distribution,

$$Z = \int_0^\infty N(D)D^6 dD, \tag{2.37}$$

Whenever the Rayleigh approximation does not apply, usually for wavelengths $\lambda < 10\ cm$ it is accepted to define de volume reflectivity as [Doviak and Zrnić, 2006],

$$\eta = \frac{\pi^5}{\lambda^4}|K_m|^2 Z_e, \tag{2.38}$$

where Z_e is the equivalent radar reflectivity factor (in units of $mm^6 \cdot m^{-3}$).

As Tatarski'i [1961] showed in its research, atmospheric random fluctuations of the refractive index of the air can be related to the reflectivity by means of spectral power-density function of the refractive index in space, $\varphi_n(k)$, where k is the wave-number vector in the radar propagation direction with $|k| = 4\pi/\lambda,$ and φ_n is the Fourier transform of the autocorrelation function of the refractive index so that [Sauvageot, 1992a],

$$\eta(k) = \frac{\pi^2}{2} k^4 \varphi_n(k). \qquad [2.39]$$

Although $\varphi_n(k)$ is defined for the entire space of the wave numbers only spatial fluctuations whose scale, following the direction of propagation, is close to $\lambda/2$ produce additive phases and are perceived by the radar (Bragg scattering); however, detection takes place only if there is sufficient spectral energy on the $\lambda/2$ scale, which is selectively observed by the radar [Sauvageot, 1992a].

In clear-air conditions, Bragg and Rayleigh scattering are the prevailing scattering mechanisms. Bragg scattering at S and C bands [Ince et al., 2003; Mahafza and Elsherbeni, 2004] is due to very strong gradients and random fluctuations of the refractive index associated with discontinuities and/or turbulences of the atmosphere. For Bragg scattering, η is commonly related to the refractive index structure function parameter, C_n^2, [Ince et al., 2003; Tatarski'i, 1961] by

$$\eta = 0.38 \cdot C_n^2\, \lambda^{-1/3} \qquad [2.40]$$

In terms of frequency, Bragg scattering composes a substantial part of the backscatter for frequencies below 3 GHz [Vaughn, 1985; Riley, 1985], whereas Rayleigh scattering tends to dominate for higher frequencies [Contreras and Frasier, 2008].

2.3.2 FREQUENCY-MODULATED CONTINUOUS-WAVE RADAR

FMCW radars have been used to monitor the atmosphere for more than three decades [Richter , 1969; Eaton et al., 1995], thanks to their ability to monitor the atmospheric refractive-index structure parameter, C_n^2, with high resolution in height and time [Ince et al., 2003] and the addition of Doppler capability. In Gossard [1990] there is a review of the new research field started by the S-band FMCW radars and in Richter [1969], Strauch et al. [1976] and in Eaton et al. [1995] some examples of this type of radar can be found.

FMCW radars may be thought as a limiting case of the pulse-compression radars where the duty cycle of the transmitted waveform approaches 100%. While pulse-compression radars operate by emitting a complex, long coded waveform of bandwidth B and duration T (e.g. a chirp signal), FMCW radars use a simple linear frequency modulation with period $T = T_m$ [Ince et al., 2003]. The improvement factor the FMCW radars gain over pulse radars of equivalent range resolution is given by the time-bandwidth product, BT, in this type of radars the cited gain can exceeds 60 dB. It is worth noting that FMCW radars, as biestatic radars with short distance between antennas, rely on the same radar equation as pulse radars.

Fig. 2.9 shows the principle of operation of a FMCW radar considering triangular-wave frequency modulation with period, T_m, and sweep frequency, Δf, over a carrier frequency, f_0, which enables to estimate range and radial speed of the target.

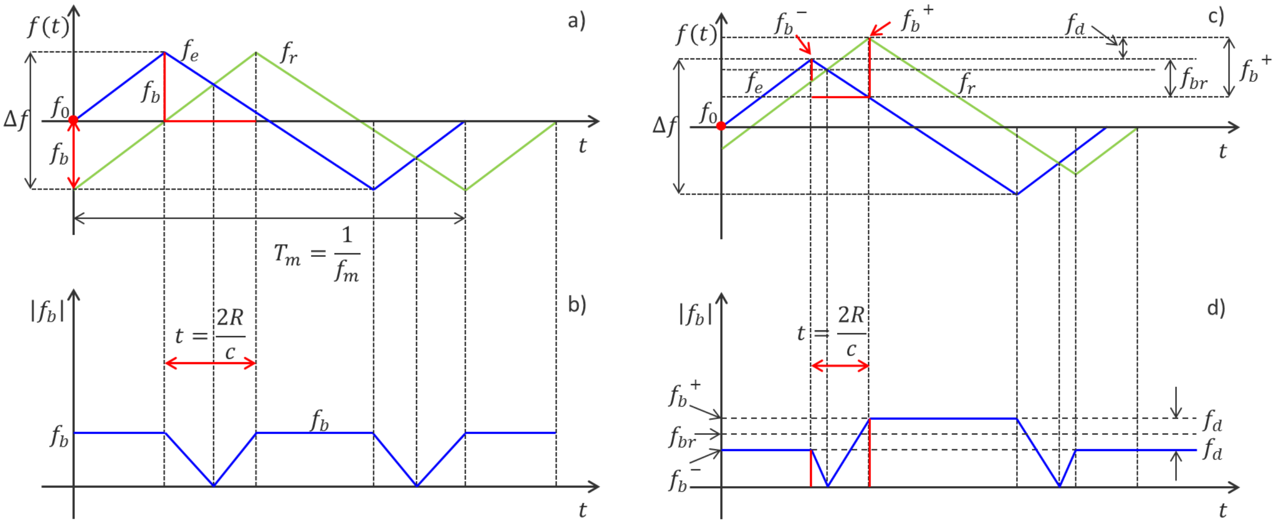

Fig. 2.9. Principle of operation of a FMCW radar, using triangular-wave frequency modulation. (a) Stationary target detection located at a distance R. f_e (blue trace) is the instantaneous emission frequency, f_r (green trace) is the instantaneous reception frequency, f_m is the modulation frequency, f_0 is the carrier frequency, and Δf is the bandwidth (frequency deviation). (b) Instantaneous beat frequency (absolute value). f_b for stationary target case (a). (c) Moving target detection located at a distance R. The maximum value of beat frequency f_b, f_b^+, is the mean beat frequency plus the Doppler shift caused by the moving target during the rising edge of the receiver frequency, $f_b^+ = f_{br} + f_d$. Likewise, the minimum value of beat frequency f_b, f_b^- , is f_b^- = $f_{br} - f_d$. The mean bean frequency is, $f_{br} = (f_b^+ + f_b^-)/2$. (d) Same as (b) but for the moving target case depicted in panel (c).). Adapted from [Lange, 2014].

To illustrate the principles of FMCW range/radial - velocity estimation, two cases are considered in the following paragraphs. The following summary is adapted from Mahafza [2005] and Lange [2014]:

(1) In the case of a *stationary target* at range R, the round-trip delay will shift the echo signal from the atmospheric target in time, which is essentially a delayed, attenuated, and possibly Doppler-shifted replica of the transmitted signal (green trace in Fig. 2.9a). This results in a frequency difference between the emitted frequency, f_e, and the delayed echo signal, f_r, or received frequency (blue trace in Fig. 2.9b), which enables to measure the distance to the atmospheric target from the beat frequency, f_b, in Fig. 2.9b. The beat frequency is given by [Mahafza, 2005],

$$f_b(R) = \dot{f}t = \dot{f}\,\frac{2R}{c} \quad (Hz), \qquad [2.41]$$

where $\dot{f}$ is the rate of frequency change (also called chirp rate),

$$\dot{f} \;\; = 2\frac{\Delta f}{T_m} = 2f_m \Delta f\ , \qquad [2.42]$$

where $f_m = 1/T_m$ is the modulating frequency and Δf is the frequency deviation or bandwidth. By inserting [2.42] into [2.41] we obtain that for stationary targets, the beat frequency and the target distance are related through

$$f_b(R) = \frac{4\Delta f f_m}{c} R \qquad (Hz), \qquad [2.43]$$

Therefore, the target distance can be estimated as

$$R = \frac{cf_b}{4\,\Delta f\, f_m} \quad (m). \tag{2.44}$$

Resolving in range is done through frequency analysis of the sampled waveform, most often through a Discrete Fourier Transform (DFT).

(2) When the target is *not stationary* (for instance a rain drop) the received signal will contain a Doppler shift term in addition to the frequency shift due to round-trip delay t, i.e. the Doppler shift moves the frequency of the entire echo signal either towards the radar (up) or away from the radar (down). Fig. 2.9c-d shows a target moving towards the radar. Because in the moving-target case the beat frequency ($f_b(t) = f_e(t) - f_r(t)$) changes between two frequencies, f_b^+ and f_b^-, the mean beat frequency is noted f_{br} to distinguish it from the stationary target case. For moving targets, the mean beat frequency and the target distance, R, are related through,

$$f_{br}(R) = \frac{f_b^+ + f_b^-}{2} = \frac{4\Delta f\ f_m}{c} R \quad (Hz), \tag{2.45}$$

where f_b^+ is the maximum beat frequency (i.e., the mean beat frequency plus the Doppler shift, $f_b^+ = f_{br} + f_d$) and f_b^- is the minimum beat frequency (i.e., the mean beat frequency minus the Doppler shift, $f_b^- = f_{br} - f_d$). From Eq. [2.45] above, the range of the moving target can be estimated as

$$R = \frac{cf_{br}}{4\Delta f\, f_m} \quad (\mathrm{m}). \tag{2.46}$$

2.4 RADIATIVE FORCING

The procedure to calculate the radiative field for a given distribution of the aerosol optical properties is the heart of all RTMs [Mayer and Kylling, 2005]. Atmospheric aerosols greatly affect the regional hydrological cycle, cloud cover, precipitations, and the atmospheric radiative budget in the Mediterranean region The impact of those aerosols on the radiative budget at the scale of the Mediterranean basin is assessed by regional climate models [Nabat et al., 2015], which do not properly take into account the possible radiative influence of the different Mediterranean aerosols, that increase significantly the optical depth as recently mentioned by Mallet et al. [2006].

Aerosol radiative effect estimates represents the changes undergone by the radiation due to the presence of aerosol and is defined as the difference between the net fluxes with and without aerosol (Eqs. 2.47 and 2.48), it is obtained with one dimensional (1-D) radiative transfer models (RTM), which have commonly been used to constrain and/or validate regional climate models. The radiative effect by atmospheric aerosol is estimated to produce a net cooling effect of the Earth's climate; however, an accurate quantification of this cooling is extremely difficult. In fact, the ARE is affected by large uncertainties. Due to the direct aerosol-radiation interaction, the ARE is estimated to be −0.27 $W \cdot m^{-2}$ on average at the global scale, with an uncertainty range of −0.77 to −0.23 $W \cdot m^{-2}$, whereas the radiative effect related to cloud adjustments due to aerosols is -0.55 $W \cdot m^{-2}$ (−1.33 to −0.06 $W \cdot m^{-2}$) [Boucher et al., 2013], being the largest unknown in the radiative effect of the atmosphere.

ARE estimates obtained with one-dimensional (1-D) RTMs have commonly been used to constrain and/or validate regional climate models. Many 1-D RTMs have been reported in the literature, and some of them are available online as open-source codes. SBDART [Ricchiazzi et al., 1998], Streamer [Key and Schweiger, 1998], MODTRAN [Berk et al., 2006], and libRadtran [Mayer and Kylling, 2005] represent some of the online available RTMs, widely accepted and used by the scientific community. The 1-D RTMs are also often used to locally estimate the ARE under clear-sky or cloudy conditions. Many studies were performed to investigate the aerosol direct radiative effects at selected Mediterranean sites [e.g., Formenti et al., 2002; Meloni et al., 2003, 2015; Roger et al., 2006; Mallet et al., 2006; Perrone et al., 2012; Sicard et al., 2012a, 2014a; Román et al., 2013; Bilbao et al., 2014; Mallet et al., 2016; Romano et al., 2016, Barragan et al., 2016]. In some of these studies, the aerosol radiative effects in the LW spectral range were commonly neglected due to the complexity of an accurate quantification of the optical properties in this spectral range [Roger et al., 2006; Mallet et al., 2008; Sicard et al., 2012].

Although the retrievals of particle properties are still affected by large uncertainties [Levy et al., 2013] most of the aerosol optical properties required in RTMs can be retrieved from experimental measurements in the SW spectral range. On the contrary, the aerosol optical properties in the LW spectral range have to be taken from look-up tables or calculated by using light scattering codes [Sicard et al., 2014a], since the current remote sensing technologies do not allow retrieving them. However, the contribution of the LW component to the ARE is non-negligible for large aerosol particles, i.e., marine aerosol or mineral dust [e.g. Markowicz et al., 2003; Vogelmann et al., 2003; Otto et al., 2007; Perrone and Bergamo, 2011; Sicard et al., 2014a,b; Meloni et al., 2018]. The contribution of mineral dust to the ARE in the infrared spectral range is especially relevant because of its large size and abundance [Meloni et al., 2018].

Most of the aerosol optical properties required in RTMs can be retrieved from experimental measurements in the SW spectral range, but, on the contrary, these optical properties in the LW spectral range have to be taken from look-up tables or estimated by using light scattering codes [Sicard et al., 2014a], since the current remote sensing technologies do not allow retrieving them. The atmospheric parameters not related to the aerosols, such as concentration of absorbing gases, relative humidity profile, surface albedo, and temperature, also influence the estimation of the radiative fluxes in the SW and in the LW spectral range, respectively. Therefore, many sources of uncertainty can affect the determination of the aerosol direct radiative effect. In order to know test the performance of RTMs and estimate the accuracy of the calculated aerosol direct radiative effect, SW and LW fluxes simulated by RTMs are commonly compared with the corresponding ones measured at the bottom of the atmosphere (BOA) and at the top of the atmosphere (TOA) [Romano et al., 2016].

The aerosol ARE, which accounts for changes in the radiation levels due to the atmospheric aerosols, is defined as the difference between the net fluxes with and without aerosol,

$$ARE_{BOA} = (F_{BOA}^{DN} - F_{BOA}^{UP}) - (F_{BOA}^{DN,0} - F_{BOA}^{UP,0}), \quad [2.47]$$

$$ARE_{TOA} = (F_{TOA}^{DN} - F_{TOA}^{UP}) - (F_{TOA}^{DN,0} - F_{TOA}^{UP,0}) = F_{TOA}^{UP,0} - F_{TOA}^{UP}, \quad [2.48]$$

where F^{DN} and F^{UP} are the downward and upward fluxes with aerosol, while $F^{DN,0}$ and $F^{UP,0}$ are the downward and upward fluxes without aerosol, respectively. A negative or positive sign of the aerosol ARE determines whether the aerosols produce a cooling or a heating effect [e.g., Seinfeld and Pandis, 1998].

To derive the local direct radiative forcing, the CommSensLab group uses the GAME (Global Atmospheric Model) model, developed at LOA (Laboratorie d'Optique Atmosphérique) in Lille (France) [Dubuisson et al., 1996, 2004, 2005, 2006]. This code allows, by solving Eqs. 2.31 and 2.32, to model the solar and thermal fluxes in the short-wave and long-wave spectral ranges assuming stratified plane and homogeneous layers in the atmosphere. Other studies like Guleria and Kuniyal (2016) and Koepke et al. (2015) show the utility of models to get the optical parameters in order to estimate the aerosol radiative forcing, concretely the optical properties of aerosol and cloud (OPAC) model (Hess et al., 1998).

The GAME code is widely described by Dubuisson et al. [2004, 2006] and more recently Sicard et al. [2014a] describe the LW spectral range module. GAME code allows calculating the solar and thermal infrared fluxes in two adjustable spectral ranges: SW ($0.3\text{–}\ 4\ \mu m$) and LW ($4\text{–}\ 50\ \mu m$), at the boundary of plane and homogenous atmospheric layers by using the discrete ordinates (DISORT) method [Stamnes et al., 1988]. Note that the GAME code has a different spectral sampling in the SW (167 as typical value depending on the spectral range considered and a wave number of 100 or $400\ cm^{-1}$) and a fixed spectral sampling (115 values) in the infrared spectral range.

About the vertical resolution of the model, the LW module uses forty vertical levels between ground and 100 km height with a resolution of 1 km from the surface to 25 km, 2.5 km between 25 and 50 km, 5 km from 50 to 60 km and 20 km between 80 and 100 km. Additionally, the SW module uses 18 vertical levels between ground and 20-km height with a resolution of 5 m from the surface to 10 m, 10 m between 10 and 50 m, 50 m between 50 and 100 m, 100 m between 100 and 200 m, 200 m between 200 and 1 km, 1 km between 1 and 2 km, 2 km between 2 and 10 km and 10 km between 10 and 20 km. The LW aerosol scattering, which is often neglected in regional and global climate models in spite of its effect on the LW radiative forcing, is one of its main capabilities [Sicard et al., 2014]. Table 2.3 lists the main parameters used as inputs of GAME in the SW and LW spectral range, it is worth noting that some of these characteristics can be tuned depending on the type and the characteristics of the research carried out.

Table 2.3: Input parameters for the GAME model and data sources in the SW and LW spectral ranges. Note that the sources of the input and some parameters can be adjusted depending on the characteristics of the research. Acronym GRASP stands for Generalized Retrieval of Aerosol and Surface Properties.

Parameters		**Shortwave GAME**	**Longwave GAME**
Spectral range (adjustable)		(typical) 0.3 – 4 μm	(typical) 4 – 50 μm
Number of sub-bands (non-adjustable)		167	115
Atmospheric parameters (different sources)	Atmospheric profile	Radio soundings + U.S. standard atmos + aircraft.	Radio soundings + U.S. standard atmos + aircraft.
	H_2O	Radio soundings	Radio soundings
	O_3	U.S. standard atmos.	U.S. standard atmos.
	Absorption coefficients of main gases	HITRAN	HITRAN
	Surface albedo	From ground-based measurements	From CERES
	LW emissivity	-	From CERES
Meteo parameters (different sources)	At the surface	Measured at the meteorological station	
	<20 km	Radio soundings	
	>20km	U.S. standard atmos.	
Aerosols (different sources)	AOD	Lidar extincton coefficient, AERONET	Mie calculation
	Single-scattering albedo	AERONET, GRASP, Aircraft	Mie calculation
	Asymmetry factor	AERONET	Mie calculation
	Aerosol vertical distribution	Lidar, GRASP, Aircraft	Lidar, GRASP, Aircraft
	Size distribution	-	AERONET
	Fine and coarse mode radius	-	AERONET
	Fine and coarse mode concentration	-	AERONET
	Refractive index	-	Krekov [1993]

CHAPTER 3

Parameterization and Evaluation of a RTM

This Chapter focuses on the evaluation / parameterization of different 1-D radiative transfer models (1-D RTMs) and their sensitivity to different inputs parameters, by means of aerosol direct radiative effect (ARE) estimations performed at Lecce (Sect. 3.3) and Granada (Sect. 3.4). The GAME and the Two-Stream models are the RTMs used to calculate the instantaneous ARE in the SW and LW spectral ranges, at the surface (BOA) and at the top of the atmosphere (TOA) in order to evaluate the importance of the spectral resolution (Sect. 3.3). The differences between GAME and Two-Stream are found in the LW range, however by means of a "optimization" of the Two-Stream model, a satisfactory agreement between the pairs of LW-ARE values is found. On the other hand, GAME code, in both SW and LW configuration, is the model chosen to study the aerosol radiative properties in order to evaluate the parameterization of the vertically-resolved properties (Sect. 3.4). This code is fed by three different datasets in order to put in contrast the fluxed retrieved against ground- and in situ airborne measurements and thus, assess the uncertainty of GAME when is tuned with different input parameters. In addition, the radiative fluxes and ARE are discussed with respect to the different input parameterizations.

This chaper is an adaptation of [Barragan et al, 2016] and [Granados et al, 2019], published in JGR Atmospheres (available as an electronic reprint with the permission of AGU: https://agupubs.onlinelibrary.wiley.com/doi/full/10.1002/2016JD025016) and Atmospheric Chemistry and Physics (available as an electronic reprint with the permission of ACP: https://www.atmos-chem-phys.net/19/523/2019/). Systematic or multiple reproduction or distribution to multiple locations via electronic or other means is prohibited and is subject to penalties under law.

3.1 INTRODUCTION

One of the areas frequently influenced by mineral dust is the Mediterranean region, affected by dust intrusions from the close Sahara Desert or the Middle-East region [Moulin et al., 1998; Israelevich et al., 2012; Gkikas et al., 2013] producing significant perturbations to the SW and the LW radiation balance [di Sarra et al. 2011; Papadimas et al., 2012; Perrone et al., 2012;] as well as the regional climate [Nabat et al., 2015]. Besides, climate change projections identify the Mediterranean region as a climatologically sensitive area especially vulnerable to global change [Giorgi, 2006; Giorgi and Lionello, 2008]. The ARE in the Mediterranean region can be responsible for a strong cooling effect both at the surface (or BOA) and the top of the atmosphere (TOA). The so-called forcing efficiency (FE), which is defined as the ratio between the ARE and the aerosol optical depth (AOD), for the SW ranges between -150 and -160 $W \cdot m^{-2}$ for solar zenith angles (SZA) in the range 50-60° [di Biagio et al., 2009], being able to reach values larger than 200 $W \cdot m^{-2}$ at the BOA during strong dust events in the Mediterranean region [Gómez-Amo et al., 2011].

The LW component accounts for an effect of up to 53% of the SW component and with an opposite sign [di Sarra et al. 2011; Perrone et al., 2012; Meloni et al. 2015]. To address these issues, the Aerosol Direct Radiative Impact on the regional climate in the MEDiterranean region (ADRIMED) field campaign within the Chemistry-Aerosol Mediterranean Experiment (ChArMEx, http://charmex.lsce.ipsl.fr) took place in the Mediterranean region from 11 June to 5 July 2013 [Mallet et al., 2016]. In the context of the ADRIMED field campaign, continuous measurements of the SW and LW radiative fluxes at the surface were carried out, and leveraged for the Sect. 3.3 of this Chapter, at the Mathematics and Physics Department of the Salento

University (Lecce, Italy) during the moderate Saharan dust outbreak that affected the Mediterranean basin from 15 up to the 25 June 2013 [Barragan et al., 2016].

Also, focusing on the second part of this Chapter, ground-based measurements were carried out at the Andalusian Institute for Earth System Research (IISTA-CEAMA) of the University of Granada (Granda, Spain) by the Atmospheric Physics Group of the University of Granada (GFAT-UGR). Besides, two ChArMEx/ADRIMED flights, F30 and F31, from the French ATR 42 environmental research aircraft of SAFIRE (http://www.SAFIRE.fr), took place above southeastern Spain during a Saharan dust episode on 16 and 17 June 2013. Lecce and Granada monitoring sites and the instrumentation used are widely described in Barragan et al., [2016] and Granados-Muñoz et al., [2019] respectively.

The main goal of this Chapter is the parameterization and the evaluation of a RTM, concretely the GAME code, introduced in Sect. 2.3. For that purpose, first, in Sect. 3.3, are presented the SW and LW-ARE at the BOA and at the TOA in Lecce from 20 to 24 June 2013 estimated by two different RTMs: GAME [Dubuisson et al., 1996, 2004, 2005, 2006] and the Two-Stream model [Tafuro et al., 2007; Perrone and Bergamo, 2011; Perrone et al., 2012]. These two models use different numerical procedures to calculate the radiative field and a different spectral resolution for the aerosol optical properties, therefore in order to decrease the differences found in the results, a spectral evaluation is needed. Two main goals are pursued in Sect. 3.3: (i) the evaluation of the capabilities of both models to reproduce the experimental flux measurements and (ii) shed light on the dependence of the flux and the ARE estimates on the used RTMs by a case study analysis and sensitivity tests. Results on the methodology used to decrease the differences between the outputs from the two models have also been provided in this Chapter.

After the spectral evaluation and parameterization, in Sect. 3.4 is presented an evaluation of the vertically-resolved properties in radiative transfer equations by means of three different dataset which act as inputs in GAME. Concretely, Sect. 3.4 consists in an analysis of the mineral dust radiative properties during the Saharan dust episode on 16 and 17 June taking advantage of the thorough database available. Multiple datasets are used as inputs in GAME to evaluate the influence of the different measurements and data processing in the retrieved ARE. An evaluation against aircraft in situ measurements of radiative fluxes is also presented. Two main goals are pursued in Sect. 3.4: (i) the quantification of the ARE for two case studies within a dust transport episode and (ii) the sensitivity evaluation of the model estimates to the aerosol input used.

This Chapter is organized as follows: In Sect. 3.2, a description of the radiative transfer models and software used is provided. The importance of the spectral resolution in radiative transfer models is presented in Sect. 3.3. In Sect. 3.4, the importance of the parameterization of the vertically-resolved properties in radiative transfer calculations is reported. Finally, concluding remarks are given in Sect. 3.5.

3.2 ALGORITHM AND SOFTWARE DESCRIPTION

3.2.1 DESCRIPTION OF THE RADIATIVE TRANSFER MODELS

The GAME and the Two-Stream RTMs have been used to simulate the SW and LW radiative fluxes with and without aerosol and, hence, to determine the ARE at the BOA and at the TOA during the investigated African dust event. The ARE, which accounts for changes in the radiation levels due to the atmospheric aerosols, is defined as the difference between the net fluxes with and without aerosol (see Eqs. 2.47 and 2.48). As commented in Sect. 2.3, a negative or positive sign of the ARE determines whether the aerosols produce a cooling or a heating effect [e.g., Seinfeld and Pandis, 1998].

3.2.1.1 THE GAME RADIATIVE TRANSFER MODEL

The GAME code is widely described by Dubuisson et al. [2004, 2006] and more recently Sicard et al. [2014a] describe the LW spectral range module. A more detailed description is already presented in Sect. 2.3.

3.2.1.2 THE TWO-STREAM RADIATIVE TRANSFER MODEL

The Two-Stream RTM used in this study is widely described in Tafuro et al. [2007], Perrone and Bergamo [2011], and Perrone et al. [2012]. It uses the two-stream approximation [Meador and Weaver, 1980] to solve the radiative transfer equation and to simulate the SW and LW radiative fluxes at the boundary of 20 homogeneous plane-parallel layers from the surface up to 25 km. In particular, 10 layers (with a resolution of 500 m) are placed below 5 km altitude, to better evaluate the effects of the lower tropospheric aerosols. In this Chapter, the radiative fluxes are determined in the SW (0.3–4 μm) and in the LW (4–37 μm) domains. In particular, 8 SW and 11 LW sub-bands were considered to properly account for the spectral dependence of the atmospheric particle properties. It is worth noting that the two-stream approximation [Meador and Weaver, 1980], which is used in the Two-Stream model, is one of the simplest techniques to solve the radiative transfer equation. The DISORT method [Stamnes et al., 1988] used in GAME is expected to be more accurate than the two-stream approximation.

3.2.2 THE GRASP CODE FOR THE RETRIEVAL OF AEROSOL PROPERTIES

The GRASP (Generalized Retrieval of Aerosol and Surface Properties) code [Dubovik et al., 2011, 2014], provides aerosol optical and microphysical properties in the atmosphere by combining the information from a variety of remote sensors [e.g. Kokhanovsky et al., 2015; Espinosa et al., 2017; Torres et al., 2017; Román et al., 2017, 2018; Chen et al., 2018 (in review)]. In this Chapter, GRASP is used to invert simultaneously coincident lidar data (range corrected signal, RCS, at 355, 532 and 1064 nm) and sun-photometer measurements (AOD and sky radiances both at 440, 675, 870 and 1020 nm) providing a detailed characterization of the aerosol properties, both column-integrated and vertically-resolved. It is worth noting that this GRASP scheme, based on Lopatin et al. [2013], presents the main advantage that it allows retrieving aerosol optical and microphysical properties for two distinct aerosol modes, namely fine and coarse modes. The aerosol extinction coefficient (α_{aer}), particle backscatter coefficient (β_{aer}), single scattering albedo (SSA) (all at 355, 440, 532, 675, 870, 1020 and 1064 nm) and aerosol volume concentration profiles obtained as output from GRASP will be used as input in GAME later in this Chapter, together with the column-integrated particle size distribution (PSD) properties (namely r_{eff} and σ for fine and coarse modes). A more in-depth analysis of GRASP output data retrieved using the lidar and sun-photometer data at Granada station for the two inversions simultaneous to the aircraft overpasses during flights F30 and F31 during ChArMEx/ADRIMED campaign can be found in Benavent-Oltra et al. [2017].

3.3 THE IMPORTANCE OF THE SPECTRAL RESOLUTION IN RADIATIVE TRANSFER MODELS

In this section, the importance of a correct parameterization of the radiative transfer model is discussed. For that purpose the outputs of GAME and Two-Stream RTMs are compared.

3.3.1 INSTRUMENTS AND DATA

Table 3.1 provides the list of the main parameters used as inputs of the two RTMs in the SW and LW spectral ranges, respectively. Note that some GAME parameters are tuned in order to both models compute the radiative fluxes in similar conditions (see Tables 2.1 and 3.1). The used broadband surface albedo values are experimentally determined as the ratio of the SW upward irradiance to the corresponding SW downward irradiance, measured by the pyranometers at the surface [Manninen et al., 2012]. The LW emissivity is calculated by averaging all the values provided by the CERES (Clouds and Earth's Radiant Energy System) SSF (Single Scanner Footprint) Level 2 data set (http://ceres.larc.nasa.gov/) for an area of 0.5° latitude by 0.5° longitude around the study site. The time dependent refractive indices from AERONET sun-photometer measurements are used in the SW spectral range, while the time-independent refractive indices for mineral dust from Krekov [1993] are used in the LW spectral range. Input data include also the columnar aerosol volume size distribution from AERONET retrievals. Air density, atmospheric pressure, and water vapor mixing ratio values at the surface are provided by a local meteorological station. Finally, the skin surface temperature (T_S) values are experimentally calculated from the downward and upward long-wave irradiances measured at the surface by the following relation [Wang et al., 2005]:

$$LWF^{UP} = \varepsilon \cdot \vartheta \cdot T_S^4 + (1-\varepsilon) LWF^{DN} \quad [3.1]$$

where ε represents the surface LW emissivity (0.015 on 20 and 21 June and 0.014 on 22 and 24 June) and ϑ is the Stefan-Boltzmann's constant.

Table 3.1: Overview of the GAME and the Two-Stream model properties and input data sources both in the SW and LW spectral ranges, including the surface parameters, profiles of meteorological variables and main gases and the aerosol parameters. Meteorological parameters include atmospheric pressure, air temperature, air density, and relative humidity.

Parameters		**Shortwave**		**Longwave**	
		GAME	**Two-Stream**	**GAME**	**Two-Stream**
Spectral Range		0.3 – 4 μm	0.3 – 4 μm	4 – 37 μm	4 – 37 μm
Number of sub-bands		167	8	115	11
Meteo Parameters	at the surface	Local data	Local data	Local data	Local data
	< 20 km	Radiosounding	Radiosounding	Radiosounding	Radiosounding
	> 20 km	US Standard Atmosphere	US Standard Atmosphere	US Standard Atmosphere	US Standard Atmosphere
Main Gases Parameters	Concentration Profile	US Standard Atmosphere	US Standard Atmosphere	US Standard Atmosphere	US Standard Atmosphere
	Absorption Coefficients	HITRAN	LOWTRAN 5	HITRAN	LOWTRAN 5
Surface Parameters	Surface Albedo	Ground-based measurements	Ground-based measurements	-	-
	LW Emissivity	-	-	CERES	CERES
Aerosol Parameters	Vertical Distribution	Lidar	Lidar	Lidar	Lidar
	Size Distribution	AERONET	AERONET	AERONET	AERONET
	Fine and Coarse Mode Radius	AERONET	AERONET	AERONET	AERONET
	Refractive Index	AERONET	AERONET	Krekov [1993]	Krekov [1993]

The temperature (T), relative humidity (RH), and pressure (P) vertical profiles are obtained from radio sounding measurements performed at the meteorological station of Brindisi (Italy) that is about 40 km northwest of the Lecce monitoring station. The T, RH, and P profiles are interpolated to the vertical resolution of the models, up to 20 km of altitude. Summer and mid-latitudes standard atmosphere data provided by the

Air Force Geophysics Laboratory (AFGL) [Anderson et al., 1986] are then used above 20 km of altitude. The water vapor mixing ratio, defined as the ratio of the mass of water vapor to the mass of dry air, is calculated from the radio sounding RH, P, and T values, according to Wagner and Pruß [2002]. The transmission function (T_v) of the atmospheric gases for a spectral interval v and an atmospheric layer at pressure P and temperature T is approximated by an exponential summation over a limited number N of absorption classes as [Sicard et al., 2014a]

$$T_v(P,T) = \sum_{i=1}^{N} a_i e^{-k_i(P,T)u(P,T)} \tag{3.2}$$

where u represents the absorber amount and a_i represents the probability associated to the mean absorption coefficient k_i for each absorption class i. The a_i and k_i values were retrieved from the HITRAN (HIgh-resolution TRANsmission molecular absorption) spectroscopic database and the Line-by-Line DOM code [Dubuisson et al., 1996] for GAME and from the LOWTRAN (LOW resolution TRANsmission model) 5 database for the Two-Stream model.

The aerosol vertical distribution is assessed in both models from the vertical profiles of the backscatter coefficient at 532nm ($\beta^{532}(R)$), retrieved from the UNILE (UNIversity of LEcce) lidar measurements. Observe from Table 3.1 that the different spectral resolution (number of sub-bands) adopted in the two models can represent a source of discrepancy in the provided values of the simulated radiative fluxes and, consequently, AREs. In fact, Hatzianastassiou et al. [2007] demonstrated by sensitivity tests that very large differences (up to 300%) could be found between AREs computed using detailed spectral and spectrally averaged aerosol optical properties. An additional source of discrepancy in the data provided by the two models could be due to the fact that the HITRAN spectroscopic database is used in GAME for the atmospheric gases, while the LOWTRAN 5 database is used in the Two-Stream model. Note that the LOWTRAN 5 database may underestimate the near-infrared water vapor absorption by about 10%, according to Halthore et al. [2005].

The SOP-1a campaign and the dust plume detected at southeastern Italy from 20 to 24 June are widely described in Mallet et al. [2016] and Barragan et al. [2016] respectively. During these days hourly mean values of the shortwave downward radiative flux (SW-F^{DN}) (Fig. 3.1a) and LW downward radiative flux (LW-F^{DN}) (Fig. 3.1b) were retrieved by two CMP 21 pyranomerer (Kipp & Zonen) and two CGR3 pyrgeometer (Kipp & Zonen) respectively to provide an overview of the local conditions during the analyzed period. In fact, the SW-F^{DN} time evolution is characterized by a typical clear-sky daily cycle on 20–22 and 24 June reaching maximum values between 940 and 970 $W \cdot m^{-2}$ around midday. Fig. 3.1 allows estimating the effect of the desert dust advection on the irradiance and reveals that the desert dust advection is responsible from midday of 21 June to midday of 22 June for a SW-F^{DN} decrease of 30 $W \cdot m^{-2}$ (3%), a LW-F^{DN} increase of 5 $W \cdot m^{-2}$ (1.5%). 23 June was a cloudy day as indicated by the multipeaks structure of the SW-F^{DN}, thus AERONET and lidar measurements were not performed.

It is worth to comment the temporal evolution of the instantaneous AERONET retrievals, for instance, the daily mean value of the AOD at 440 nm increases from 0.19 on 20 June up to 0.25 on 22 June because of the large advection of desert dust. Consequently, the Ångström exponent calculated between 440 and 870 nm ($AE_{440–870}$) daily mean value, which is equal to 1.92 on 20 June, decreases down to 0.90 on 22 June. Note that a combination of large AODs with small AE values may indicate a significant contribution of coarse mode particles, as mineral dust, to the aerosol load [e.g., Cachorro et al., 2008].

Some works performed at Mediterranean sites [e.g., Valenzuela et al., 2012; Romano et al., 2016; Sicard et al., 2016b] found that the SSA (the ratio between scattering and extinction coefficient) exhibited a substantial increase from 440 to 675 nm and, then, a slight increase as a function of the wavelength on dusty days. Accordingly, the SSA daily mean values are equal to 0.892, 0.906, 0.912, and 0.921 at 440, 675, 870, and 1020 nm, respectively, on 22 June (dusty day), whereas, the SSA values decrease with the wavelength increase on 20 June, which likely represented a day weakly affected by desert dust. In particular, the SSA daily mean value decreases from 0.944 at 440 nm to 0.885 at 1020 nm on 20 June. According to Russell et al. [2010] the SSA spectral behavior of 20 June is typical of urban/industrial or mixed aerosols (see Fig. 4 in Barragan et al. [2016] for further information about the temporal evolution of the AERONET retrievals).

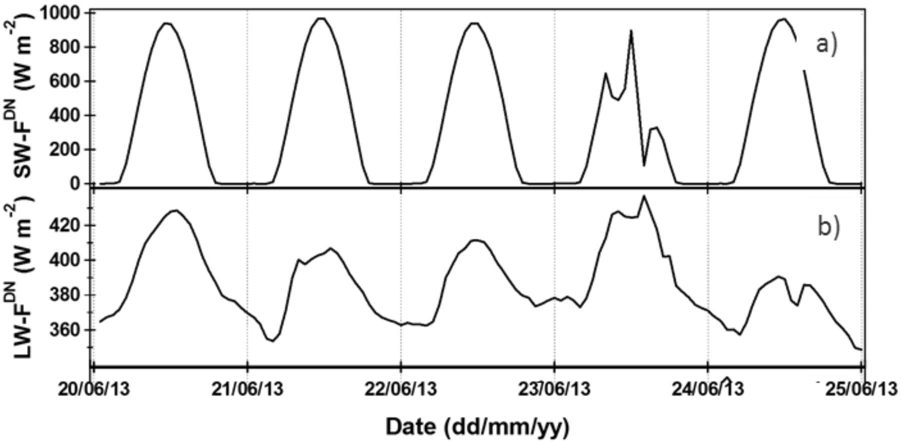

Fig. 3.1. Temporal evolution of the hourly mean values of (a) shortwave downward radiative flux (SW-F^{DN}), (b longwave downward radiative flux (LW-F^{DN}) in Lecce (Italy), from 20 to 24 June 2013.

3.3.2 COMPARISON OF MODELED AND EXPERIMENTAL RADIATIVE FLUXES

The SW and LW radiative fluxes monitored at Lecce from 20 to 24 June 2013 during the ChArMEx/ADRIMED campaign are compared with the corresponding fluxes modeled by the GAME and the Two-Stream code, respectively, to obtain a first estimate of the accuracy of both RTMs. Model simulations are only performed at the times in which collocated in space and time lidar and AERONET sun-photometer measurements are available. Therefore, 21 values of SW and LW radiative fluxes are simulated during the four analyzed days.

Fig. 3.2 shows the calculated SW downward (a), SW upward (b), LW downward (c) and LW upward fluxes (d), versus the corresponding measured fluxes at the surface. The radiative fluxes plotted in Fig.3.2 are calculated by averaging the measured flux values over a 10 min interval centered at the mean time of the lidar signals averaged to obtain a single profile. Finally, the error bars in this figure represent ±1 standard-deviation of the measured flux mean values. Figs. 3.2c and 3.2d show that calculated GAME and Two-Stream LW downward fluxes on average slightly overestimate the corresponding experimental fluxes. In particular, the mean bias percentage is +1.6% and +1.3% for the GAME and the Two-Stream flux values, respectively while Figs. 3.2a and 3.2b show that the GAME and the Two-Stream SW flux values on average slightly underestimates and overestimates, respectively, the corresponding experimental values.

In fact, the percentage value of the mean bias between simulated and experimental SW downward fluxes is -0.3% and +2.0% for GAME and the Two-Stream model, respectively. Figs. 3.2a, 3.2b and 3.2d reveal that both the GAME and the Two-Stream simulated SW and LW upward fluxes are in good agreement with the corresponding experimental values, being the correlation coefficient $R^2 = 0.99$, while Fig.3.2c shows that the correlation coefficient between the GAME and the Two-Stream LW downward fluxes and the corresponding experimental fluxes is equal to 0.93 and 0.82. Analogously, GAME and the Two-Stream model on average underestimate by 1.5% and overestimate by 1.8% the corresponding SW upward fluxes measured at the surface. These uncertainties are inside the total uncertainty of the CMP 21 pyranometers (Kipp & Zonen) (2%). It is also worth noting that both models consider the spherical particle approximation to determine the radiative fluxes and Kahnert et al. [2007] found that the assumption of spherical particles in the simulation of SW downward fluxes implies errors between 5 and 10% for Saharan dust samples. However, it must be assume that desert particles monitored few thousand kilometers away from the source may have more regular shapes, according to Chou et al. [2008] and Sicard et al. [2014a].

Also, another possible source of discrepancy between the simulated and the experimental SW fluxes is that the pyranometer measurements are performed in the 0.31–2.80 μm spectral range, while the GAME and Two-Stream fluxes are calculated in the range 0.3–4 μm. Fig.3.2d reveals that on average the GAME and the Two-Stream LW upward fluxes overestimate by +0.2% and +0.04%, respectively, the corresponding fluxes measured at the surface, because of the strong dependence of the modeled LW upward fluxes at the BOA on the experimentally determined skin temperature (see Eq. 3.1), which is retrieved from the pyrgeometers measurements and represented an input parameter for both RTMs. The uncertainty of these instruments is ±3%, hence, (Figs. 3.2c and 3.2d) reveals that the modeled LW fluxes at the surface are also in good agreement with the corresponding experimental fluxes. Note that the pyrgeometers measurements are performed in the 4.5–42 μm spectral range, while the GAME and the Two-Stream LW fluxes are calculated in the 4–37 μm spectral range. Therefore, the different spectral range of the measured and calculated flux values could represent a possible source of discrepancy between the modeled and the experimental fluxes.

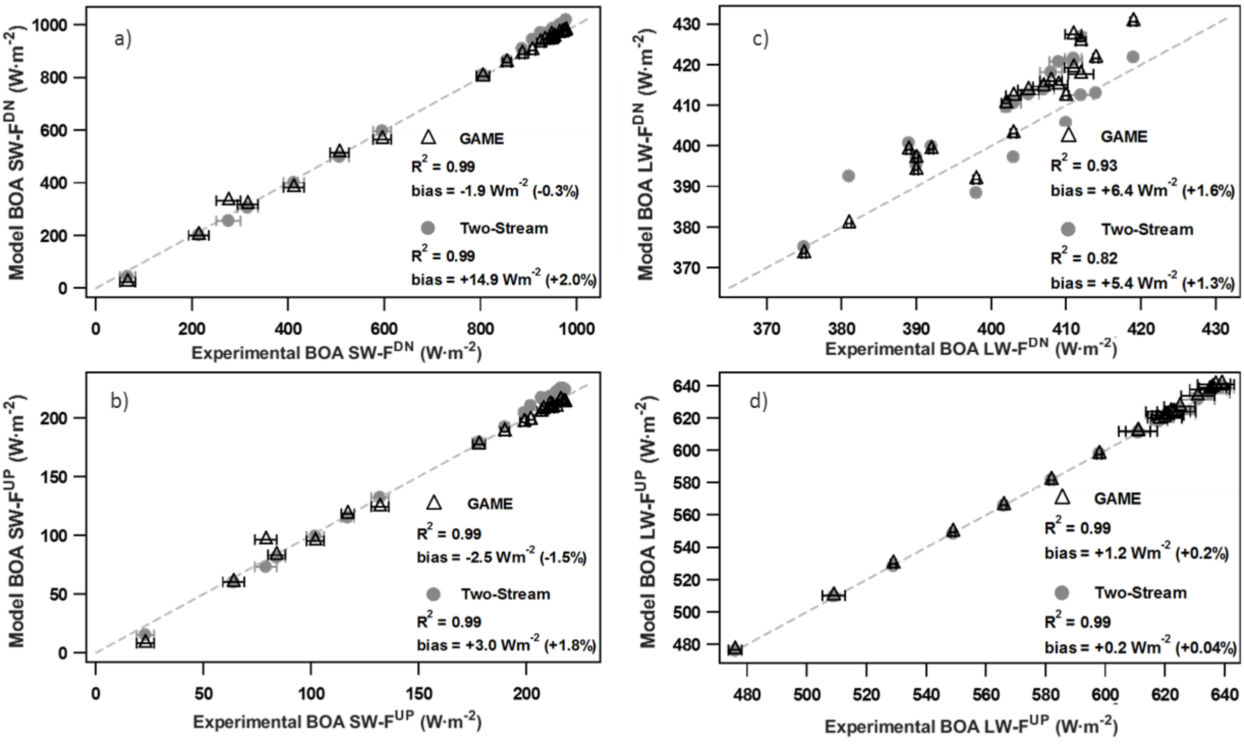

Fig.3.2. Comparison between experimental and simulated short-wave (a) downward and (b) upward long-wave (c) downward and (d) upward radiative fluxes at the surface from 20 to 24 June 2013. Open black triangles and full grey dots represent the fluxes simulated by GAME and Two-Stream, respectively. Error bars represent the standard-deviation of the measured radiative fluxes, which are obtained by averaging the related values within 10-min interval centered at the selected time. The square of the linear correlation coefficient (R^2) and the mean bias are also reported. The grey dotted line represents the 1:1 line.

Figs. 3.3a and 3.3b show by open boxes the Two-Stream upward fluxes at the TOA versus the corresponding GAME fluxes in the SW and LW range, respectively, to investigate the correlation between the TOA flux values provided by the two tested RTMs. Figs. 3.3a and 3.3b reveal that the TOA Two-Stream upward fluxes are well correlated with the corresponding GAME fluxes in the SW ($R^2 = 0.99$) and LW ($R^2 = 0.96$) spectral range even if the Two-Stream upward fluxes overestimate the corresponding GAME fluxes: the mean bias percentage is of +9% and +6% in the SW and LW spectral ranges, respectively and are mainly due to the poor spectral resolution of Two-Stream and in addition to the change of optical and microphysical of aerosol and water vapor. The differences between GAME and Two-Stream TOA fluxes vary significantly with the monitoring day (not shown in Fig.3.3).

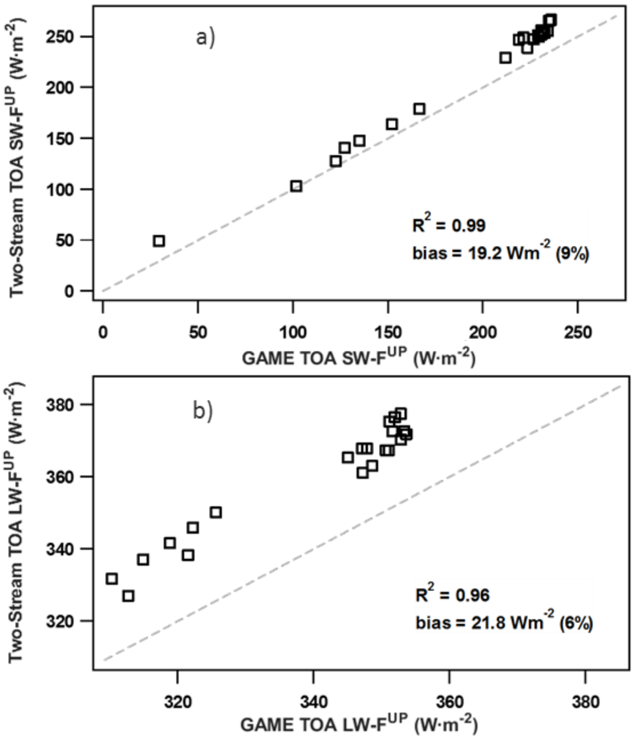

Fig.3.3. (a) Comparison between the upward radiative fluxes at the TOA simulated by GAME and Two-Stream in the (a) short- and (b) long-wave spectral range, from 20 to 24 June 2013. The square of the linear correlation coefficient (R^2) and the mean bias are also reported. The grey dotted line represents the 1:1 line.

3.3.3 AEROSOL RADIATIVE EFFECT IN LECCE DURING 20-24 JUNE 2013

Fig.3.4a shows the BOA SW-AREs from the Two-Stream model versus the corresponding GAME values, and can be observed that the Two-Stream data are well correlated with the corresponding GAME data ($R^2 = 0.86$) in the SW spectral range. The GAME LW-ARE, at the surface, ranges from +1.3 to +5.6 $W \cdot m^{-2}$, while, the corresponding Two-Stream LW-AREs vary between +1.6 and +18.0 $W \cdot m^{-2}$ (see Table 3.2). Table 3.2 reveals that the mean value of the modeled SW-ARE at the surface is about -13 $W \cdot m^{-2}$ on 21 June and increases (in absolut terms) to about -44 $W \cdot m^{-2}$ on 22 June due to a significant dust advection. At the BOA, the LW-ARE value determined by GAME is about +2.5 $W \cdot m^{-2}$ on 21 June and increases to about +5.6 $W \cdot m^{-2}$ on 22 June, this behavior can be explained again by a significant dust advection. It is worth noting from Table 3.2 that the LW-ARE values calculated from the Two-Stream model are significantly greater than the corresponding ones calculated from GAME on 22 and 24 June, which represent the days most affected by the Saharan dust intrusion.

In particular, Fig.3.4b shows the BOA LW-AREs from the Two-Stream model versus the GAME corresponding values and reveals a poor correlation ($R^2 = 0.43$) and a quite large bias (+4.9 $W \cdot m^{-2}$) that characterized the relationship between the two data sets. Figs. 3.4c and 3.4d show the TOA SW- and LW-AREs from the Two-Stream model, respectively, versus the corresponding GAME data. In these figures, can be observed that the TOA SW- and LW-AREs from the Two-Stream model are relatively well correlated with the corresponding GAME data, being the square of the linear correlation coefficient equal to 0.77 and 0.64 for the SW (Fig.3.4c) and LW data set (Fig.3.4d),respectively. However, it is worth noting that on average the Two-Stream model overestimates the corresponding TOA AREs from GAME.

Consequently, the mean bias, which is equal to +1.1 $W \cdot m^{-2}$ in the SW spectral range (Fig.3.4c), increases up to +3.1 $W \cdot m^{-2}$ in the LW spectral range (Fig.3.4d). The results of Fig.3.4 reveal that the differences between the AREs provided by the two models are on average larger in the LW spectral range. In particular, the largest differences are found at the TOA and at the surface on 22 June, which is the day characterized by the largest AODs and the smallest AE values because of the large contribution of coarse particles.

Table 3.2 data also reveal that the differences between the LW-ARE values from GAME and the Two-Stream model vary significantly with the monitoring day, pointing out that the optical and microphysical properties of aerosol and water vapor, which represent the atmospheric components characterized by the highest day-to-day variability, are likely responsible for the high bias values revealed from Figs. 3.4b and 3.4d in the LW spectral range. The strong dependence on the monitoring day of the differences resulting from the LW-ARE estimates provided by the two models may also suggest that those differences are weakly or not affected by the different numerical procedure used by the two models, supporting this argument the good agreement in the SW spectral range between the AREs from the two models. Besides, the poor spectral resolution of the Two-Stream model in the LW spectral range with respect to the one of GAME is likely responsible for the differences revealed from Figs. 3.4b and 3.4d, according to Hatzianastassiou et al. [2007]. Therefore, an optimization procedure is needed.

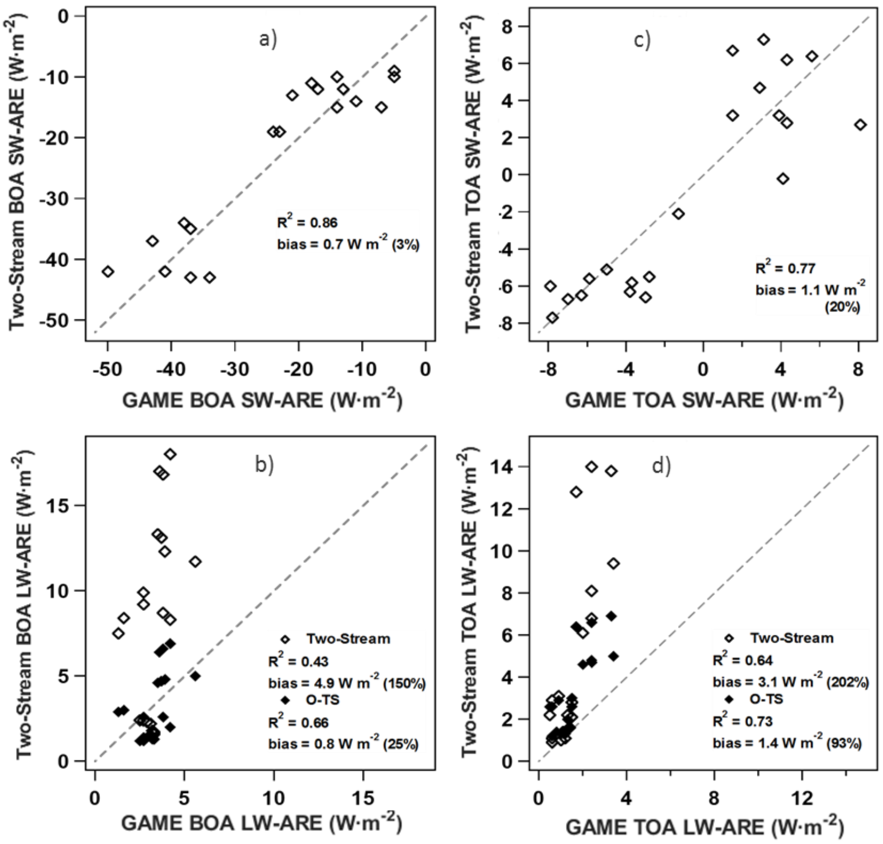

Fig.3.4. Comparison between the ARE simulated by GAME and Two-Stream in the (a) short- and (b) long-wave range (open diamonds) at the surface and in the (c) short- and (d) long-wave range at the TOA. Full diamonds in (b) and (d) illustrate the comparison between the long-wave ARE at the surface simulated by GAME and O-TS (Optimized Two-Stream). The square of the linear correlation coefficient (R^2) and the mean bias are reported. The grey dotted line represents the 1:1 line.

Table 3.2: Instantaneous, Clear-Sky, Short-Wave (SW), and Long-Wave (LW) ARE at the Bottom of the Atmosphere (BOA) and at the Top of the Atmosphere (TOA) Simulated by GAME (G) and Two-Stream (TS) Radiative Transfer Model for 21 Selected Times/Days of June 2013. O-TS stands for the ARE values simulated by the TS model by using optimized water vapor absorption coefficients and dust particle refractive indices. SZA represents the solar zenith angle. AOD and SSA indicate the AOD at 440 nm and the SSA at 440 nm, respectively, from the AERONET sun-photometer measurements. *alb* indicates the surface albedo obtained as the ratio of the upward SW flux to the downward SW flux, from the pyranometer measurements.

day	**SZA (deg)**	**AOD**	**SSA**	***alb***	**BOA SW-ARE (Wm^{-2})**		**TOA SW-ARE (Wm^{-2})**		**BOA LW-ARE (Wm^{-2})**		**TOA LW-ARE (Wm^{-2})**	
					G	**TS**	**G**	**TS**	**G**	**TS (O-TS)**	**G**	**TS (O-TS)**
20	53	0.19	0.94	0.22	-14	-15	-6	-6	3.1	2.2 (1.9)	1.4	1.6 (1.6)
20	59	0.19	0.94	0.23	-14	-15	-6	-6	2.9	2.3 (2.0)	1.1	1.4 (1.4)
20	64	0.19	0.94	0.25	-14	-15	-8	-8	2.7	2.4 (1.8)	0.8	1.3 (1.4)
20	70	0.19	0.94	0.27	-11	-14	-7	-7	2.5	2.4 (1.8)	0.6	1.1 (1.2)
20	76	0.19	0.94	0.30	-13	-12	-8	-6	2.7	2.4 (1.7)	0.6	0.9 (1.2)
21	17	0.12	0.90	0.22	-14	-10	2	3	3.2	1.8 (1.5)	1.0	1.0 (1.3)
21	18	0.12	0.90	0.22	-17	-12	4	3	3.3	1.6 (1.5)	1.2	1.1 (1.3)
21	22	0.12	0.90	0.22	-18	-11	4	3	3.3	1.7 (1.5)	1.2	1.1 (1.3)
22	22	0.28	0.89	0.22	-34	-43	3	5	3.6	17.0 (7.7)	1.7	12.8 (6.4)
22	18	0.28	0.89	0.22	-37	-43	4	6	3.8	16.8 (7.9)	2.4	14.0 (6.6)
22	17	0.28	0.89	0.22	-50	-42	6	6	4.2	18.0 (8.0)	3.3	13.8 (6.9)
22	18	0.22	0.91	0.22	-38	-34	8	3	5.6	11.7 (5.8)	3.4	9.4 (5.0)
22	25	0.22	0.91	0.22	-37	-35	4	0	3.9	12.3 (5.8)	2.4	8.1 (4.8)
22	30	0.22	0.91	0.22	-43	-37	-1	-2	3.7	13.1 (5.7)	2.4	6.8 (4.7)
22	36	0.22	0.91	0.22	-41	-42	-4	-6	3.5	13.3 (5.6)	2.0	6.1 (4.6)
24	21	0.14	0.90	0.22	-23	-19	2	7	2.7	9.2 (2.7)	0.6	2.9 (2.6)
24	18	0.14	0.90	0.23	-24	-19	3	7	2.7	9.9 (2.8)	0.5	2.2 (2.6)
24	17	0.18	0.98	0.22	-21	-13	-4	-6	1.6	8.4 (3.2)	1.5	2.1 (3.0)
24	18	0.18	0.98	0.22	-7	-15	-3	-7	1.3	7.5 (3.2)	0.9	3.1 (2.9)
24	72	0.18	0.98	0.29	-5	-10	-3	-6	3.8	8.7 (4.3)	1.5	2.8 (2.6)
24	85	0.18	0.98	0.35	-5	-9	-5	-5	4.2	8.3 (4.1)	1.3	2.2 (2.0)

3.3.3.1 IMPACT OF THE WATER VAPOR ABSORPTION COEFFICIENTS ON THE LW FLUXES BY THE TWO-STREAM MODEL

As mentioned in Sect. 3.3.1 the LOWTRAN 5 database may underestimate the near-infrared water vapor absorption by about 10%, according to Halthore et al. [2005]. Fig.3.5 shows the water vapor absorption coefficient values as a function of the wavelength used by GAME (open black triangles) and Two-Stream (open grey dots) at 09:47 UTC on 22 June 2013 and clearly reveals the differences on the water vapor spectral absorption of the two models. Therefore, the water vapor absorption coefficients from the LOWTRAN 5 database at the 11 wavelengths that define the Two-Stream model resolution within the LW spectral range (4–37 μm, Table 3.1) are modified to make the water vapor spectral absorption of the Two-Stream model closer to the one of GAME.

The full grey dots in Fig.3.5 show the optimized water vapor (OWV) absorption spectrum at 09:47 UTC on 22 June 2013. The OWV absorption coefficient values are obtained by averaging the high spectral resolution GAME values in the corresponding Two-Stream LW sub-bands. The LW downward flux at the BOA and the LW upward flux at the TOA without aerosol (LW-$F^{DN,0}$ and -$F^{UP,0}$, respectively) have been simulated by using the OWV spectrum to evaluate its impact on the LW flux values. While at 09:47 UTC on 22 June 2013 the value of the BOA LW-$F^{DN,0}$ increases from 403.4 $W \cdot m^{-2}$ up to 413.9 $W \cdot m^{-2}$, conversely, the value of the TOA LW-$F^{UP,0}$ decreases from 373.9 $W \cdot m^{-2}$ down to 357.9 $W \cdot m^{-2}$ by using the OWV absorption coefficient. The corresponding GAME values of the BOA LW-$F^{DN,0}$ and TOA LW-$F^{UP,0}$ are equal to 411.4 and 348.9 $W \cdot m^{-2}$, respectively. Therefore, the use of the OWV spectrum has allowed reducing the differences between the values of LW flux without aerosol provided by the two models up to 0.6% and 2.5% at the BOA and at the TOA, respectively. Figs. 3.6a and 3.6b (open boxes) show the Two-Stream model instantaneous BOA LW-$F^{DN,0}$ and TOA LW-$F^{UP,0}$ values, respectively, versus the corresponding GAME values.

Full boxes represent in Figs. 3.6a and 3.6b the corresponding values of LW flux without aerosol calculated by using the OWV spectrum in the Two-Stream model, denoted as OWV-TS. The use of the OWV-TS has allowed improving the correlation and decreasing the mean bias between the BOA LW-$F^{DN,0}$ and the TOA LW-$F^{UP,0}$values provided by the two models and, therefore, decreasing the LW-ARE differences. Sensitivity tests revealed that the optimization of the water vapor absorption coefficients at 5.35, 6.25, and 7.35 μm is mainly responsible for the results of Fig.3.6 and revealed also that the use of the OWV absorption profile allowed decreasing by about 10% the differences between the LW-AREs by GAME and the Two-Stream model, both at the BOA and at the TOA.

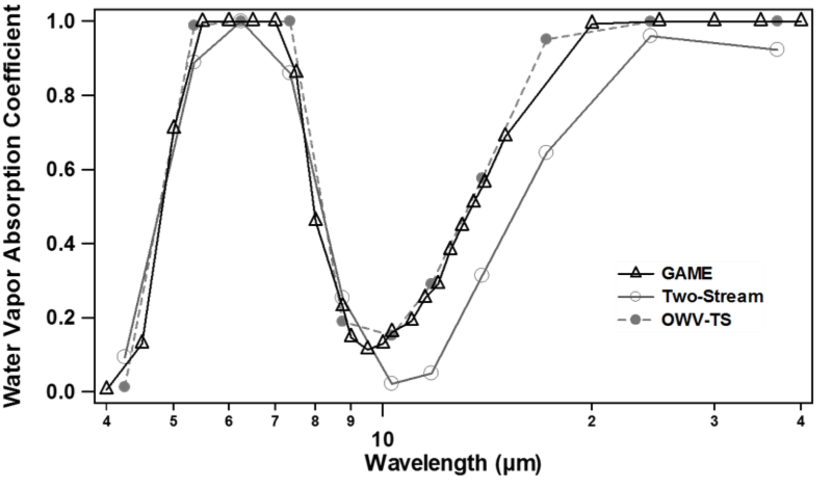

Fig.3.5. Water vapor absorption coefficient values used as input in the long-wave spectral range for GAME (open black triangles) and Two-Stream (open grey dots) related to the simulation at 09:47 UTC of 22 June 2013. The full grey dots represent the optimized water vapor profile for Two-Stream (OWV-TS) at the selected time.

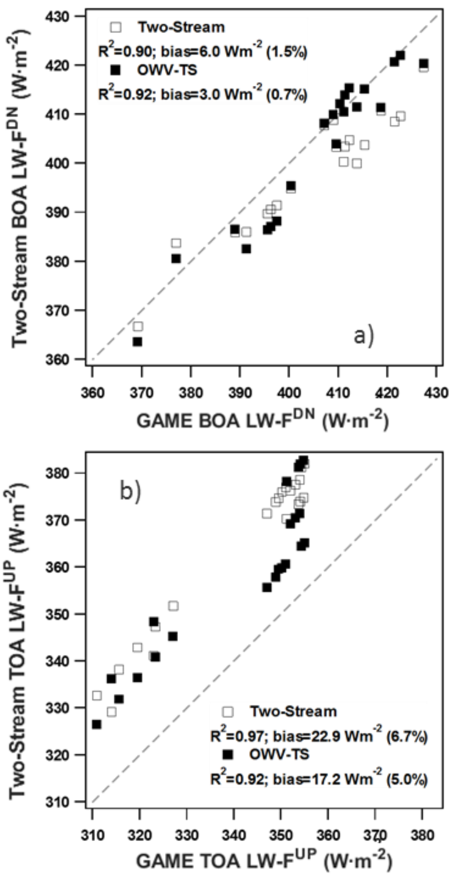

Fig.3.6. LW (a) BOA downward and (b) TOA upward fluxes without aerosol simulated by the TS model (open boxes) and the OWV-TS model (full boxes) versus the corresponding GAME values. The square of the linear correlation coefficient (R^2) and the mean bias values are also reported. The grey dotted line represents the 1:1 line.

3.3.3.2 Impact of the Optimization of Refractive Index Values on the LW-AREs by the Two-Stream Model

Fig.3.7 shows the spectral dependence of the real (*n*) and imaginary (*k*) parts of the refractive index values in the LW spectral range. In particular, open triangles in Figs. 3.7a and 3.7b show the *n* and *k* values, respectively, at the 115 LW sub-bands that characterize the GAME spectral resolution within the 4–37 μm spectral range (Table 3.1). To this end, it is worth noting that Krekov [1993] provides the LW refractive index values in 27 spectral intervals. Grey open dots show the *n* and *k* values (Figs. 3.7a and 3.7b, respectively) at the 11 LW sub-bands that characterize the Two-Stream model spectral resolution within the 4–37 μm spectral range (Table 3.1).

Figs. 3.7a and 3.7b reveal that the GAME *n* and *k* peak values at 9.5 μm are not accounted for in the Two-Stream model, because of its lower spectral resolution. Then, the Two-Stream *n* and *k* values at 8.75 μm have been set equal to 2.60 and 0.62, respectively, and the *k* value at 11.5 μm has been set equal to 0.12 to improve the agreement between the refractive index values used by the two models. Grey full dots in Figs. 3.7a and 3.7b show the optimized *n* and *k* values, respectively. The LW-ARE has been calculated with the Two-Stream model to evaluate the impact of the optimized values of *n* (at 8.75 μm) and *k* (at 8.75 and 11.5 μm). In fact, sensitivity tests revealed that the LW-ARE values are sensitive to changes of the refractive index values only within the 7.35–11.5 μm LW spectral range. In particular, the use of the optimized *n* and *k* values in the Two-Stream model allows decreasing up to 80% the mean differences with the corresponding GAME LW-AREs, both at the BOA and at the TOA. Therefore, the impact of the optimization of the refractive index values on the LW-ARE values is significantly larger than the one due to the optimization of the water vapor absorption profile (Sect. 3.3.3.1).

Table 3.2 show the LW-AREs at the surface and at the TOA, respectively, calculated with the Two-Stream model by taking into account both the OWV spectrum and the optimized n and k values at 8.75 and 11.5 μm, denoted as O-TS (Optimized Two-Stream). The optimization of the Two-Stream model has allowed increasing the square of the linear correlation coefficient (R^2) from 0.43 (Fig.3.4b) to 0.66 and decreasing the mean bias value from +4.9 to +0.8 $W \cdot m^{-2}$. Analogously, it can be deduced also that the O-TS model has also allowed improving the agreement with the TOA LW-AREs from GAME, by increasing the R^2 value from 0.64 (Fig.3.4d) to 0.73 and decreasing the mean bias value from +3.1 to +1.4 $W \cdot m^{-2}$. Note that the impact of the O-TS model on the LW-ARE values is largest on 22 June, which represented the day most affected by desert dust. Therefore, the LW spectral resolution impact on the LW-AREs on average decreases with the decrease of the aerosol load and, more specifically, with the decrease of the coarse particle contribution. In fact, the LW radiation is mostly affected by coarse particles, such as sea salt and/or desert dust particles [Sicard et al., 2014b].

In general the effects of a low spectral resolution in the RT calculations can be reduced by a suitable choice of the aerosol parameters at the available wavelengths. As previously reported, the optimization of the n and k values at 8.75 and 11.5 μm has allowed decreasing the mean LW-ARE by about 80%, both at the surface and at the TOA. Hatzianastassiou et al. [2007] in their research evaluated the ARE within the 0.85–10 μm spectral range on a planetary scale by using both detailed spectral and spectrally averaged aerosol optical properties and found that the use of spectrally averaged aerosol optical properties in the near-infrared spectral range, instead of detailed spectral ones, determined mostly an overestimation of the ARE both at the TOA and at the BOA, in accordance with the results presented in this Chapter.

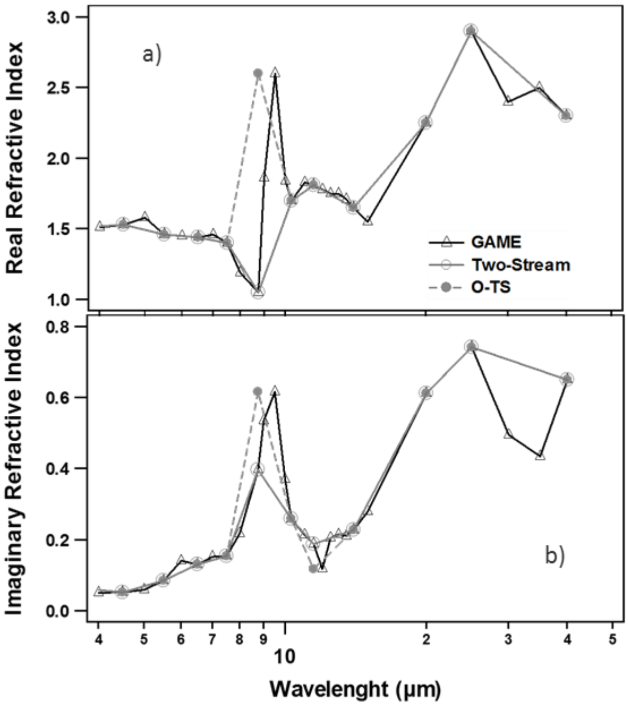

Fig.3.7. (a) Real and (b) imaginary parts of the refractive index values (as a function of the wavelength, on logarithmic scale) used as input in the long-wave spectral range for GAME (open black triangles) and Two-Stream (open grey dots). Full grey dots represent the optimized (a) real and (b) imaginary refractive index values used as input in the long-wave spectral range for Two-Stream (O-TS).

3.3.3.3 COMMENTS ON THE CALCULATED SW- AND LW-AREs AND COMPARISON WITH PREVIOUS STUDIES

Figs. 3.8a–3.8c show the SW-ARE at the TOA calculated by GAME (open symbols) and the Two-Stream model (full symbols) versus the SSA at 440 nm, the experimentally determined surface albedo (*alb*), and the SZA, respectively, for 20 (dots), 21 (triangles), 22 (boxes), and 24 (diamonds) June 2013. In Fig. 3.8 the positive TOA SW-ARE values are associated with small values of SSA, *alb*, and SZAs. The SSA, which measures the scattering versus absorption properties of an aerosol layer, represents the key parameter governing the amount of cooling versus heating. In fact, positive values of the ARE at the TOA reflect a strong absorption by the aerosol layer. Conversely, negative TOA AREs indicate that the scattering processes by the aerosol particles predominate with respect to the absorption ones. However, one must be aware that for a given aerosol layer the critical SSA value (SSAc), which defines the boundary between cooling and heating, also depends on the surface albedo and the aerosol backscatter fraction ($\beta_{aer}(\lambda, R)$) values [e.g., Seinfeld and Pandis, 1998, Fig. 22.16].

In fact, the SSAc value on average increases with the increase of the surface albedo and the decrease of the aerosol backscatter fraction, for a given aerosol layer. At this point, it is worth noting that $\beta_{aer}(\lambda, R)$ increases with the solar zenith angle. More specifically, from Fig. 3.8a can be estimated that during the Saharan dust event described above, the SSAc value is equal to 0.91 and is associated with *alb* values smaller than 0.23 (Fig. 3.8b) and SZA values smaller than 25° (Fig. 3.8c). During 22 June positive and negative TOA SW-AREs are provided by the two RTMs at SSA = 0.91 (Fig. 3.8a, boxes). Fig. 3.8c (boxes) reveals that the negative TOA SW-AREs are associated with SZAs greater than 29° and, hence, with greater backscatter fraction values than the ones associated with SZAs smaller than 29°. Sicard et al. [2014a] estimated with GAME the instantaneous, clear-sky, TOA SW-ARE during 11 dust outbreaks, which affected Barcelona (Spain) from 2007 to 2012. They found that the TOA SW-ARE reached a positive value (+8.5 $W \cdot m^{-2}$) only on 22 July 2009 for SSA (at 440 nm) = 0.83, SZA = 21.1°, and *alb* = 0.017.

The low values of SSA, SZA, and *alb* are responsible for the positive value of the TOA SW-ARE, in agreement with the results of this study (Fig. 3.8). In fact, Sicard et al. [2014a] found that the SSA (at 440 nm) reached a rather small value (0.79) also on 21 July 2009. Nevertheless, they found that the TOA SW-ARE value was negative (-22.8 $W \cdot m^{-2}$) for *alb* = 0.017 and SZA = 77°. The larger SZA value is likely responsible for the negative sign of the TOA SW-ARE, according to Fig. 3.8c. This last comment is supported by Liao and Seinfeld [1998], who have numerically investigated the TOA ARE for a uniform aerosol layer (from the Earth's surface to 5 km) made of pure ammonium sulfate, pure soot, internal mixture, and external mixture. They found at SZA = 0° that the SW-ARE is equal to -2.0 and +5.5 $W \cdot m^{-2}$ for pure ammonium sulfate and soot, respectively, and that the internal and external mixtures are also responsible for positive TOA SW-AREs (+4.6 $W \cdot m^{-2}$ and +3.6 $W \cdot m^{-2}$, respectively).

It is worth noting that the SSA (at 440 nm) daily averaged value was smaller on 22 June than on 20 and 21 June. This behavior is explained because the small SSA values of 22 June are likely due to a mixing of desert dust with polluted particles. In fact, Romano et al. [2016] shown that the Two-Stream RTM could reproduce the experimental SW- and LW-AREs at the surface by replacing the refractive indices typical of desert dust with the ones obtained for a mixture made of dust and soot particles. The dust contamination by anthropogenic particles during its transport to monitoring sites located a few thousand kilometers away from the source region is considered responsible for this last result. Also, the low SSA values found by Sicard et al. [2014a] on 22 July 2009 and 21 June 2009 are also ascribed to the mixing of Saharan dust with pollution and biomass burning particles.

The BOA SW-AREs presented here related to 22 June 2013 are in satisfactory agreement with the experimentally determined SW-AREs at the surface reported by Romano et al. [2016] for 10 July 2012, which was a day characterized by aerosol properties similar to the one of this study. Gómez-Amo et al. [2011] calculated, during the June 2007 Saharan dust event in the cental Mediterranean by using the MODTRAN4 RTM, values of SSA (at 416 nm)smaller than the ones found at Lecce, likely as a consequence of a greater dust contamination by anthropogenic particles. In fact, the Rome SSA values are even smaller than the ones of Lecce, during the June 2007 Saharan dust event. Nevertheless, Gómez-Amo et al. [2011] found negative TOA SW-AREs at SZA = 60° both at Rome and Lecce, in accordance with the above reported comments.

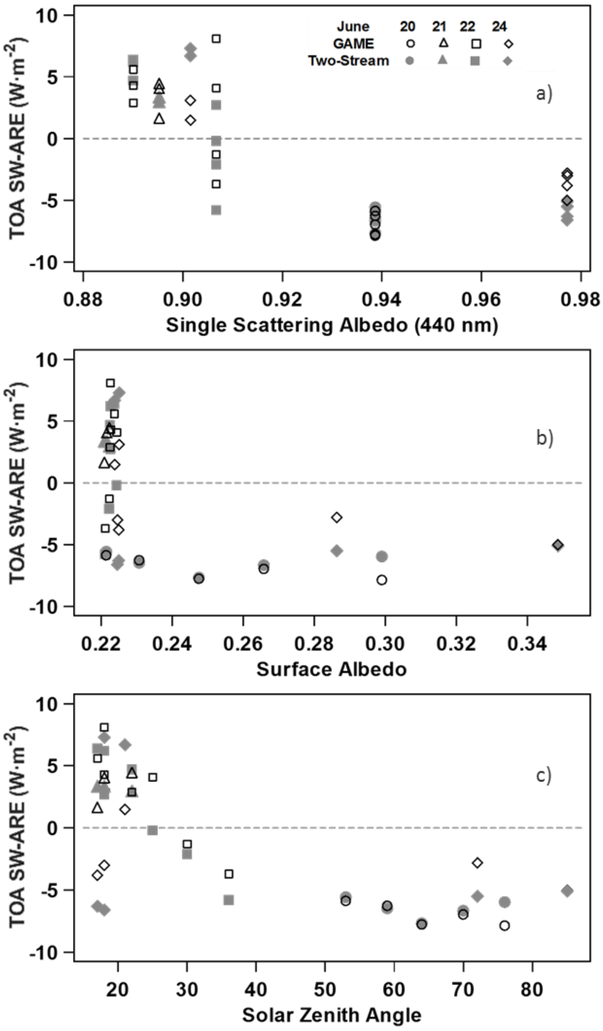

Fig. 3.8. The instantaneous values of short-wave ARE at the top of the atmosphere simulated by GAME (open black symbols) and Two-Stream (full grey symbols) for 20 (circles), 21 (triangles), 22 (boxes), and 24 (diamonds) June 2013 in Lecce (Italy) as a function of (a) SSA at 440 nm from AERONET sun-photometer measurements, (b) surface albedo from pyranometers measurements, and (c) solar zenith angle. The dashed grey line represents TOA SW-ARE = 0 $W \cdot m^{-2}$.

It is also worth mentioning that the SW-AREs of this study are both at the TOA and at the surface in good agreement with the ones reported by several authors and related to Mediterranean sites [e.g., Perrone and Bergamo, 2011; Gómez-Amo et al., 2011; Perrone et al., 2012; Sicard et al., 2014a, and references therein], if the SSA, AOD, *alb*, and SZA values are properly accounted for in the inter comparison analysis. Recently, Mallet et al. [2016] have reported calculations of the 3-D (clear-sky) surface SW-ARE indicated an average from about -20 to -10 $W \cdot m^{-2}$ (from 11 June ti 5 July 2013) over the Mediterranean Sea, together with maxima (-50 $W \cdot m^{-2}$) over northern Africa. The TOA ARE is shown to be highly variable within the domain, due to moderate absorbing properties of dust and changes in the surface albedo. Indeed, 3-D simulations indicated negative effect over the Mediterranean Sea and Europe, and positive effect over northern Africa. In particular, at Lampedusa the TOA SW-ARE values were at noon equal to about -7, -10, -15, and -20 $W \cdot m^{-2}$ on 20–22, and 24 June, respectively. They have ascribed the negative values of the TOA SW-ARE found at Lampedusa and all over the Mediterranean to the low *alb* values of the ADRIMED monitoring stations, since most of them were located over islands.

Several works have investigated the desert dust radiative impact mostly in the SW spectral range [e.g., Gómez-Amo et al., 2011, and references therein] over the Mediterranean area. Less attention is paid to the dust radiative impact in the LW spectral range, which is generally of opposite sign. Consequently, it is of peculiar importance to account for both the SW- and the LW-ARE to properly evaluate the desert dust role in the Earth's radiation budget. The results presented in this Chapter revealed that the LW-ARE at the surface varied from +1.3 to +5.6 $W \cdot m^{-2}$ and from +1.5 to +8.0 $W \cdot m^{-2}$ for GAME and O-TS model, respectively. Also have been found that the TOA LW-ARE ranged between +0.5 and +3.4 $W \cdot m^{-2}$ and between +1.2 and

+6.9 $W \cdot m^{-2}$ for GAME and O-TS model, respectively. Results similar to the ones presented here are also reported by Sicard et al. [2014a], which evaluated with GAME the instantaneous and clear-sky LW-AREs at the TOA and BOA during 11 desert dust outbreaks that occurred at Barcelona (Spain). In particular, they found that the TOA and BOA LW-ARE is equal to +2.1 and +6.9 $W \cdot m^{-2}$, respectively, on 21 May 2007 at SZA = 56.8° and to +0.6 and +2.8 $W \cdot m^{-2}$, respectively, on 12 April 2011 at SZA = 41°. Romano et al. [2016] estimate the instantaneous, clear-sky, aerosol TOA and BOA LW-ARE by the Two-Stream model at the study site, during the 9–13 July 2012 desert dust event, reporting values in satisfactory agreement with the ones of this Chapter.

3.4 THE IMPORTANCE OF THE PARAMETERIZATION OF THE VERTICALLY-RESOLVED PROPERTIES IN RADIATIVE TRANSFER CALCULATIONS

In this section, the importance of the selected inputs for a RTM is discussed. For that purpose, different parameterizations are used as inputs of the GAME code.

3.4.1 INSTRUMENTS AND DATA

3.4.1.1 GROUND BASED MEASUREMENTS

Ground based measurements were carried out at the IISTA-CEAMA by a sun-photometer which belongs to the AERONET network [Holben et al., 1998], used to derive AOD and sky radiance measurements both at the nominal wavelengths (440, 670, 870 and 1020 nm). All AERONET data are downloaded from the AERONET web page at http:// aeronet.gsfc.nasa.gov/. Only AERONET Version 2 Level 1.5 (Level 2.0 when available) data is used.

The accuracy of AERONET (Version 2 Level 1.5 and Version 2 Level 2.0) inversion products is evaluated and discussed in Dubovik et al. [2000, 2002a], Holben et al. [1998, 2006] and Eck et al. [1999]. This accuracy of some products has been estimated with numerical sensitivity tests for different aerosol types, namely water soluble, dust and biomass burning [Dubovik et al., 2000, 2006]. The AOD products provided by AERONET have an uncertainty of ±0.01 for λ > 440 nm and of ±0.02 for λ < 440 nm [Holben et al., 1998; Eck et al., 1999]. AERONET also provides aerosol optical and microphysical properties used in this Chapter, such as columnar particle size distribution (PSD), real and imaginary parts of the refractive indices (n and k, respectively), asymmetry factor (g) and SSA, using the AOD and sky radiance values in an inversion algorithm [Dubovik and King, 2000; Dubovik et al., 2006]. The uncertainty in the retrieval of SSA is ±0.03 for high aerosol load (AOD_{440} > 0.4) and solar zenith angle > 50°; while for measurements with low aerosol load (AOD_{440} < 0.2), the retrieval accuracy of SSA drops down to 0.02–0.07 [Dubovik and King, 2000]. For high aerosol load and solar zenith angle > 50°, errors are about 30%–50% for the k. For particles in the size range 0.1< r <7 μm (being r the aerosol radius), errors in PSD retrievals are around 10–35%, while for sizes lower than 1 μm and higher than 7 μm retrieval errors rise up to 80–100%. By means of these variables, the GRASP code, introduced in Sect. 3.2.2, provides as output additional variables such as the volume concentration, effective radius, r_{eff}, and geometric standard deviation of the equivalent lognormal distribution, σ, for fine and coarse modes of the retrieved PSD.

The multi-wavelength aerosol Raman lidar MULHACEN, based on a customized version of LR331D400 (Raymetrics S.A.), is operated at Granada station as part of EARLINET/ACTRIS [Pappalardo et al., 2014] since April 2005. The aerosol particle backscatter coefficient profiles ($\beta_{aer}(\lambda, R)$) obtained from the multi-wavelength lidar are calculated by means of the Klett-Fernald method [Fernald et al., 1972; Fernald, 1984; Klett, 1981; 1985]. For the retrieval of the aerosol extinction coefficient profiles, $\alpha_{aer}(\lambda, R)$, is assumed a height-independent lidar ratio obtained by forcing the vertical integration of $\alpha_{aer}(\lambda, R)$ to the AOD from AERONET photometer [Landulfo et al., 2003].

The assumption of a constant lidar ratio introduces uncertainty in $\alpha_{aer}(\lambda, R)$ retrievals, especially when different types of aerosol appear at different layers. In this Chapter, the idar ratios used for the Klett-Fernald retrieval are very similar to those provided by GRASP [see Benavent-Oltra et al., 2017]. Considering the different uncertainty sources, total uncertainty in the profiles obtained with Klett-Fernald method is usually 20% for $\beta_{aer}\ (\lambda, R)$ and 25-30% for $\alpha_{aer}(\lambda, R)$ profiles [Franke et al., 2001]. Additionally, surface temperature and pressure are continuously monitored at IISTA-CEAMA by a meteorological station located 2 m above the ground. At the same location, the global and diffuse downward radiative fluxes for the SW are continuously measured with a CM11 pyranometer (Kipp & Zonen) and diffuse downward radiative fluxes for the LW are measured with a PIR pyrgeometer (Eppley) [Antón et al., 2012, 2014].

3.4.1.2 AIRBORNE MEASUREMENTS

The Safire ATR 42 aircraft performed two overpasses above Granada on 16 (flight F30) and 17 (flight F31) June in 2013 during the ChArMEx/ADRIMED campaign. Flight details can be found in Denjean et al. [2016], Mallet et al. [2016], Benavent-oltra et al. [2017] and Román et al. [2018]. Also the aircraft trajectories are detailed in Fig. 1 from Benavent Oltra et al. [2017].

The airborne instrumentation includes a Scanning Mobility Particle Sizer (SMPS) and an Ultra-High Sensitivity Aerosol Spectrometer (UHSAS), for measuring aerosol number size distribution in the submicron range. The Forward Scattering Spectrometer Probe model 300 (FSSP-300) and the GRIMM OPC (sky-OPC 1.129) were used to measure the optical size distributions in the diameter nominal size range between 0.28 and 20 μm and between 0.3 and 32 μm, respectively. A nephelometer (TSI Inc, model 3563) was used to measure the particle scattering coefficient at 450, 550 and 700 nm, and a Cavity Attenuated Phase Shift (CAPS-PMex, Aerodyne Inc.), was employed to obtain the α_{aer} at 530 nm. For more details on the aircraft instrumentation see Denjean et al. [2016] and references therein. The PLASMA (Photomètre Léger Aéroporté pour la Surveillance des Masses d'Air) system, which is an airborne sun-tracking photometer, was additionally used to obtain AOD with wide spectral coverage (15 channels between 0.34 – 2.25 μm) with an accuracy of approximately 0.01, as well as the vertical profiles of the aerosol extinction coefficient [Karol et al., 2013; Torres et al., 2017].

Airborne radiative fluxes (F) were measured with Kipp & Zonen CMP22 pyranometers and CGR4 pyrgeometers. SW-F^{UP} and SW-F^{DN} were measured in the spectral range 297-3100 nm by two instruments located above and below the aircraft fuselage. The same setup was used for the pyrgeometers, which provided the LW-F^{UP} and LW-F^{DN} for wavelengths larger than 4 μm. Both pyranometers and pyrgeometers were calibrated in January 2013 and data were corrected for the temperature dependence of the radiometer's sensitivity following Saunders et al. [1992].

Downward pyrgeometer measurements are filtered out for large pitch and roll angles and corrected from the rapid variations of the solar incidence angle around the solar zenith angle due to the aircraft attitude (pitch and roll). Also, data are corrected from variations of the SZA during the flight to ease the comparison with GAME retrievals. After these various corrections taking into account the accuracy of the calibration and of the acquisition system together with the consistency of airborne measurements [Meloni et al., 2018], an estimated uncertainty of ±6 $W \cdot m^{-2}$ is considered to affect the data.

3.4.2 GAME INPUT DATA PARAMETERIZATION

The two considered SAFIRE ATR 42 flights, F30 and F31, took place on 16 (between 14:15 and 14:45 UTC, averaged SZA=31.49^{o}) and 17 (07:15 to 07:45 UTC, averaged SZA=61.93^{o}) June 2013, respectively, simultaneously to ground-based lidar and sun-photometer measurements performed at the station. Unfortunately, the airborne vertical profile of extinction by the CAPS measurements was not available during the second flight. During these days, mineral dust from southern Morocco, reached Granada after about 4 days of travelling, according to back-trajectories analysis (not shown) and the results presented in Denjean et al. [2016]. This event is widely described in Benavent-Oltra et al. [2017]. The sun-photometer microphysics data were not available until 16:22 UTC, even though the retrieved AOD and its spectral dependence (represented by the Angström exponent) are very stable between the time of the lidar measurements and the time of the sun-photometer inversion. Besides, on 17 June after 15:00 UTC, the lidar detected clouds. Furthermore, the ground-based pyranometer and pyrgeometer data indicate cloud contamination in the radiation data much earlier (around 09:00 UTC), preventing also satellite retrievals in the region.

In Table 3.3 the data used as input for GAME calculations during these two days studied is summarized, including surface parameters and atmospheric profiles of meteorological variables, main gases concentrations and aerosol properties. The aerosol properties used in the present study are parameterized by means of three different datasets, based on the different instrumentation and retrievals available, i.e. Dataset 1 (DS1), Dataset 2 (DS2) and Dataset 3 (DS3). A more detailed description of the different parameters is provided next.

3.4.2.1 SURFACE PARAMETERS AND PROFILES OF METEOROLOGICAL VARIABLES

The surface parameters required for GAME are the *alb*(λ) and land-surface temperature (LST). The *alb*(λ) for the SW range is obtained from the sun-photometer data using the AERONET retrieval at 440, 675, 880 and 1020 nm, and for the LW from the emissivity provided by the Single Scanner Footprint (SSF) Level2 products of the CERES (Clouds and the Earth’s Radiant Energy System; (http://ceres.larc.nasa.gov/) instrument (Table 3.4). LST values are obtained from MODIS (Moderate Resolution Imaging Spectroradiometer) 1 km daily Level-3 data [Wan et al., 2014] on 16 June. Unfortunately, on 17 June MODIS data are not available due to the presence of clouds and the local surface temperature is obtained from temperature measurements at Granada site, where the meteorological station is located at 2 m above the ground. LST and *alb*(λ) values used for the two analyzed cases are included in Table 3.4.

Table 3.3: Summary of the data sources used to obtain the input data parameterizations for GAME computations both in the SW and LW spectral ranges, including the surface parameters (albedo, *alb*, and Land-surface temperature, LST), profiles of meteorological variables and main gases and the aerosol parameters. For the aerosol parameters (aerosol extinction, α_{aer}, SSA, and asymmetry parameter, g) three different datasets are used (DS1, DS2 and DS3) based on different instrumentation and retrievals. The indications below the sources of the aerosol parameters indicate whether the parameter is column integrated (col) or if it is vertically resolved (R) and the number of wavelengths at which it is given (n λ).

Parameters		**Shortwave**			**Longwave**		
Spectral Range		0.3 – 3.1 μm			4.5 – 40 μm		
Number of sub-bands		167			115		
Meteo Parameters	at the surface	IISTA-CEAMA			IISTA-CEAMA		
	< 20 km	Aircraft			Aircraft		
	> 20 km	US Standard Atmosphere			US Standard Atmosphere		
Main Gases Parameters	Concentration Profile	US Standard Atmosphere			US Standard Atmosphere		
	Absorption Coefficients	HITRAN			HITRAN		
Surface Parameters	Surface Albedo	Ground-based measurements			CERES		
	LST	IISTA-CEAMA			MODIS		
		DS1	DS2	DS3	DS1	DS2	DS3
Aerosol Parameters	α_{aer}	GRASP (R, 7 λ)	Klett (R, 3 λ)	Aircraft (R, 1 λ)	Mie Calculation (see Table 3.6)		
	SSA	GRASP (R, 7 λ)	AERONET (col, 4 λ)	Aircraft (col, 1 λ)			
	g	AERONET (col, 4 λ)	AERONET (col, 4 λ)	AERONET (col, 4 λ)			

Table 3.4: Surface albedo, *alb(λ)*, values provided by AERONET for the SW spectral range and by CERES for the LW. LST on 16 June is obtained from MODIS whereas on 17 June is estimated from the meteorological station at Granada site. These surface parameters are common to all parameterizations.

	***alb*(440nm)**	***alb*(675nm)**	***alb*(870nm)**	***alb*(1020nm)**	***alb*(LW)**	**LST (K)**
16 June	0.05	0.15	0.30	0.30	0.016	314.5
17 June	0.05	0.15	0.31	0.31	0.013	298.1

3.4.2.2 AEROSOL PARAMETERIZATION

For the SW wavelengths, $\alpha_{aer}(\lambda, R)$, SSA(λ, R) and $g(\lambda, R)$ are obtained from the measurements performed with the instrumentation available during the campaign; namely the lidar, the sun-photometer and the in situ instrumentation onboard the aircraft. On the other hand, direct measurements of the aerosol properties in the LW are not so straightforward and thus scarce. Hence, the aerosol LW radiative properties are calculated by a Mie code, which introduces negligible uncertainties [Granados-Muñoz et al., 2019].

For the SW simulations, GAME is using three different aerosol input datasets in order to evaluate their influence on the ARE calculations. DS1 relies on a parameterization based on the advanced post-processing GRASP code (see Sect. 3.2.2), DS2 relies on Klett-Fernald lidar inversions and AERONET products and corresponds to a reference parameterization (easily reproducible at any station equipped with a single- or multi-wavelength lidar and an AERONET sun-photometer and without the need of an advanced post-processing algorithm); and DS3 relies on in situ airborne measurements and corresponds to an alternative parameterization to DS1 and DS2.

Table 3.5: Column-integrated number concentration (*N*), effective radii (r_{eff}) and standard deviation (σ). The subscripts f and c stand for fine and coarse aerosol modes respectively. AOD at 550 nm for DS1, DS2 and DS3 on 16 and 17 June.

	16 June (SZA=31.49^{o})						
	N_f ($\# \cdot \mu m^{-2}$)	**N_c ($\# \cdot \mu m^{-2}$)**	**$r_{eff,f}$ (μm)**	**$r_{eff,c}$ (μm)**	**σ_f (μm)**	**σ_c (μm)**	**AOD (550 nm)**
DS1	9.04	0.018	0.12	2.22	0.48	0.73	0.18
DS2	7.53	0.014	0.12	1.9	0.57	0.65	0.23
DS3	-	-	0.11	1.92	0.63	0.66	0.23
	17 June (SZA=61.93º)						
	N_f ($\# \cdot \mu m^{-2}$)	**N_c ($\# \cdot \mu m^{-2}$)**	**$r_{eff,f}$ (μm)**	**$r_{eff,c}$ (μm)**	**σ_f (μm)**	**σ_c (μm)**	**AOD (550 nm)**
DS1	9.04	0.014	0.1	2.4	0.45	0.72	0.16
DS2	8.03	0.012	0.11	2.08	0.53	0.68	0.19
DS3	-	-	0.11	2.56	0.64	0.59	0.18

In Benavent-Oltra et al. [2017] is presented a detailed analysis and discussion on the comparison between aerosol extinction profiles provided by the aircraft measurements, GRASP and the lidar system at Granada. In Granados-Muñoz et al. [2019] is also presented a detailed description of the α_{aer} profiles, the SSA values retrieved by GRASP algorithm, used as input for GAME in DS1; the SSA taken from AERONET columnar values and assumed to be constant with height, used as input for GAME in DS2; the SSA values at 530 nm obtained from the nephelometer and the CAPS or PLASMA onboard the ATR, used as input for GAME in DS3 and the profiles of aerosol volume concentration for the fine and coarse mode obtained from GRASP/DS1 and aircraft in-situ/DS3 measurements on 16 and 17 June.

In general, the lidar, GRASP and the CAPS data are in accordance, observing the same aerosol layers and similar values, with discrepancies within 20%. GRASP slightly overestimates CAPS data by 3 Mm^{-1} on average, whereas the differences with PLASMA are larger, reaching a 30% (or 11 Mm^{-1}). In the case of the Klett-Fernald retrieval, values are lower than those retrieved with GRASP by up to 19%. Considering that the uncertainty in aerosol extinction is around 30% for both GRASP and the Klett-Fernald retrieval and 3% for the CAPS data, this discrepancy is well below the combined uncertainty of the different datasets. Differences in the aerosol extinction profiles translate into differences in the integrated extinction and, hence, in differences in the AOD values used as input in the radiative fluxes retrievals. The AOD values presented in Table 3.5 are obtained by integrating the aerosol extinction profiles, interpolated at 550 nm, from the surface up to the top of the aerosol layer (4.3 km on 16 June and 4.7 km on 17 June). In GRASP retrieved α_{aer} profiles, values above the top of the aerosol layer are slightly larger than zero, thus the approach used here to calculate the AOD leads to lower values compared to the column-integrated AOD provided by the sun-photometer. Differences among the three datasets are more noticeable on 16 June, when the AOD for DS1 is 0.05 lower than for DS2 and DS3, whereas on 17 June the maximum difference is 0.03, obtained between DS1 and DS2. The AOD values at 550 nm reveal that GRASP input data (DS1) and in a lesser extent the aircraft in situ data (DS3) underestimate the aerosol load in the analyzed dust layer compared to AERONET (DS2) due to the differences in the retrieval techniques, e.g. whereas AERONET provides integrated AOD for the whole column, low aerosol extinction values above the aerosol layer are neglected for the AOD calculations in DS1 and DS3.

The mean SSA at 440 nm is equal to 0.92 on 16 June, whereas on 17 June it is 0.85. On 17 June the SSA profiles present lower values and more variation with height than on 16 June; the lower SSA values indicate the presence of more absorbing particles on 17 June. The vertical variation on 17 June is associated to the presence of two different layers, whereas a more homogeneous dust layer is observed on 16 June. The SSA at 440 nm is 0.89 and 0.83 on 16 and 17 June respectively, so, SSA values are lower on 17 June due to the intrusion of more absorbing particles. In order to reduce the uncertainty of the measured data, only averaged SSA values at 530 nm for the column are considered, being 0.88 and 0.83 on 16 and 17 June. Therefore, differences of up to 0.04 and 0.02 are observed on 16 and 17 June, respectively, among the SSA values obtained with the three datasets. Despite these difference, the retrieved SSA values obtained are within the range of typical values for dust aerosols [Dubovik et al., 2002a; Lopatin et al., 2013] and differences are still within the uncertainty limits, which range between 0.02 and 0.07 depending on the aerosol load for AERONET data [Dubovik et al., 2000] and is 0.04 for the aircraft values. In the case of g values, the same data are used for the three aerosol input datasets. Multispectral values of g are taken from AERONET columnar values and assumed to be constant with height.

Summing up, for the SW aerosol parameterization in GAME, three datasets are tested. In DS1, GRASP code provides spectral profiles at 7 wavelengths of the aerosol extinction and SSA. In DS2, the Klett retrieved extinction profiles at 3 wavelengths are used together with the AERONET SSA columnar values at 4 wavelengths, which are assumed to be constant with height. For DS3, one extinction profile at 550 nm and a column-averaged monospectral value of the SSA from the airborne measurements are considered. In the three cases, the column-integrated AERONET asymmetry parameter at 4 wavelengths is assumed to be constant with height and used as input.

For the LW calculations, the Mie code is used to obtain $\alpha_{aer}(\lambda, R)$, SSA(λ, R) and $g(\lambda, R)$ from the information on the aerosol PSD, complex refractive index and density, following a similar approach to that used in previous studies [Meloni et al., 2015; 2018; Peris-Ferrús et al., 2017]. A summary of the aerosol parameters used in the Mie calculations is included in Table 3.6. Three different datasets are also used for the aerosol parameterization in the LW calculations. In this case, the sensitivity of the model to the PSD used is tested. A similar scheme to that presented for the SW is used, where DS1 relies on GRASP retrievals, DS2 on AERONET products and DS3 relies on in situ airborne measurements.

Table 3.6: Summary of the data used to obtain $\alpha_{aer}(\lambda, R)$, SSA(λ, R) and $g(\lambda, R)$ in the LW from Mie calculations, i.e. the refractive index, RI, effective radius, r_{eff}, geometric standard deviation, σ, and number concentration, *N*. Three different datasets are used (DS1, DS2 and DS3) based on different particle size distribution (PSD) data used. The indications below the sources of the aerosol parameters indicate whether the parameter is column integrated (col) or if it is vertically resolved (R) and the number of wavelengths at which it is given ($n\ \lambda$). DB(2017) stands for Di Biagio et al., [2017].

		LW		
		DS1	**DS2**	**DS3**
Mie calculations	**RI**	DB (2017), (col, 601 λ)	DB (2017), (col, 601 λ)	DB (2017), (col, 601 λ)
	r_{eff}	GRASP (col),	AERONET (col)	Aircraft (R)
	σ	GRASP (col)	AERONET (col)	Aircraft (R)
	N	GRASP (R)	AERONET (col)	Aircraft (R)

The spectral real (n) and imaginary (k) parts of the refractive index of mineral dust in the LW are obtained from Di Biagio et al. [2017], using the Morocco source, and assumed constant with height. The analysis by Di Biagio et al. [2017] only covers the spectral range 3-16 μm, so an extrapolation assuming the spectral dependence presented in Krekov [1993] for shorter and longer wavelengths is performed. This assumption is not exempt of uncertainty, since the refractive index present a certain variability associated to the different nature of mineral dust properties. For example, the use of the refractive index provided for the Algerian and Mauritanian sources from Di Biagio et al., [2017] leads to variations in the ARE of 0.8 and 0.3 $W \cdot m^{-2}$ at the BOA and the TOA respectively.

Additionally, vertical variations of the refractive index are also a source of uncertainty in the obtained radiative fluxes. The mineral dust particle density is assumed to be 2.6 $g \cdot cm^{-3}$ [Hess et al., 1998]. Regarding the PSD, three parameters (namely the effective radii, r_{eff}, standard deviation, σ, and the numeric concentrations, N) for fine and coarse modes are used. The fine mode comprises particles within the diameter range 0.1–1 μm, whereas for the coarse mode the range 1-30 μm is considered. In the case of DS1, N values are obtained from the volume concentration profiles provided by GRASP assuming spherical particles in the range between 0.05 and 15 μm radii. Values of r_{eff} and σ provided by GRASP (Table 3.6) are column-integrated and thus assumed to be constant with height. This is the case also for DS2, in which the PSD parameters are column-integrated values provided by the AERONET retrieval in Granada (see Table 3.6).

For DS3, the volume concentration (or the equivalent N), r_{eff} and σ profiles for the fine and coarse modes, are calculated from the data provided by the aircraft in situ measurements in the range 0.02-40 μm diameter. Benavent-Oltra et al. [2017] found in their research a general good accordance between the volume concentration profiles measured by the instrumentation onboard the SAFIRE ATR 42 and retrieved with GRASP, with differences in the total volume concentration profiles for the dust layers lower than 8 $\mu m^{-3} \cdot cm^{-2}$ (20%), which fall within the combined uncertainty. Nonetheless differences are still noticeable, especially in the fine mode. On 17 June, GRASP overestimates the aircraft measurements for the fine mode and underestimates them for the coarse mode, which in turns results in a quite different fine to coarse concentration ratio for DS1 and DS3. Differences are mostly technical, i.e., GRASP retrieval is based on 30-min averaged lidar profiles while the aircraft provide instantaneous measurements, but they can be also partially caused by the discrepancies between the vertical aerosol distribution above Granada (sampled by the lidar) and the concentration measured during the aircraft trajectory as they are not exactly coincident. In addition, for 16 June, there is a 2 hours' time difference between the sun-photometer retrieval used in GRASP calculations and the airborne measurements which can lead to slight differences in the aerosol properties despite the homogeneity of the dust event during this period. In the following, the impact that these differences may introduce in the calculations of F is quantified. As a result of the simulation, GAME provides vertical profiles of radiative fluxes in the shortwave (SW-F) and longwave (LW-F) spectral range. The net flux can be calculated from the obtained profiles for both spectral ranges as,

$$NetF = F^{DN} - F^{UP} \qquad [3.3]$$

3.4.3 MINERAL DUST EFFECT ON SHORTWAVE AND LONGWAVE RADIATION

3.4.3.1 SW RADIATIVE FLUXES

Fig. 3.9 shows the radiative fluxes profiles for the SW spectral range obtained with GAME using the three different input datasets described above, as well as the Net SW-F. The radiative fluxes measured by the pyranometer, onboard the SAFIRE ATR 42, are also included in Fig. 3.9. The three GAME simulations show similar values with differences below 8 $W \cdot m^{-2}$ on average, which represents less than 1% variation. The differences in the obtained fluxes are mostly due to the differences in the aerosol load considered depending on the inputs. Even though the differences in the AOD among the different datasets are small (lower than 0.05), they can lead to differences in SW-F and ultimately in the SW-ARE. In order to quantify these differences, a sensitivity test is performed, varying the AOD while the other parameters are kept constant. As a result, is observed a maximum variation in the SW-F of 6.5 $W \cdot m^{-2}$ (0.7%) at the surface, decreasing with height, for changes in the AOD of up to 0.05, which is the difference observed between the AOD for DS2 and DS1 on 16 June.

This result partly explains the differences among the three datasets. In addition, a sensitivity test performed by varying exclusively the SSA indicates that more absorbing particles are related to less SW-F^{DN} at the surface, namely a variation of 1% is observed at the BOA for a decrease in the SSA of 0.03. The influence of the SSA decreases with height being negligible at the TOA. For the SW-F^{UP}, a decrease of 0.8% is observed at the BOA if more absorbing particles are present, but in this case the influence at the TOA is larger (2.2%). Besides, the larger AOD assumed for DS2 on both days (see Table 3.5), causes the SW-F^{DN} to be slightly lower compared to DS1. For DS3 the AOD is also lower than for DS2, but the SSA values used, which are relatively smaller compared to those measured by AERONET, lead to lower values of the radiative fluxes than for DS2. The evaluation against the aircraft measurements shows larger differences for altitudes below 2.5 km (about 860 mbar) on 16 June, whereas a better agreement is found above. On 17 June, no SW-F^{UP} aircraft data are available below 2 km. Relative differences between the model and the aircraft measured data (calculated as ($\frac{F_{GAME}-F_{aircraft}}{F_{aircraft}}$) are well below 7%, being the largest discrepancies observed for the SW-F^{DN}. Dfferences between the three GAME outputs and the aircraft pyranometer are lower than 5% for the Net SW-F on both days. Considering the very different approaches followed by the model and the direct measurements by the airborne pyranometer (i. e. vertical resolution, temporal sampling and data acquisition and processing), together with the uncertainty of the pyranometer (6 $W \cdot m^{-2}$) and the estimated uncertainty of the model outputs, which can be as large as 19 $W \cdot m^{-2}$), these differences are quite reasonable. A conclusive result on which input dataset provides a better performance is unlikely because of the similar results obtained with the three datasets.

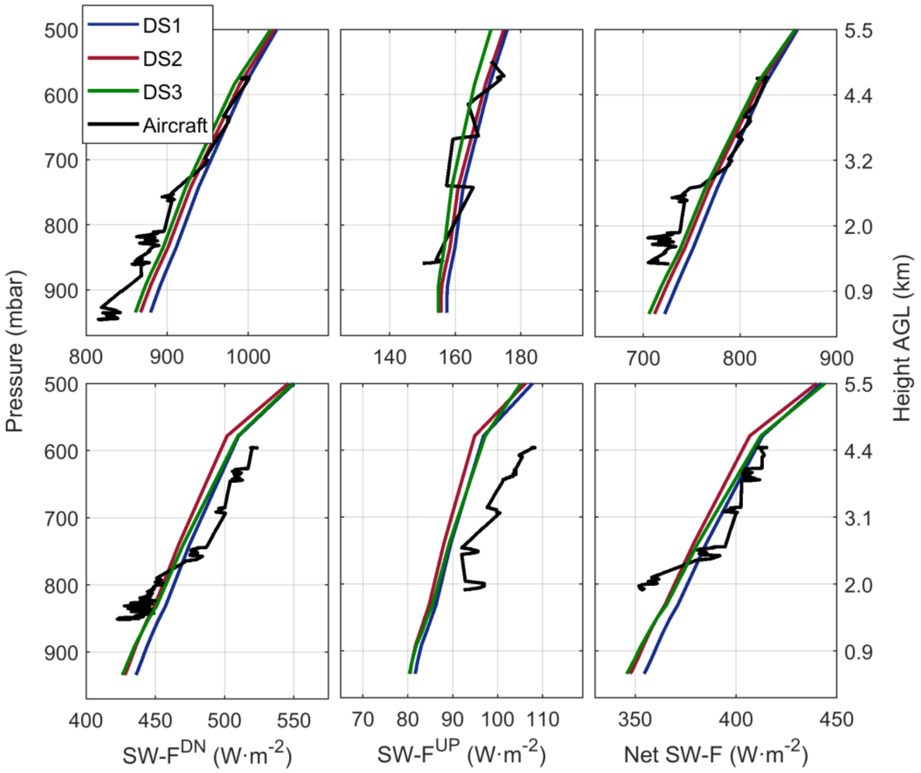

Fig. 3.9. Radiative fluxes for the SW spectral range for 16 (upper row) and 17 (bottom row) June simulated with GAME using different input aerosol datasets (DS1 in blue, DS2 in red and DS3 in green). The black lines are the aircraft in situ measurements distant from about 20 km.

The values at the BOA and at the TOA for the different radiative fluxes are also evaluated against the measurements performed at the surface by the CM11 pyranometer for the SW-F^{DN} located at the ground-station in Granada and the AERONET values of the SW-F^{DN} and SW-F^{UP} at both the BOA and the TOA. The time series for these measurements corresponding to 16-17 June and the results obtained with GAME for the different datasets are shown in Fig. 3.10. AERONET surface radiative fluxes have been extensively validated at several sites around the world [e.g. Garcia et al., 2008] and, in addition, all AERONET sun-photometers are mandatorily calibrated once a year. Thus, in order to compare GAME results with AERONET data, additional simulations have been performed for the time of the closest AERONET measurement on 16 June (at 16:22 UTC), assuming that the aerosol parameterization is constant with time between the flight time and the photometer measurement. SW-F^{DN} values at the surface obtained with GAME are 564.8, 551.8 and 547.0 $W \cdot m^{-2}$ for DS1, DS2 and DS3 respectively, very similar to the 531.4 $W \cdot m^{-2}$ provided by AERONET. On 17 June, GAME simulations at 07:40 UTC (instead of 07:30 UTC, which is the time of the flight), provide SW-F^{DN} at the surface of 466.3, 468.3 and 456.4 $W \cdot m^{-2}$, very close to the AERONET value of 463.7 $W \cdot m^{-2}$.

At the TOA, the SW-F^{UP} between GAME and AERONET are in quite good agreement on both days. On 16 June, the SW-F^{UP} obtained with GAME simulations is equal to 152.0, 153.0 and 148.5 $W \cdot m^{-2}$ and with AERONET is equal to 146.2 $W \cdot m^{-2}$. On 17 June, the obtained values with GAME are 133.6, 136.6 and 130.9 $W \cdot m^{-2}$ for DS1, DS2 and DS3 and 131.6 $W \cdot m^{-2}$ for AERONET.

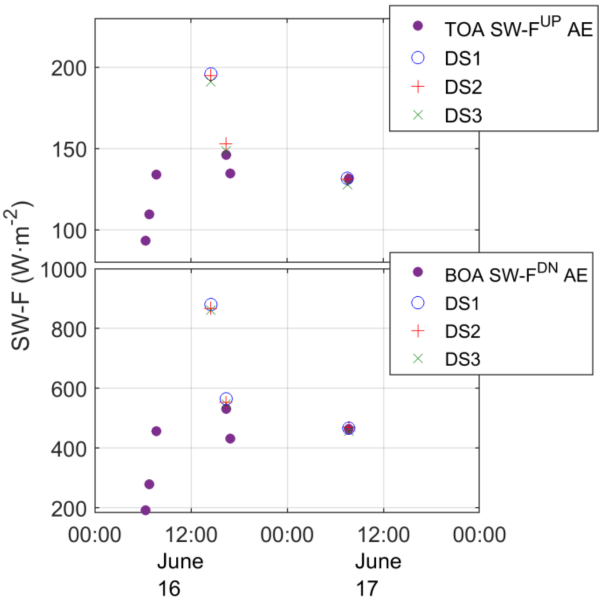

Fig. 3.10. Time series of the SW-F^{UP} at the TOA (top) and SW-F^{DN} at the BOA (bottom) for the period 16-17 June. The purple dots are AERONET fluxes, and GAME ouput data for different inputs are represented by the blue circles (DS1), red (DS2) and green (DS3) crosses.

The SW-ARE profiles calculated by means of Eqs. 2.47 and 2.48 and GAME simulations for the three input datasets are shown in Fig. 3.11, together with the simultaneous values provided by AERONET on 17 June at the BOA and TOA. Comparing the three GAME simulations, it is clear that the low discrepancies in the F profiles from Fig. 3.9 lead to variations in the SW-ARE of 10-27% (3-10 $W \cdot m^{-2}$) over the averaged profile depending on the input dataset used. The variations in the SW-ARE are tightly connected to differences in the AOD considered as input in the model, as already observed in previous studies [Sicard et al., 2014a; Lolli et al., 2018; Meloni et al., 2018]. The SSA and the vertical distribution of the aerosol also plays an important role, as observed for DS3, which shows a profile quite different from DS2 despite the AOD being quite close for both datasets and in agreement with previous studies [Guan et al., 2010; Gómez-Amo et al., 2011]. Differences are also observed when comparing SW-ARE values obtained from GAME to those retrieved by AERONET. Contrary to GAME simulations, AERONET does not consider the vertical distribution of the aerosols when calculating the

SW-ARE, and the definition of the SW-ARE at the BOA is slightly different. Indeed, AERONET SW-ARE at the surface is calculated as the difference between the downward fluxes with and without aerosols, the difference between the upward fluxes (reflected by the Earth) is neglected. Considering this, the SW-ARE at the BOA provided by AERONET can be corrected multiplying by a factor (1- *alb*(λ)). The corrected SW-ARE at the BOA value on 17 June is thus -31.9 $W \cdot m^{-2}$, which is within the range of values provided by GAME at the surface. All discrepancies observed here are mostly intrinsic to the different techniques used for the acquisition of the data and the retrieval algorithms. The effect of the data processing has also been observed in previous studies [Lolli et al., 2018].

The sensitivity tests performed reveal that an increase in the AOD of 0.05 can produce a stronger effect of the ARE both at the BOA (up to 6.7 $W \cdot m^{-2}$) and the TOA (up to 2.5 $W \cdot m^{-2}$), and more absorbing particles (decrease in the SSA of 0.03) produce more ARE at the BOA and less at the TOA (4 and 2 $W \cdot m^{-2}$ in absolute terms, respectively). Therefore, the differences among the datasets are within the estimated uncertainty.

The SW-ARE values obtained at the BOA and TOA for the three datasets and the averaged values, as well as the forcing efficiency (FE), are included in Table 3.7 and Fig. 3.11. Both at the BOA and TOA, the SW-ARE has a cooling effect, as expected for mineral dust in this region according to values obtained in the literature [e.g. Sicard et al. 2014a, Mallet et al., 2016]. The values of the SW-ARE and the SW-FE are highly dependent on the SZA and a straightforward comparison with previous studies is not simple. Nonetheless, the values obtained for this case are within the range of previous values observed in the western Mediterranean region for similar values of SZA, e.g. FE between -263.4 and -157.1 $W \cdot m^{-2}$ at the BOA and -23.8 and -86.2 $W \cdot m^{-2}$ for SZA=60° or ARE values ranging between −93.1 to −0.5 $W \cdot m^{-2}$ at the BOA and -34.5 to +8.5 $W \cdot m^{-2}$ at the TOA for different SZA values [e.g. Gómez-Amo et al., 2011; Sicard et al., 2014a, b; Barragan et al., 2017].

Table 3.7: ARE (and FE indicated between parenthesis) at the BOA and the TOA for the SW spectral range obtained with GAME using as inputs DS1, DS2 and DS3 for 16 and 17 June, 2013. The averaged values and standard deviation are also included.

	16 June		**17 June**	
	BOA SW-ARE (FE) ($W \cdot m^{-2}$)	**TOA SW-ARE (FE) ($W \cdot m^{-2}$)**	**BOA SW-ARE (FE) ($W \cdot m^{-2}$)**	**TOA SW-ARE (FE) ($W \cdot m^{-2}$)**
DS1	-18.1 (-100.6)	-6.3 (-35.0)	-27.1 (-169.4)	-10.3 (-64.4)
DS2	-28.6 (-124.4)	-5.5 (-23.9)	-34.0 (-178.9)	-9.6 (-50.5)
DS3	-34.3 (-149.1)	-1.5 (-6.5)	-35.8 (-198.9)	-6.5 (-36.1)
Avg ± std. dev	-27.0± 8.2 (-124.7±24.3)	-4.4±2.6 (-21.8±14.4)	-32.3±4.6 (-182.4±15.1)	-8.8±2.0 (50.3±14.2)

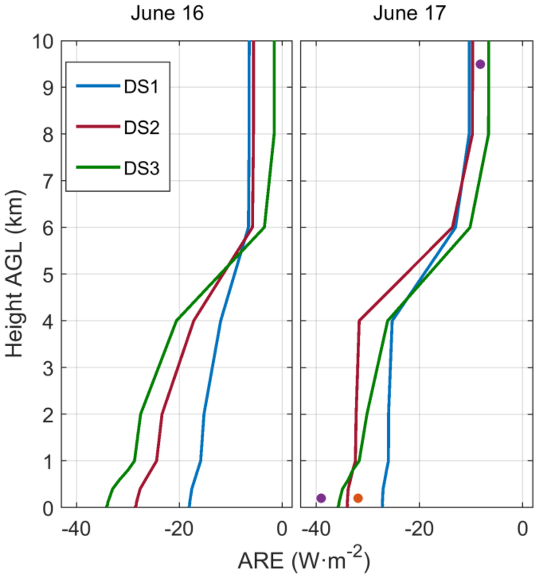

Fig. 3.11. ARE profiles in the SW spectral range simulated using DS1 (blue line), DS2 (red line) and DS3 (green line) as aerosol input data in GAME for 16 June (a) and 17 June (b). The purple dots represent the ARE provided by AERONET at the BOA and the TOA and the orange dot, the AERONET corrected for the surface albedo effect ARE at the BOA.

3.4.3.2 LW RADIATIVE FLUXES

Fig. 3.12 shows LW-F calculated with GAME after obtaining the aerosol properties in the LW spectral range from Mie calculations for the three mentioned datasets (see Sect. 3.4.2.2). LW-F measured by pyrgeometers located onboard the ATR are also shown.

In general, differences in the LW-F are always lower than 6% (lower than 10 $W \cdot m^{-2}$ on average), with the airborne values being overestimated by the model on 16 June and underestimated on 17 June. On this latter day, larger differences are observed on the NetLW-F compared to 16 June, which might be explained by the inaccurate value of LST used due to the lack of precise data. A sensitivity test performed by increasing the air surface temperature measured at the meteorological station up to 5K indicates that the LW-F^{UP} increases its value up to 30 $W \cdot m^{-2}$ at the surface, and around 10 $W \cdot m^{-2}$ from 1 km onwards which is non-negligible. This would produce an overestimation of the aircraft measured values, but still within a 6% difference. This highlights the need for accurate LST measurements for radiation simulations in the LW spectral range. Additionally, a sensitivity test performed by assuming a 10% uncertainty in the PSD parameters (r_{eff}, N and σ) shows an estimated uncertainty of the LW-F retrieved by GAME of around 1.2 $W \cdot m^{-2}$. As stated before, the assumption of the refractive index can also introduce variations as large as 0.8 $W \cdot m^{-2}$. Considering the uncertainty of the pyrgeometer and the fact that the aircraft and the model present different vertical resolutions and time samplings and the uncertainties due to the use of the standard atmosphere or the parameterization of the surface properties the obtained differences are not significant.

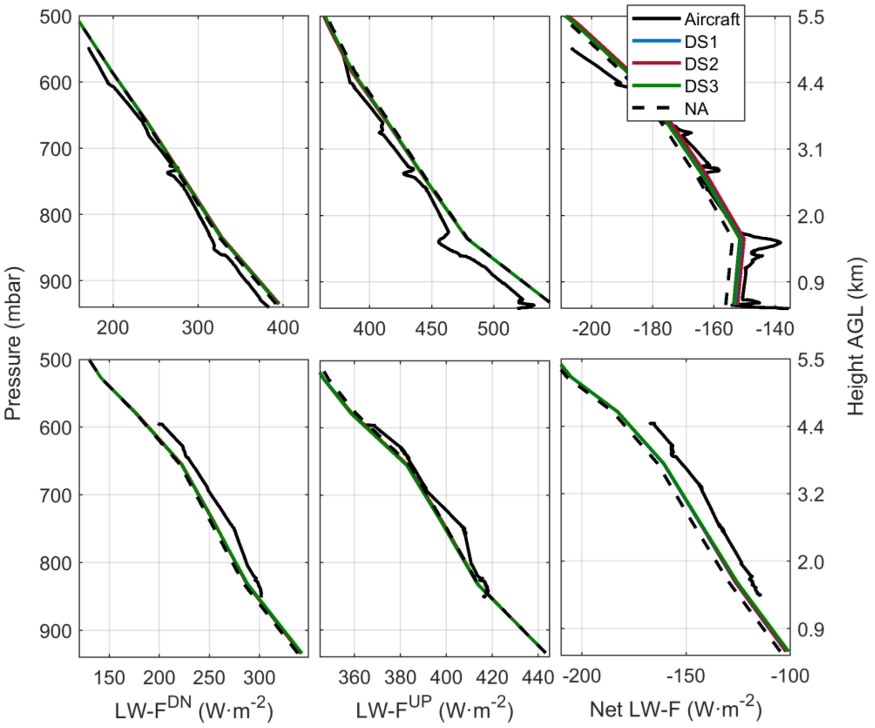

Fig. 3.12. Radiative fluxes for the LW spectral range for June 16 (upper row) and 17 (bottom row) simulated with GAME using different input aerosol datasets (DS1 in blue, DS2 in red and DS3 in green). The black line represents the aircraft in situ measurements.

A comparison of GAME results against the observations from ground-based pyrgeometer at Granada station is included in Fig. 3.13. At the BOA, the longwave radiation measured by the pyrgeometer is in quite good agreement with GAME calculations on 16 June, with differences within 1 $W \cdot m^{-2}$. However, GAME overestimates the pyrgeometer data by 5 $W \cdot m^{-2}$ (1.3%) on 17 June. These differences on 17 June, even though larger than on 16 June, are still within the uncertainty limits.

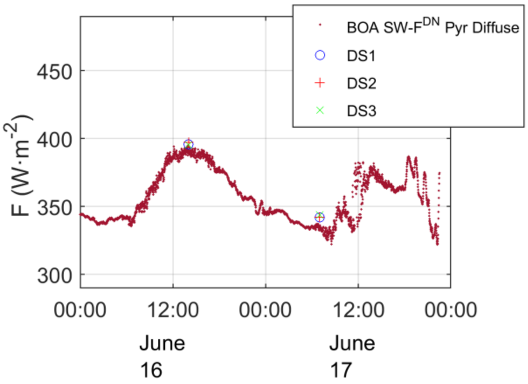

Fig. 3.13. Time series of the LW-F^{DN} at the BOA during the period 16-17 June. Surface measurements of diffuse (red) radiation from the ground-based pyranometer at Granada station are included. GAME ouput data for different inputs are represented by the blue circles (DS1), red (DS2) and green (DS3) crosses.

As for the LW-ARE, Fig. 3.14 shows the profiles obtained with GAME using the three datasets as inputs. Values at the BOA and TOA for each dataset and the average values are included in Table 3.8, together with the FE. Opposite to the SW, the LW-ARE produces a heating effect both at the BOA and TOA, with positive values. The slight differences in the LW-F in Fig. 3.12 due to the use of different aerosol input datasets lead to variations of up to 2 $W \cdot m^{-2}$ in the LW-ARE at the BOA (ranging from 20 to 26%), which must be considered in the interpretation of the results and reduced for a better estimate of the direct ARE. Despite this, values obtained for this dust event (3.2 $W \cdot m^{-2}$ on average for both days) are in agreement with previous studies performed for mineral dust in the infrared region [Sicard et al., 2014a, b] and the FE obtained are comparable to those reported by Meloni et al., [2018].

It is extremely interesting to look at the differences between the two days in terms of AOD (ΔAOD) and the effective radius for the coarse mode, $r_{eff,c}$, ($\Delta r_{eff,c}$) and their implication on the differences in the LW-ARE at the BOA (BOA ΔLW-ARE). For DS1 ΔAOD ($\Delta r_{eff,c}$) is -0.02 (+0.18 μm) which produces a decrease in LW-ARE at the surface (BOA ΔLW-ARE = -0.5 $W \cdot m^{-2}$). For DS2 ΔAOD (Δ $r_{eff,c}$) is -0.04 (+0.18 μm) which produces a decrease in LW-ARE at the surface (BOA ΔLW-ARE = -1.0 $W \cdot m^{-2}$). Relating these variations to the sensitivity study of Sicard et al. [2014a], in both cases the expected LW-ARE increase due to the increase of the coarse mode radii is counterbalanced by the LW-ARE decrease when AOD decreases. Oppositely, for DS3 ΔAOD (Δr_c) is -0.05 (+0.64 μm), producing an increase of LW-ARE at the surface (BOA ΔLW-ARE = +1.6 $W \cdot m^{-2}$). Here, the large increase of the coarse mode radius dominates over the AOD decrease. Sicard et al. [2014a] show in their research that the largest positive gradient of LW-ARE occurs for median radii ranging from 0.1 to 2.0 μm. For DS3 the increase of LW-ARE at the BOA produced by a positive Δr_c is larger than the decrease of LW-ARE at the BOA that would have produced ΔAOD alone. At the TOA, same trends, but much less marked, are observed.

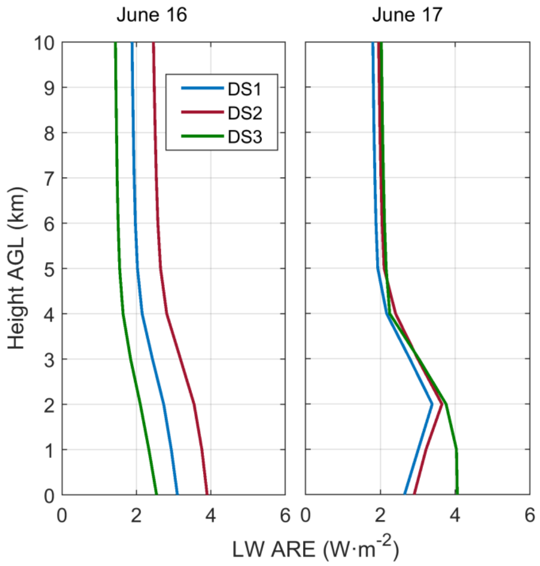

Fig. 3.14. Direct ARE profiles in the LW spectral range simulated using DS1 (blue line), DS2 (red line) and DS3 (green line) as aerosol input data in GAME for 16 June (a) and 17 June (b).

Table 3.8. ARE (and FE indicated between parenthesis) at the BOA and the TOA for the LW spectral range obtained with GAME using as inputs DS1, DS2 and DS3 for 16 and 17 June, 2013. The averaged values and standard deviation are also included. The last three columns include variations (Δ) of AOD, $r_{eff,c}$ and ARE at the BOA between June 16 an 17 for the three datasets.

	16 June		**17 June**				
	BOA LW-ARE (FE) ($W \cdot m^{-2}$)	**TOA LW-ARE (FE) ($W \cdot m^{-2}$)**	**BOA LW-ARE (FE) ($W \cdot m^{-2}$)**	**TOA LW-ARE (FE) ($W \cdot m^{-2}$)**	**ΔAOD**	**$\Delta r_{eff,c}$ (μm)**	**$\Delta^{BOA}ARE_{LW}$ ($W \cdot m^{-2}$)**
DS1	+3.1 (+17.2)	+2.2 (+12.2)	+2.6 (+16.3)	+1.6 (+10.0)	-0.02	0.18	-0.5
DS2	+3.9 (+17.0)	+2.9 (+12.6)	+2.9 (+15.3)	+1.7 (+8.9)	-0.04	0.18	-1
DS3	+2.5 (+10.9)	+1.3 (+5.7)	+4.1 (+22.8)	+1.8 (+10.0)	-0.05	0.64	1.6
Avg ± std. dev	+3.2±0.7 (+15.0±3.6)	+2.1±0.8 (+10.2±3.9)	+3.2±0.8 (+18.1±4.1)	+1.7±0.1 (+9.6±0.6)			

3.4.3.3 TOTAL MINERAL DUST RADIATIVE EFFECT

The total ARE, including both the SW and LW component, is included in Fig. 3.15 and Table 3.9. As observed, mineral dust produces a net cooling effect both at the surface and the TOA on both days. Depending on the input dataset used for the aerosol properties, values can change by up to 15 $W \cdot m^{-2}$. On average, the ARE at the BOA (FE at the BOA) values are -23.8 ± 8.4 (-109.5±27.4) and -29.2 ± 4.0 (-164.7±11.5) $W \cdot m^{-2}$, and the ARE at the TOA (FE at the TOA) is equal to -2.6 ± 2.2 (-13.0±12.3) and -7.0 ± 2.1 (-40.3±14.1) $W \cdot m^{-2}$ on 16 and 17 June, respectively. These values of the FE are comparable to those values which can be found in the literature [Di Biagio et al., 2009; Meloni et al., 2015]. The total averaged ARE values are 15 and 13% lower than for the SW spectral range, confirming that the LW fraction cannot be neglected. The LW-ARE represents approximately 20% of the SW-ARE near the surface (except for DS3 on 16 June), and reaches up to 50% at higher altitudes where the total ARE is quite low (see 16 June on Fig. 3.15). At higher altitudes low values of the ARE are obtained due to the moderate nature of the analyzed dust event, leading to a large variability of the LW-ARE/SW-ARE and larger values than those observed in previous studies. Overall these LW-ARE/SW-ARE ratios are in agreement with those found at the BOA in previous studies for the Mediterranean region, which ranged between 9 and 26% [di Sarra et al. 2011; Perrone and Bergamo 2011; Sicard et al. 2014a; Meloni et al., 2015].

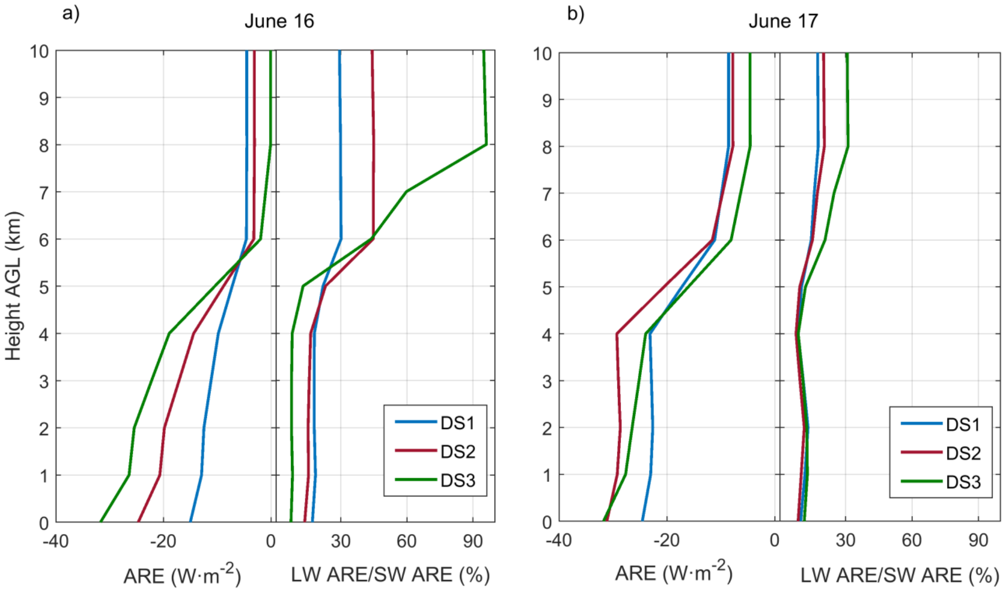

Fig. 3.15. Direct ARE for the total spectrum (left) and the ratio between the ARE LW and the ARE SW in percentage for DS1 (blue), DS2 (red) and DS3 (green) on 16 June at 14:30 UTC (a) and 17 June at 07:30 UTC (b).

Table 3.9. ARE (and FE indicated between parenthesis) at the BOA and the TOA for the total (SW+LW) spectral range obtained with GAME using as inputs DS1, DS2 and DS3 for 16 and 17 June, 2013. The averaged values and standard deviation are also included.

	16 June		**17 June**	
	ARE BOA ($W \cdot m^{-2}$)	**ARE TOA ($W \cdot m^{-2}$)**	**ARE BOA ($W \cdot m^{-2}$)**	**ARE TOA ($W \cdot m^{-2}$)**
DS1	-15.0 (-83.3)	-4.5 (-25.0)	-24.6 (-153.8)	-8.6 (-53.8)
DS2	-24.7 (-107.4)	-3.1 (-13.5)	-31.1 (-163.7)	-7.8 (-41.1)
DS3	-31.71 (-137.9)	-0.1 (-0.4)	-31.8 (-176.7)	-4.6 (-25.6)
Avg ± std. dev	-23.8±8.4 (-109.5±27.4)	-2.6±2.2 (-13.0±12.3)	-29.2±4.0 (-164.7±11.5)	-7.0±2.1 (-40.3±14.1)

3.5 SUMMARY AND CONCLUSIONS

The SW and LW radiative fluxes calculated by GAME and the Two-Stream RTM have firstly been compared with the corresponding radiative fluxes measured at the surface, to obtain a first estimate of the reliability of the data provided by the two tested RTMs. A good agreement between modeled and experimental fluxes have been found, both in the SW and in the LW range, within the experimental uncertainties of the measured flux values. Therefore, the validation of the modelled fluxes has not revealed any significant impact of the numerical method to solve the RT equation and the spectral resolution used by the two RTMs.

The SW-AREs at the TOA and at the BOA estimated by GAME are in good agreement with the ones estimated by Two-Stream (see Fig. 3.4a and 3.4c). However, on the days significantly affected by desert dust the Two-Stream model overestimates the GAME LW-ARE up to about 5 and 7.5 times at the surface and at the TOA, respectively, on 22 June (see Fig. 3.4b and 3.4d), suggesting that the spectrally averaged resolution of the Two-Stream model in the LW spectral range, to account for the aerosol properties and the water vapor absorption coefficients, is responsible for the LW-ARE overestimates by the Two-Stream model. Hence, thanks to the "optimization" (Fig. 3.5) of the water vapor absorption coefficients it is possible to decrease the differences between the LW-AREs calculated by the two models by about 10%, both at the BOA and at the TOA. Moreover, the low spectral resolution of the real (n) and imaginary (k) parts of the refractive index is mainly responsible for the LW-ARE overestimates by the Two-Stream model. Then, the "optimization" of the *n* and k values at 8.75 and 11.5 μm is sufficient to obtain a satisfactory agreement (the differences decrease up to 80%) between the LW-AREs from the two models, both at the TOA and at the surface.

On the other hand, the evaluation of GAME calculated radiative fluxes against the aircraft data reveals differences between the model fluxes and the measurements below 7%, with better agreement at altitudes above the planetary boundary layer. The differences between the retrievals with the three aerosol datasets are quite insignificant (less than 1%), especially taking into account the different approaches followed by the model and the pyranometers. Thus a conclusion on which input dataset provides a better performance is unlikely. These small differences in the radiative fluxes produce variations in the SW-ARE of up to 33% (see Fig 3.10) depending on the used input parameterization. For the LW, GAME retrievals using the three aerosol datasets reveal differences in the fluxes lower than 2 $W \cdot m^{-2}$ (less than 1%). The comparison of the modelled fluxes with the pyrgeometer data measured at the ATR reveals however differences around 7% (14 $W \cdot m^{-2}$). Considering the low influence of the aerosol in the LW radiative fluxes, the influence of the assumed CO_2, O_3 and the used water vapor profiles and LST are needed to fully explain this discrepancy between the aircraft and the simulated profiles. For the LW-ARE, differences of up to 26% are obtained depending on the aerosol input dataset used (see Fig. 3.14). According to these results, it is necessary to obtain an accurate vertically-resolved aerosol properties database in order to reduce uncertainties in the estimation of the ARE since small variations affecting the input data are related to considerable changes in the obtained ARE.

In general, the positive TOA SW-ARE values are associated with low values of SSA, *alb*, and SZA. The dust contamination by anthropogenic particles during its transport to the monitoring sites, which are located a few thousand kilometers away from the source region, is likely responsible for the increase of the light absorption by aerosol particles and, hence, for the decrease of the SSA values. The effect of the aerosol in the radiative properties is lower and of opposite sign compared to the SW, but certainly non-negligible. On average, the LW-ARE represents a 20% of the SW-ARE at the surface, therefore clearly indicating that global model estimates need to consider the complete spectrum to avoid an overestimation on mineral dust cooling effect. The use of advanced remote sensing data and processing, in combination with closure studies on the optical/microphysical properties from in situ aircraft measurements when available, is recommended.

CHAPTER 4

Aerosol Optical and Radiative Properties in the Mediterranean Basin

This Chapter focuses on the evaluation of the seasonal variability of the aerosol background optical and radiative properties in the Western Mediterranean Basin (WMB) (Sect. 4.2) and on the study of the spatio-temporal (4D) evolution of a mineral dust outbreak (Sect. 4.3), that took place over the WMB in summer 2013, all in the framework of the ChArMEx program. The seasonal analysis is performed by means of microphysical and radiative properties derived from AERONET data (Level 2.0) in two background sites in the WMB (Sect. 4.2): Ersa (Corsica Island, France) and Palma de Mallorca (Mallorca Island, Spain). The AERONET AREs are compared with ground and satellite-based flux measurements. A third site, Alborán (Alborán Island, Spain) is considered for examining possible northeast-southwest (NE-SW) gradients of the aerosol properties. On its behalf, in order to describe the physical and optical properties of mineral dust in the WMB (Sect. 4.3), it is used the multi-intrusion detected by some EARLINET/ACTRIS (Granada, Barcelona, Naples, Potenza, Lecce and Serra la Nave) and ADRIMED/ChArMEx (Cap d'en Font (Minorca Island, Spain) and Ersa) ground-based lidar stations during 15-24 June 2013 with the support of collocated AERONET sun-photometers and the Falcon 20 aircraft. In order to estimate the AREs, the GAME code, previously evaluated in Chapter 3, is used. Finally the multi-intrusion aspect of the event is examined by means of air- and space-borne lidar measurements, satellite images and back-trajectories.

This Chapter is an adaptation of [Sicard et al, 2016], [Sicard et al, 2014] and [Barragan et al, 2017]. These works have been published in Atmospheric, Chemistry and Physics (available as an electronic reprint with the permission of ACP: www.atmos-chem-phys.net/16/12177/2016/), SPIE Proceedings (available as an electronic reprint with the permission of SPIE: https://www.spiedigitallibrary.org/conference-proceedings-of-spie/9242/1/Variability-of-Mediterranean-aerosols-properties-at-three-regional-background-sites/10.1117/12.2068694.short?SSO=1) and Journal of Remote Sensing and Air Quality, Atmosphere & Health (available as an electronic reprint with the permission of Air Quality, Atmosphere & Health: https://link.springer.com/article/10.1007/s11869-016-0447-7).. Systematic or multiple reproduction or distribution to multiple locations via electronic or other means is prohibited and is subject to penalties under law.

4.1 INTRODUCTION

As it has been commented in Sect. 3.1 and references therein, the Mediterranean atmosphere is largely affected by maritime particles, urban/industrial aerosols from European and North African urban areas, extreme biomass burning episodes and mineral dust from North African arid areas; therefore it is mandatory to perform long-term analyses of those aerosols. A detailed list of these long-term analyses or case studies about one or several types of aerosols can be found in Mallet et al. [2016].

In order to quantify the atmospheric aerosol, which has a direct effect on the solar and infrared radiation reaching the Earth's surface, the AOD, which represents the extinction of radiation at a certain wavelength that results from the presence of atmospheric aerosols, is usually used. For that reason, long time series of AOD satellite-based observations [Moulin et at., 1998; Barnaba and Gobbi, 2004; Papadimas et al., 2008; Nabat et al., 2012, 2013; Gkikas et al., 2016, among others] and to a lesser extent on ground-based remote sensing observations [Mallet et al., 2013; Lyamani et al., 2015, among others] are often used to quantify the aerosol impact on the surface solar radiation. Although the spectral AOD is a key parameter to understand the variability of the aerosol impact on the Earth's energy budget, its analysis is not sufficient to assess this variability at the scale of the Mediterranean Basin because of the great complexity of the aerosol composition and distribution over the basin. Consequently, other parameters like the absorption properties, the size of the particles, their shape, etc. are needed. Therefore, taking advantage of the ChArMEx program, a long-term analysis is presented in this Chapter, using data from 10 different stations spread over the WMB, which also includes the ARE, computed by the GAME code (introduced in Chapter 2 and characterized in Chapter 3).

The main objective of this Chapter is to assess the spatio-temporal evolution of the aerosol microphysical and optical properties and to know the effect of this evolution in the aerosol radiative fluxes. For that purpose, in Sect. 4.2 is presented a seasonal analysis of the aerosol optical, microphysical and radiative columnar properties at two regional background insular sites in the western Mediterranean at Ersa (Corsica, France) and Palma de Mallorca (Mallorca, Spain) with multiyear data from a recent period (2011–2015). In addition, in order to extend the study of north–south gradients to the southern part of the whole WMB, a case study is presented by complementing the dataset with 5 months of coincident measurements in 2011 in the remote island of Alborán (Spain) between Spain and Morocco.

In Sect. 4.2 are pursued two main goals: (i) the spatio-temporal quantification of the effect of long-range transport on the aerosol optical, microphysical and radiative properties in the WMB and (ii) the spatio-temporal variation of aerosol absorption properties during strong aerosol events (aerosol optical depth at 440 nm greater than 0.4). After this analysis, it is shown in Sect. 4.3 the spatio-temporal (4D) evolution of a dust event, which took place in summer 2013, and its radiative properties over the whole WMB by means of the interactions and complementarities of both EARLINET/ACTRIS and ChArMEx as well as introduce to characterize the multi-intrusion aspect of the dust event. The spatio-temporal evolution of the radiative properties is analyzed by means of continuous measurements of the SW and LW radiative fluxes performed during the dust event. It is worth mentioning that a multi-intrusion is an event which has more than one dust source, in this case, the multi-intrusion aspect of the event is further investigated using airborne lidar measurements performed from the French Falcon 20 research aircraft deployed during the field campaign, space-borne lidar measurements from the CALIOP (Cloud-Aerosol Lidar with Orthogonal Polarization) instrument, satellite images from SEVIRI and back-trajectories. The main objectives pursued in this Sect. 4.3 are: (i) to show the collaboration between a European research infrastructure (ACTRIS) and an international project (ChArMEx) on topics of interest for both parties, and more generally for the atmospheric community, (ii) to assess the spatio-temporal evolution of the dust properties including the radiative ones and (iii) to characterize the multi-intrusion aspect of the dust event studied.

This Chapter is organized as follows: In Sect. 4.2 is provided a long-term analysis based in AERONET retrievals. In Sect. 4.3 are presented the results of a field campaign including radiative computations made with the GAME code. Finally, concluding remarks are given in Sect. 4.4.

4.2 LONG-TERM AERONET MEASUREMENTS IN BACKGROUND SITES IN THE WMB: OPTICAL AND RADIATIVE PROPERTIES OF THE MEDITERRANEAN AEROSOL

In this section, the evolution of the aerosol optical properties during its transport over the WMB is discussed. Also, how the evolution of these properties affect the aerosol radiative effect is presented.

4.2.1 INSTRUMENTS AND DATA

The sites selected for the analysis presented in this Section have to fulfill the following criteria: (i) to be located in the WMB, (ii) to be insular sites in order to be representative of aerosol regional background conditions and (iii) to be approximately aligned on a north–south axis and to have a recent database with at least 2 years of data. The first site selected is a supersite installed, in the framework of the ChArMEx EOP, 2 years from June 2012 to July 2014 at Ersa on the northern tip of Corsica Island, France [Lambert et al., 2011; Dulac, 2014, Mallet et al., 2016], which have, among other instruments, an AERONET sun-photometer, in operation since June 2008. Applying the previously mentioned criteria, the second site selected is Palma de Mallorca in the Balearic Islands (Spain), in operation since August 2011. Both sites are on the northeast–southwest (NE–SW) axis, a major route for aerosol transport in the WMB [Moulin et al., 1998]. In Sect. 4.2.2.4, a third site is considered for examining possible NE–SW gradients is Alborán (Spain, 15 m a.s.l.) situated east of Gibraltar midway between the Spanish and the Moroccan coasts. There, an AERONET sun-photometer was operated between June 2011 and January 2012. Indeed all three sites fall onto NE– SW straight line and Palma, situated in the middle, is approximately equidistant to both Ersa (~ 670 km) and Alborán (~ 640 km).

The data used in this Section are based on AERONET (Version 2 Level 2.0), cloud-screened and quality-assured data [Smirnov et al., 2000; Holben et al., 2006]. The estimated accuracy of AOD_λ is ±0.02 [Eck et al., 1999], the accuracy of the Ångström exponent (AE) is estimated to be ±0.25 for $AOD_{440} \geq 0.1$ and of the order of 50 % for $AOD_{440} < 0.1$ [Toledano et al., 2007]. The accuracy of the aerosol volume size distribution is estimated to be 15 % for water soluble, 35 % for dust and 25 % for biomass burning in the intermediate particle size range ($0.1 \leq$ radius $r \leq 7\ \mu m$) and 15–100 % for water soluble, 35–100 % for dust and 25–100 % for biomass burning for the edges ($0.05 \leq r < 0.1$ and $7 < r \leq 15\ \mu m$). The accuracy of the real (imaginary in %) part of the aerosol refractive index is estimated to be ±0.025 (50 %) for $AOD_{440} > 0.2$ for water soluble and ±0.04 (50 and 30 %, respectively) for $AOD_{440} \geq 0.5$ for dust and biomass burning. The retrieved aerosol absorption optical depth at wavelength λ ($AAOD_\lambda$) has an accuracy of ±0.01 at $\lambda \geq 440$ nm. Finally the accuracy of the aerosol single scattering albedo at wavelength λ (SSA_λ) is estimated to be ±0.03 for $AOD_{440} > 0.2$ for water soluble and for $AOD_{440} \geq 0.5$ for dust and biomass burning, and the uncertainty of the aerosol asymmetry factor at wavelength λ (g_λ) ranges between ±0.03 and ±0.08 for pollution and biomass burning aerosols and is ±0.04 for desert dust particles.

It is important to comment that some products such as the AAOD, the real (n) and the imaginary (k) parts of the refractive index and the SSA are retrieved only when the criterion $AOD_{440} > 0.4$ is fulfilled. Such aerosol loads are associated with high turbidity events such as desert dust outbreaks or severe pollution episodes [Gkikas et al., 2012, 2016]. Other parameters of interest delivered by the AERONET inversion algorithm are the instantaneous solar broadband (0.2–4 μm) downward and upward fluxes, as well as the ARE and radiative forcing efficiency (FE) at the surface and at the top of the atmosphere. A brief description on how the fluxes are calculated is given in the AERONET version 2 inversion product descriptions [AERONET, 2016]. The gaseous absorption is calculated by the GAME model [Dubuisson et al., 1996, 2004, 2005, 2006]. Only AERONET daily means are considered in the section about the seasonal and annual variability (Sect. 4.2.3). Monthly and seasonal means are calculated from the daily means and the annual mean from the four seasonal means. In Sects. 4.2.3.5 and 4.2.3.6 AERONET instantaneous measurements are considered because in Sect. 4.2.3.5 it is necessary to limit SZA between 50 and 60° in order to rely on AERONET flux retrievals (see Sect. 4.2.3.5.1 for explanation) and in the case study of Sect. 4.2.3.6 only a very short period of time (5 months) is considered. The seasonal variations shown in this Chapter are made for the following four seasons: summer (JJA, June–July– August), autumn (SON, September–October–November), winter (DJF, December–January–February) and spring (MAM, March–April–May).

Also, the AE is needed. It is calculated between two wavelengths λ_1 and λ_2 and defined as

$$AE_{\lambda_1-\lambda_2} = -\frac{ln\left[\frac{AOD_{\lambda_1}}{AOD_{\lambda_2}}\right]}{ln\left[\frac{\lambda_1}{\lambda_2}\right]} \quad [4.1]$$

is commonly used as a good indicator of the dominant size of the atmospheric particles contributing to the total AOD: values of AE < 1 indicate size distributions dominated by coarse-mode aerosols (radii > 0.5 μm) while values of AE > 1.5 indicate size distributions dominated by fine-mode aerosols.

The atmospheric dynamics of the WMB and the peculiarities of each one of the three sites selected in this Section (Ersa, Palma de Mallorca and Alborán) are widely described in Sect. 4 of Sicard et al., [2016].

4.2.2 METHODOLOGY

The methodology followed in this Section to classify the aerosols based on AERONET Level 2.0 inversion products is twofold: (i) a simple graphical method (AE vs. AOD) as suggested by Holben et al. [2001] primarily for background conditions and (ii) the graphical method from Gobbi et al. [2007] for higher AODs. In the first method $AE_{440–870}$ vs. AOD_{440} is plotted and distinguish between low (AOD_{675} < 0.15) and moderate-to-high (AOD_{675} > 0.15) AOD cases. This simple graphical method used by Holben et al. [2001] with AERONET daily products helps to determine the signature of aerosols from different origins, for instance clean continental, marine, urban/industrial, mineral dust and biomass burning. However, the aerosol classification that can be deduce from this method presents some limitations because some aerosol types have the same signature (e.g., urban/industrial and biomass burning). When different aerosol types are present in the atmospheric column, AE does not provide information on the relative contribution of coarse- and fine-mode particles. For this reason, the Ångström exponent difference ($\delta\alpha$) is introduced and the Gobbi et al. [2007] method consists in deriving the $AE_{440–870}$ and the $\delta\alpha$, defined as a measure of the Ångström exponent curvature, $dAE/d\lambda$, the fine-mode aerosol radius and the contribution of the fine-mode aerosol to the total AOD. Several authors have investigated how the spectral variation of AE can provide further information on the aerosol size distribution [Schuster et al., 2006, and references therein]. In particular, Kaufman [1993] pointed out that negative values of $AE_{440–613}$–$AE_{440–1003}$ indicate the dominance of fine-mode particles, while positive differences indicate the effect of two separate modes with a significant coarse-mode contribution. The graphical method developed by Gobbi et al. [2007] uses these complementarities between AE and $\delta\alpha$. The method has been applied, among others, by (i) Gobbi et al. [2007] at sites characterized by high pollution, biomass burning and/or mineral dust concentrations; (ii) Basart et al. [2009] to quantify the contribution of mineral dust on a yearly basis at sites in and around the Sahara–Sahel region; and (iii) Perrone et al. [2014] to distinguish between pollution and mineral dust in Lecce.

Daily values of the $\delta\alpha$ vs. the AE, ($\delta\alpha$, AE), are plotted on a classification framework with reference model points determined for a variety of fine-mode (r_f) and coarse-mode (r_c) radii and of fine-mode fractions of total AOD (f). To this end, Mie calculations are performed to calculate the aerosol spectral extinction coefficients for r_f values of 0.05, 0.1, 0.15, 0.2, 0.3 and 0.5 μm, for r_c values of 0.75, 1, 2, and 4 μm, and for f fractions of 1, 10, 30, 50, 70, 90 and 99 %, assuming a bimodal, lognormal size distribution. Each ($\delta\alpha$, AE) grid point is obtained as the average of the four pairs obtained for the four r_c values. The grid used in this Chapter is taken from Gobbi et al. [2007] with a refractive index of 1.4–0.001i, typical of urban/industrial aerosols, in order to both provide a common reference and address the relative changes (fine-mode growth/hydration or coarse particle growth/cloud contamination; see Gobbi et al. [2007] for definition) at each location. As suggested by Gobbi et al. [2007], the condition AOD_{675} > 0.15 is applied on all the ($\delta\alpha$, AE) plots in order to guarantee errors less than 30 % on $\delta\alpha$. It is worth noting that with this condition the predominant aerosol conditions, marine aerosols (with AOD_{440} < 0.15 according to Smirnov et al. [2002]), are removed. The values of $\delta\alpha$ provided in Table 4.1 are also given following this criterion: AOD_{675} > 0.15. Note, however, that the AOD plotted in the ($\delta\alpha$, AE) plots of this Chapter is AOD_{440} (and not AOD_{675}) in order to be directly comparable with the AERONET criteria based on AOD_{440}.

Table 4.1. Seasonal and annual variations of the following aerosol properties with their standard deviation (and number of observations in parenthesis): aerosol optical depth at 440 nm (AOD_{440}), the Ångström exponent calculated between 440 and 870 nm ($AE_{440–870}$), the Ångström exponent difference ($\delta\alpha$ = $AE_{440–675}$– $AE_{675–870}$), the fine-mode volume median radius (r_f^v) and concentration (C_f^v), the coarse-mode volume median radius (r_c^v) and concentration (C_c^v), the aerosol absorption optical depth at 440 nm ($AAOD_{440}$), the absorption Ångström exponent ($AAE_{440–870}$) and the real (n_{440}) and imaginary (k_{440}) part of the refractive index at 440 nm at Ersa and Palma derived from AERONET Version 2 Level 2.0 daily inversion products available for the period 2011–2015. The values of $\delta\alpha$ are given for AOD_{675} > 0.15 as suggested by Gobbi et al. [2007]. The values of $AAOD_{440}$, $AAE_{440–870}$, n_{440} and k_{440} are given for 50 < solar zenith angle < 80° and AOD_{440} > 0.40.

		Summer	Autumn	Winter	Spring	Year
$\mathbf{AOD_{440}}$	**Ersa**	0.19±0.10 (433)	0.14±0.09 (193)	0.08±0.04 (193)	0.16±0.11 (247)	0.14±0.05
	Palma	0.25±0.13 (196)	0.16±0.11 (211)	0.08±0.05 (84)	0.11±0.06 (76)	0.15±0.07
$\mathbf{AE_{440\text{-}870}}$	**Ersa**	1.41±0.42 (433)	1.24±0.51 (307)	1.06±0.44 (193)	1.27±0.47 (247)	1.25±0.14
	Palma	1.10±0.46 (169)	1.11±0.47 (211)	1.07±0.40 (84)	1.08±0.43 (76)	1.05±0.05
$\boldsymbol{\delta\alpha}$	**Ersa**	0.06±0.18 (78)	0.14±0.19 (33)	0.05±0.00 (1)	0.08±0.20 (31)	0.08±0.04
	Palma	0.29±0.16 (72)	0.16±0.21 (32)	-(0)	0.44±0.00 (1)	0.30±0.14
$\boldsymbol{r_f^v}$ $(\boldsymbol{\mu m})$	**Ersa**	0.16±0.02 (254)	0.17±0.02 (160)	0.17±0.03 (84)	0.17±0.02 (131)	0.17±0.01
	Palma	0.14±0.02 (176)	0.15±0.02 (136)	0.15±0.02 (50)	0.15±0.02 (54)	0.15±0.01
$\boldsymbol{C_f^v}$ $(\boldsymbol{\mu m^3 \mu m^{-2}})$	**Ersa**	0.020±0.011 (254)	0.014±0.010 (160)	0.009±0.005 (84)	0.018±0.012 (131)	0.0015±0.005
	Palma	0.027±0.013 (176)	0.020±0.016 (136)	0.010±0.007 (50)	0.012±0.008 (54)	0.017±0.008
$\boldsymbol{r_c^v}$ $(\boldsymbol{\mu m})$	**Ersa**	2.51±0.39 (254)	2.71±0.43 (160)	3.68±0.40 (84)	2.30±0.43 (131)	2.55±0.19
	Palma	2.43±0.40 (176)	2.64±0.36 (136)	2.45±0.35 (50)	2.18±0.39 (54)	2.43±0.19
$\boldsymbol{C_c^v}$ $(\boldsymbol{\mu m^3 \mu m^{-2}})$	**Ersa**	0.032±0.034 (254)	0.026±0.045 (160)	0.019±0.020 (84)	0.032±0.067 (131)	0.028±0.006
	Palma	0.070±0.073 (176)	0.042±0.060 (136)	0.014±0.010 (50)	0.028±0.022 (54)	0.039±0.024
$\mathbf{AAOD_{440}}$	**Ersa**	0.019±0.013 (14)	0.023±0.018 (4)	-(0)	0.032±0.028 (6)	0.025±0.007
	Palma	0.041±0.020 (21)	0.035±0.026 (7)	-(0)	-(0)	0.038±0.004
$\mathbf{AAE_{440\text{-}870}}$	**Ersa**	1.61±0.52 (14)	1.28±0.12 (4)	-(0)	1.88±0.90 (6)	1.59±0.30
	Palma	1.89±0.52 (21)	1.73±0.64 (7)	-(0)	-(0)	1.81±0.11
$\boldsymbol{f_{440}}$	**Ersa**	1.46±0.03 (14)	1.45±0.07 (4)	-(0)	1.43±0.05 (6)	1.45±0.01
	Palma	1.44±0.05 (21)	1.42±0.07 (7)	-(0)	-(0)	1.43±0.02
$\boldsymbol{k_{440}}$ $\mathbf{(\cdot 10^{-3})}$	**Ersa**	2.8±1.2 (14)	3.6±1.7 (4)	-(0)	3.8±1.8 (6)	3.4±0.5
	Palma	4.7±1.4 (21)	4.2±1.8 (7)	-(0)	-(0)	4.4±0.4

4.2.3 SEASONAL AND ANNUAL VARIABILITY OF AEROSOL PROPERTIES AT ERSA AND PALMA

4.2.3.1 AOD, AE AND FINE-MODE CONTRIBUTION

The seasonal aerosol classification based on the first graphical method described in Sect. 4.2.2 ($AE_{440–870}$ vs. AOD_{440}) is presented in Fig. 4.1. The graphs are made with the whole daily AOD dataset. Seasonal mean values of AOD, AE and $\delta\alpha$ are given in Table 4.1. The relationship between daily $AE_{440–870}$ and AOD_{440} shows three principal features visible at both sites: (i) a wide range of $AE_{440–870}$, between 0 and 2.5, year-round, (ii) a narrower range of $AE_{440–870}$, between 1 and 2, at high AOD_{440} (> 0.4) especially during summer at Ersa and during autumn at Palma and (iii) a narrow range of $AE_{440–870}$, between 0 and 0.5, also at high AOD_{440} (> 0.4), especially marked in summer, autumn and spring at Ersa and in summer and autumn at Palma. The first feature indicates a wide range in particle size with higher inter-season variations at Ersa (yearly $AE_{440–870}$ = 1.25 ± 0.14, see Table 4.1) than at Palma (yearly $AE_{440–870}$ = 1.05 ± 0.05). The second and third features are characteristics of, respectively, pollution/biomass burning and mineral dust [Holben et al., 2001], but the method does not allow distinguishing pollution from biomass burning. For the mineral dust feature, the tendency of AE$_{440–870}$ is shifted approximately 0.1–0.2 lower at Palma than at Ersa. The percentage of days with the predominant aerosol conditions (AOD$_{675}$ < 0.15) is greater than 80% except in summer at Palma (63%). In winter this percentage is 100% at both sites. This result indicates that mineral dust events in winter in the WMB are of low intensity (AOD$_{675}$ < 0.15) and cannot be distinguished from the predominant marine aerosols so far with this method.

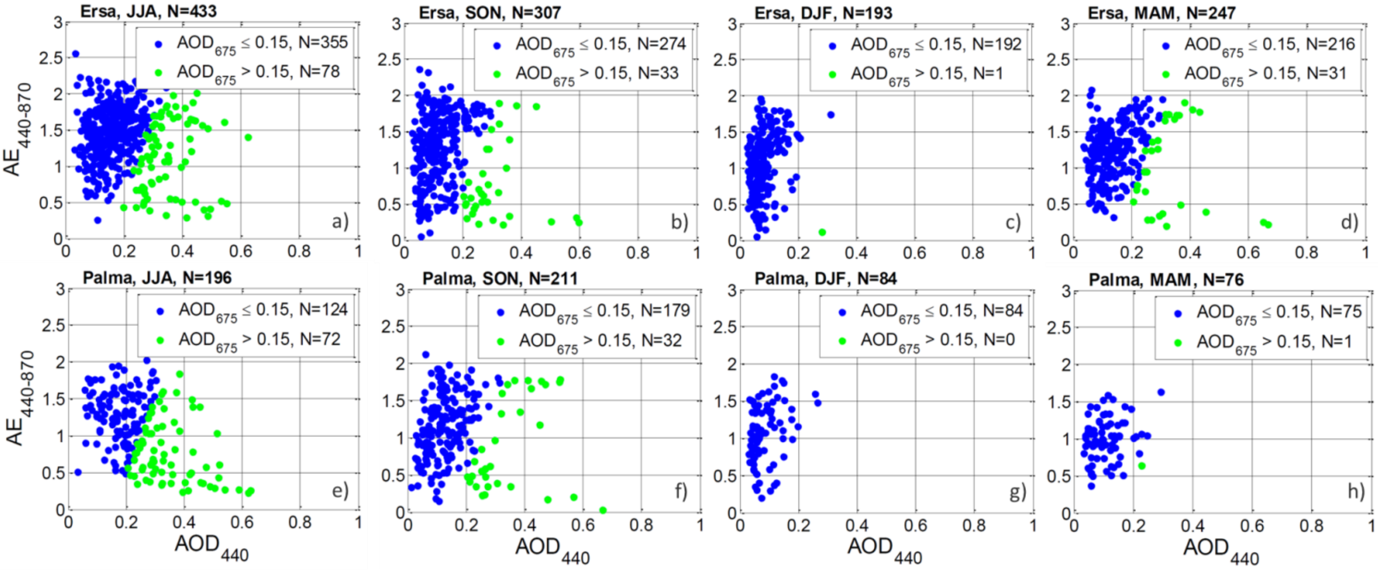

Fig. 4.1. Ångström exponent calculated between 440 and 870 nm (AE$_{440-870}$) as a function of the aerosol optical depth at 440 nm (AOD$_{440}$) at Ersa and Palma during (a, e) summer, (b, f) autumn, (c, g) winter and (d, h) spring, for the whole 2011–2015 AERONET Level 2.0 daily AOD dataset. Blue bullets are for AOD$_{675}$ < 0.15 and green bullets for AOD$_{675}$ > 0.15. In this figure and in the rest of the Chapter N represents the number of points or observations shown in the plot or used to calculate the means shown in the plot.

A further aerosol classification is performed for the second and third features mentioned above with the method from Gobbi et al. [2007]. It is presented in Fig. 4.2. As expected from the above discussion the criteria AOD$_{675}$ > 0.15 removes a lot of points (the number of remaining points per season is lower than 78) and makes the database unexploitable in winter (N = 1 at Ersa and N = 0 at Palma, see Table 4.1). Besides, the statistics in spring at Palma (N = 1 for AOD$_{675}$ > 0.15) are not sufficient to be representative of the second (pollution/biomass burning) and third (mineral dust) features introduced above.

For the rest of the seasons, moderate to large AODs (AOD$_{440}$ > 0.4, yellow, dark and light green and red bullets in Fig. 4.2) gather in two well-differentiated clusters. In summer, Ersa and Palma present an important fine-mode cluster marked by AE > 1.0; $\delta\alpha$ < 0.2 and AE > 1.3; $\delta\alpha$ < 0.1, respectively associated with 55 < f < 90 %; 0.09 < r_f < 0.14 μm and f > 60 %; 0.10 < r_f < 0.15 μm, respectively, and corresponding to polluted and continental air masses. In this fine-mode cluster the largest AODs are logically found at Ersa, which is closer to the European continent than Palma. During the same summer season, both sites also present an important coarse-mode cluster in turn marked by AE < 0.5; −0.1 < $\delta\alpha$ < 0.3 at Ersa and AE < 0.8; 0 < $\delta\alpha$ < 0.3 at Palma associated with f < 40 % at both sites and corresponding to mineral dust. In this coarse-mode cluster, the largest AODs are logically found at Palma, which is closer to the African continent than Ersa. The AOD increase is linked to a decrease of $\delta\alpha$ towards 0, which is related to almost pure mineral dust as observed in sub-Sahelian sites [Basart et al., 2009]. The points of this coarse-mode cluster for which $\delta\alpha$ exhibits positive values indicate the presence of small particles mixed with this coarse mode.

The difference between the summer mean values of AE (higher at Ersa than at Palma; 1.41 vs. 1.10 respectively) and $\delta\alpha$ (lower at Ersa than at Palma; 0.06 vs. 0.29) given in Table 4.1 reflects the general trends found from Figs. 4.2a and 4.2e. In autumn the frequency of moderate to large AOD events reduces by half at both sites compared to summer, both fine- and coarse-mode clusters are also present but with less variability. The fine-mode cluster at Ersa and Palma is marked by AE > 1.5; $\delta\alpha < -0.1$ and AE > 1.1; $\delta\alpha < 0.0$ respectively, and is associated with $70 < f < 90\%$; $0.11 < r_f < 0.13\ \mu m$ and $60 < f < 85\%$; $0.10 < r_f < 0.14\ \mu m$), while the coarse-mode cluster is in turn marked by AE $\sim$ 0.3; $0 < \delta\alpha < 0.2$ and 0 < AE < 0.2; $0 < \delta\alpha < 0.2$ and is associated with $f < 20$ and $f < 10$ %. The spring plot for Ersa (Fig. 4.2d) is similar to that of summer but with fewer occurrences. The most interesting differences are a greater number of high-AOD dust events (AOD$_{440}$ > 0.6, coarse-mode cluster) in spring compared to summer and conversely a greater number of high AOD pollution events (AOD$_{440}$ > 0.4, fine-mode cluster) in summer compared to spring.

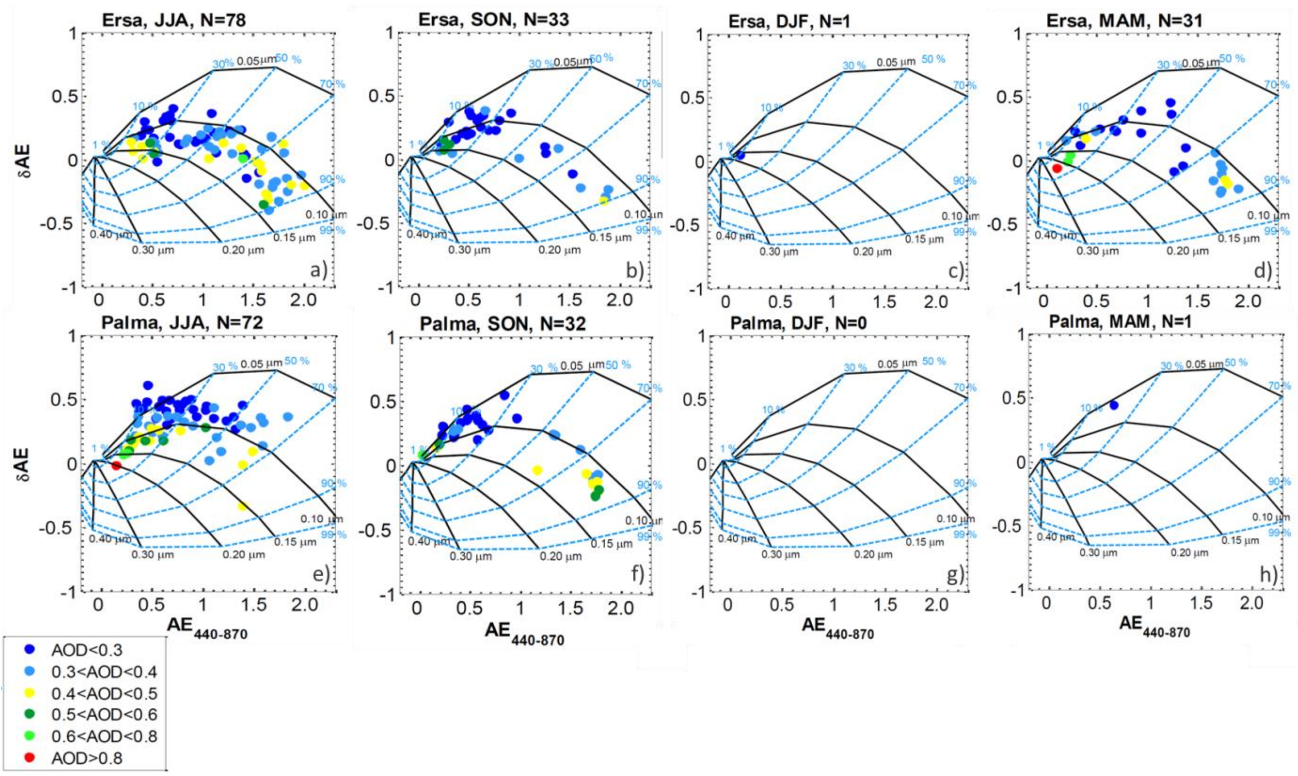

Fig. 4.2. Ångström exponent difference ($\delta\alpha = \mathrm{AE}_{440-675} - \mathrm{A}_{\mathrm{E}675-870}$) as a function of the Ångström exponent calculated between 440 and 870 nm (AE$_{440-870}$) at Ersa and Palma during (a, e) summer, (b, f) autumn, (c, g) winter and (d, h) spring, for the whole 2011–2015 AERONET Level 2.0 daily aerosol optical depth (AOD) dataset. Only points with AOD$_{675}$ > 0.15 are represented. However, the AOD plotted is AOD$_{440}$ (and not AOD$_{675}$) in order to be directly comparable with the AERONET inversion criteria based on AOD$_{440}$. The legend applies for all plots. A bimodal, lognormal size distribution and a refractive index of 1.4–0.001i are considered to construct the grid. The black solid lines are each for a fixed fine mode radius and the dashed blue lines for a fixed fraction of the fine-mode contribution to the AOD at 675 nm.

In the 5-year study period 2011–2015, while Ersa station has at least 3 full years of data, Palma de Mallorca station has more sparse data. Therefore, before starting with the monthly analysis, the representativeness of Palma data must be checked with Ersa data by taking the subset of Ersa data coincident in time with those of Palma (which are comprised of the period August 2011–December 2013). In Fig. 4.3a the monthly means of this restricted dataset (black bullets) are superimposed on the monthly means of the whole dataset (red bullets). In all cases the monthly means of the August 2011–December 2013 dataset are within the monthly variability of the whole dataset. In summer and autumn, the representativeness of the August 2011–December 2013 dataset is good: the difference between both datasets is lower than 0.01. The highest differences, 0.02–0.03, are reached during the period March–May. In the Palma restricted dataset only spring 2013 contributes to the spring mean. Curiously during that spring no moderate to large AODs (AOD_{440} > 0.4) are observed (see Fig. 4.2h). This result may produce the underestimation in AOD of the August 2011–December 2013 dataset compared to the whole dataset observed at Ersa in March and April and suggests that Palma monthly means during those months may also be underestimated. Taking into account the restriction of the Palma dataset, the discussion of the Palma spring means has to be taken cautiously in the following.

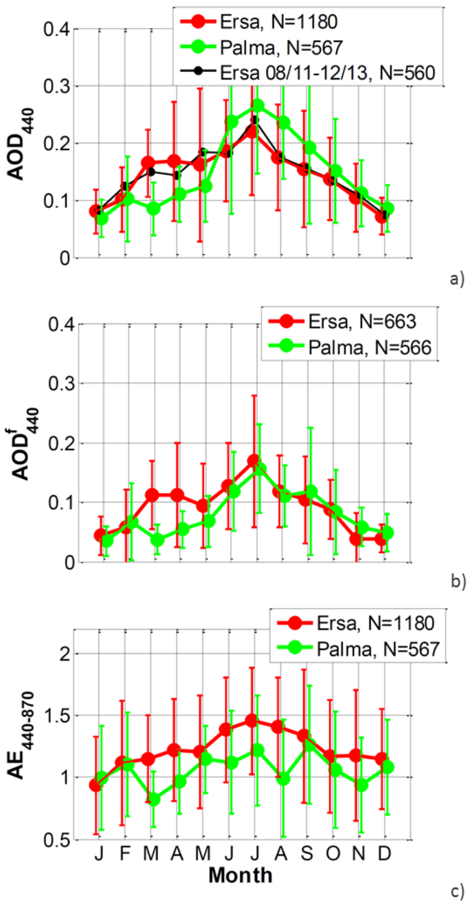

Fig. 4.3. Monthly average variations calculated with daily measurements of (a) aerosol optical depth at 440 nm (AOD_{440}), (b) fine-mode aerosol optical depth at 440 nm (AOD^{f}_{440}) and (c) the Ångström exponent calculated between 440 and 870 nm ($AE_{440–870}$) derived from AERONET Level 2.0 inversion products available for the period 2011–2015. The error bars represent the standard deviation. On the AOD_{440} plot it is also plotted the monthly values at Ersa calculated over the limited period for which data are also available at Palma, i.e., August 2011–December 2013.

Fig. 4.3a shows clearly that the monthly mean AOD_{440} has annual cycle at Ersa and Palma. The maximum values found at Ersa (0.22) and at Palma (0.27) are observed in July. Those maximum values are due to a combination of mineral dust outbreaks and pollution events at Ersa and mostly to mineral dust outbreaks at Palma (see the seasonal aerosol frequency and classification in Sect. 4.2.3.3). The decreasing trend in AOD_{440} during the autumn months (from September to November) is identical at both sites, while the AOD_{440} in spring is lower at Palma than at Ersa and it is the opposite in summer/autumn. The background AOD_{440} in spring at Ersa is dominated by small particles located in the marine boundary layer, present throughout the year [Sciare et al., 2014], while at Palma the predominance of the Atlantic advection meteorological scenario in spring leads to the renovation of air masses at regional scale through the Gulf of Lion and to the cleaning of the atmosphere [Escudero et al., 2007]. The summer mean AOD_{440} (± standard deviation) is 0.19±0.10 and 0.25±0.13 at Ersa and Palma, respectively, while the winter averages are equals (0.08).

In order to see the contribution of the fine-mode particles, the fine-mode AOD_{440}, AOD^{f}_{440} are plotted in Fig. 4.3b. Except for March and April, the annual cycles at both sites, Ersa and Palma, are similar in shape and magnitude. Similar maximum values are found in summer, 0.14±0.09 and 0.13±0.07 at Ersa and at Palma respectively. In March and April AOD^{f}_{440} is more than double at Ersa than at Palma. In addition to the possible underestimation of the Palma dataset in spring (explained above), the maps of AOD per aerosol type from Barnaba and Gobbi [2004] suggest a contribution of aerosols of continental origin already in spring over

Corsica and not before summer over the Balearic Islands. But this result cannot be confirmed with the ($\delta\alpha$, AE) plots because of the limited representativeness of Palma data during the spring months.

The monthly $AE_{440–870}$ plot (Fig. 4.3c) shows different seasonal patterns at both sites. At Ersa, the monthly $AE_{440–870}$ increases from winter until summer and reaches a maximum value of 1.46 in July. At Palma, it oscillates between 0.82 and 1.26 in March and September respectively, without any significant seasonal trend. The higher values at Ersa compared to Palma indicate the presence of finer particles at Ersa throughout the year. The $AE_{440–870}$ annual means at Ersa and Palma are 1.25 ± 0.14 and 1.05 ± 0.05, respectively, with maxima in summer (1.46±0.45 and 1.14±0.47, respectively). The coarse-mode fraction (not shown; see Sicard et al. [2014]) looks reversely correlated to the AE: it decreases at Ersa from winter until summer and reaches a minimum in July, while no marked trend is observed at Palma. The fact that $AE_{440–870}$ is lower in spring than in summer at Ersa reflects the higher frequency of dust events in spring compared to summer as found earlier from our aerosol classification.

4.2.3.2 VOLUME SIZE DISTRIBUTION

Fig. 4.4 shows the seasonal variability of the aerosol particle size distribution in the atmospheric column at both sites. Seasonal mean values are given in Table 4.1 for the volume median radius and the volume concentration of the fine (r_f^v , C_f^v) and coarse (r_c^v , C_c^v) modes. The annual volume concentration values, ranging between 0.015 and 0.017 $\mu m^3 \mu m^{-2}$ for the fine mode and between 0.028 and 0.039 $\mu m^3 \mu m^{-2}$for the coarse mode, at both sites are typical of maritime [Smirnov et al., 2002] and/or background/rural [Omar et al., 2005] environments. The annual values at Palma are very similar to the mean size distribution averaged over several sites in the WMB found by Mallet et al. [2013].

During winter, fine-mode volume concentrations are similar at both sites (about 0.010 $\mu m^3 \mu m^{-2}$). In spring the fine-mode volume concentration doubles, with respect to winter, at Ersa while it is stable at Palma. This behavior is reflected in AOD^f_{440} (Fig. 4.11b), which doubles from winter to spring at Ersa because of the contribution of aerosols with origin in the continent already in spring over Corsica and not before summer over the Balearic Islands. The domination of large particles, as mineral dust, is particularly remarkable during the summer period at both sites, for instance relatively large coarse-mode concentrations are also visible in spring at Ersa and in autumn at Palma. During summer, a clear difference between both sites can be observed on the coarse-mode volume concentration (0.032 ± 0.034 at Ersa vs. 0.070 ± 0.073 at Palma) and also on the C_c^v/C_f^v ratio (1.6 vs. 2.6, at Ersa and Palma respectively).

The summer coarse-mode volume median radii (2.51 ± 0.39 and 2.43 ± 0.40) fall in the range of values for dusty sites (1.90–2.54 μm; [Dubovik et al., 2002b]) and are in agreement with the average value of 2.34 μm found for the WMB by Mallet et al. [2013]. According to Dubovik et al. [2002b], the absence of dynamics between the particle radius and the aerosol loading explains that dust median radii are smaller than those of urban/industrial aerosols. The influence of European pollution decreases from Ersa to Palma, therefore, the coarse-mode volume median radius decreases. In the same line, the inter-season r_c^v decreases with increasing mineral dust frequency (see the seasonal aerosol frequency and classification in Sect. 4.2.3.3).

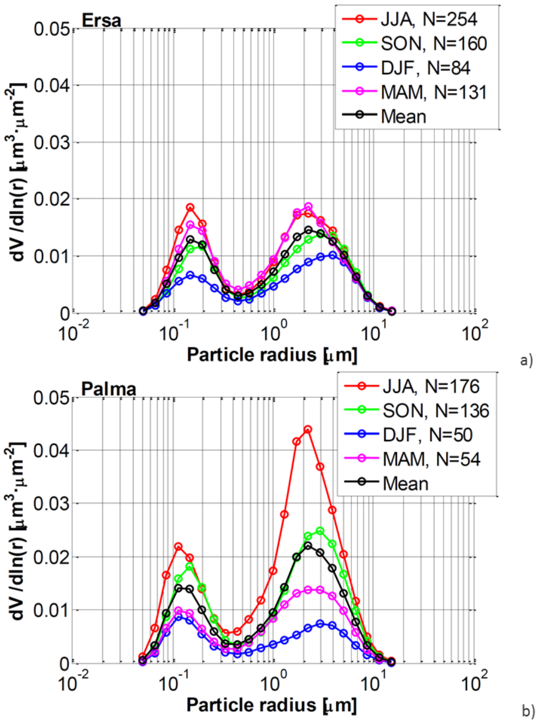

Fig. 4.4. Seasonal variation of the particle volume size distribution in the atmospheric column at (a) Ersa and (b) Palma derived from AERONET Level 2.0 daily inversion products available for the period 2011–2015.

4.2.3.3 AAOD, ABSORPTION ÅNGSTRÖM EXPONENT (AAE) AND REFRACTIVE INDEX

Besides aerosol amount and size, other important aerosol properties are those related to their absorbing ability. It is worth noting that AERONET Level 2.0 inversion products linked to the aerosol absorption properties like the AAOD, the absorption Ångström exponent (AAE) and the refractive index are performed with the following restrictions: 50 < SZA < 80◦ and $AOD_{440} > 0.4$. In order to give light to the seasonal frequency, intensity and aerosol type under such restrictions, Fig. 4.5 shows the ($\delta\alpha$, AE) plots only for those AERONET Level 2.0 daily inversion products in the dataset used in this Chapter that meet those criteria (50 < SZA < 80◦ and $AOD_{440} > 0.4$).

The plots for both sites show without ambiguity that such restrictions lead to only two types of aerosols, mineral dust corresponding to the coarse-mode cluster ($\delta\alpha < 0.3$; $AE_{440-870} < 0.75$; $f < 40\%$) and pollution corresponding to the fine-mode cluster ($AE_{440-870} > 1.0$; $f > 60\%$). In the following, the adjective “strong” is used to define these mineral dust and pollution events, i.e. days with at least one instantaneous $AOD_{440} > 0.4$ that allows the Level 2.0 inversion, in order to differentiate them from the rest of the mineral dust and pollution events. The seasonal number and ratio of each of these two aerosol types and their respective seasonal mean AOD_{440} are summarized in Table 4.2. In summer the ratio of mineral dust/pollution for strong aerosol cases is 50/50% and 76/24% at Ersa and Palma respectively. In autumn strong pollution episodes predominate at Ersa and Palma, being the ratios 25/75% and resp. 43/57 %. At Ersa, strong mineral dust and pollution events have the same frequency during spring and during summer. The seasonal mean AOD_{440} for strong pollution cases is higher at Palma (0.41±0.08 and 0.46±0.06 in summer and autumn respectively) than at Ersa (0.38±0.07 and 0.41±0.03), suggesting that the strong European pollution episodes with the lowest AOD observed at Ersa do not reach Palma and thus do not contribute to decrease the seasonal mean at Palma.

The seasonal mean AOD_{440} for mineral dust is larger and more variable, presents higher standard deviations than for pollution, for instance the summer and autumn seasonal means AOD_{440} for mineral dust at Palma are 0.50±0.17 and 0.53±0.21, only little variations are observed between both seasons, while stronger events are detected at Ersa in autumn, AOD_{440} = 0.66±0.00 (note that the latter is estimated with only one point of observation, therefore the standard deviation is nil), and spring, 0.63±0.38, than in summer, 0.42±0.08. The limitation of the graphical method used here is that no information related to the aerosol absorption properties is retrieved. In the following, the dominant aerosol size, type and frequency found will be linked with the absorption properties. Bergstrom et al. [2007] report that the spectral AAOD for aerosols representing the major absorbing aerosol types (pollution, biomass burning, desert dust and mixtures) decreases with wavelength and can be approximated with a power-law wavelength dependence, the AAE which can be calculated between two wavelengths $\lambda 1$ and $\lambda 2$, $AAE_{\lambda1-\lambda2}$, as

$$AAE_{\lambda_1-\lambda_2} = -\frac{ln\left(\frac{AAOD_{\lambda_1}}{AAOD_{\lambda_2}}\right)}{ln\left(\frac{\lambda_1}{\lambda_2}\right)} \quad [4.3]$$

The range of values of AAE provides useful information on shortwave absorption produced by different types of aerosols, namely black carbon (BC), organic carbonaceous matter and mineral dust [Russell et al., 2010]. However, recently Mallet et al. [2013] highlighted the difficulties in attributing AAE values higher than 1 over the Mediterranean, the value for pure BC, to organic species (and/or mineral dust) or to coated BC since they all produce AAE > 1 [Lack and Cappa, 2010].

Table 4.2. Seasonal number with their standard deviation (and percentage of data in parenthesis) and aerosol optical depth at 440 nm (AOD_{440} ± standard deviation (σ)) for the pairs ($\delta\alpha$, AE) of Ångström exponent difference ($\delta\alpha$) and Ångström exponent (AE) fulfilling ($\delta\alpha$ < 0.3, AE < 0.75) and corresponding to strong mineral dust outbreaks and fulfilling (AE > 1) and corresponding to strong pollution events. The data are those of Fig. 4.5 (AERONET Level 2.0 daily inversion products available for the period 2011–2015, which means that the following criteria apply on these data: 50 < SZA < 80° and AOD_{440} > 0.4).

		Summer	Autumn	Winter	Spring	Year
		N (percentage)				
Strong mineral dust	**Ersa**	7 (50%)	1 (25%)	-	3 (50%)	11 (46%)
($\delta\alpha$ < 0.3, AE < 0.75)	**Palma**	16 (76%)	3 (43%)	-	-	19 (61%)
Strong pollution	**Ersa**	7 (50%)	3 (75%)	-	3 (50%)	13 (68%)
(AE > 1)	**Palma**	5 (24%)	4 (57%)	-	-	9 (32%)
		$AOD_{440}\pm\sigma$				
Strong mineral dust	**Ersa**	0.42±0.08	0.66±0.00	-	0.63±0.38	0.57±0.13
($\delta\alpha$ < 0.3, AE < 0.75)	**Palma**	0.50±0.17	0.53±0.21	-	-	0.51±0.02
Strong pollution	**Ersa**	0.38±0.07	0.41±0.03	-	0.36±0.08	0.38±0.03
(AE > 1)	**Palma**	0.41±0.08	0.46±0.06	-	-	0.44±0.04

The seasonal variations of the spectral dependency of the AAOD are shown in Fig. 4.6a. Seasonal mean values are given in Table 4.1. At each site the spectra are shown for the whole dataset, denoted as All in Fig. 4.6, and for strong mineral dust, denoted as MD in Fig. 4.6, and strong pollution, Pol in Fig. 4.6, cases determined with the classification obtained from Fig. 4.5 (see first paragraph of this Section). In both Ersa and Palma the AAOD decreases with increasing wavelength. The annual $AAOD_{440}$ is about 0.025±0.007 at Ersa and about 0.038±0.004 at Palma. Besides, the associated $AAE_{440–870}$ is 1.59±0.30 and 1.81±0.11, at Ersa and Palma respectively.

The spectra of AAOD for pollution are quite similar in shape and magnitude at both sites, presenting weak inter-season variations. Also, these spectra are rather low (< 0.02), with low spectral dependency (AAE oscillates between 1.09 and 1.28). On their behalf, the mineral dust AAOD (0.029 < $AAOD_{440}$ < 0.061) and AAE (1.28 < AAE < 2.67) are much higher than those for pollution and present larger inter-season and inter-site variations, for instance, at Ersa during spring the $AAOD_{440}$ (AAE) reaches its highest value, 0.050 (2.67), when the strong mineral dust outbreaks represent 50% (the highest percentage) of the cases; at Palma the highest values of $AAOD_{440}$ (AAE), 0.061 (2.37), are found in autumn (Table 4.2) and correspond to an intense mineral dust outbreak. The average value of AAOD$_{440}$ in summer at Ersa (0.019) measured over the whole dataset is within the error bar of the value of 0.020 found by Mishra et al. [2014] at the same site from a larger dataset of AERONET observations. However, this value is lower than the average value given in Mallet et al. [2013] for the WMB calculated at sites characterized mostly as urban and dusty, which could indicate that they considered more dusty sites than urban ones in the computing of their basin average.

The mineral dust AAOD spectra found at Ersa and Palma sites are similar in magnitude and shape to the results found during PRIDE (Puerto Rico Dust Experiment, 2000; aerosols: Saharan dust) and ACE-Asia (Aerosol Characterization Experiment-Asia, 2001; aerosols: Asian dust, urban and industrialized) [Bergstrom et al., 2007; Russell et al., 2010]. The pollution and MD AAE found here are in agreement with the mean values observed at several Mediterranean AERONET sites for urban sites (1.31) and dusty sites (1.96), respectively [Mallet et al., 2013]. The annual mean values of AAE (1.59 and 1.81 at Ersa and Palma, respectively) fall within the range 1.5–2, in which the AAE at different wavelength pairs vary at the dusty site of Solar Village, Saudi Arabia [Russell et al., 2010]. As a conclusion, it can be affirmed that AAE is strongly influenced by strong mineral dust outbreaks, even at Ersa.

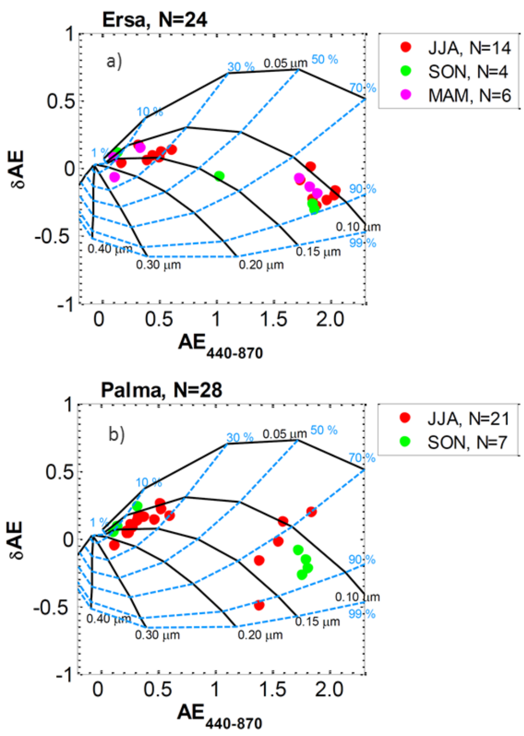

Fig. 4.5. Ångström exponent difference ($\delta\alpha$ = AE$_{440-675}$– AE$_{675-870}$) as a function of the Ångström exponent calculated between 440 and 870 nm (AE$_{440-870}$) at (a) Ersa and (b) Palma, derived from AERONET Level 2.0 daily inversion products available for the period 2011–2015, which means that the following criteria apply on these data: 50 < solar zenith angle < 80° and aerosol optical depth at 440 nm (AOD$_{440}$) > 0.4. A bimodal, lognormal size distribution and a refractive index of 1.4–0.001i are considered to construct the grid. The black solid lines are each for a fixed fine-mode radius and the dashed blue lines for a fixed fraction of the fine-mode contribution to the AOD at 675 nm.

The seasonal spectral variations of the real and the imaginary part of the refractive index (*n* and *k*, respectively) are shown in Fig. 4.6b and c. Seasonal mean values at 440 nm (n_{440} and k_{440}) can be found in Table 4.1. Figure 4.6b shows a large inter-season and inter-site variability in the shape and amplitude of the *n* spectra. n_{440} has an annual mean value of 1.45±0.01 at Ersa and 1.43±0.02 at Palma. These values are on the order of magnitude of those found by Mallet et al. [2013] from AERONET observations at various sites around the Mediterranean Basin and they are in the upper limit of urban/industrial aerosols (1.33– 1.45) and lower than pure dust (1.48–1.56; [Dubovik et al., 2002b]). However, the values significantly differ by aerosol type: 1.37 < n_{440} < 1.46 and 1.44 < n_{440} < 1.55 for pollution and mineral dust, respectively, being in agreement with the results from Dubovik et al. [2002b].

The high variability of n_{440} for mineral dust is probably linked to variations in the dust mineralogy, while *n* spectra are nearly constant for pollution. *n* shows in all cases a decrease of about 0.02–0.03 towards ultraviolet wavelengths for mineral dust, whereas Petzold et al. [2009] determined wavelength-independent *n* from airborne measurements of dust during the SAMUM (Saharan Mineral Dust Experiment) campaign with an iterative method employing Mie computations. This difference may be due to differences in the measurement techniques and in particular to the assumption of spherical particles (Mie theory) by Petzold et al. [2009]. Indeed Dubovik et al. [2000b; 2002a] showed that treating nonspherical particles (like mineral dust) as spheres result in an erroneous decrease of *n* with decreasing wavelength.

The values found of n_{440} for MD are in agreement with previous works such as Petzold et al. [2009], who found 1.55–1.56 at 450 nm for dust during SAMUM, and Denjean et al. [2016], who found 1.50–1.55 at 530 nm in dust layers from airborne measurements over the WMB during the ChArMEx 2013 field campaign. k_{440} (Fig. 4.6c) has an annual mean value of $(3.4\pm0.5) \cdot 10^{-3}$ at Ersa and $(4.4\pm0.4) \cdot 10^{-3}$ at Palma. The annual k_{440} are in the lower limit of the values found from AERONET observations by Mallet et al. [2013] at various sites around the Mediterranean Basin (3.5–$11.9 \cdot 10^{-3}$) where the minimum value ($3.5 \cdot 10^{-3}$) is found at the Italian island of Lampedusa. Although previously was explained that AAOD_{440} is higher for MD than for pollution, the reverse occurs for k_{440}, which is in general higher for pollution than for MD. This result indicates that these higher MD AAOD values are the result of larger amounts of MD (compared to pollution) in terms of optical depth and not of MD absorption properties. k_{440} ranges between 2.6 and 4.9 and between 2.8 and $4.5 \cdot 10^{-3}$ for MD and pollution, respectively, and in general higher values are found at Palma. Even though the pollution spectrum of *k* is nearly wavelength independent, towards ultraviolet wavelengths presents the opposite behavior of *n* spectra of MD showing a strong increase. As the imaginary part of the refractive index is driven by iron oxide content (especially hematite; [Sokolik and Toon, 1999]), it results in a higher *k* at shorter wavelengths during episodes with high dust concentrations [Moosmüller et al., 2009].

The ranges of k_{440} found for pollution and MD are in agreement with previous works performed during the TARFOX (Tropospheric Aerosol Radiative Forcing Observational Experiment) campaign in 1996, where values between 1 and 8×10^{-3} were found off the US Atlantic coast in horizontal layers of distinct aerosol refractive indices using a retrieval based on aerosol in situ size distribution and remote sensing measurements [Redemann et al., 2000]; besides, during SAMUM, Petzold et al. [2009] retrieved values of desert dust *k* at 450 nm ranging between 3.1 and 5.2×10^{-3}; on their behalf, Denjean et al. [2016] found values of *k* at 530 nm between 0 and 5×10^{-3} at different heights in dust layers during the ChArMEx 2013 field campaign.

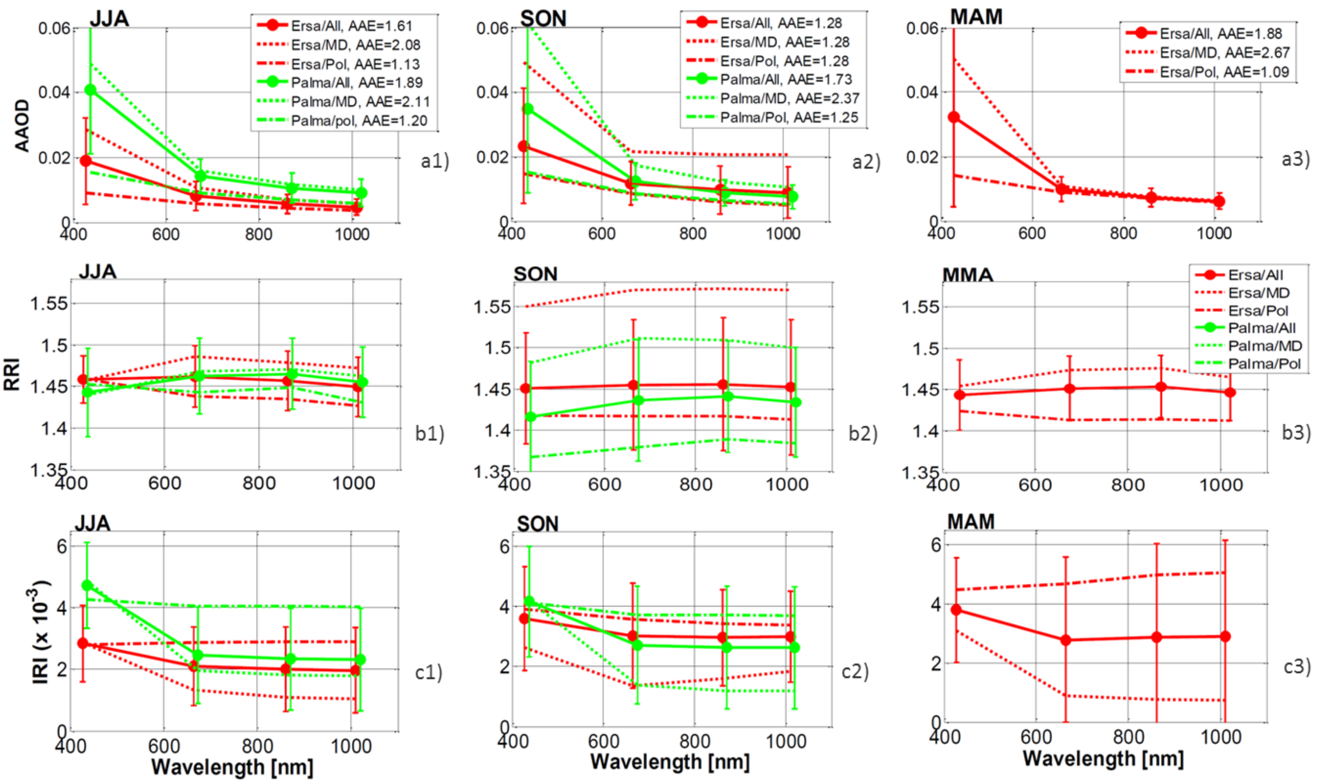

Fig. 4.6. Seasonal variation of the spectra of (a) the aerosol absorption optical depth (AAOD), (b) the real part of the refractive index (*n*) and (c) the imaginary part of the refractive index (*k*) during (1) summer, (2) autumn and (3) spring, derived from AERONET Level 2.0 daily inversion products available for the period 2011–2015. The legend in plot (b3) applies for all plots (b) and (c). All three parameters are retrieved with the following restrictions: 50 < solar zenith angle < 80◦ and aerosol optical depth at 440 nm (AOD$_{440}$) > 0.4. The error bars represent the standard deviation. The seasonal mean is represented for the whole dataset (All), and separately for strong mineral dust (MD) and strong pollution (Pol) cases determined with the classification obtained from Fig. 4.5.

4.2.3.4 SINGLE SCATTERING ALBEDO AND ASYMMETRY FACTOR

The SSA is the ratio of aerosol scattering to total extinction (i.e., scattering plus absorption) that provides some information on the aerosol absorption properties. It is useful to relate the AAOD to the AOD

$$AAOD_{\lambda} = (1 - SSA_{\lambda})AOD_{\lambda} \qquad [4.4]$$

On its behalf, the asymmetry factor (*g*) represents a measure of the preferred scattering direction and varies between −1 (only backward-scattering, i.e., at 180◦ relative to the incident direction) and +1 (only forward-scattering at 0◦). Both variables, the SSA and the asymmetry factor are of special interest for radiative transfer studies. The seasonal spectral variations of SSA and *g* are shown in Fig. 4.7 and seasonal mean values at 440 nm (SSA$_{440}$ and g_{440}) are given in Table 4.3. It is worth noting that while SSA is restricted to cases with AOD$_{440}$ > 0.4, *g* has no restrictions.

Taking a look to Table 4.3, it is clear that, on average, both sites appear as “moderately” absorbing, with annual SSA$_{440}$ ranging between 0.95±0.01 and 0.93±0.01, even though the minimum values observed are around 0.89 and 0.87 at Ersa and Palma, respectively. In agreement with the results reported previously (higher AAOD$_{440}$ at Palma than at Ersa), lower SSA is found at Palma compared to Ersa at all wavelengths but especially at 440 nm. MD and pollution SSA spectra have very distinct behaviors, while the first one (MD SSA) increases with increasing wavelength, the second (pollution SSA) decreases. This result is in agreement with the climatological SSA spectra obtained worldwide by Dubovik et al. [2002b] and plotted by Russell et al. [2010] showing that SSA_λ decreases with increasing wavelengths for urban/industrial aerosols and biomass burning and conversely increases with increasing wavelengths for desert dust. During autumn and spring at Ersa and autumn at Palma, the seasonal mean of SSA_λ calculated with the whole dataset (MD plus pollution) increases from 440 to 675 nm and decreases afterwards, being this behavior representative of a combination of both MD and pollution. During summer at Palma the SSA spectra (calculated with the whole dataset) are very similar to that of MD (76 % of the dataset corresponds to mineral dust, see Table 4.2). MD and pollution SSA_{440} vary in the range 0.89–0.94 and 0.97–0.98, respectively. For comparison, Denjean et al. [2016] found SSA at 530 nm ranging from 0.90 to 1.00 in layers of different aerosol types in the WMB during the ChArMEx summer 2013 field campaign. Variations among the different seasons are more pronounced for MD than for pollution, thus as a consequence of higher MD $AAOD_{440}$ in autumn, MD SSA_{440} is smaller in autumn than in summer.

The annual mean values of the asymmetry factor at 440 nm (g_{440}) are 0.70±0.01 at both sites. The mean values of both pollution and MD g_{440} show very little inter-season and intersite variations, they range between 0.69 and 0.70 and between 0.71 and 0.73, respectively. Fig. 4.7b shows that the spectra of g have a general tendency to decrease with increasing wavelengths for pollution, while it is nearly constant for MD. These results are in agreement with the climatology from Dubovik et al. [2002b] who found similar g_{440} for urban/industrial aerosols and desert dust (0.68–0.73) and a decreasing tendency with increasing wavelength for urban/industrial aerosols. Lyamani et al. [2006], who compared the asymmetry factor spectra at Granada for dust events and urban/industrial aerosols (European contamination), found in their research that the decrease of g with increasing wavelengths is much stronger for urban/industrial aerosols than for mineral dust, implying that at near-infrared wavelengths (λ > 670 nm), constant AOD and low SZA, the solar radiation scattered to the surface is greater for mineral dust than for urban/industrial aerosols. Here, as in the previous case, the seasonal means calculated with the whole dataset (MD plus pollution) have the signature of neither MD nor pollution, but on the contrary they are representative of a combination of both MD and pollution.

Table 4.3. Seasonal and annual variations of the following aerosol properties with their standard deviation (and number of observations in parenthesis): single scattering albedo at 440 nm (SSA_{440}), asymmetry factor at 440 nm (g_{440}), the solar aerosol radiative effect (ARE) and the solar aerosol radiative forcing efficiency (FE) at Ersa and Palma derived from AERONET Level 2.0 daily inversion products available for the period 2011–2015. BOA and TOA stand for bottom of the atmosphere and top of the atmosphere, respectively. The values of SSA_{440} are given for 50 < solar zenith angle (SZA) < 80◦ and an aerosol optical depth at 440 nm (AOD_{440}) > 0.40. The values of ARE and FE are given for 50 < SZA < 60◦.

		Summer	Autumn	Winter	Spring	Year
SSA_{440}	**Ersa**	0.96±0.03 (14)	0.96±0.02 (4)	-(0)	0.95±0.03 (6)	0.95±0.01
	Palma	0.92±0.03 (21)	0.94±0.04 (7)	-(0)	-(0)	0.93±0.01
g_{440}	**Ersa**	0.69±0.02 (254)	0.70±0.03 (160)	0.71±0.04 (84)	0.70±0.03 (131)	0.70±0.01
	Palma	0.70±0.03 (176)	0.71±0.03 (136)	0.68±0.03 (50)	0.70±0.03 (54)	0.70±0.01
SW-ARE BOA ($W \cdot m^{-2}$)	**Ersa**	-17.5±9.5 (413)	-13.6±10.0 (205)	-17.6±8.3 (23)	-18.0±9.2 (195)	-16.7±9.7
	Palma	-22.8±13.4 (282)	-16.5±12.1 (193)	-6.7±3.3 (14)	-9.6±6.0 (65)	-18.7±13.2
SW-ARE TOA ($W \cdot m^{-2}$)	**Ersa**	-11.4±6.2 (413)	-8.6±5.9 (205)	4-6.6±4.4 (23)	-9.7±5.1 (195)	-9.1±2.0
	Palma	-11.5±6.1 (282)	-9.5±5.7 (193)	4.9±2.5 (14)	-6.1±3.2 (65)	-8.0±3.1
FE BOA ($W \cdot m^{-2}\ AOD_{550}^{-1}$)	**Ersa**	-139.1±23.6 (413)	-137.8±18.8 (205)	-182.9±31.4(23)	-157.9±39.7 (195)	-144.4±29.3
	Palma	-136.4±40.9 (282)	-129.6±27.4 (193)	-130.7±13.9 (14)	-122.0±24.6 (65)	-132.2±34.8
FE TOA ($W \cdot m^{-2}\ AOD_{550}^{-1}$)	**Ersa**	-90.0±9.1 (413)	-89.5±10.7 (205)	-66.4±10.3 (23)	-85.6±13.5 (195)	-82.9±11.2
	Palma	-70.8±16.8 (282)	-78.7±13.7 (193)	-95.1±11.8 (14)	-83.4±11.5 (65)	-82.0±10.2

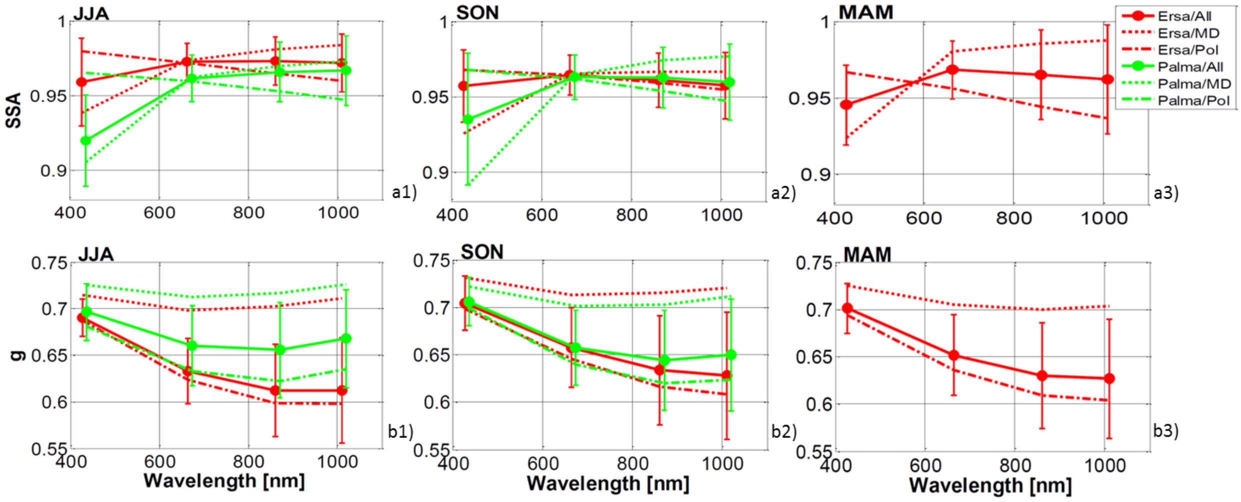

Fig. 4.7. Seasonal variation of the spectra of (a) the single scattering albedo (SSA) and (b) the asymmetry factor (*g*) during (1) summer, (2) autumn and (3) spring, derived from AERONET Level 2.0 daily inversion products available for the period 2011–2015. The legend in plot (a3) applies for all plots (a) and (b). SSA is retrieved with the following restrictions: 50 < solar zenith angle < 80◦ and an aerosol optical depth at 440 nm (AOD_{440}) > 0.4. The error bars represent the standard deviation. The seasonal mean is represented for the whole dataset (All) and separately for strong mineral dust (MD) and strong pollution (Pol) cases determined with the classification obtained from Fig. 4.5.

4.2.3.5 SOLAR DIRECT RADIATIVE EFFECT AND FORCING EFFICIENCY AT ERSA AND PALMA

The AERONET Version 2.0 retrieval provides a set of radiative quantities in the solar, SW, spectrum range including spectral downward and upward total fluxes at the surface, diffuse fluxes at the surface and broadband upward and downward fluxes as well as ARE and FE both at the BOA and at the TOA. The radiative effect accounts for changes in the solar radiation levels due to changes in the atmospheric constituents; it is defined previously by means of Eq. 2.47 and Eq. 2.47 (see Chapter 2).

In Chapter 3 is also defined the FE as the ratio of ARE per unit of AOD. The ARE analytical definitions used by AERONET [AERONET, 2016] are slightly different than Eqs. 2.47 and 2.48,

$$ARE_{BOA}^{AER} = F_{BOA}^{DN} - F_{BOA}^{DN,0} \quad [4.5]$$

$$ARE_{TOA}^{AER} = F_{TOA}^{UP,0} - F_{TOA}^{UP} \quad [4.6]$$

While Eq. 4.6 is equivalent to Eq. 2.49 because the downward flux at the TOA is independent of the presence or not of aerosols in the atmosphere ($F_{TOA}^{DN} = F_{TOA}^{DN,0}$), the use of Eq. 4.5 yields an overestimation with respect to the real value since the upward fluxes with and without aerosols are not taken into account.

In the AERONET retrieval approach, the flux calculations account for the thermal emission, absorption and single and multiple scattering effects using the Discrete Ordinates Radiative Transfer (DISORT) method [Stamnes et al., 1988], same method as GAME code. The solar broadband fluxes are calculated for SZA between 50 and 80◦ and by spectral integration in the range from 0.2 to 4.0 μm (SW spectral range). The integration of atmospheric gaseous absorption and molecular scattering effects are conducted using the GAME code [Dubuisson et al., 1996, 2004, 2006]. It is worth noting that flux calculations are performed for a multilayered atmosphere with a gaseous vertical distribution calculated with the U.S. standard atmosphere model and a single fixed aerosol vertical distribution (exponential decrease with aerosols up to a height of 1 km). Detailed information on the radiative transfer module used by the operational AERONET inversion algorithm can be found in García et al. [2011, 2012a, b].

García et al. [2008] tested in their research different vertical profiles and their sensitivity tests led to differences of less than 1 $W \cdot m^{-2}$ on the downward solar flux at the BOA and estimated negligible those differences, being about 0.2–3 % with respect to the instantaneous ARE. Besides, García et al. [2008] made an intensive validation of AERONET estimations of fluxes and radiative forcings using ground-based measurements from solar databases at nine stations worldwide but AERONET estimations of the aerosol direct radiative effect are little used in the literature. Cachorro et al. [2008], on their behalf, used the AERONET ARE estimations to study the impact of an extremely strong desert dust intrusion over the Iberian Peninsula. Derimian et al. [2008] used the AERONET estimates of the ARE for mineral dust mixed with biomass burning and for pure mineral dust at M'Bour, Senegal, and tested the impact of neglecting aerosol nonsphericity on radiative effect calculations. García et al. [2011] did a similar work but at regional level for mixtures of mineral dust and biomass burning and mineral dust and urban/industrial aerosols. Valenzuela et al. [2012] checked AERONET estimates of the radiative fluxes against SBDART (Santa Barbara DISORT Atmospheric Radiative Transfer; [Ricchiazzi et al., 1998]) computations for desert dust events affecting the southeastern Iberian Peninsula. Finally, García et al. [2012a, b] have used AERONET estimates of the ARE at 40 stations grouped in 14 regions worldwide for the study of six aerosol types: mineral dust, biomass burning, urban/industrial, continental background, oceanic and the free troposphere.

4.2.3.5.1 COMPARISON OF AERONET RADIATIVE FLUXES WITH GROUND-BASED AND SATELLITE DATA

A comparison of AERONET estimations of the two following solar fluxes that are the most critical for aerosol forcing calculations is performed.

Firstly, to study the solar downward flux at the surface, SW-F_{BOA}^{DN} a comparison between AERONET estimations and pyranometer measurements is performed using the closest AERONET/SolRad-Net (Solar Radiation Network) site to the study area in the WMB, located at Barcelona, where collocated AERONET and solar flux measurements are available. All SolRad-Net Level 1.5 data (cleared of any operational problem) are downloaded from the SolRad-Net web page at http: //solrad-net.gsfc.nasa.gov/. The period with coincident measurements is May 2009–October 2014. The pyranometer located at Barcelona, close to the sun-photometer is a Kipp and Zonen CMP 21, already introduced in Sect. 3.3.1 (see Chapter 3). It is worth to comment that coincident AERONET and pyranometer measurement times are restricted to ±1 min.

Secondly, to study the solar upward flux at the TOA, SW-F_{TOA}^{UP} a comparison between AERONET estimations and CERES (Clouds and the Earth's Radiant Energy System) satellite measurements at Ersa, Palma and Alborán is performed. Using CERES Single Scanner Footprint (SSF) Level 2 products (CERES/Aqua and CERES/Terra products are used indistinctly), namely the shortwave (0–5 μm) upward flux at the TOA given for a spatial resolution equivalent to its instantaneous footprint (nadir resolution 20 km equivalent diameter). All CERES data are downloaded from the CERES subsetting and browsing web page at https://ceres-tool.larc.nasa.gov/ord-tool/products?CERESProducts=SSFlevel2. These CERES SW-F_{TOA} are derived from CERES radiance measurements using angular distribution models described by Loeb et al. [2005] and Kato and Loeb [2005].

The CERES data need to be screened before perform the comparison spatially for the pixels in which one of the ground sites falls and by temporally allowing a time difference of ±15 min, taking into account that the time of overpass of both CERES/Aqua and CERES/Terra over the three sites varies in the range of 10:00–14:00 UTC. The CERES/Terra instantaneous SW-F at the TOA uncertainties can be found in CERES [2016] and are estimated to be 13.5 $W \cdot m^{-2}$ for all-sky conditions, being the CERES/Aqua TOA flux errors similar, according to Loeb et al. [2007]. Because of the CERES overpass time range (10:00–14:00 UTC), the SZA restriction for

AERONET Level 2.0 data (50 < SZA < 80◦) rejects many measurements that coincide in time but are for SZA < 50◦, hence the use of AERONET Level 2.0 data provides very few points for comparison. Consequently AERONET Level 1.5 data is selected, in this kind of data the SZA restriction is 40 < SZA < 80◦, representing the cases with 40 < SZA < 50◦ about a 33% of the total.

The periods with available AERONET Level 1.5 data are 2008–2014 at Ersa, 2011–2014 at Palma and 2011–2012 at Alborán. It is necessary also to solve two issues in order to further filter CERES data points: (i) sometimes CERES pixels are affected by clouds when at the coincident time AERONET is not and (ii) because the three sites are in coastline regions, CERES pixels (20 km footprint) contain information from land and water. The first issue is due to the different techniques used by both, AERONET sun-photometers and CERES, which make the air mass volumes sampled by both instruments quite different. The second one is in general not problematic, except at given periods of the year and at given hours of the day when the sunglint (the sunlight is reflected off the surface of the ocean at the same angle that the sensor is viewing the surface) produces a significant increment of the upward fluxes in the direction of the spaceborne sensor. Both cases result in an increase of CERES upward fluxes at the TOA and are discarded by using two more products of CERES SSF Level 2 files: (i) the cloud fraction derived from MODIS radiances using the algorithms described by Minnis et al. [2003] and (ii) the CERES measured shortwave radiance. CERES fluxes are discarded when the cloud fraction is greater than 5 % and when the shortwave upward radiance is higher than 50 $W \cdot m^{-2} sr^{-1}$. This value of 50 $W \cdot m^{-2} sr^{-1}$ is fixed having a look at the annual evolution of the CERES measured shortwave radiance at the three sites during the period of interest. This radiance shows a clear annual cycle (not shown) with climatological values lower than 50 $W \cdot m^{-2} sr^{-1}$ and a significant numbers of outliers with radiances higher than 50 $W \cdot m^{-2} sr^{-1}$.

Comparing the downward solar fluxes at the BOA measured by the pyranometers to that estimated by AERONET, a very good agreement is found between both quantities (R > 0.99). To quantify the level of accuracy the average difference between the AERONET modeled and observed flux is calculated, bringing as a result an overestimation of AERONET fluxes (12 $W \cdot m^{-2}$), in relative terms, an overestimation of +3.0%. This increment is found by dividing the average AERONET modeled flux by the observed one. This overestimation is in the range of mean relative errors (from −0.6 to +8.5%) found by García et al. [2008] under different aerosol environments at nine stations worldwide. Also, Derimian et al. [2008] found an overestimation of approximately +4 % in M'Bour, Senegal. According to García et al. [2008] that overestimation is due mostly to the cosine effect (the pyranometer angular response which can deviate by up to ±3% from the truth at SZA of 70–80◦) and to the surface albedo and bidirectional reflectance distribution function (BRDF) assumed by AERONET. The leastsquare fit linear equation relating the AERONET (AER) fluxes to the observation (OBS) is $OBS = 0.98 \cdot AER - 4.50$.

The results presented in this Section are in total agreement with García et al. [2008] who found $OBS = 0.98 \cdot AER - 5.32$. Since the comparison of SW-F_{BOA}^{DN} is performed regardless of the aerosol load, can be easily assumed that the fluxes with turbid (high aerosol load) or clean (low aerosol load) atmospheres follow the same regression line $OBS = 0.98 \cdot AER - 4.50$. Finally, to correct for the missing upward fluxes in the definition of ARE_{BOA}^{AER}, the latter can be multiplied by the term $1 - SA$ where SA stands for the surface albedo. Indeed,

$$ARE_{BOA} = \Delta F_{BOA} - \Delta F_{BOA}^{0} = (F_{BOA}^{DN} - F_{BOA}^{UP}) - \left(F_{BOA}^{DN,0} - F_{BOA}^{UP,0}\right) = (F_{BOA}^{DN} - SA \cdot F_{BOA}^{DN}) - \left(F_{BOA}^{DN,0} - SA \cdot F_{BOA}^{DN,0}\right) = \left(F_{BOA}^{DN} - F_{BOA}^{DN,0}\right)(1 - SA) \quad [4.7]$$

Consequently the corrected estimated solar ARE at the BOA, $\mathrm{ARE}_{\mathrm{BOA}}^{\mathrm{C}}$ in $W \cdot m^{-2}$, is calculated from the original AERONET radiative forcing, $\mathrm{ARE}_{\mathrm{BOA}}^{\mathrm{AER}}$, as

$$ARE_{BOA}^{C} = 0.98 \cdot ARE_{BOA}^{AER} \cdot (1 - SA) \quad [4.8]$$

where the term 0.98 comes from the correction of the fluxes after comparison to pyranometer measurements and the value of SA considered is calculated as the average of the surface albedo at the four AERONET wavelengths (440, 675, 870 and 1020 nm). In their research, García et al. [2012b] explained that considering the surface albedo at the four AERONET wavelengths leads to differences lower than 10% considering spectral surface albedo in the whole solar spectral range (0.2– 4.0 μm). The corrected solar FE at the BOA, $\mathrm{FE}_{\mathrm{BOA}}^{\mathrm{C}}$, in $W \cdot m^{-2} \cdot AOD_{550}^{-1}$, defined in Eq. 4.9 as the ratio of forcing per unit of AOD at 550 nm, can be simply calculated from the original AERONET FE, $\mathrm{FE}_{\mathrm{BOA}}^{\mathrm{AER}}$, as

$$FE_{BOA}^{C} = 0.98 \cdot FE_{BOA}^{AER} \cdot (1 - SA) \qquad [4.9]$$

The comparison of upward solar fluxes at the TOA measured by CERES vs. estimated by AERONET, only the pair of points with a cloud fraction < 5 % and shortwave upward radiance < 50 $W \cdot m^{-2} sr^{-1}$, shows an underestimation by AERONET estimates, probably due to an increment of the upward fluxes in the direction of the spaceborne sensor caused by clouds or sunglint. Here again, but to a lesser extent compared to the comparison of SW-F_{BOA}^{DN}, the pairs of points taken into account in the fit calculation show a good agreement between both AERONET modeled and the observed fluxes (R = 0.87). The average difference between the AERONET modeled and observed flux is +0.18 $W \cdot m^{-2}$ which, in relative terms, corresponds to a difference of 0.2 %. At the moment of this research were performed, AERONET fluxes at the TOA weren't being compared with satellite measurements before. Finally, it is worth noting that the least square fit linear equation relating the AERONET fluxes to the OBS is $OBS = 0.88 \cdot AER + 8.7$. Like at the BOA, since the comparison of SW-F_{BOA}^{UP} is performed regardless of the aerosol load, the correction of the fluxes can be assumed the same for atmospheres with and without aerosols. Then the corrected ARE at the TOA, $\mathrm{ARE}_{\mathrm{TOA}}^{\mathrm{C}}$, and the corrected FE at the TOA, $\mathrm{FE}_{\mathrm{TOA}}^{\mathrm{AER}}$, can be expressed as

$$ARE_{TOA}^{C} = 0.88 \cdot ARE_{TOA}^{AER} \qquad [4.10]$$

$$FE_{TOA}^{C} = 0.88 \cdot FE_{TOA}^{AER} \qquad [4.11]$$

4.2.3.5.2 SOLAR DIRECT RADIATIVE EFFECT AND FORCING EFFICIENCY: MONTHLY VARIATIONS AT ERSA AND PALMA

The monthly means of the corrected AERONET Level 2.0 instantaneous solar ARE and FE are shown in Fig. 4.8 at both the BOA and TOA. By plotting the whole dataset of ARE and FE as a function of SZA, the behavior of both quantities is independent of SZA, remaining approximately constant. However, as SZA increases, the slant path increases and it is logical to expect a decrease of the ARE/FE related to the decrease in solar radiation reaching the Earth. This effect has been observed on instantaneous FE observations by di Sarra et al. [2008] and Di Biagio et al. [2009], among others. Therefore filter Fig. 4.8 is filtered for SZA ≤ 60◦.

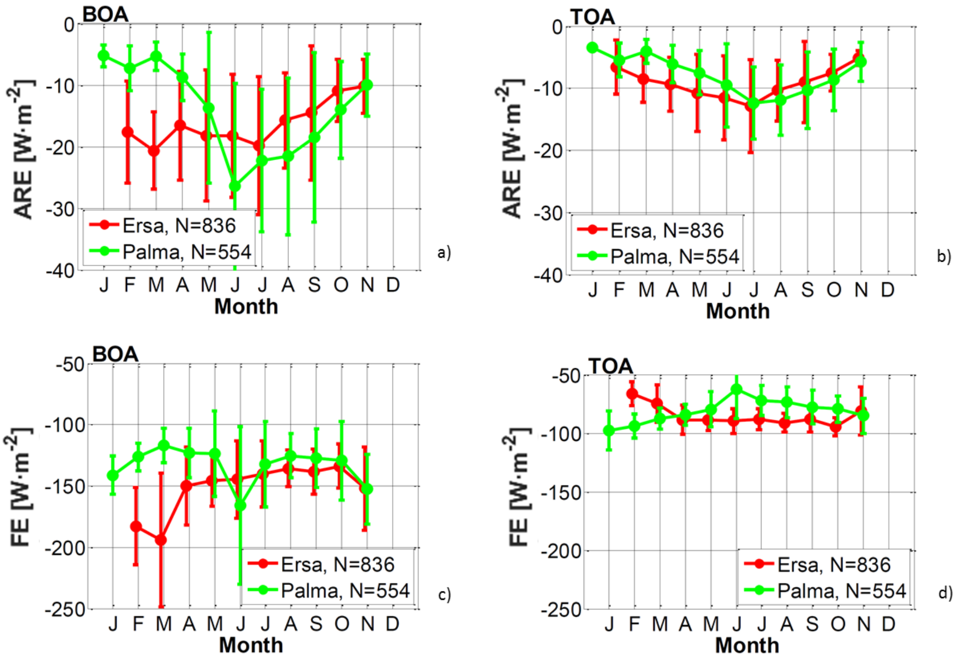

Fig. 4.8. Monthly variation of (a, b) the solar aerosol radiative effect (ARE) and (c, d) the solar aerosol radiative forcing efficiency (FE) at the (a, c) bottom of the atmosphere (BOA) and (b, d) top of the atmosphere (TOA), derived from AERONET Level 2.0 inversion products available for the period 2011–2015. Both the ARE and the FE are estimated for 50 ≤ solar zenith angle ≤ 60°. The error bars represent the standard deviation.

The solar ARE is strictly negative and shows a marked annual cycle (at both the BOA and the TOA) at both Ersa and Palma. In absolute values, the solar ARE is lower during the winter months and reaches its maximum values in spring and summer. At the BOA, a maximum (in absolute value) of −20.6 $W \cdot m^{-2}$ is reached at Ersa in March (with a seasonal maximum of −18.0 $W \cdot m^{-2}$ in spring) while the strongest forcing at Palma, −26.4 $\cdot m^{-2}$, is reached in June (with a seasonal maximum of −22.8 $W \cdot m^{-2}$ in summer). These maximum values correspond to the season with the maximum occurrences of mineral dust outbreaks relatively to high pollution events at each site (64 % at Ersa in spring and 84 % at Palma in summer; see Table 4.2).

During the first three months of the year, the ARE is more than double at Ersa than at Palma. It reflects a similar result found earlier on fine-mode AOD$_{440}$ (see Sect. 4.2.3.1 and Fig. 4.3) and may be attributed to (i) the contribution of aerosols with origin in the continental Europe already in spring over Corsica and not before summer over the Balearic Islands, hence a higher amount of small particles that causes more cooling [Tegen and Lacis, 1996], and (ii) the absence of representative measurements during the spring season at Palma (see Sect. 4.2.3.1) The marked peak in during summer months at Palma (correlated with a peak in AOD$_{440}$; see Fig. 4.3a) is clearly due to mineral dust outbreaks, considering that these outbreaks are more frequent in summer and during the summer time studied here, the AAOD$_{440}$ (Fig. 4.6) is more than double at Palma (0.043; SSA$_{440}$ about 0.92) than at Ersa (0.018; SSA$_{440}$ about 0.96).

Finally, it is worth noting that according to Boucher and Tanré [2000], the surface forcing is enhanced when the aerosol absorption is larger. At the TOA, the seasonal cycles are similar at both sites. Again, talking about Fig. 4.8 in absolute values, maximum values of ARE are reached during the same season, summer, concretely, during July. The July and summer ARE mean values are, respectively, −12.9 and −11.4 $W \cdot m^{-2}$ at Ersa and −12.4 and −11.5 $W \cdot m^{-2}$ at Palma. The same difference observed on ARE BOA during the first months of the year is also visible on ARE TOA: ARE TOA at Ersa is almost double (in absolute values) that at Palma, whereas the stronger influence of the dust outbreaks at Palma (vs. Ersa) on ARE BOA during the summer months is not visible at the TOA. This behavior seems to indicate that ARE TOA is not as much affected by long-range transport of dust as it is by long-range transport of small particles of continental origin. This result is only valid for the summer season since the relative differences of the annual means between both sites at the TOA and at the BOA, on the order of 12 %, are similar. As far as aerosol absorption is concerned, Boucher and Tanré [2000] showed in their research that increasing the aerosol absorption decreases the aerosol effect at the TOA.

This comparison with the literature is very important because of the definition of Ersa and Palma as clean, insular sites located at the crossroads of European and North African air masses and the limited sun position (50 < SZA < 60◦). Concerning the background aerosols, García et al. [2012a] showed that for oceanic and clean sites the annual ARE given for SZA = 60 ± 5◦ is low (< 10 $W \cdot m^{-2}$) and rather similar at the BOA and TOA (ARE TOA/ARE BOA > 0.7). The situation ARE TOA/ARE BOA > 0.7 is found only at Palma in winter and may indicate the predominance of background aerosols on the solar ARE.

It is worth comparing the results presented here to those of García et al. [2012a, b], in particular from their regions R1 (the northern part of the Sahara–Sahel desert area; mineral dust) and R8 (Europe; urban and industrial pollution) which surround the study area of this research. It is interesting that in R8 the largest ARE BOA is reached during winter/spring (−65 < ARE BOA < −45 $\cdot m^{-2}$). The same phenomenon occurs at Ersa but with lower values (ARE BOA is about −18 $W \cdot m^{-2}$). The results presented here are usually lower than results from case studies as the one presented by Derimian et al. [2008] in which the dust ARE BOA (ARE TOA) at SZA = 50◦ and AOD_{440} = 0.54 is on the order of −80 (−25) $W \cdot m^{-2}$ at M'Bour, Senegal, or the case study found in Cachorro et al. [2008] which shows dust ARE BOA (ARE TOA) at 53 < SZA < 75◦ and $AOD_{440} \sim 0.5$ on the order of −60 (−30) $W \cdot m^{-2}$ at El Arenosillo, Spain. Also Lyamani et al. [2006] found ARE BOA (ARE TOA) at SZA = 50◦ of −43 (−8) $W \cdot m^{-2}$ for dust and −33 (−8) $W \cdot m^{-2}$ for European– Mediterranean air masses at Granada, Spain; Formenti et al. [2002] found for aged biomass burning with AOD_{500} = 0.39 an ARE BOA (ARE TOA) relatively constant with SZA on the order of −78 (−26) $W \cdot m^{-2}$ over northeastern Greece. Conversely, under a weak dust intrusion (AOD_{500} = 0.23 and SSA = 0.96) at Lampedusa, Italy, Meloni et al. [2005] found an ARE BOA (ARE TOA) at SZA = 50◦ on the order of −13 (−7) $W \cdot m^{-2}$, lower than the summer means at Ersa and Palma. A few years later at the same site but under a stronger dust intrusion (AOD_{500} = 0.59), Meloni et al. [2015] found an ARE BOA (ARE TOA) at SZA = 55◦ on the order of −63 (−45) $W \cdot m^{-2}$, much higher than the summer means found in the research presented in this Chapter.

The FE at Ersa shows an annual cycle (Fig. 4.8c, d), being at TOA reverse than the cycle found at the BOA. Some relatively constant minimum absolute values at the BOA (−150; −134 $W \cdot m^{-2}$) are reached during the period April–October while maximum absolute values at the TOA (−88.2; −94.4 $W \cdot m^{-2}$) are reached during the same period. The FE at Palma also shows a clear annual cycle but with some irregularities compared to Ersa. FE BOA reaches minimum absolute values from February to October (−133; −117 $\cdot m^{-2}$), excepting the month of June, while FE TOA has a triangular shape with a maximum value in January (−97.9 $W \cdot m^{-2}$) and a minimum value in June (−62.7 $W \cdot m^{-2}$). The reverse behavior of FE BOA (maximum) and FE TOA (minimum) in June is due to the combination of (i) the strong increase (in absolute value) of FE BOA between May and June while ARE TOA increases very little and (ii) the strong increase of AOD from May to June (Fig. 4.11a). The FE TOA summer mean is lower at Palma (−70.8 $W \cdot m^{-2}$, SSA_{440} about 0.92) than at Ersa (−90.0 $W \cdot m^{-2}$, SSA_{440} about 0.96), which shows that more absorbing aerosols produce a lower absolute FE TOA [García et al., 2012b].

García et al. [2012b] found summer mean values of FE BOA (FE TOA) for SZA = 60 ± 5◦ in regions R1 (dust) and R8 (urban/industrial) of approximately −150 (−50) and −165 (−70) $W \cdot m^{-2}$, respectively, and winter mean values in R13 (oceanic) of approximately −145 (−100) $W \cdot m^{-2}$. The annual FE BOA at Ersa (−144.4 $W \cdot m^{-2}$) and at Palma (−132.2 $W \cdot m^{-2}$) estimated here are slightly lower than the values given by García et al. [2012b] but are within the error bars. The explanation is probably that neither Ersa nor Palma are dominated by any of the aforementioned aerosol types but is rather representative of a combination of them.

García et al. [2012b] also found that the mean FE BOA in other dust regions (R2, western Africa) could be lower (−100 $W \cdot m^{-2}$). The relatively large (in absolute value) annual FE TOA at Ersa (−82.9 $W \cdot m^{-2}$) and at Palma (−82.0 $W \cdot m^{-2}$) compared to the results of García et al. [2012b] indicate that FE TOA, like ARE TOA, is not strongly affected by long-range transport aerosols.

Other works like Derimian et al. [2008] found dust FE BOA (FE TOA, both with respect to AOD_{440}) at SZA = 50◦ on the order of −150 (−45) $W \cdot m^{-2}$ at M'Bour, Senegal. di Sarra et al. [2008] made a multiannual statistical study at Lampedusa, Italy, and found FE BOA (with respect to AOD_{496}) at 50 < SZA < 60◦ on the order of −155 $W \cdot m^{-2}$ for dust and −135 $W \cdot m^{-2}$ for biomass burning/industrial aerosols. All studies show that while FE BOA is hardly dependent on AOD_{λ} for mineral dust, it is highly dependent on AOD_{λ} for biomass burning/industrial aerosols. Likewise, Di Biagio et al. [2009] also found FE BOA (with respect to AOD_{496}) at Lampedusa at 50 < SZA < 60◦ on the order of −180 $W \cdot m^{-2}$ for dust and −140 $W \cdot m^{-2}$ for urban/industrial aerosols. During a strong dust intrusion at Lampedusa (AOD_{500} = 0.59), Meloni et al. [2015] found an FE BOA (FE TOA, both with respect to AOD_{500}) at SZA = 55◦ on the order of −107 (−77) $W \cdot m^{-2}$, much lower than two previous works at the same site [di Sarra et al., 2008; Di Biagio et al., 2009] and lower than the summer means found here. The reason given by Meloni et al. [2015] is that they used higher SSA values than the ones associated with mineral dust at Lampedusa. In summary, the aerosol radiative forcing at 50 < SZA < 60◦ in the WMB is usually lower than case studies at sites dominated by only one aerosol type (dust or urban/industrial aerosols).

During the spring (at Ersa) and summer (at Palma) months when dust episodes are more frequent, an increase of ARE BOA is observed. At the TOA a maximum is reached in summer at both sites (Ersa and Palma have roughly the same ARE TOA). The annual cycle of the FE, which does not depend on the column aerosol amount, is not as marked as that of the ARE. The explanation comes from the higher dependency of the FE to absorption properties which are quite variable over the WMB, especially for mineral dust.

4.2.3.6 ON THE POSSIBLE NE-SW GRADIENTS OF THE AEROSOL PROPERTIES DURING AUGUST-DECEMBER 2011

In this section it is also considered the third site, located at Alborán Island, to examine possible gradients of the aerosol properties along the important NE–SW pathway of dust plumes over the WMB. Although data at Alborán are available from June 2011 to January 2012, the coincident period with simultaneous measurements at all three sites is limited to August to December 2011. The following analysis is based on instantaneous measurements from this 5- month period. In that particular period, very few AERONET Level 2.0 inversion products (i.e., with the following restrictions: 50 < SZA < 80◦ and AOD_{440} > 0.4) are available, only three measurements at Ersa, seven at Palma and five at Alborán. Thus, for that reason the AERONET products for which these restrictions apply (AAOD, AAE, *n*, *k* and SSA) are not analyzed in the following. In addition, two products, ARE and FE, have too few measurements available in December and are shown only in the period August to November 2011.

Fig. 4.9 shows the ($\delta\alpha$, AE) plots at the three sites giving an insight into the aerosol types found during the period August–December 2011. The fraction of points with AOD_{675} > 0.15 with respect to the total number of measurements increases from north to south, being 7, 11 and 38 % at Ersa, Palma and Alborán, respectively. In all three sites only a small number of cases correspond to a fine-mode cluster (f > 70 %; 0.10 < r_f < 0.15 μm). At Ersa most of the points have a fine-mode radius between 0.10 and 0.15 μm. One can easily distinguish a cluster formed most probably by maritime plus continental aerosols (0.75 < AE < 1.3; 30 < f < 70 %) and another one formed by mineral dust ($\delta\alpha$ < 0.3; AE < 0.75). These two aerosol types also appear in the Palma plot. Compared to Ersa, the cluster formed by maritime plus continental aerosols at Palma is moved towards (0.5 < AE < 1.2; 10 < f < 50 % and r_f < 0.10 μm). At Alborán a single large cluster is visible at (0 < $\delta\alpha$ < 0.4; AE < 1.3), which indicates that maritime plus continental aerosols and mineral dust have a similar signature in the

($\delta\alpha$, AE) representation. This first analysis reveals that the considered period from August to December 2011 seems to have been dominated by rather large particles and an increasing number from north to south of cases with large AODs. It is important to recall that at Alborán 35 % of the days are dominated by maritime plus continental aerosols and 31 % by mineral dust during the period June 2011–January 2012 [Lyamani et al., 2015; Valenzuela et al., 2015].

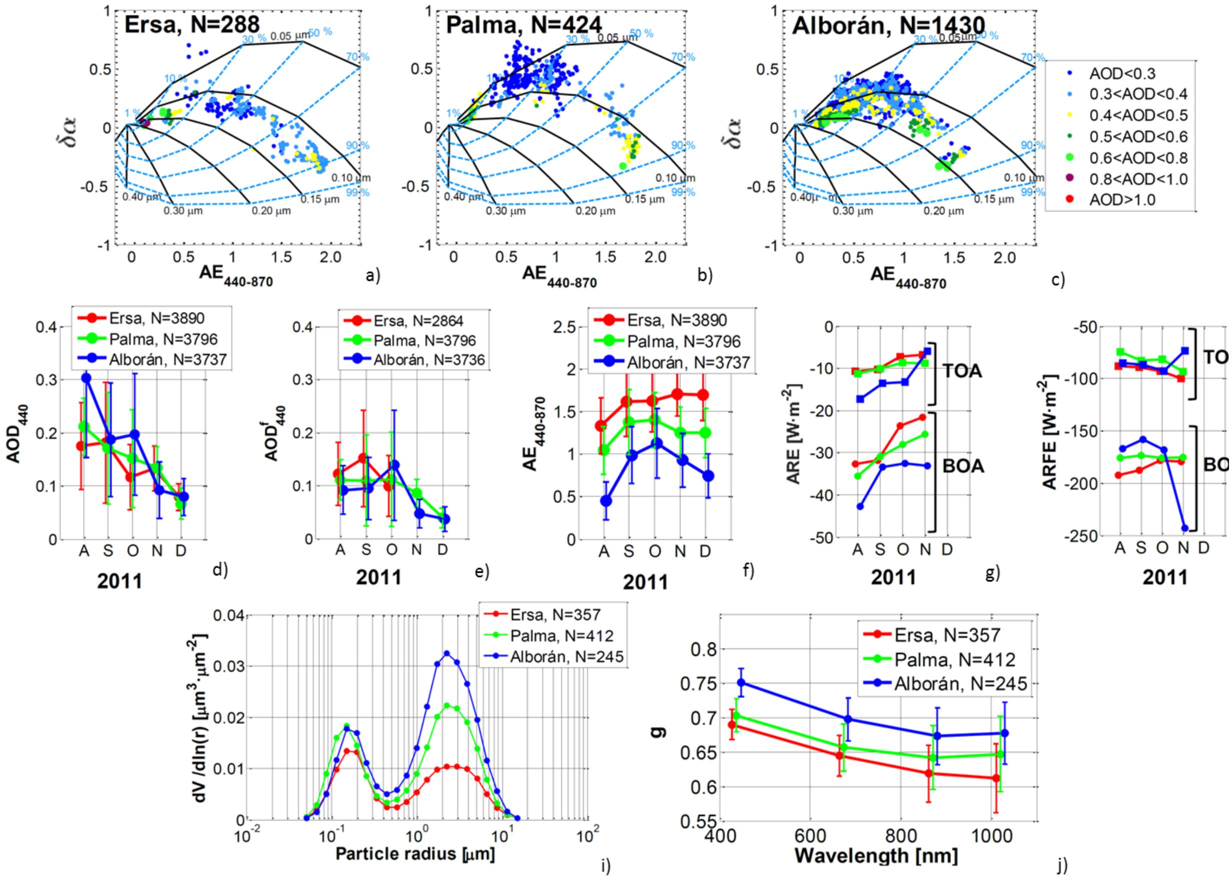

Fig. 4.9. ($\delta\alpha$, AE) plot at (a) Ersa, (b) Palma and (c) Alborán over the whole period from August to December 2011; monthly variations of (d) aerosol optical depth at 440 nm (AOD_{440}), (e) the fine-mode aerosol optical depth at 440 nm (AOD^{f}_{440}), (f) the Ångström exponent $AE_{440–870}$, (g) the aerosol radiative effect (ARE) and (h) the aerosol radiative forcing efficiency (FE); (i) the columnar size distribution and (j) spectra of the asymmetry factor, *g*, averaged over the whole period. The data are from AERONET Level 2.0 inversion products during the period August to December 2011. BOA and TOA stand for bottom and top of the atmosphere, respectively. The numbers of points in the plots (g) and (h) (not indicated in the plots for the sake of clarity) are 123, 133 and 101 for Ersa, Palma and Alborán, respectively. The color code is the same in all figures (d)–(j): red, green and blue for Ersa, Palma and Alborán, respectively. In (g)–(h) the error bars are omitted for the sake of clarity.

The same general decreasing tendency in AOD_{440} (Fig. 4.9d) is observed at all three sites from August to December 2011, while during the first 3 months an increasing NE–SW gradient is observed. The NE–SW gradient of the amount of the fine-mode particles, shown by AOD^{f}_{440} (Fig. 4.9e), is not that clear, for instance, in August and September AOD^{f}_{440} seems to follow a slightly decreasing NE–SW gradient, although all monthly means are within the standard deviations. In agreement with Lyamani et al. [2015], the results find here suggest a rather homogeneous spatial distribution of the fine particle loads over the three sites in spite of the distances between the sites and the differences in local sources. $AE_{440–870}$ (Fig. 4.9f) presents a clear decreasing NE–SW gradient during the whole period August– December 2011, which is the signature of an increasing contribution of large particles from north to south. This result is also reflected by the average size distribution shown in Fig. 4.9i, where the coarse-mode volume concentration has a clear increasing NE–SW gradient. It is worth noting that the fine-mode volume concentration is not significantly different at all three sites, which supports the previous hypothesis of a rather homogeneous spatial distribution of the fine particles as already highlighted by Lyamani et al. [2015] in the southwestern part of the basin.

The asymmetry factor at 440 nm (Fig. 4.9j) shows an increasing NE–SW gradient with g_{440} values in the range 0.69–0.70 at Ersa and Palma and about 0.75 at Alborán. According to Dubovik et al. [2002b], urban/industrial aerosols and desert dust have a similar g_{440} (0.68–0.73) and maritime aerosols have a slightly higher g_{440} ($\sim$ 0.75). Both g spectra at Ersa and Palma are indeed similar to the autumn average (Fig. 4.7b). Therefore, can be deduced that g is associated with pollution at Ersa (low g and strong spectral dependency), to pollution and mineral dust at Palma (low g and low spectral dependency) and could be attributed to maritime aerosols and mineral dust at Alborán (high g and low spectral dependency). At least two other types of aerosol are often found in the southern part of the WMB, from North African urban/industrial origin [Rodríguez et al., 2011] and/or from ship emissions [Valenzuela et al., 2015]. The emissions of both types of aerosols have been quantified in the Bay of Algeciras by Pandolfi et al. [2011], however, without further information on the aerosol properties at Alborán, this cannot be confirmed from the dataset used in this Chapter.

Fig. 4.9g shows the aerosol direct radiative effect at the BOA, which presents an increasing (in absolute value) NE–SW gradient. At the TOA, ARE is higher (in absolute value) at Alborán but it is similar at Ersa and Palma. Alborán measurements can be compared to ARE of dust in Granada (140 km N–NW of Alborán) from Valenzuela et al. [2012], who found annual means of ARE BOA (ARE TOA) at SZA = 55±5◦ for African desert dust events of approximately −50 (−20) $W \cdot m^{-2}$. The difference at the TOA between Alborán and the other two sites may come from low aerosol absorption properties at Alborán ($AAOD_{440} < 0.02$; see Sicard et al. [2014]), producing an increase in ARE TOA [Boucher and Tanré, 2000]. The FE at the BOA has a decreasing (in absolute value) NE–SW gradient which denotes that particles with higher absorption properties (like Ersa and Palma) will be more efficient in producing forcing at the surface. At the TOA the FE has no marked gradient.

4.3 FIELD CAMPAIGNS AND RADIATIVE COMPUTATIONS

In this section, the spatio-temporal evolution of a Saharan dust event over the Western Meditteranean Basin is discussed focusing in the optical and radiative properties of the dust detected by eight different lidar stations.

4.3.1 INSTRUMENTS AND DATA

In the framework of ChArMEx [Dulac et al. 2012], and the SOP-1a [Mallet et al., 2016], a few EARLINET/ACTRIS lidar stations provided several measurements during a multi-intrusion dust event that took place over the western and central Mediterranean Basin between 15 and 24 June, in order to perform a detailed 4D (spatio-temporal) monitoring of the dust event. Besides the lidar data, it is also used in this Chapter the data obtained from the French Falcon 20 aircraft, equipped with the LNG airborne lidar [Pelon et al. 2002] providing attenuated backscatter vertical profiles at three wavelengths (1064, 532 and 355 nm). The LNG lidar was mainly used in the downward-looking mode. Also, Meteosat Second Generation/Spinning Enhanced Visible and Infrared Imager (MSG/SEVIRI, described in Thieuleux et al [2005]) images (Fig. 4.10) and BSC-DREAM8b v2.0 model are used to set the days affected by Saharan dust (see Sect. 4.3.2.1). On its behalf, the BSC-DREAM8B v2.0 model (Dust REgional Atmospheric Model), operated by the Barcelona Supercomputing Center (http://www.bsc.es/projects/earthscience/BSC-DREAM/) [Pérez et al. 2006a, 2006b; Basart et al. 2012] providing forecasts of the columnar dust load every 6 h, makes possible to investigate the potential detection of a Saharan dust event at the observing stations spread over the WMB. The atmospheric variables taken into account by the BSC-DREAM8b v2.0 model are turbulent parameters in the early stage when the dust is lifted from the ground to upper levels, winds when the dust is travelling away from the sources, in addition to thermodynamic processes, rainfall and land cover features.

In total, six EARLINET lidar stations provided support to the SOP-1a and two ChArMEx supersites provided the data presented here in Sect. 4.3. The details of the eight stations are reported below in Table 4.4. Also, a total of eight flights overpassed or passed in the vicinity of the ground-based lidars. The flight trajectories can be found in Mallet et al. (2016).

Table 4.4. Characteristics of the lidar systems and the presence of collocated AERONET Sun-photometers.

Station	Location	Altitude ASL (m)	Channels	λ_β (nm)	Spatial resolution (m)	Reference	AERONET Sun-photometer
Granada	37.16, -3.61	680	$3\beta + 2\alpha + 1\delta$	532, 355, 1064	7.5	Guerrero-Rascado et al. [2008]	Y
Barcelona	41.39, 2.17	115	$3\beta + 2\alpha + 1\delta +$ WV	532, 355, 1064	3.75	Kumar et al. [2011]	Y
Cap d'en Font	39.49, 4.12	10	$1\beta + 1\alpha + 1\delta$	355	5.25	Chazette et al. [2016]	Y
Ersa	48.42, 2.10	20	$1\beta + 1\alpha + 1\delta$	355	15	Leon et al. [2015]	Y
Potenza	40.60, 15.72	760	$3\beta + 2\alpha + 1\delta$	532, 355, 1064	60	Madonna et al. [2011]	Y
Naples	40.50, 14.10	118	$2\beta + 1\delta$	532, 355	15	Boselli et al. [2004]	N
Lecce	40.30, 18.10	30	$3\beta + 2\alpha + 1\delta +$ WV	532, 355, 1064	3.75	Perrone et al. [2014]	Y
Serra la Nave	37.68, 14.98	1735	$1\beta + 1\delta$	355	60	Leto et al. [2015]	N

4.3.2 SPATIO-TEMPORAL EVOLUTION OF THE MINERAL DUST OUTBREAK

4.3.2.1 CHARACTERIZATION OF THE DUSTY DAYS

The presence of dust is evaluated by means of the MSG/SEVIRI near real time AOD at 550 nm provided every 15 min and dust load maps (Fig. 4.10) and concentration profiles from the BSC-DREAM8bv2 with a time resolution of 6 hours.

Fig. 4.10 and Table 4.5 show the dusty days identified at the different stations detailed above. These dusty days are also reported as red boxes in Fig. 4.11. Fig. 4.10 shows MSG/SEVIRI daily mean AOD at 550 nm from 15 to 24 June over the ocean and provides an overview of the horizontal distribution of the dust plumes during the period of the studied event. These AOD at 550 nm values vary for this event between 0.3 (light blue areas) and 0.8 (red areas), therefore according to Lee et al. [2012] the dust event studied here can be classified as a regional scale Saharan dust outbreak. A general overview of this Saharan dust outbreak is provided by Sicard et al. [2016a] and Barragan et al. [2017].

Table 4.5. Maximum and Minimum AERONET Level 2.0 AOD and AE values for the days with aerosol presence at each station, 15-16-17 at Granada, 16-17 at Cap d'en Font, 17-18-19-20 at Ersa, 21–22-23 at Potenza and 21–22-23 at Lecce.

Station	**AOD_{440}**		**$AE_{440-870}$**	
	Max (date)	**Min (date)**	**Max (date)**	**Min (date)**
Granada	0.27 (16 June 16:22)	0.19 (15 June 17:47)	0.66 (15 June 16:53)	0.42 (16 June 16:22)
Barcelona	-	-	-	-
Cap d'en Font	0.38 (16 June 17:19)	0.15 (16 June 07:07)	1.03 (16 June 06:11)	0.42 (16 June 15:52)
Ersa	0.36 (19 June 17:33)	0.06 (18 June 17:32)	1.75 (19 June 05:47)	0.86 (19 June 15:33)
Potenza	0.16 (21 June 17:03)	0.07 (23 June 15:08)	1.56 (23 June 17:03)	0.55 (21 June 16:35)
Lecce	0.33 (23 June 04:48)	0.12 (21 June 14:57)	1.78 (21 June 04:48)	0.72 (23 June 04:48)

Note that the MSG/SEVIRI data, presented in Fig. 4.10, is considered as the truth when the BSC-DREAM8B v2.0 model results are not in agreement with the corresponding satellite data. During the studied dust event, the areas with high dust load ($g \cdot m^{-2}$) in the BSC-DREAM8B model are in agreement with the light blue, yellow and red areas in Fig. 4.10. These areas with high dust load correspond to presence of dust in the atmosphere, thus both models identify the mineral dust over the same areas at the same time. Comparing this temporal evolution with the AERONET AOD_{440} values reported in Table 4.5, one can observe that in Granada the maximum value of AOD_{440} is reported during 16 June (0.27), a day affected by mineral dust in agreement with Fig. 4.10. Cap d'en Font is also affected during 16 June according to the models and it is during this day when the maximum of AOD_{440} is found in this station (0.38).

Ersa starts to be affected during 19 June, the same day in which the maximum value of AOD_{440} is 0.36. According to the models, the maximum value in Ersa is found during 20 June, this difference can be explained because the AERONET sun-photometers measure the total atmospheric column, given greater values owing to mineral dust mixed with other atmospheric components. Potenza is a similar case than Ersa, while the maximum value of AOD_{440} retrieved by AERONET is found during 21 June (0.16); according to the models, Potenza is affected during 21 June but to a greater extent during 22 June. Finally, in Lecce, the maximum value of AOD_{440} is 0.33 during 23 June; both models agree with this value showing the dust load over this station during 23 June, being 24 June as a clear day in south Italy.

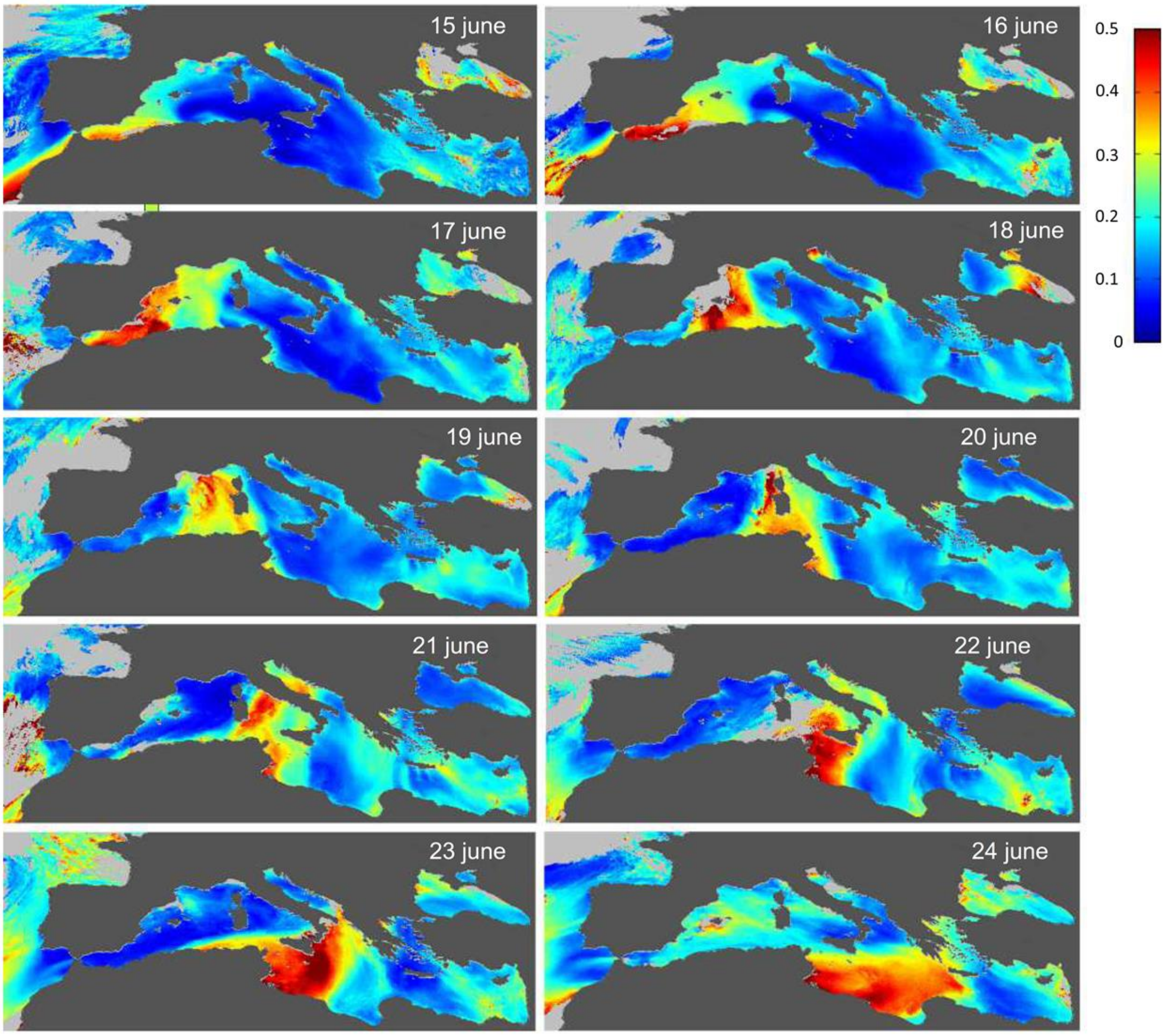

Fig. 4.10. Colour map of the aerosol optical depth (at 550 nm) daily mean values over the Mediterranean Sea from the MSG/SEVIRI instrument—ICARE Thematic Center (www.icare.univ.lille1.fr), from 16 to 24 June 2013, following Thieuleux et al. [2005] algorithm.

4.3.2.2 SPATIO-TEMPORAL EVOLUTION OF COLUMNAR PROPERTIES

Once the dusty days are characterized in each station (and labeled by means of red boxes in Fig. 4.11), it is necessary to study the temporal evolution of the mineral dust plume and to assess the multi-intrusion aspect of the event. For these purposes AERONET products, namely AOD_{440}, Ångström exponents calculated at the wavelength pair 440–870 nm, SSA and the coarse mode fraction at 440 nm are used, considering only AERONET Level 2.0 data, except in Barcelona, where only Level 1.5 data are available.

Fig. 4.11a provides an overview of the AERONET AOD_{440} and the AE calculated between the wavelengths of 440 and 675 nm. It is worth noting that during the dust event in Barcelona there are not AERONET data available whereas there are no data in Granada outside of the dust event. The stations are sorted from the west to the east matching with the main transport path of the dust plume (Fig. 4.10). It is clear how the combination of high AOD_{440} values with $AE_{440-870}$ values around, and below 1 is in most of the cases inside the red rectangles. According to Cachorro et al. [2008] and Valenzuela et al. [2015], this combination of large AOD_{440} with small $AE_{440-870}$ values may indicate a significant contribution of coarse mode particles to the aerosol load. The maximum value of AOD_{440} is found in Ersa on 19 June (0.36 at 17:33 UTC) and the minimum value is found in Potenza on 21 June (0.16 at 17:03 UTC). Meloni et al. [2003, 2004, 2008] pointed out in their researches AOD values at 415.6 nm of about 0.23–0.26 to 0.51 for moderate dust events and AOD values at

500 nm between 0.29 and 1.18 for the 1999–2006 period, which will be indicative in order to compare with the AOD values shown in this Section.

Fig. 4.11b shows the temporal evolution of the AOD measured by the lidars, only in the mineral dust layer. The lidar daytime measurements falling into the period of interest (red boxes) are inverted with the two-component algorithm and a given lidar ratio [Fernald et al., 1972; Fernald, 1984; Klett, 1981; 1985], whereas the night-time measurements are inverted with the elastic-Raman algorithm [Ansmann, Riebesell, and Weitkamp 1990]. Most of the lidar stations considered here are equipped by Raman channels, allowing for direct extinction measurements. However this capability is typically limited to night-time conditions owing to the solar background saturating the photodetectors of the Raman channels.

Both, daytime and night-time measurements are inverted and provided by each station by using their own algorithms. For that reason, the daytime profiles are inverted with different values of lidar ratios. For instance, at 532 nm, constant values of 55, 50, and 45 sr are used in Granada, Barcelona, and Potenza, respectively, while a synthetic profile of values ranging between 44 and 65 sr is used in Naples and Serra La Nave (at 355 nm), respectively. In Lecce, on its behalf, a height-independent value of 60–80 sr is used as a function of the hour of the day. Thanks to these inversions, from the backscatter coefficient profiles, β, at 532 nm (355 nm in the case of Serra la Nave) and the LPDR (δ) at 532 nm (355 nm in the case of Serra la Nave and Lecce), can be retrieved the tropospheric dust layer bottom and top heights (h_{bottom} and h_{top} respectively) as well as the height of their centre of mass (h_{CM}) by applying the following criteria:

- In case of marked transitions (planetary boundary layer (PBL) – dust layer and dust layer – free troposphere (FT)), h_{bottom} is found by means of a sharp positive (negative in case of h_{top}) peak of the first derivative of β.

- If, near the top of the dust layer, β decreases very slowly with increasing height, the previous criterion is not sufficient. Thus it is necessary to smooth the profile with a 5-point sliding window in order to avoid negative values due to the noise, determining h_{top} as the height at which the smoothed backscatter is two orders of magnitude (10^{-2}) lower than the maximum backscatter in the dust layer.

- When the dust layer is coupled to the PBL, those heights are found by a sharp positive peak of the first derivative of δ.

Those heights, as well as the AOD of the dust layer at 532 and 355 nm, $\mathrm{AOD}_{532/355}^{\mathrm{MD}}$ are reported in Table 4.6.

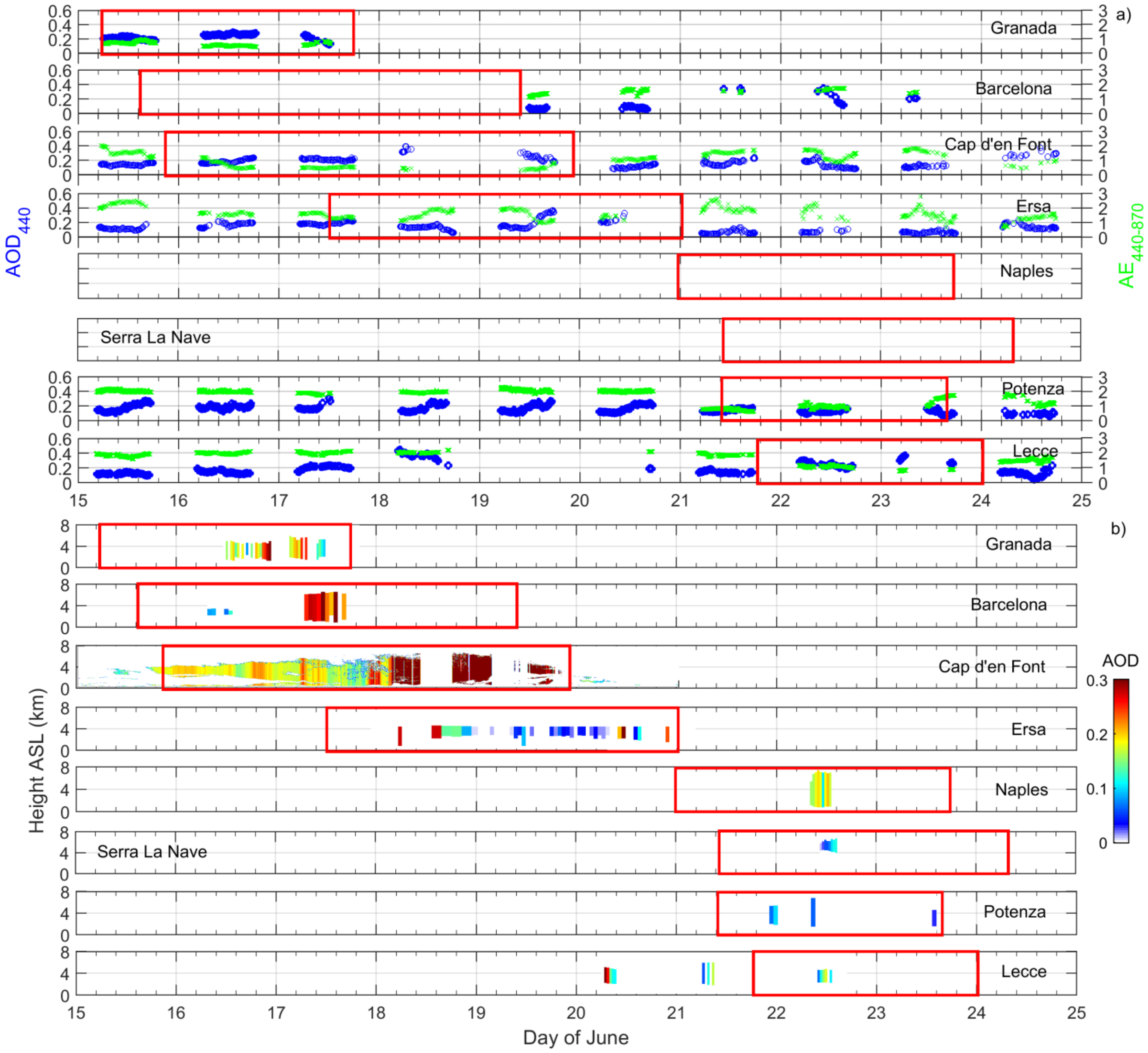

Fig. 4.11. (a) Temporal evolution of the AERONET AOD (blue circles) and AE (green crosses) in the eight stations during the 15-25 June 2013 period; the red boxes show the presence of mineral dust following the criteria explained in Sect. 4.3.2.1. (b) Mineral dust AOD at 532 and 355 nm, $\mathrm{AOD}_{532/355}^{\mathrm{MD}}$ (at 355 nm in Serra La Nave), as a function of altitude and time during June 2013. The red rectangles indicate the presence of mineral dust over the site. Black crosses indicate the centre of mass of the dust layer. There is no AERONET data in Serra La Nave and no sun-photometer instrument in Naples.

Table 4.6. Instantaneous, at the peak moment, and mean bottom, top and centre of mass (h_{bottom}, h_{top} and h_{CM} respectively) heights of the event, in each station. The thickness has been calculated by subtracting the bottom height from the top height. The mineral dust AOD at 532 and 355 nm (Cap d'en Font, Ersa and Serra La Nave only provide data at 355 nm), $\mathrm{AOD}^{\mathrm{MD}}_{532/355}$ values are the values of the optical depth retrieved from lidar measurements only in the mineral dust layer. The associated error to the mean $\mathrm{AOD}^{\mathrm{MD}}_{532/355}$ is the standard deviation.

Station	Number of profiles	h_{bottom} (km)		h_{top} (km)		h_{CM} (km)		Thickness (km)		$\mathrm{AOD}^{\mathrm{MD}}_{532/355}$	
		peak	**mean**	**peak**	**mean**	**peak**	**mean**	**peak**	**mean**	**peak**	**mean**
Granada	3	1.62	1.53±0.3	5.29	5.41±0.2	3.37	3.34±0.3	3.67	3.88±0.3	0.26	0.18±0.07
Barcelona	13	1.21	1.62±0.6	6.58	5.45±1.4	3.93	3.51±0.5	5.37	3.83±1.0	0.37	0.22±0.11
Cap d'en Font	340	0.21	0.22±0.2	5.79	5.52±0.7	3.32	3.14±0.2	5.58	5.30±0.5	0.37	0.24±0.05
Ersa	33	1.36	2.21±0.3	4.00	4.00±0.0	3.18	3.25±0.4	2.64	1.79±0.3	0.25	0.18±0.04
Potenza	4	1.63	1.74±0.2	5.53	5.52±0.9	3.01	2.89±0.6	3.90	3.78±0.6	0.10	0.07±0.03
Naples	9	1.17	0.88±0.1	7.21	6.86±0.6	3.39	3.13±0.5	6.04	5.98±0.4	0.20	0.17±0.03
Lecce	8	2.10	2.10±0.0	4.68	4.62±0.1	3.74	3.52±0.1	2.58	2.52±0.1	0.22	0.15±0.04
Serra la Nave	8	4.01	4.31±0.2	7.91	6.29±0.3	5.33	5.18±0.1	3.90	1.98±0.3	0.11	0.07±0.04

During this event, the AERONET AOD_{440} measurements range between 0.15 (Ersa, Corsica island) and 0.30 (Barcelona), indicating that the mineral dust properties are modified during the transport, this behavior points out that the coarse distribution may be lost by wet or dry deposition [Osada et al. 2014]. The maximum value of AOD measured by the lidar inside the mineral layer is 0.36 at 532 nm in Barcelona, and the mean value of the peak days is 0.20 at 532 and 0.21 at 355 nm. These values, according to previous researches [Meloni et al. 2003, 2004, 2008; Mona et al. 2012 and Papayannis et al. 2009], confirm that the event studied during the SOP-1a campaign is as a moderate dust event.

It is worth noting that in the Spanish stations (except in Barcelona where AERONET measurements were not performed during the dusty days), the coarse mode fraction, estimated by AERONET sun-photometers, reaches values of 0.56 and 0.53 on 16 and 17 June for Granada and Cap d'en Font, respectively.16 and 17 June are days with presence of mineral dust in the atmosphere, so that those coarse mode fraction values correspond to dusty days. In Ersa, the coarse mode fraction is almost half of the values found at the Spanish stations and is very constant in time, the mean value for the four dusty days is about 0.26 and the highest value found in Ersa is 0.27 on 19 June.

In Ersa, the highest values of coarse mode fraction and of AOD_{440} are found on 19 June (about 0.27). In spite of the AOD_{440} mean value is similar to the AOD_{440} mean value found in the Spanish stations (0.27, 0.38, 0.36 found in Granada, Cap d'en Font and Ersa respectively), the coarse mode fraction is half. Despite these low coarse mode fraction values, Ersa can be consider a station with presence of dust in this period because during clear days, for instance 2 and 5 June 2013, this coarse mode fraction is around 0.10, pointing out the presence of dust in the atmosphere during the period 17-20 June. The wet deposition of the coarse component during the transport of the mineral dust over the Mediterranean Sea, can be the reason of the decrease observed in the coarse mode fraction values between the Spanish stations and Ersa [Osada et al. 2014].

The Italian stations are characterized by coarse mode fraction values higher than in Ersa in the dusty days. In fact, on 21 June, the coarse mode fraction increases up to 0.5 at Potenza. During 22 June, the coarse mode fraction is similar in Potenza and Lecce, 0.39 and 0.33, respectively; on 23 June, the value increases to 0.41 at Lecce and decreases to a background conditions value (0.19) at Potenza. The higher coarse mode fraction values found at Potenza (21 and 22 June) and Lecce (22 and 23 June) with respect to the values found at Ersa is likely due to the intrusion of a second dust event, which crossed directly from Africa to southern Italy.

In the case of the SSA_{440}, the lower daily mean values are observed in Granada during 17 June (0.83) and Lecce during 22 June (0.89), while the higher values are found in Ersa on 17 and 18 June (0.99). Some previous works [Valenzuela et al. 2012; Romano et al. 2016; Sicard et al. 2016b] found that the SSA exhibits a substantial increase from 440 to 675 nm on dusty days. Accordingly, the SSA mean values in the six Sun-photometers taken into account in this Section are equal to 0.86, 0.93, 0.94, 0.95 and 0.89 at 440 nm; 0.90, 0.96, 0.96, 0.96 and 0.9 at 675 nm and 0.92, 0.97, 0.97, 0.96, 0.89 at 1020 nm in Granada, Cap d'en Font, Ersa, Potenza and Lecce respectively on dusty days. In Lecce, the SSA seems to be wavelength independent, this behavior according to Russell et al. [2010] is typical of urban/industrial or mixed aerosols.

4.3.2.3 SPATIO-TEMPORAL EVOLUTION OF THE DUST PLUME PROPERTIES

The peak moments reported in Table 4.6, are observed over Granada, Barcelona, Cap d'en Font and Ersa on 16 June at 19:30 UTC, 17 June at 14:13 UTC, 18 June at 06:00 UTC and 20 June at 22:00 UTC, respectively. The peak moments over Italian stations are observed during 22 June. In spite of the few observations available for the Italian stations (Naples, Serra La Nave, Potenza and Lecce), the distribution of the plume on 22 June can be investigated over these stations because all the profiles retrieved during that day are available.

By taking a look to the data reported in Fig. 4.11b and Table 4.6 it is clear the temporal evolution of the $\mathrm{AOD}_{532/355}^{\mathrm{MD}}$, hence it is easy to deduce how the dust plumes travel from the west to the east. $\mathrm{AOD}_{532/355}^{\mathrm{MD}}$ values are greater in the Spanish stations, at the beginning of the event, with peak day values (daily mean values) of 0.26 (0.18±0.07), 0.37 (0.22±0.11) at 532 nm and 0.37 (0.24±0.05) at 355 nm in Granada, Barcelona and Cap d'en Font respectively; than in the Italian stations, with peak day values (daily mean values) of 0.10 (0.07±0.03), 0.20 (0.17±0.03) and 0.22 (0.15±0.04) at 532 nm and 0.11 (0.07±0.04) at 355 nm for Potenza, Naples, Lecce and Serra la Nave, respectively. This point is supported by the decrease of the dust coarse fraction following a west-east gradient.

Finally, except in Barcelona, where clouds might have contaminated the aerosol profile after 12:00 UTC on 17 June, the AOD in the dust layer is quite constant with time: the standard deviations are equal or lower than 0.07. The fact that the peak moments are observed in different days in the Spanish stations but are observed in the same day in the southern Italian stations suggests the presence of a second event in the south of Italy during 22 June. Also, it is clear how the $\mathrm{AOD}_{532}^{\mathrm{MD}}$ values are greater in Naples and Lecce than in Potenza during 22 June, denoting an entry of mineral dust from the south, on its behalf, in Serra La Nave the $\mathrm{AOD}_{355}^{\mathrm{MD}}$ values increase during 22 June, as shows Fig. 4.11b, reaching the highest value in the two last measurements (0.11 at 13:46 UTC and 14:27 UTC), see Table 4.6. Note also that Naples is the first station in Italy to be reached by the dust plume and has the highest $\mathrm{AOD}_{532}^{\mathrm{MD}}$ (a peak of 0.20 at 12:21 UTC on 22 June). Potenza is only 150 km from Naples and the dust plume arrived there during 22 June but the $\mathrm{AOD}_{532}^{\mathrm{MD}}$ is lower (0.06 at 08:53 UTC); however, the dust plume arrived at Lecce a few hours after Potenza and the $\mathrm{AOD}_{532}^{\mathrm{MD}}$ increases again (0.10 at 09:46 UTC and 0.22 at 13:22 UTC). It is clear that a new moderate intrusion of Saharan dust joined to the first during the morning of 22 June.

The dust vertical distribution is also quite stable with time, although it differs from one site to another. The bottom (h_{bottom}), top (h_{top}) and centre of mass (h_{CM}) heights reported in Table 4.6 are retrieved by the lidar measurements. The vertical extension is important as in Naples and Serra La Nave the mean values of h_{top} exceed 6 km. In the case of the Spanish stations, Granada, Barcelona and Cap d'en Font; h_{top}, and h_{CM} mean values are very similar and in the three stations the centre of mass is close to the geometrical centre of the layer, pointing out that dust is well mixed in the layer. h_{bottom} mean value is clearly lower in Cap d'en Font than in Granada and Barcelona, due to the full overlap of the lidar located at Cap d'en Font is about 200 m [Totems and Chazette, 2016]. Also h_{top} is very similar among Granada, Barcelona and Cap d'en Font, pointing out that the dust plume is limited in their upper part by an stable atmospheric layer.

In general daily mean values of h_{bottom} are higher in southern Italy than in the Iberian Peninsula, and the centre of mass mean values are displaced towards h_{bottom} with respect to the geometrical centre of the layer (see Naples and Potenza in Table 4.6), because of a reload of the coarse mode fraction caused by the entry of a second event. Two very different vertical distributions between Serra La Nave, situated at 1735 m asl next (< 10 km) to the Mount Etna (3329 m high), where the dust plume is found in average between 4.31 and 6.29 km, and the other Italian stations, where the dust plume h_{bottom} mean values range between 0.88 ± 0.1 and 2.10 ± 0.0 and h_{top} mean values range between 4.62 ± 0.1 and 6.86 ± 0.6. The dust plume detected at Serra La Nave seems to be lifted because of the orography of Mount Etna. Disregarding Serra La Nave due to its proximity to Mount Etna, there is a clear evolution in the thickness of the dust layer. In the Spanish stations (Granada, Barcelona and Cap d'en Font) the mean thickness of the dust layer is greater than 4 km, decreasing at Ersa to 2 km. In the Italian stations the thickness increase again to the thickness values observed in the Spanish stations, i.e., about 6 km in Naples, 4 km at Potenza and 3 km at Lecce. This behavior is interpretable as the presence of a second event.

Fig. 4.12 shows the optical profiles of a case with high dust load at each station. As night-time measurements are available only for Granada and Potenza, the rest of the stations the measurements are inverted with the Klett-Fernald method algorithm. The LPDR is an indicator of non-spherical particles [Burton et al. 2015] and its typical value for the mineral dust is 0.3 [Tafuro et al. 2006; Mamouri et al. 2016]. This product oscillates between 0.20 and 0.27 in Granada, on its behalf, in Cap d'en Font, the backscatter coefficient suggests the presence of mineral dust between 1.2 and 5.4 km, while the LPDR only confirms (LPDR values ranging between 0.20 and 0.35) the presence of pure dust between 2.8 and 4.3 km. The structure observed in the backscatter coefficient can be identified as dust mixed with marine or continental aerosols, but the truncated LPDR profile hampers this identification. In spite of the backscatter coefficient is extremely low in Ersa, the LPDR ranges between 0.20 and 0.3 pointing out that between 2.5 and 4.5 km there is a dust plume in the atmosphere. In Potenza the LPDR values in the aerosol structure range between 0.26 and 0.33 and similar values are found in Naples between 2 and 4 km of height. In Lecce and Serra La Nave, the LPDR (at 355 nm) is quite constant around 0.26 and around 0.20, respectively. These LPDR values point out that there is mineral dust in the atmosphere but not pure, likely mixed during its transport over the Mediterranean Sea and urban areas.

Finally in Barcelona there were no depolarization capabilities implemented until 2016, but the backscatter coefficient shows clearly a structure between 1.5 and 6 km of height which can be identified as mineral dust thanks to the models (Sect. 4.2.3.1) and the AERONET data and the lidar AOD (Fig. 4.11).

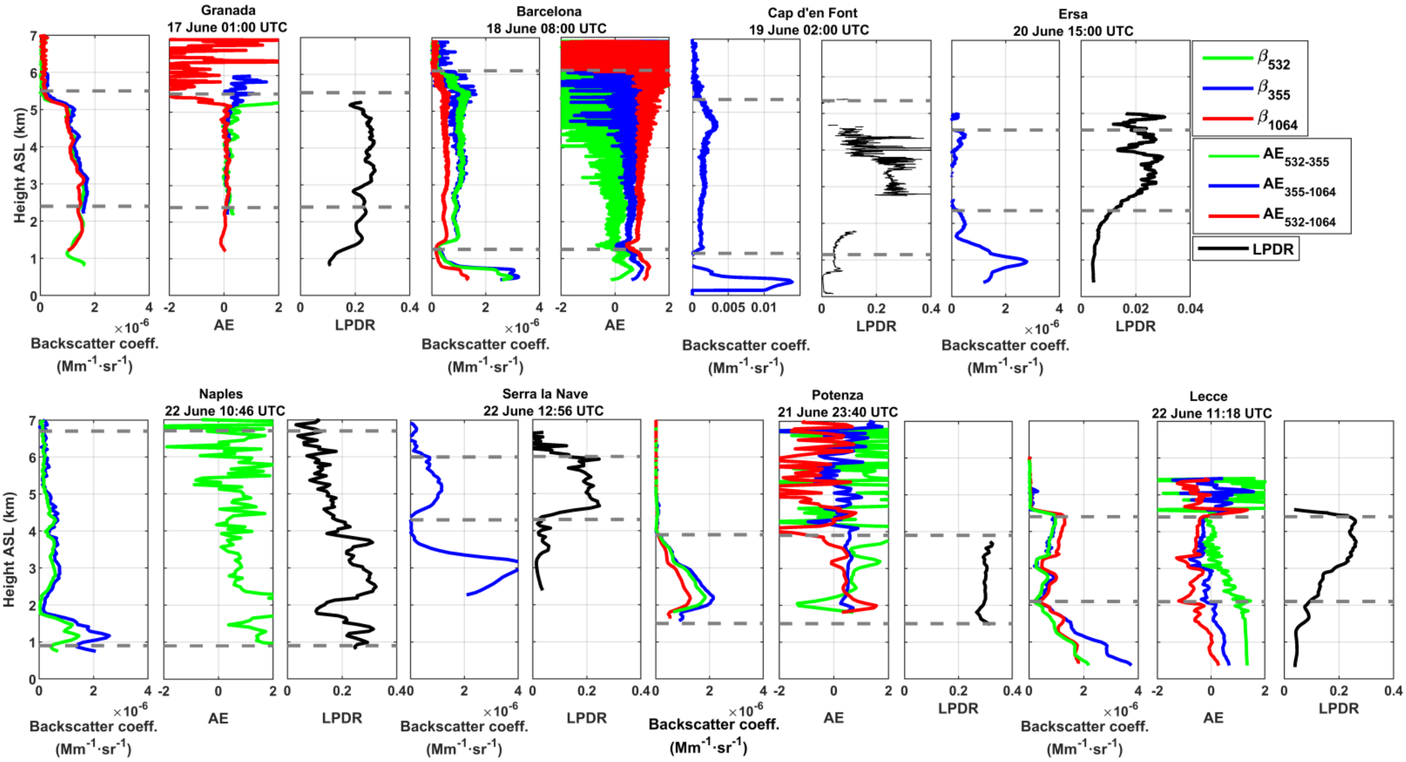

Fig. 4.12. Optical profiles at a selected time at the eight lidar stations (blue, 355 nm; green, 532 nm; red, 1064 nm): Granada on 17 June at 01:00 UTC, Barcelona on 17 June at 08:00 UTC, Cap d'en Font on 19 June at 02:00 UTC, Ersa on 20 June 15:00 UTC, Naples on 22 June at 10:46 UTC, Serra la Nave on 22 June at 12:56 UTC, Potenza on 22 June at 23:40 UTC, and Lecce on 22 June at 11:18 UTC. Backscatter coefficient, AE and LPDR stands for the backscatter coefficient, Ångström coefficients and lidar particle depolarization ratio respectively. In the AE plots, only the backscatter-related Ångström coefficients calculated between the wavelengths λ_1 and λ_2 are shown. The horizontal dashed lines indicate the dust layer bottom and top heights. No lidar ratios and no extinction-related AE are shown. The color codes shown for Granada are used in all the stations. Cap d'en Font, Ersa and Serra La Nave only have one lidar wavelength and therefore no AE can be shown in these stations. Barcelona in 2013 had no implemented depolarization capabilities.

4.3.2.4 DUST RADIATIVE EFFECT

In this section, is presented and analysis of the model-based SW and LW ARE values estimated during the Saharan dust event that affected the western and central Mediterranean Basin on June 2013. In order to estimate the SW and LW radiative fluxes with (SW- LW-F) and without (SW- LW-F^0) aerosol and to determine the ARE at the BOA and the TOA, it is used the GAME radiative transfer model, introduced in Sect. 2.3 and widely characterized in Chapter 3. Table 4.7 provides the list of the main inputs of GAME in the SW and LW spectral range. The AOD, asymmetry factor (g) and SSA from AERONET or estimated by Mie calculation used as inputs in GAME are interpolated in the whole atmospheric column, these values are used in the GAME heights where the presence of mineral dust is confirmed by the lidar systems, while in the remaining GAME heights standard values retrieved from clear-sky days are used.

Table 4.7. Summary of the data sources used to obtain the input data for GAME computations both in the SW and LW spectral ranges, including the surface parameters, profiles of meteorological variables and main gases and the aerosol parameters (aerosol extinction, SSA, and asymmetry parameter, g).

Parameters		**Shortwave GAME**	**Longwave GAME**
Spectral Range		0.3 – 4 μm	4 – 37 μm
Number of sub-bands		167	115
Meteo Parameters	at the surface	Local data	Local data
	< 20 km	Radiosounding	Radiosounding
	> 20 km	US Standard Atmosphere	US Standard Atmosphere
Main Gases Parameters	Concentration Profile	Radio soundings + US Standard Atmosphere	Radio soundings + US Standard Atmosphere
	Absorption Coefficients	HITRAN	HITRAN
Surface Parameters	Surface Albedo	Ground-based measurements	-
	LW Emissivity	-	CERES
Aerosol Parameters	AOD	Lidar extinction coefficient	Mie calculation
	SSA	AERONET	Mie calculation
	g	AERONET	Mie calculation
	Vertical Distribution	Lidar	Lidar
	Size Distribution	AERONET	AERONET
	Fine and Coarse Mode Radius	AERONET	AERONET
	Refractive Index	AERONET	Krekov (1993)

In Table 4.8 the ARE values estimated for the 12 cases with all the necessary data available are presented by means of Eqs. 2.47 and 2.48. These 12 cases are spread out in three different places: Granada, Cap d'en Font and Lecce.

Table 4.8. Instantaneous shortwave (SW) and longwave (LW) aerosol radiative effect (ARE) at the bottom and the top of the atmosphere simulated by GAME (BOA/TOA SW- LW-ARE) and retrieved from AERONET measurements (BOA/TOA SW-ARE-AER) for the 12 selected cases of June 2013. SZA stands for the solar zenith angle, which is representative of the hour of the lidar measurement.

Station	Day	SZA(°)	$\mathbf{AOD}^{\mathbf{MD}}_{532/355}$	SSA	BOA SW-ARE ($W \cdot m^{-2}$)	TOA SW-ARE ($W \cdot m^{-2}$)	BOA LW-ARE ($W \cdot m^{-2}$)	TOA LW-ARE ($W \cdot m^{-2}$)	BOA SW-ARE-AER ($W \cdot m^{-2}$)	TOA SW-ARE-AER ($W \cdot m^{-2}$)
Granada	16	67	0.26	0.87	-36.9	+5.8	+6.3	+7.0	-42.6	-11.8
	16	55	0.17	0.87	-16.9	+1.3	+5.8	+3.7	-38.3	-15.3
	17	32	0.12	0.83	-42.3	+0.7	+0.3	+0.2	-39.0	-8.2
Cap d'en Font	16	27	0.34	0.91	-45.3	-34.5	+10.8	+7.2	-17.5	-12.7
	17	27	0.37	0.91	-44.9	-29.9	+17.7	+8.5	-28.4	-19.0
	18	85	0.27	0.96	-25.3	-6.8	+1.6	+4.6	-18.1	-9.4
	19	28	0.23	0.96	-18.3	-9.2	+9.8	+8.9	-16.9	-9.6
	20	28	0.12	0.98	-3.5	-2.2	+1.9	+0.5	-17.7	-8.5
Lecce	20	30	0.13	0.94	-15.1	-5.6	+1.9	+1.6	-20.7	-9.7
	21	25	0.12	0.85	-12.0	+3.2	+1.5	+1.3	-19.7	-4.7
	22	26	0.22	0.89	-37.2	+4.3	+3.8	+2.4	-36.9	-14.8
	24	18	0.14	0.99	-7.4	-2.9	+1.3	+0.9	-14.4	-6.0

It is easy to observe that the impact of the radiative effect due to mineral dust is greater when the $\mathrm{AOD}^{\mathrm{MD}}_{532/355}$ values are high. In general, the AERONET-derived SSA is higher than 0.90 (in seven of the cases), but in five cases, the SSA values are lower than 0.90 (0.87, 0.87, 0.83, 0.85, 0.89). The latter cases correspond to the presence of mineral dust with strong absorbing properties caused by a mixing of dust with polluted aerosols [Dubovik et al. 2002b; Sicard et al. 2012, 2014; Barragan et al. 2016].

At the BOA, the SW-ARE has always a cooling effect, ranging between -3.49 and -45.3 $W \cdot m^{-2}$ and reaching -42.3 $W \cdot m^{-2}$ in Granada and -37.0 $W \cdot m^{-2}$ in Lecce, because of the presence of mineral dust in the atmosphere. Cap d 'en Font, during 16 and 17 June (classified as dusty days according to Fig. 4.10), presents the strongest cooling effect due to the aerosols, −45.3 and −44.9 $\cdot\, m^{-2}$, respectively. In this station, during 18 and 19 June, the aerosol load is decreasing (see $\mathrm{AOD}^{\mathrm{MD}}_{355}$ in Table 4.8) and, hence the cooling effect is lower (-25.3 and -18.3 $W \cdot m^{-2}$ respectively) than the previous days. Finally, the BOA SW-ARE computed on 20 June in Cap d'en Font, classify as a day free of mineral dust according to Fig. 4.10, is −3.5 $W \cdot m^{-2}$, which means a decreasing of about 92% of the cooling effect.

At the TOA, the SW-ARE has a cooling effect in seven of the cases and a heating effect in five cases, related with values of SSA lower than 0.9 (mineral dust mixed with polluted aerosols). A cooling effect (TOA SW-ARE about +8.5 $W \cdot m^{-2}$) was also found by Sicard et al. [2014] during 22 July 2009 (SZA of 21.1°) related to an AERONET SSA_{440} value about 0.83. Although, Sicard et al. [2014] found the lowest value of SSA_{440} (0.79) on 21 July 2009, day with a negative TOA SW-ARE (-22.8 $W \cdot m^{-2}$), the SZA during the lidar measurement used to estimate this negative TOA SW-ARE is 77.0°, pointing out that the positive values of TOA SW-ARE are caused by a combination of values of SSA lower than 0.90 and low values of SZA (lidar measurements performed during the central hours of the day). Besides, studies like Seinfeld and Pandis [1998] suggest that the heating effect at TOA in the SW might be due to the aerosol backscatter fraction, which increases with the SZA, on their behalf, Liao and Seinfeld [1998] found for a uniform aerosol layer (from the Earth's surface to 5 km) made of pure ammonium sulphate, pure soot, internal mixture and external mixture, positive TOA SW-ARE at SZA equal to 0°, being the internal and external mixtures also responsible of the positive TOA SW-ARE.

In Table 4.8 are shown also the ARE values from AERONET retrievals, TOA/BOA SW-ARE-AER. These AREs, at the TOA, ranges between −6.0 (Lecce) and −19.0 (Cap d'en Font), therefore, showing a cooling effect in all the cases, and in general the cooling effect is greater than the effect of the AREs estimated by GAME. This behavior can be explained because the AREs estimated by GAME are estimated only in the dust layer while the AERONET AREs are estimated for the total atmospheric column. At the BOA, the AERONET AREs ranges between −14.4 (Lecce) and −42.6 (Granada), again all the cases present a cooling effect. At the BOA, as at the TOA the SW-AREs are in general lower than the AERONET AREs, this situation can be explained again because the AERONET AREs are estimated taking into account the whole atmospheric column.

The temporal evolution of the BOA SW-ARE in Lecce is worth to comment separately. This station is affected by the mineral dust outbreak on 21, 22 and 23 June and presents a lower mean value of $\mathrm{AOD}_{532}^{\mathrm{MD}}$ (0.15±0.04) than the mean values found in Granada (0.18±0.07) and Cap d'en Font (0.24±0.05). These data lead to cooling effects lower (in absolute terms) than the previous sites, except for the 22 June when the SW-ARE value at the BOA is similar (−37.2 $W \cdot m^{-2}$) to the values found in Granada and Cap d'en Font. This cooling effect may be due to the increase of the $\mathrm{AOD}_{532}^{\mathrm{MD}}$ in two times in Lecce, compared to the previous days in this Italian station. This result supports the theory of a new mineral dust outbreak which reaches south Italy directly from Africa.

The BOA LW-ARE (Table 4.8) has always a heating effect and varies between +0.3 $W \cdot m^{-2}$ (Granada) and +17.7 $W \cdot m^{-2}$ (Cap d'en Font), being these results consistent with the AREs estimated by Sicard et al. [2014]. In cases with low values of $\mathrm{AOD}_{532/355}^{\mathrm{MD}}$, the LW-ARE values is near to zero; for example, in Lecce the 21 June the $\mathrm{AOD}_{532}^{\mathrm{MD}}$, the BOA and the TOA LW-ARE found are 0.12, +1.5 and +1.3 $W \cdot m^{-2}$ respectively while during 22 June, in the same station, the values found are 0.22, +3.8 and +2.4 $W \cdot m^{-2}$. An increase of 45.5% in the $\mathrm{AOD}_{532/355}^{\mathrm{MD}}$ cause an increase of about 60.5% and 45.8% in the BOA and TOA LW-AREs, hence, it is clear the relationship between the presence of mineral dust in the atmosphere and the increase of the heating effect in the LW spectral region.

4.3.2.5 MULTI-INTRUSION ASPECT OF THE SAHARAN DUST EVENT

Fig. 4.13 shows the back-trajectories calculated each 72 hours with the Hybrid Single Particle Lagrangian Integrated Trajectory (HYSPLIT) model [Stein et al. 2015] operated by the National Oceanic and Atmospheric Administration – Air Resources Laboratory (NOAA-ARL), using the 1-° Global Data Assimilation System (GDAS) archives. The heights selected at the beginning of the back-trajectories correspond to the heights of the aerosol layers detected by the lidars (see Fig. 4.12 and Table 4.6) The back-trajectories that arrive in Granada (Fig. 4.13a1) and in Barcelona (4.13a2) present the origin of the dust in North Morocco and Algeria, concretely the back-trajectories that arrive in Granada at 2.5 km and in Barcelona at 4.4 km are similar and their origin is clearly located at northern Sahara in Algeria.

Fig. 4.13b shows the origin of the dust which affected Cap d'en Font in the 4 days with presence of mineral dust (see Sect. 4.3.2.1). Concretely, Fig. 4.13b1 shows that the back-trajectory that reaches Cap d'en Font on 16 June at 1.5 km crosses the Iberian Peninsula, while the back-trajectory that reaches the insular station at 4.5 km has its origin in North Algeria. Fig. 4.13b2 shows the same origin of the dust on 17 June as for Granada and Barcelona at the three heights: North Morocco and Algeria, thus, the dust plume has previously travelled over the Iberian Peninsula before arriving Cap d'en Font. Fig. 4.13b3 shows that the origin of the dust on 18 June is Algeria at all the heights. The spatial evolution of the dust plume, from the West to the East, became evident in these back trajectories. Fig. 4.13b4 shows that for the 19 June, the origin for the higher back trajectories is North Africa again, but at low heights, the air masses are coming from the Iberian Peninsula, therefore there is only pure dust above 1.5 km, as shows the values of LPDR at 355 nm in Fig. 4.12.

Fig. 4.13c shows the back-trajectory for the 19 June at 12:00 UTC, the same day and the same hour as Fig. 4.13b4 but in the station of Ersa. The origin of the air masses reaching Ersa above 3 km is located in North

Algeria, same origin as Fig. 4.13b4, and the origin of the lower air masses is located in Tunisia, that explains the behavior of the back trajectory shown in Fig. 4.13b4; the strong component of the Saharan dust event is entering in the area of Ersa during 19 June (see Fig. 4.10).

In Fig. 4.13d1 are represented the back-trajectories calculated for Naples on 22 June at 09:00 UTC, these back-trajectories come from the West–Southwest, similar to that in Granada and Barcelona. Fig. 4.13d1 indicates a dust origin from northern Sahara for the dust arriving in Naples, the comparison of those trajectories with the MSG/SEVIRI AOD (Fig. 4.10) suggests that the dust plume arriving in Naples comes directly from the source region without traveling over the Mediterranean, it is therefore extremely unlikely that the dust plume arriving in Naples might have previously travelled over the Iberian Peninsula. The back-trajectories calculated for Serra La Nave (Fig. 4.13d2) have two different origins, North Algeria (above 5 km) and Northwestern Libya, suggesting that at 09:00 UTC (Fig. 4.13d1) the second event haven't reach South Italy yet, but this secondary dust plume, which source region is Northwestern Libya and travels over Tunisia, is arriving in South Italy during 22 June below 5 km. Finally, the back-trajectories between 1.6 and 3.6 km in Potenza and Lecce (Figs. 4.13d3 and 4.13d4 respectively), originate mostly in the northern part of the Sahara situated at South Tunisia, and Northwestern Libya; are different to the ones observed in Serra La Nave above 5 km and similar to the back-trajectory calculated in Serra La Nave at 3.6 km. Hence, this analysis shows that the first intrusion detected first over the Iberian Peninsula has its origin in northern Sahara in Algeria and that the second intrusion detected only in south Italy finds its origin in the Saharan region situated at the corner of south Tunisia, and northwestern Libya.

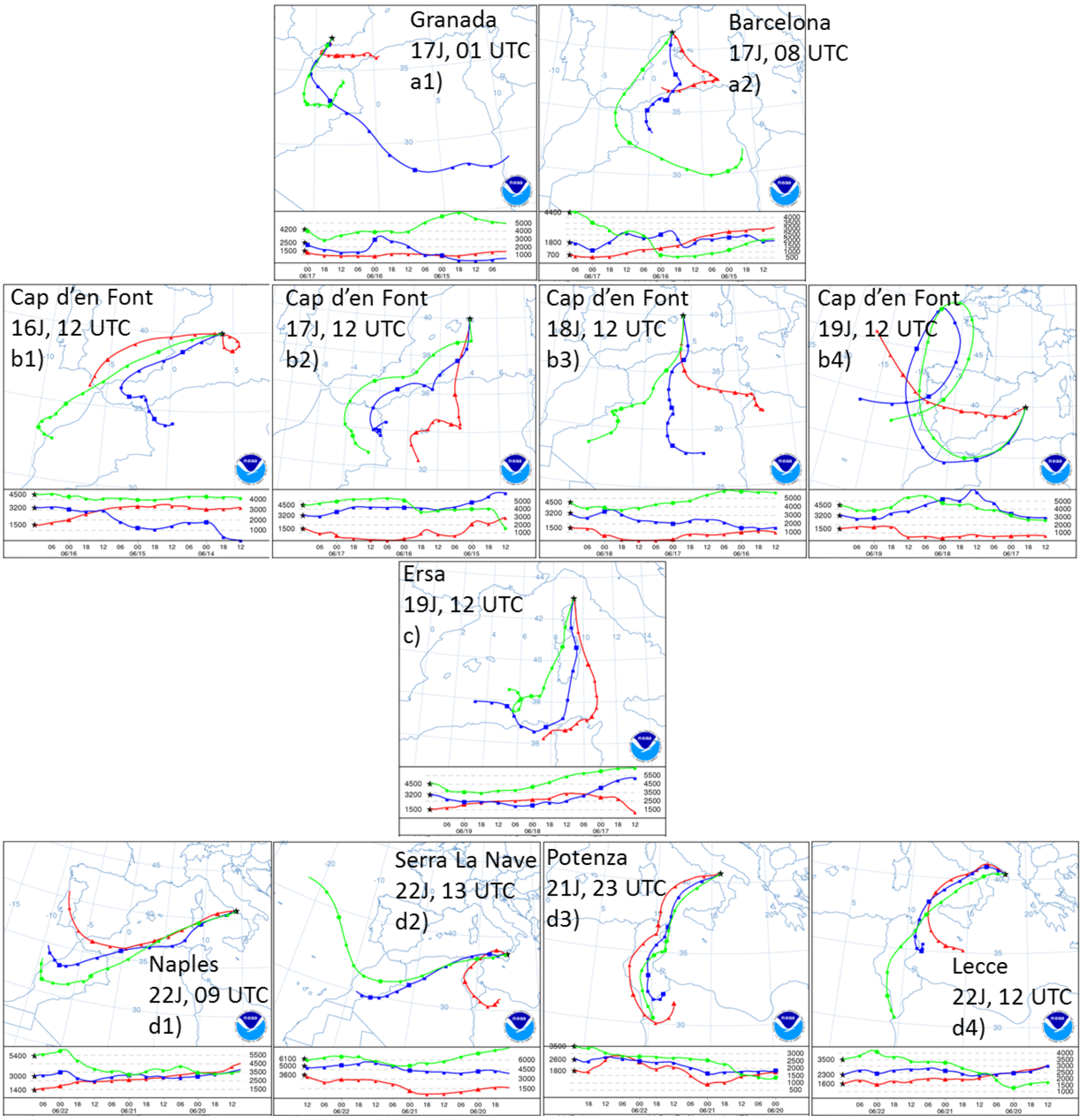

Fig. 4.13. Back trajectories simulated with HYSPLIT model. The green lines correspond to the top height of the dust layer, the red lines with the bottom height and the blue lines with the middle of the dust layer in each station calculated by the lidar measurements. The (a) back-trajectories are the back-trajectories for the Spanish peninsular stations. (b) back-trajectories are back trajectories for Cap d'en Font. (c) back-trajectories correspond with the back-trajectory computed for Ersa. (d) back-trajectories are the back-trajectories simulated for the Italian stations.

Fig. 4.14a shows the quicklook of attenuated backscatter at 532 nm from the LNG lidar on board the F20 aircraft on 22 June between approximately 10:30 and 13:00 UTC. The stations of Serra la Nave, Lecce and Naples are marked in white in the figure, the red areas correspond to mineral dust presence and the yellow areas correspond to clouds.

The flight track is shown in Fig. 4.14b and the Cloud-Aerosol Lidar and Infrared Pathfinder Satellite Observation (CALIPSO) overpass track during the previous night, i.e. on 22 June around 01:00 UTC in Fig. 4.14c. From almost the beginning of the flight until the latitude of Serra La Nave, a dust layer is clearly visible between 4 and 6.5 km. Indeed in Serra La Nave a unique layer is detected at 11:19 UTC between 4.5 and 6.5 km (reported in Figure 4.14a with horizontal white ticks). It appears that this layer is associated with the second intrusion previously mentioned. Over southern Italy, a dust layer is observed from the ground up to approximately 4 km and then up to 5–6 km. This behavior matches with the local observations performed in Lecce at 11:18 UTC (despite the distance between Lecce and the flight track, approximately 100 km), where the dust plume is detected between 2.1 and 4.4 km ($\mathrm{AOD}_{532}^{\mathrm{MD}}$ about 0.22 and LPDR at 355nm around 0.26), and the observations performed in Naples at 10:46 UTC, where the dust plume is detected between 0.9 and 6.8 km ($\mathrm{AOD}_{532}^{\mathrm{MD}}$ about 0.19 and LPDR at 532nm ranging between 0.20–0.35). No measurement is available in Potenza.

It is quite probable that the dust plume observed in Naples is only associated with the first intrusion, whereas in Lecce the plume from both intrusions may be present. Between 3.3 and 4.5 km (Fig. 4.12), the LPDR at 355 nm measured in Lecce, is about 0.26, whereas the LPDR at Serra La Nave (Fig. 4.12) between 4.4 and 6 km, is constant (around 0.20) during the whole day. This LPDR, which is higher in Lecce than in Serra La Nave, indicates that the dust of the second intrusion which reached Lecce, is mixed with dust from different origins and most probably with dust from the first intrusion. The overpass track, shown in Fig. 4.14b, passes east of Potenza and Serra La Nave, where the measurements closest in time are at 23:40 UTC and at 10:48 UTC (on 21 June), respectively.

The height of the dust layers detected at both stations is reported on the quicklook of the LPDR at 532 nm measured by the Cloud- Aerosol Lidar with Orthogonal Polarization (CALIOP) lidar on board CALIPSO and reported on Fig. 4.14c. it is clear the presence of an homogeneous depolarizing plume with a large horizontal distribution extending from Africa to central Europe. Over the Mediterranean Sea and the African continent the thickness of this plume is about 1–1.5 km, high, with an altitude greater than 2.5 km, it is worth noting also that the plume is not connected to the ground. This result suggests that this plume is already advected and finds its origin probably in a region west of the satellite track according to the horizontal transport seen in Fig. 4.10. It is the same plume observed by the LNG lidar at the south of Sicily (Fig. 4.14a).

The height of the dust plume detected in Potenza at 23:40 UTC on 21 June is reported on the CALIOP quicklook (Fig. 4.14c) by small horizontal white ticks: while the dust layer is reported between 1.6 and 3.9 km ($\mathrm{AOD}_{532}^{\mathrm{MD}}$ about 0.10 and LPDR at 532 nm ranging between 0.26 and 0.33) in Fig. 4.12, the layer is detected by CALIPSO between 1.8 and 5.4 km, this difference between the top heights of the dust layer is due to the distance (around 80 km) between Potenza and the satellite track, being the agreement with the depolarizing layer observed by CALIOP quite good. In the measurement performed at Serra la Nave at 10:48 UTC, the dust layer is detected between 4.4 and 5.9 km ($\mathrm{AOD}_{355}^{\mathrm{MD}}$ about 0.01 and LPDR at 355 nm around 0.2), which indicates either that the lofted plume has been advected during the night and the morning, or that the flanks of Mount Etna, close to which the Serra La Nave station is installed, act as a ramp for the air masses travelling northwards (Serra La Nave is situated upwind of Mount Etna with respect to the second intrusion). The dust plume LPDR at 532 nm from the CALIOP quicklook is rather homogeneous and ranges between 0.10 and 0.30, but it does not allow distinguishing the different dust plumes of the scene. Further analysis with higher-level products of CALIOP and possibly spatial integration will hopefully help distinguish both types of mineral dust observed by the ground-based lidar stations.

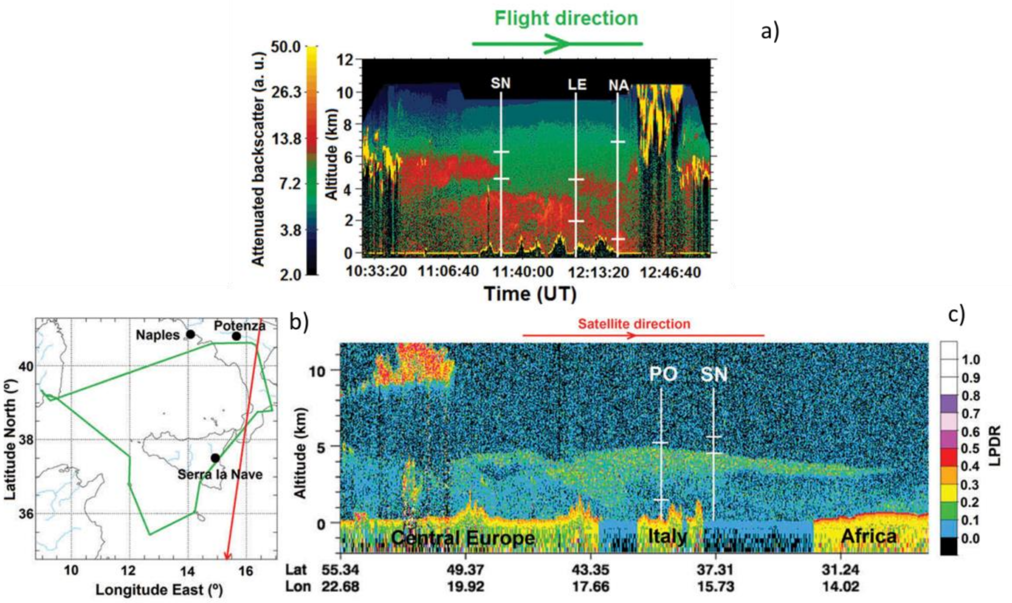

Fig. 4.14. (a) LNG quicklook of the attenuated backscatter coefficient at 532 nm (in arbitrary units) on 22 June between 10:30 and 13:00 UTC. The horizontal white bars indicate the height of the dust plume detected at the EARLINET stations and coincident in time. The position of the airborne lidar was approximately 10 km east of Serra la Nave, 100 km west of Lecce, and 40 km southwest of Naples. (b) Trajectory of the F20 aircraft on 22 June between 10:30 and 13:00 UTC (green) and of the CALIPSO overpass on 22 June around 01 UTC (red); (c) CALIOP quicklook of the particle depolarization ratio at 532 nm. The horizontal white bars indicate the height of the dust plume detected at Potenza (on 21 June at 23:40 UTC) and Serra La Nave (on 22 June at 10:48 UTC). Adapted from Sicard et al. [2016a].

4.4 SUMMARY AND CONCLUSIONS

A N–S increasing gradient exists in the WMB for the aerosol amount (AOD) and especially its coarse-mode volume concentration (0.028 vs. 0.039 $\mu m^3 \cdot \mu m^{-2}$), pointing out that on average larger particles are found at Palma (vs. Ersa), which suggests that African dust is the main driver of these properties on a yearly basis. The moderate event observed by EARLINET stations during the SOP-1a, which swept almost completely the WMB from the West to the East (Fig. 4.10), presents different effects and characteristics depending on the day and the latitude and shows a SW-NE decreasing gradient caused by the transport of the mineral dust over the WMB. Inter-season and inter-site variations have been also observed in most of the aerosol properties. Higher AOD$_{440}$ values are observed at Ersa in spring and at Palma in summer and reflect a contribution of aerosols of continental origin in spring over Ersa and not before summer over Palma and a higher frequency of mineral dust outbreaks at Palma in summer (Fig. 4.3). The mineral dust cases are associated with higher AAOD and AAE (0.029 <AAOD$_{440}$ < 0.061 and 1.28 <AAE< 2.67) and lower SSA (0.89 < SSA$_{440}$ < 0.94) than pollution (AAOD$_{440}$ < 0.02, 1.09 <AAE< 1.28 and 0.97 < SSA$_{440}$ < 0.98) and present larger inter-season and inter-site variations, while g shows very little inter-season and inter-site variations: g_{440} ranges within 0.71–0.73 for mineral dust with no spectral dependency and within 0.69–0.70 for pollution with a general tendency to decrease with increasing wavelengths.

The aerosol fine mode is rather homogeneously distributed, except in spring, when the presence of aerosols of continental origin over Ersa contributes to increase AOD$^{f}{}_{440}$, suggesting a homogeneous spatial distribution of the fine loads in the WMB. Absorption properties, focusing on pollution and mineral dust, are quite variable because of the many and different sources of anthropogenic particles in and around the WMB, except in summer at Palma, where the total and the mineral dust seasonal means are nearly equal (mineral dust represents 76% of the total of high aerosol load events) and the seasonal averaged absorption properties of the total present the signature of a combination of pollution and mineral dust. As a result, the FE, more dependent on absorption than the ARE, has no marked gradient, while the ARE present the same gradient as the coarse mode. The ARE at the surface filtered for 50<SZA<60^o reaches its maximum (in absolute value) during spring at Ersa (-18.0 $W \cdot m^{-2}$) and summer at Palma (-22.8 $W \cdot m^{-2}$). In spring at the BOA, the cooling effect (negative AREs) is almost double at Ersa with respect to Palma, being spring the season of the beginning of pollution episodes and of the peak of mineral dust events at Ersa (Fig. 4.8). At the TOA no clear gradient is observed for both quantities, due to the large variability of the absorption properties, especially for mineral dust, supporting the hypothesis of an anthropogenic influence as already formulated by Valenzuela et al. [2015]. The comparison between the three sites shows an increasing number of events with large AOD and with larger particles from north to south during this period (Fig. 4.9).

Focusing on the mineral dust event detected during June 2013, it is worth noting that the dust particles reached higher altitudes in the Italian stations, than in the Spanish stations, due to the loss of coarse mode particles during the transport of the mineral dust plume. The AOD measured during the event is greater in the Spanish stations than in the Italian stations, however, during 22 June is observed an increase of the AOD in Naples and Lecce, as well as the coarse mode fraction, denoting the entry of a second Saharan dust event (Table 4.8). This hypothesis is confirmed by a detailed analysis made by means of back-trajectories, CALIPSO and airborne lidar observations collected during the investigated period in the study area (Figs. 4.13 and 4.14).

It is observed also, a SW-NE gradient in products as $AE_{440\text{-}870}$, AOD_{440}, coarse mode fraction and the estimated AREs. For the 18 cases studied, negative values (cooling effect) of BOA SW-ARE are found, ranging between -7 and -45.3 $W \cdot m^{-2}$ in Lecce on 24 June (clear sky day) and Cap d'en Font on 16 June (dusty day) respectively. The LW-AREs at the BOA are always positive (heating effect) with a maximum value of +17.7 $W \cdot m^{-2}$ on 17 June in Cap d'en Font, might be due to the high AOD measured that day (0.37). In general the SW and LW-AREs modelled at the BOA are in agreement with the values found in the literature. However, five cases present positive TOA SW-AREs, associated to low values of SSA (< 0.90) and SZA (Table 4.8). The low values of SSA found in these five cases, may be are associated to mineral dust mixed with anthropogenic particles, that increase the light absorbing properties of the aerosol particles. Finally, the TOA LW-AREs are always in agreement with the literature.

By comparing the radiation budget at Granada on 16 June (−36.9 (BOA SW), +6.3 (BOA LW), +5.8 (TOA SW) and +7.0 $W \cdot m^{-2}$ (TOA LW)), a dusty day, with the radiation budget at Lecce on 22 June (−37 (BOA SW), +3.8 (BOA LW), +4.3 (TOA SW) and 2.4 $W \cdot m^{-2}$ (TOA LW)), when the second event hits the Italian station, the AREs obtained are similar in both stations in spite of the SW-NE gradient, pointing out a mineral dust reload caused by the second event. Before the second event, the SW-NE gradient observed in the AREs is directly related with the gradient observed in the coarse mode fraction.

CHAPTER 5

Ceilometer-Based Rainfall Rate Estimation

Attenuated backscatter measurements from a Vaisala CL31 ceilometer and a modified form of the well-known slope-method are used to derive ceilometer extinction profiles during rain events. Rain rate (RR) estimates from collocated S-band radar and portable disdrometer are used to derive RR-to-extinction correlation models for the ceilometer-radar and ceilometer-disdrometer combinations. The data were collected during an intensive observation period of the Verification of the Origins of Rotation in Tornadoes Experiment Southeast (VORTEX-SE) conducted in northern Alabama. These models are used to estimate the RR from the ceilometer observations in similar situations that do not have a collocated radar or the disdrometer. Such correlation models are, however, limited by the different temporal and spatial resolutions of the measured variables, measurement capabilities of the instruments, and the inherent assumption of a homogenous atmosphere. An empirical method based on extinction- and RR-uncertainty scoring and covariance fitting are proposed to solve, in part, these limitations.

The contents of this Chapter are part of the paper [Rocadenbosch et al, 2018] submitted to IEEE Transac. Geosc. Rem. Sensing. Systematic or multiple reproduction or distribution to multiple locations via electronic or other means is prohibited and is subject to penalties under law.

5.1 INTRODUCTION

The first Verification of the Origins of Rotation in Tornadoes EXperiment-Southeast (VORTEX-SE, http://www.nssl.noaa.gov/projects/vortexse/) field campaign took place during March and April 2016 around Belle Mina, Alabama (34.6902°N, -86.8845°E) [Rasmussen and Koch, 2016] . The University of Massachusetts Microwave Remote Sensing Laboratory (UMASS MIRSL) and Purdue University deployed a mobile S-band FMCW radar operating at 2.94 GHz, a near-infrared Vaisala CL-31 lidar ceilometer, and a OTT Parsivel^2 disdrometer with the aim to study the spatial and temporal evolution of liquid water clouds (LWC) and moderate rain events during two months of continuous measurements [Tanamachi et al., 2016]. Also, the NOAA National Severe Storms Laboratory deployed a Doppler lidar nearby as part of their CLAMPS atmospheric profiling system [Wagner et al., 2019]. A key parameter in precipitation studies is the rainfall rate (RR), which is defined as the depth of accumulated liquid precipitation per unit time. The RR is mostly influenced by the drop size distribution (DSD) [e.g., Marshall and Palmer, 1948; Telford, 1955; Komabayasi et al., 1964; Ulbrich and Atlas, 1984; Williams and Gage, 2009], which encodes the growth, diameter and lifetime of raindrops besides how quickly they evaporate below cloud base and the rate at that raindrops settle in different atmospheric layers [Doviak and Zrnić, 2006; Westbrook et al., 2010]. Another important factor that influences the RR is the median drop diameter, directly related to the shape of the drops and the processes of coalescence and breakup [Pruppacher and Pitter, 1971].

To monitor LWC and to study the variability of rain, disdrometer and radars have been successfully used [Rogers, 1984; Krajewski and Smith, 2002; Nikolopoulos et al., 2008]. However, disdrometers cannot provide, in a direct way, information about the vertical characteristics of the rain and measurements can be skewed in situations with exceptionally small raindrops (less than 1 mm diameter) during intervals with a small number of raindrops [Krajewski et al., 2006]. On their behalf, vertically pointing S-band radars have difficulty providing reliable information of the vertical distribution of rain close to ground level because of near-field and/or parallax effects. These gaps can be filled by using mono-axial ceilometers thanks to the low height of the laser-telescope cross-over function (typically below 100 m) [Kotthaus et al., 2016], which allows profiling very close to the surface, and to the good SNR that ceilometers present during light rain events. As with any active profiing system, the ceilometer return signal is affected by the number and type of raindrops and the extinction between the scatterer and the receiver.

In order to correlate RR and atmospheric optical extinction (*RR-to-extinction* models; hereafter, *RR*-α models) retrieved form fixed-orientation ceilometer signals, must be kept in mind that droplets maintan symmetry in the fall direction [Rensch and Long, 1970; Vasseur and Gibbins, 1996]. Otherwise, geometric optics calculations of light scattering by non-spherical raindrops reveal a strong dependence on the phase matrix that invalidate ceilometer measurements [Kokhanovsky and Macke, 1997; Macke and Großklaus, 1998]. Besides it is worth noting the importance of the fixed-orientation, since rain extinction coefficients vary strongly depending on the laser beam zenith angle [Roy and Bissonnette, 2001].

A first approach to the study of the small-scale spatial and temporal evolution of precipitation over a sampling area (1-2 km measurement line) by means of laser signals is the one made by Lewandowski et al. [2009]. In this research it is used a 25 mJ energy, 50 Hz repetition rate, 1064 nm wavelength, 25 m aperture lidar in horizontal configuration to retrieve the optical extinction and correlate, then, this optical extinction with the RR measured by a collocated disdrometer (*RR*-α model), assuming a Marshall-Palmer (MP) drop-size distribution and neglecting the molecular (Rayleigh) and aerosol (Mie) background extinction contributions.

The main goal of this Chapter is to provide a complementary study to the one made by Lewandowski et al. [2009]. For that purpose, in Sect. 5.2 are presented the instrumentation used and the data retrieval methods, besides, pre-processing methods. In Sect. 5.3 are presented the results concerning to the 29-30 April case pursuing two main goals: (i) to study the inherent intercomparison uncertainty among data retrieved by the three different instruments and (ii) to derive the RR-α dependence for the ceilometer-radar and ceilometer-disdrometer combinations upon an appropriate fitting procedure. Finally Sect. 5.4 summarizes the results of the 31 March case and presents two main goals: (i) to verificate the methodology followed in Sects. 5.2 and 5.3 and (ii) to demonstrate the feasibility of using a vertically-pointed ceilometer under low-to-moderate rain-rate measurements (0.5-9 $mm \cdot h^{-1}$) to measure RR.

This Chapter is organized as follows: Sect. 5.2 describes the instrumentation, pre-processing techniques used and the radar and ceilometer data retrieval procedures. Sect. 5.3 formulates the error treatment associated to the RR and rain-extinction estimates and presents the *RR*-α models for the 29-30 April case. Sect. 5.4 describes the model verification performed by means of the 31 March rain event. And finally Sect. 5.5 gives concluding remarks.

5.2 RAIN EVENT AND DATA RETRIEVAL

5.2.1 INSTRUMENTS AND DATA

In the framework of the VORTEX-SE field campaign, carried out in the northern Alabama region from 1 March to 8 May 2016, the instruments summarized in Table 5.1 were deployed in Belle Mina, AL (34.69N, 86.88W) [Rasmussen and Koch, 2016]. The ceilometer and the S-band radar were collocated in a truck and the portable disdrometer [Dawson et al., 2016] was collocated with these instruments from April 27, 2016 to May 1, 2016 only. The Doppler lidar was installed approximately 100 m to the west of the radar/ceilometer setup.

The Vaisala CL-31 lidar ceilometer is widely described in Kotthaus et al. [2016], but it is worth mentioning that this instrument presents a starting range of full overlap of about 70 m. The ceilometer gives the profile of the attenuated atmospheric backscatter; however, as it lacks absolute calibration [O'Connor et al., 2004], here it is simply referred to as the "range-corrected lidar signal". The CL-31 presents also one more issue: the atmospheric molecular return (Rayleigh) cannot be measured as it falls below the ceilometer noise level

[Kotthaus et al. 2016], hampering the use of the Klett-Fernald method [Fernald et al., 1972; Fernald, 1984; Klett, 1981; 1985].

Because the radar observation volume is larger than that of the ceilometer, the S-band FMCW radar, described in İnce et al. [2003], was collocated with the ceilometer in the same vehicle and vertically aligned, so as to provide information representative of the same vertical column of the atmosphere.These instruments instrument operated continuously during the VORTEX-SE campaign providing vertical atmospheric profiles. This type of radars, S-band, can detect both precipitation and clear-air echo [Gossard, 1990; Ralph 1995], thereby enabling studies of both precipitation and the evolution of the atmospheric boundary layer. The one used here uses separate parabolic antennas (2.4 m diameter), each with 34 dB gain, for transmission and reception, that results in a reduction in reflectivity which does not reach 0 dB until about 300 m in height (i.e., measurements made in the lowest 300 m are not well-calibrated). This radar provides vertical profiles of the reflectivity factor (from the measured volume spectral reflectivity), vertical velocity, and spectrum width at 5 m vertical resolution (Table 5.1). In the case of low RR intervals radar data can be noise corrupted so that a RR threshold must be set (0.2 – 0.5 $mm \cdot h^{-1}$), below this threshold the RRs are not considered reliable [Martner et al., 2008; Lin and Hou 2012].

Table 5.1. Main specs of the instruments deployed in VORTEX-SE campaign, 2016. FOV stands for Field Of View (angle is full width), HPBW stands for Half Power Band-Width, CNR stands for Carrier-to-Noise Ratio.

Instrument	Wavelength	Pointing	Measured parameter	Raw spatial resol.	Raw temporal resol.	References
Ceilometer	910 nm	Vertical (0.1 deg FOV)	Attenuated backs. (uncal.)	10 m	16 s	[Kotthaus et al., 2016]
S-band Radar	10 cm	Vertical (3 deg HPBW)	Volume reflectivity (m^{-1})	5 m	1 s	[İnce et al., 2003]
Disdrometer	780 nm	Horizontal In-Situ	Rainfall rate ($mm \cdot h^{-1}$)	54 cm^2	10 s	[Tokay et al., 2014]
Doppler lidar	1540 nm	Vertical	Vertical velocity ($m \cdot s^{-1}$) and CNR (dB)	100 m	1 s	[Leosphere, 2017]

The OTT Parsivel^2 Disdrometer [OTT Messtechnik, 2004; Tokay et al., 2014] developed by Purdue University and the U.S. National Severe Storms Laboratory [Dawson et al. 2016], is part of the Portable In situ Precipitation Station (PIPS). The disdrometer is an in-situ, ground-based, 1D optical instrument which provides precipitation size data by means of an infrared laser which illuminates a linear array of photodiodes (measurement area). When the precipitation particles cross the measurement area, they cause variations to the photodiodes signals. These variations depend on the diameter of the particles and their fall velocity, causing an inferred DSD from which the RR is derived.

Finally, the Leosphere Windcube 100S [Leosphere, 2017], used to confirm the presence of rain, is a conically scanning Doppler lidar that operates at 1.54 μm, combined with the VAD (Vertical Azimuth Display) algorithm [Browning and Wexler, 1968] can perform 3D-wind measurements up to typically 3 km in height (100 m resolution, 1 s accumulation time).

Among the 54 days of observation during VORTEX-SE, only two days fulfill the need of a time-continuous rain courtain (over 2 hours), March 31 and April 29-30 (overnight), being the latter the most useful to study because during that day, the disdrometer was collocated with the radar and the ceilometer. Fig. 5.1 shows an overview of the April 29-30, 2016 rain event (22:00 UTC – 02:00 UTC) and qualitatively shows that the rain event is stronger at the middle of the period (23:00 UTC - 00:30 UTC), getting weaker with time, ending at 01:15 UTC. Furthermore, the melting zone can be appreciated at 3 km of height; hence, to avoid this melting zone, the analysis of data is restricted to below 3 km.

Before start the analysis of the data it is necessary first, because of the different raw temporal resolutions among the radar, the ceilometer and the disdrometer (Table 5.1); to resample the measurement time series from the instruments to a common master-time resolution, $\Delta T_{master} = 16$ s. Then, before deriving the extinction coefficient (Sect. 5.2.3), the ceilometer attenuated backscatter profiles are averaged to a new temporal resolution, $\Delta T_{clean}^{ceilo} = 80\ \text{s}$ (hereafter, the smoothed temporal resolution or time bin, ΔT) and smoothed to a new spatial resolution, $\Delta R_{clean}^{ceilo} = 200\ \text{m}$. Besides, a low-pass Finite Impulse Response (FIR) digital filter (order = 50, cut-off frequency = 0.1 (Nyquist-normalised)) is applied to the ceilometer raw profiles. The filter uses a Hamming-window based design to achieve high noise-rejection and linear phase [Proakis and Manolakis, 2007]. Thanks to these processes, the mean SNRs found at the starting and end ranges heights (R_1 and R_2, respectively) of the slope-method processing interval (see Sect. 5.2.3) are above 19 and 14 dB, respectively, in rainy conditions and above 18 dB, in clear conditions. These SNR values ensure a virtually noiseless log-range-corrected signal, $U(R)$, over the whole processing range [Rocadenbosch et al., 1998]. The noise variance has been estimated according to the procedure described in [Reba et al. 2007]. In what follows, the temporal resolution of the retrieval products (RR and rain-extinction coefficient) is one time bin (80 s).

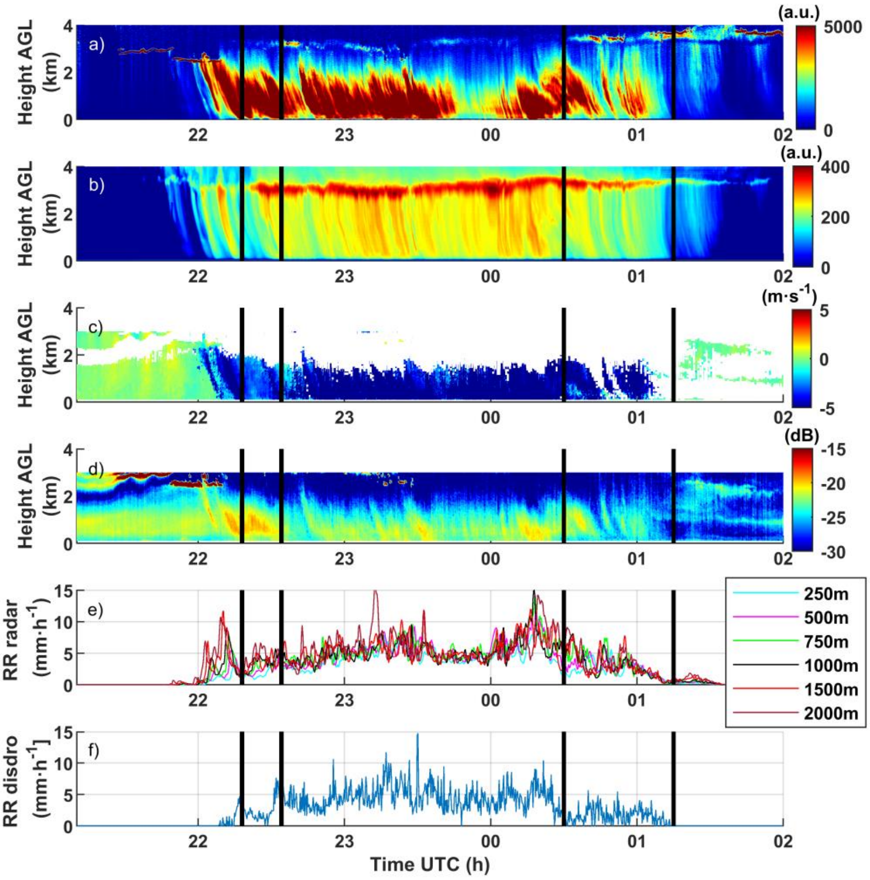

Fig. 5.1. Overview of April 29-30, 2016 rain episode. (a) Ceilometer range-corrected lidar signal (arbitrary units, (a.u.)) versus time. (b) Radar reflectivity factor (dBZ) computed after Eq. 5.11. (c) Doppler lidar vertical velocity ($m \cdot s^{-1}$). (d) Doppler lidar CNR (dB). (e) RR ($mm \cdot h^{-1}$) time series measured by the radar at different heights, from 250 m up to 2000 m. (f) RR ($mm \cdot h^{-1}$) time series measured by the disdrometer. Temporal resolution (panels a-f) is 16 s. Spatial (height) resolution (panels a-f), see Table 5.1. Vertical black lines delimit the time intervals discussed in Sect. 5.2.4.

Fig. 5.1a shows the height-range profiles of the range-corrected attenuated backscatter signal measured by the ceilometer. Warm colors are associated to high backscatter values caused by the presence of rain, while cold colors are associated to low backscatter levels, which means clear air intervals (cross-examine with Figs. 5.1e and 5.1f) or the ranges where the laser beam becomes extinguished due to the rain (usually, above 2 km). Below approximately 1.5 km, the falling rain curtain (warm colors) traces diagonal streakes in height-time domain over the entire analysis period [Fabry and Zawadski 1995], causing a shifting of about 1-2 bins at ground level. The change in slope of these diagonal signatures, particularly around 00:20-00:55 UTC, suggest compression and dilation of the rain curtain, which can be indicative of variations of the horizontal wind component with time (i.e. horizontal shear varies with time) due to the episodic passage of the storm's outflow over the instrumented site.

Fig. 5.1b shows the radar reflectivity factor computed from Eq. 5.10 (see Sect. 5.2.2). In contrast to the ceilometer, the radar suffers from very little attenuation by rain and hence, the rain curtain is clearly seen from 3 km (melting zone) downwards. In addition, Fig. 5.1b shows the diagonal signatures, as Fig. 5.1a, below 2km but shows also a nearly vertical trace up to 3 km, which is indicative of light horizontal advection.

Figs. 5.1c and 5.1d show the vertical velocity and the CNR (Carrier-to-Noise Ratio), respectively, measured by the Doppler lidar. In Fig. 5.1c, bluish areas indicate negative velocities, hence, corresponding to the fall velocities of raindrops, while greenish ones indicate near-zero velocities associated to the movement of aerosol particles which trace the vertical motion. In Fig. 5.1d, dark blue areas point out low values of CNR and yellow and green areas indicate high values of CNR (presence of rain), confirming the information provided by Fig. 5.1c. As the ceilometer (Fig. 5.1a), both instruments present that above 2.2 km the laser beams become extinguished, when the optical depth of the atmosphere is about 2.

Fig. 5.1e plots the radar RR time series computed from Eq. 5.9 (see Sect. 5.2.2) as a function of height, from 250 m up to 2000 m. As expected from the falling delay of rain drops, the lower the radar measurement height, the longer the delay with respect to the 2000 m time series. Thus, the peak RR of about 7 $mm \cdot h^{-1}$ at 22:02 UTC for the 2000 m RR time series, is found at 22:03 for the 1500 m time series, with lower intensity, at 22:06 for the 750 m time series, and at 22:08 for the 250 m one. The different amounts of horizontal shear with time, differential rain sedimentation and size may be contributing mechanism, which cause the rain curtain to dilate and expand with time (Fig. 5.1a and 5.1b). A detailed study is needed to disentangle thee processes, but this study falls out of the scope of this Chapter. Finally, Fig. 5.1f shows the disdrometer RR time series.

5.2.2 RADAR CASE: RR AND Z RETRIEVAL

FMCW radars, previously introduced in Sect. 2.3.2, transmit a linear frequency-modulated signal over a short interval, typically a few milliseconds. Then, the received radar echoes are mixed with a copy of the transmitted signal and low-pass filtered yielding a beat frequency that indicates the range of the target (Eq. 2.43 in the case of a stationary target and Eq. 2.45 in the case of a moving target). All targets are sorted in range by applying a Fourier transform to the recorded echo data. Following this process, the resulting complex (In-phase and Quadrature) samples can be treated like any pulsed radar echo. Doppler spectra are computed in the normal fashion by applying a Fourier transform to the time series of echoes at each range over a given time interval. The Doppler spectra may be represented either versus Doppler frequency or versus radial (vertical) velocity, given the relation between the two,

$$v_n = n\Delta v = f_n \frac{\lambda}{2}, \qquad [5.1]$$

where $n = 1..\mathrm{N}$ ($\mathrm{N} = 64$) is the index of the Doppler spectrum, Δv is the velocity resolution ($\Delta v = \Delta f\ \lambda/2$), λ is the radar wavelength (Table 5.1), and, $f_n = n_i \Delta f$ is the discrete frequency, with i the range index ($i = 1..\mathrm{I}, \mathrm{I} = 32$ gates) and Δf the frequency resolution of the Doppler spectrum (190.735 Hz).

Fig. 5.2 shows the steps followed to estimate the radar reflectivity factor (Z) and RR as a function of height from the radar volume reflectivity follow those described in METEK (Meteorologische Messtechnik GmbH) [2009] and Doviak and Zrnić [2006].

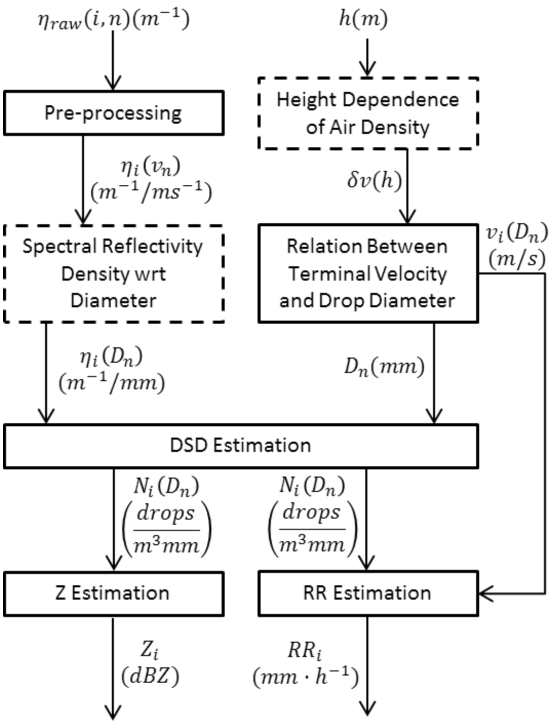

Fig. 5.2. Algorithm block diagram used to estimate the rainfall rate and radar reflectivity factor (Z) from S-band FMCW radar measurements.

The first block in the upper left branch of Fig. 5.2 is the pre-processing block; its main goal is to remove artefacts such as insects or the effect of ground clutter. The input of this block is the raw volume spectral reflectivity, $\eta_{RAW}(i,n)$, as a function of range and velocity index. This block computes the clean volume spectral reflectivity density, hereafter the reflectivity density, as $\eta_i(f_n) = \eta_{RAW}(i,n)/\Delta f\ (m^{-1}/Hz)$. At the output of the pre-processing block, the reflectivity density with respect to velocity, $\eta_i(f_n)\ (m^{-1}/m \cdot s^{-1})$, is computed as follows using that $d\eta = \eta(v_n)dv_n = \eta(f_n)df_n$,

$$\eta_i(v_n) = \eta_i(f_n)\frac{\partial f_n}{\partial v_n}, \qquad [5.2]$$

where $\frac{\partial f_n}{\partial v_n} = \frac{2}{\lambda}$ from the basic Doppler relationship of Eq. 5.1. It is worth noting that whereas the input the pre-processing block is a reflectivity, its output is a reflectivity density. The next step is the estimation of the drop-size distribution (DSD), denoted as $N(D)\ \left(\frac{drops}{m^3 \cdot mm}\right)$ and defined as the ratio of the reflectivity density with respect to drop diameter, $\eta(D)\ (m^{-1}/\mathrm{mm})$, to the single particle backscattering cross section of a drop of diameter D, $\varrho(D)\ (m^2/drop)$. That is, the number of drops per unit volume and diameter,

$$N(D) = \frac{\eta(D)}{\varrho(D)}. \qquad [5.3]$$

The DSD is estimated in the drop size distribution estimation block, where is modelled using theoretical size distributions introduced by several authors including e.g., Marshall and Palmer [1948], Marshall et al. [1955], Sekhon and Srivastava [1971], Willis and Tattelman [1989] and Tokay and Short [1996]. It is worth noting that, because the size of a raindrop is much smaller than the radar wavelength (i.e., $D \leq \lambda\ /\ 16$, Rayleigh approximation), the backscattering cross section is well approximated by that of a spherical raindrop, $\varrho(D) = (\pi^5/\lambda^4)|K_w|^2 D^6$, where $K_w = (m^2-1)/(m^2+2)$ and m is the complex refractive index of water. For non-spherical raindrops, the diameter is defined as the drop-volume equivalent diameter. $|K_w|^2 \approx 0.92$ for water at the radar operating frequency (2.94 GHz) and it is practically independent of temperature [Battan, 1973; Doviak and Zrnić, 2006]. This analytical expression of the backscattering cross section enables to rewrite Eq. 5.3 as

$$N(D_n) = \frac{\eta(D_n)}{D_n{}^6}\frac{\lambda^4}{\pi^5}\frac{1}{|K_w|^2}\ , \qquad [5.4]$$

where D_n stands for the discrete set of diameters directly related to the terminal velocity set v_n. Note that in Eq. 5.4 above, range index i has been skipped in reflectivity density $\eta(D_n)$ because Doppler spectra is computed at a given range (or reference height).

In order to compute the DSD (Eq. 5.4), two steps are needed: (i) to relate $\eta(D_n)$, the reflectivity density with respect to drop diameter, to $\eta(v_n)$, the reflectivity density with respect to velocity defined in Eq. 5.2, and (ii) to compute the discrete raindrop diameter set, D_n from the Doppler velocity set, v_n, (Eq. 5.1).

The first step uses that $d\eta = \eta(D_n)dD_n = \eta(v_n)dv_n$ to yield

$$\eta(D_n) = \eta(v_n)\frac{\partial v_n}{\partial D_n}, \qquad [5.5]$$

where $\frac{\partial v_n}{\partial D_n}$ addresses the relationship between terminal fall velocity and drop diameter [Gunn and Kinzer, 1949]. The analytical form of the velocity-diameter model was given by Atlas et al. [1973] and is computed by the top right branch blocks of Fig. 5.2 as

$$v(D_n) = (9.65 - 10.3e^{-0.6\cdot D_n})\delta v(R), \quad \text{for } 0.109 \le D \le 6 \text{ mm}, \qquad [5.6]$$

where $v(D_n)$ is the terminal velocity as a function of drop diameter and $\delta v(R)$ is the height-dependent density correction for the terminal fall velocity [Foote and Du Toit, 1969],

$$\delta v(R) = 1 + 3.68 \cdot 10^{-5}R + 1.71 \cdot 10^{-9}R^2\ , \qquad [5.7]$$

and where R is the height in meters, $R = i\Delta R$, with ΔR the height resolution. Eq. 5.7 model assumes U.S. standard atmosphere conditions and is based on the terminal-velocity-to-air-density relationship, $v \propto \rho^{0.4}$.

Them, given the reflectivity density with respect to velocity, $\eta_i(v_n)$, which is available at the output of the pre-processing block, and by using (after Eq. 5.6) that

$$\frac{\partial v_n}{\partial D_n} = 6.18e^{-0.6D_n}\delta v(h)\ , \qquad [5.8]$$

the reflectivity density with respect to diameter is computed by Eq. 5.5, i.e., the sought-after $\eta(D_n)$ to be inserted in Eq. 5.4, finishing the first step to compute the DSD.

The second step uses Eq. 5.6 in reciprocal form, i.e., $D_n = -\frac{1}{0.6}ln\left[\frac{9.65}{10.3} - \frac{v_n}{10.3\delta v(h)}\right]$, to compute the raindrop diameter set, D_n , given the discrete and uniformly spaced Doppler velocity set, v_n (Eq. 5.1). Because of the log-transformation involved, the diameter set, D_n, becomes non-uniformly spaced with diameter resolution, $\Delta D_n = \left.\frac{\partial D_n}{\partial v_n}\right|_{v_n} \Delta v$. From these two steps the DSD (Eq. 5.4) can be computed for each range gate (see block Drop Size Distribution Estimation in Fig. 5.2).

The last two blocks of Fig. 5.2 concern estimation of the RR and Z. The RR ($mm \cdot h^{-1}$) is defined as

$$RR = \frac{\pi}{6}\int_0^\infty N(D)D^3 v(D)dD. \qquad [5.9]$$

Eq. 5.9 is computed by replacing integration by summation over the discrete size range, and dD by ΔD_n. The input variables for the RR estimation block are the DSD and the terminal velocity as a function of discrete diameter, D_n.

The DSD is used to both estimate the RR and also Z independently from the measured RR (e.g., Z-RR relationships [Battan, 1973; Tokay et al., 2009]). The reflectivity factor is defined as the sixth power of the raindrop diameter summed over all the size distribution,

$$Z = \int_0^\infty N(D) D^6 dD \, , \tag{5.10}$$

and it is numerically computed in similar fashion as the RR (Eq. 5.9) by the Z estimation block of Fig. 5.2.

Finally, the reflectivity factor from Eq. 5.10 can alternatively be computed as the equivalent reflectivity factor, Z_e, which is related to the volume reflectivity η (m^{-1}) as $Z_e = \frac{\lambda^4}{\pi^5} \frac{1}{|K_w|^2} \eta$ [Doviak and Zrnić, 2006]. This reflectivity factor is rewritten next as a function of the reflectivity density with respect to diameter, $\eta = \int_0^\infty \eta(D) dD$, as

$$Z_e = \frac{\lambda^4}{\pi^5} \frac{1}{|K_w|^2} \int_0^\infty \eta(D) dD. \tag{5.11}$$

When Eqs. 5.10 and 5.11 are equaled over an integration (summation) bin, $dD = \Delta D_n$, Eq. 5.4 is also reencountered.

Fig. 5.3 shows a computation example at 1000 m of height. In the left panel is shown the 1 hout time-average measured reflectivity density with respect to velocity, a vertical air-motion correction has been applied to this reflectivity density to ensure that the clear-air echo (dark and red areas) is at 0 $m \cdot s^{-1}$. In the central panel, the reflectivity factor, Z, is computed by plotting the reflectivity density at the chosen height scaled by the factor $\frac{\lambda^4}{\pi^5} \frac{1}{|K_w|^2}$ and by finding the area under the curve (Eq. 5.11). The right panel plots the DSD, $N(D)$, as well as integrand kernels $N(D)\ D^3$ and $N(D)\ D^6$ used in Eqs. 5.9 and 5.10 to compute the RR and Z, respectively, from the DSD. Results are quality assured by comparing the reflectivity factor obtained after Eq. 5.11 (26.5 dBZ, area under the curve, central panel) to the reflectivity factor estimated from the RR obtained after Eq. 5.9 (5.7 $mm \cdot h^{-1}$, right panel) via the WSR-88D default model, $Z = 300(RR)^{1.4}$ [Vieux and Bedient, 1998]. This WSR model gives 26.5 dBZ in perfect coincidence. The Marshall-Palmer (MP) $Z = 200(RR)^{1.6}$ [Marshall and Palmer, 1948] and the WSR-88D tropical model, $Z = 250(RR)^{1.2}$ (TRP) have also been considered with slightly poorer agreement (25.4 and 24.8 dBZ, respectively).

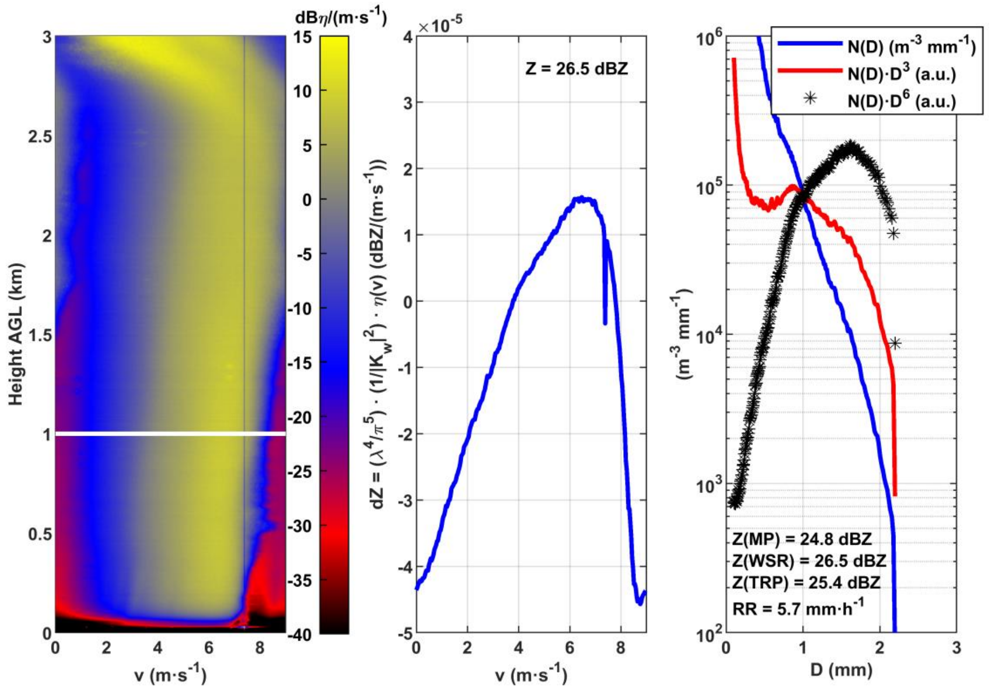

Fig. 5.3. Computed radar data products at 1000 m reference height (case 1, 30 April 2016, 00:00-01:00 UTC, vertical air-motion correction 2 $m \cdot s^{-1}$ [Williams, 2012]). (Left) Volume reflectivity density with respect to velocity as a function of height, $\eta(v)$, $(dB\eta/(m \cdot s^{-1}))$ (Eq. 5.2), $dB\eta = 10log\eta$). Horizontal white line indicates the reference height (1000 m). (Center) Reflectivity factor density $dZ = \frac{\lambda^4}{\pi^5}\frac{1}{|K_w|^2}\eta(v)$ $(dB\eta/(m \cdot s^{-1}))$ with respect to velocity (equivalently, Eq. 5.11) using that $\eta = \int_0^\infty \eta(v)dv$). Label shows the reflectivity factor (dBZ) computed as the area under the curve. (Right) (blue trace) Drop-size distribution $(drops \cdot m^{-3}mm^{-1})$; (red trace) RR integrand term $N(D)D^3$ (arbitrary units, (a.u.)), Eq. 5.9; (black dashed trace) reflectivity-factor integrand $N(D)D^6$ (a.u.) (Eq. 5.10) as a function of velocity (Eq. 5.6). MP, WSR and TRP stand for the different Z-RR models considered.

5.2.3 CEILOMETER CASE: EXTINCTION COEFFICIENT RETRIEVAL

Because the ceilometer operates at 910 nm wavelength the molecular backscattering cross section is very small (λ^{-4} spectral dependency of Rayleigh scattering) and hence, molecular backscatter cannot be measured [Kotthaus et al., 2016]. Besides, this is hampered by the fact that the ceilometer is a low energy-aperture-product lidar. As a result, range-resolved inversion methods like the Klett-Fernald method [Fernald et al., 1972; Fernald, 1984; Klett, 1981; 1985], which enable range-resolved retrieval of the vertical profile of the aerosol extinction coefficient given a calibration in a molecular reference range and assumption of an aerosol-to-molecular extinction ratio, cannot be used. Alternatively, the selected method to estimate the optical extinction coefficient from the ceilometer is an adapted version of the classic slope-method [Kunz and de Leeuw, 1993], which departs from the single-scattering monostatic lidar equation in differential form [Kovalev and Eichinger, 2004],

$$\frac{dU(R)}{dR} = \frac{1}{\beta(R)}\frac{d\beta(R)}{dR} - 2\alpha(R), \qquad [5.12]$$

where $U(R)$ is the logarithm of the measured range-corrected lidar signal $(ln[P(R)R^2])$, $\alpha(R)$ is the total atmospheric extinction-coefficient profile, $\beta(R)$ is the total backscatter-coefficient profile, and R is range(height). The slope-method assumes a homogenous horizontally stratified atmosphere along the lidar's observing path; being the most limiting assumption of the method, and allows to estimate the average atmospheric extinction based on linear regression analysis applied to the logarithm of the range-corrected lidar signal,

$$U(R) = ln[P(R)R^2] = ln\, K\beta - 2\alpha R, \qquad [5.13]$$

where K is the ceilometer instrument constant (unknown) and where the homogeneity approximation, $\alpha(R) \approx \alpha$, $\beta(R) \approx \beta$ has been used. Because of the 910-nm measuring wavelength of the ceilometer, the backscattering cross-section is negligible and therefore the total extinction coefficient is equal to the aerosol extinction coefficient ($\alpha \approx \alpha_{aer}$).

Under noiseless ideal conditions, when a linear fit of the form, $y = mR + n$, $R \in [R_1, R_2]$, is applied to Eq. 5.13 the estimated slope and intercept are $\hat{m} = -2\alpha$ and $\hat{n} = ln\, K\beta$. Therefore, the average extinction coefficient in the range interval $I = [R_1, R_2]$ (so-called slope-method processing interval) is retrieved as minus one half of the logarithm of the range-corrected lidar signal, $U(R)$.

Fig. 5.4 plots the logarithm of the range-corrected ceilometer signal versus height for a rain measurement (Fig. 5.4a) and a non-rain measurement (Fig. 5.4b) just before the start of the rain event (Sect. 5.2.1). Fig. 5.4c summarizes the retrieved total-extinction coefficient for the whole rain event.

The slopes found in the rainy profiles of Fig. 5.4a are greater than the slopes of the profiles of Fig. 5.4b (clear-sky profiles), because during the rain measurements, the ceilometer signal undergoes extinction due to aerosols and raindrops,

$$\alpha = \alpha_{aer} + \alpha_{rain}\ , \qquad [5.14]$$

while during non-rain measurements the total extinction is only due to aerosols ($\alpha_{no\_rain} = \alpha_{aer}^{no\_rain}$). In Eq. 5.14, subscript “rain” stands for rain. Under the approximation that the aerosol background with and without rain is similar ($\alpha_{aer} \approx \alpha_{aer}^{no\_rain}$), the rain extinction is estimated as the differential extinction,

$$\alpha_{rain} = \alpha - \alpha_{no\_rain}. \qquad [5.15]$$

This approximation essentially requires closely time-spaced rain/no-rain measurements and the assumption that the rain even does not significantly reduce the aerosol load via scavenging. Under low rain rates, background extinction, α_{no_rain}, might be comparable to the rain extinction. Hence, as discussed in Sect. 5.1, Eq. 5.15 represents an important refinement over Lewandowski et al. [2009], where the approximation $\alpha \approx \alpha_{rain}$ for low rain rates can lead to large errors.

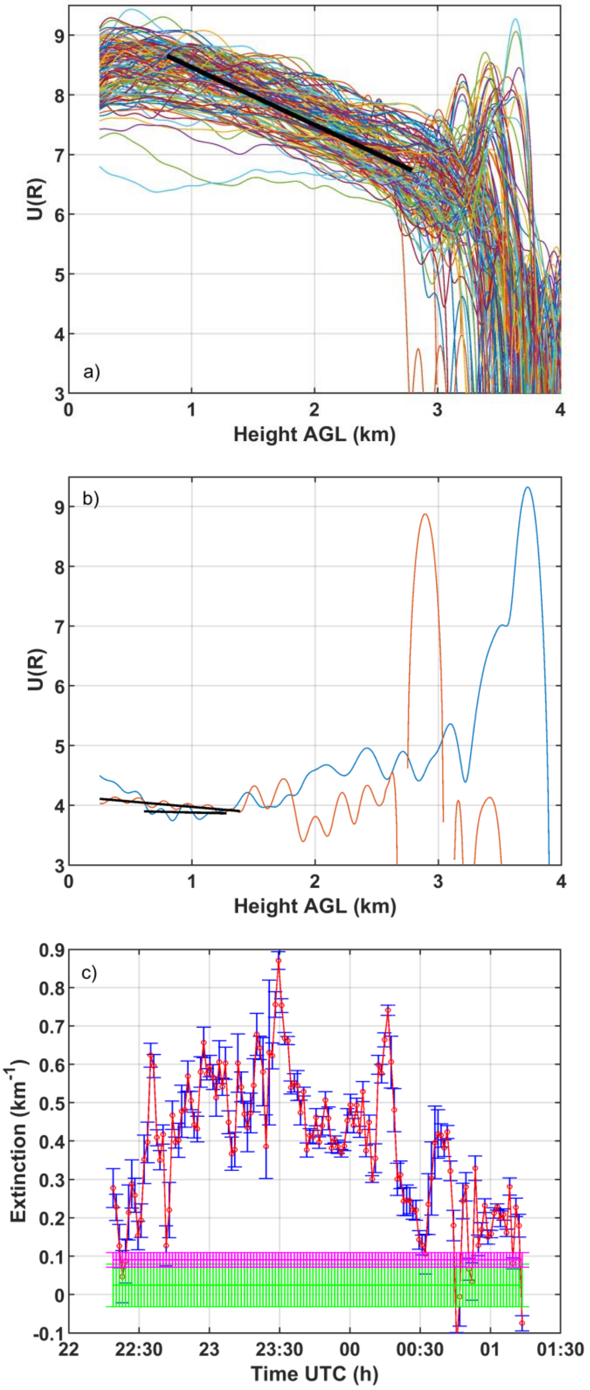

Fig. 5.4 Slope-method results (Belle Mina, AL, 29-30 April 2016, 21:36 UTC to 01:45 UTC). Time resolution is one bin (80 s), spatial resolution is 200 m. (a) Logarithm of the range-corrected ceilometer signals, $U(R)$, during the rain interval (22:19 UTC to 01:15 UTC), 132 profiles. (b) Logarithm of the range-corrected background signal, $U(R)$, before the start of the rain episode (21:36 UTC to 21:40 UTC, orange trace) and after ending (01:41 UTC to 01:45 UTC, blue trace). Solid lines represent the linear fits used to respectively derive the background total extinction coefficients ($\alpha_{before}^{\propto\_no\_rain} = 0.09 \pm 0.02\ km^{-1}$, $I_{before} = [0.3, 1.4]\ km$; $\alpha_{after}^{\propto\_no\_rain} = 0.02 \pm 0.05\ km^{-1}$, $I_{after} = [0.6, 1.3]\ km$). (c) Total extinction coefficients (red circles), α (Eq. 5.14), with errorbars (blue), derived from the rain profiles of panel (a) by means of the slope-method. Purple and green traces represent the background extinction coefficient, α_{no_rain}, with errorbars, before and after the rain episode, respectively.

5.2.4 Selection of the Processing Ranges of the Slope-Method and Radar Reference Height

5.2.4.1 Processing Ranges of the Slope-Method

Selection of starting and end height ranges, R_1 and R_2, respectively, is not easy because of the inhomogeneities encountered in the profile of $U(R)$ with height, that break the homogeneity assumption inherent to the slope-method. Thus, the selection of height ranges R_1 and R_2 must fulfill the following criteria: (i) a minimum height of 0.3 km is required for starting height R_1 to ensure that this height is greater than the spatial resolution of the smoothing spatial filter used ($\Delta R_{clean}^{ceilo} = 200\ m$, Sect. 5.2.1) and, therefore, free from initial filter transients. (ii) The maximum height allowed for R_2 is 2.8 km in order to be well below the cloud base (Fig. 5.1b). This maximum height is often further limited by the proximity of notches in the profile of $U(R)$ (Figs. 5.4a and 5.4b). These notches are caused by negative measurement-noise spikes, that when combined with low backscattered power levels, translate into singularities in the logarithm of the range-corrected power (i.e., $P(R)$ negative in Eq. 5.13). By experiment, (iii) a minimum distance between R_1 and R_2 of 600 m ($3\Delta R_{clean}^{ceilo}$) is also required so that the slope-method linear fit averages out the residual oscillatory overshoot caused by the smoothing filter (Sect. 5.2.1). The selection of height ranges R_1 and R_2 has been done in semi-supervised way, departing from an initial guess $[R_1, R_2] = [0.7{,}2.0]$ km and trying to obtain the lowest relative root-mean-square error (RMSE) in each retrieval case upon manual small perturbation of the initial guess. In what follows, the starting and end ranges used will be denoted by the range interval $I = [R_1, R_2]$.

The relative RMSE on the retrieved total-extinction coefficient is defined as

$$RMSE_{\alpha,rel} = \frac{RMSE_{\alpha}}{\propto}, \tag{5.16}$$

where $RMSE_{\alpha}$ is the absolute RMSE on the total-extinction coefficient, the extinction RMSE, estimated as

$$RMSE_{\propto} = \frac{1}{2}\frac{RMSE_y}{R_2 - R_1}, \tag{5.17}$$

where $RMSE_y$ is the RMSE of linear regression over the measurements, $y_i = U(R_i), i = 1..N$. The factor 2 accounts for the fact that extinction is retrieved as minus one half of the estimated slope because of the two-way travelling path of the laser beam. Hence, the incurred error is also one half of the RMSE on the retrieved slope. The term $RMSE_m = \frac{RMSE_y}{R_2 - R_1}$ in Eq. 5.17, allows estimating the RMSE on the retrieved slope. As a result, the intervals found for the 29-30 April study case are $I_1 = [0.3, 1.8]\ km$, 22:19 UTC to 22:34 UTC; $I_2 = [0.8, 2.8]\ km$, 22:34 UTC to 00:29 UTC; and $I_3 = [0.5, 2.4]\ km$, 00:29 UTC to 01:15 UTC for the rainy profiles of Fig. 5.4a. Besides, the before and after rain intervals, necessary when estimating the background-extinction profiles (Fig. 5.4) are $I_{before} = [0.3, 1.4]\ km$, 21:36 UTC to 21:40 UTC and $I_{after} = [0.6, 1.3]\ km$, 01:41 UTC to 01:45 UTC.

5.2.4.2 RADAR REFERENCE HEIGHT

As has been explained before, radar RR is heavily affected by the expansion of the rain curtain (sect. 5.2.1) and radar data can be affected by the parallax effect, the disdrometer RR is provided as one single value at ground level (Fig. 5.1) and the ceilometer extinction coefficient is retrieved as one single value for the total observed atmospheric column (see Sect. 5.2.3), therefore it is necessary to find a radar reference height in order to compare the estimated RR and Z, to the data retrieved from the other instruments. In order to make this selection, the maximum correlation between the radar and the RR time series (Figs. 5.1e and 5.1f) has been found.

In Fig. 5.5a the cross-covariance function between the radar and the disdrometer RR time series is shown. The cross-covariance (often called cross-correlation or shifted dot product) measures the similarity between two time series by comparing one of them to a shifted (lagged) copy of the other. The maximum correlation coefficient as a function of height is obtained at 1-bin lag giving $\rho = 0.78\ (250\ m)$, $\rho = 0.71\ (500\ m)$ and $\rho = 0.60\ (750\ m)$. Although 250 m presents the highest correlation, at this height the parallax effect is still responsible for 1 dB attenuation in the radar reflectivity (see Fig. 3 in İnce et al. [2003]) and above 750 m the correlation coefficient starts to fall dramatically, therefore, 500 m is selected as the radar reference height. Similarly, when the radar RR is compared to the ceilometer extinction in Fig. 5.5b, both 250 m and 500 m in height attain similar maximum correlation, $\rho = 0.65$.

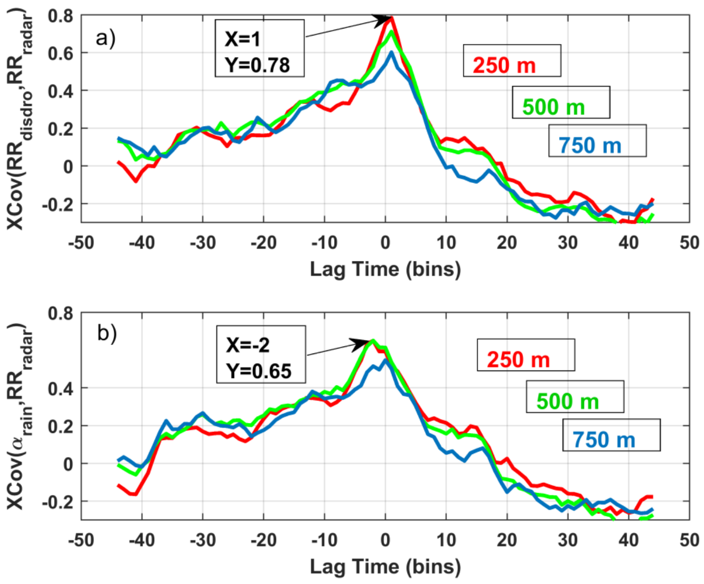

Fig. 5.5. Cross-covariance analysis (29-30 April 2016) among the radar RR, the disdrometer RR, and the ceilometer extinction-coefficient time series for different radar reference heights (250, 500, and 750 m). (a) Cross-covariance between the radar and the disdrometer RRs. (b) Cross-covariance between the radar RR and the ceilometer rain extinction.

It is worth noting that the studied rain event, introduced in Fig. 5.1 (Sect. 5.2.1), has been divided into three different time intervals attending to the intensity of the rain. Thus, the change of the intensity in the time domain involves variations in the slope-method processing intervals. As a result, from the procedures explained in Sects. 5.2.4.1 and 5.2.4.2, and using 500 m as the radar reference height, the following data are obtained for the three time interval subdivisions:

- Time interval 1 (22:19UTC – 22:34 UTC): is the beginning of the rain episode and is characterized by a weak discontinuous rain curtain (2.7 $mm \cdot h^{-1}$ on average measured by the disdrometer and 2.4 $mm \cdot h^{-1}$ by the radar). The average rain extinction is $\alpha_{rain} = 0.15 \pm 0.06\ km^{-1}$ (slope-method fitting interval, $I_1 = [0.3, 1.8]\ km$,see Sect 5.2.3 and Fig. 5.5), and the average Z at 500 (see Sect. 5.2.1.1) m is 17.7 dBZ.
- Time interval 2 (22:34 UTC – 00:29 UTC) is the central portion of the rain event having the highest rain intensity (4.4 $mm \cdot h^{-1}$ on average measured by the disdrometer and 4.6 $mm \cdot h^{-1}$ by the radar). The average rain extinction coefficient is $\alpha_{rain} = 0.42 \pm 0.05\ km^{-1}$, $I_2 = [0.8, 2.8]\ km$) and the average Z is 24.8 dBZ.
- Time interval 3 (00:29 UTC – 01:15 UTC) is the last interval of the rain event. Similarly to time interval 1, time interval 3 is characterized by light intermittent rain. The precipitating cloud has advected over the site and the instruments are measuring near the edge of it. Thus, the instruments are seeing fewer backscattering rain droplets in the downfall path because the rain is abating and the wind is moving the droplets away from them. This casuses weak backscatter (Fig. 5.1a) and reflectivity (Fig. 5.1b) close to ground level and low disdrometer RRs (1.6 $mm \cdot h^{-1}$ on average, Fig. 5.1f) as compared to the radar ones at 500 m (2.8 $mm \cdot h^{-1}$, Fig. 5.1e; average radar reflectivity, 19.4 dBZ). Similarly, the Doppler lidar shows nearly nil vertical velocities (Fig. 5.1c, greenish patches) and nil CNRs (-30 dB, bluish shades) close to ground level. The average rain extinction is $\alpha_{rain} = 0.19 \pm 0.07\ km^{-1}$ ($[0.5, 2.4]\ km$), similar to that of time interval 1.

Besides, the background total extinction coefficients before and after the rain event are $\alpha_{before}^{\propto\_no\_rain} = 0.09 \pm 0.02\ km^{-1}$ ($I_{before} = [0.3, 1.4]\ km$), and, $\alpha_{after}^{\propto\_no\_rain} = 0.02 \pm 0.05\ km^{-1}$ ($I_{after} = [0.6, 1.3]\ km$).

5.3 29-30 APRIL RAIN EVENT INTERCOMPARISON

5.3.1 ERROR TREATMENT

In this Section the error treatment is limited to the random error associated to the mean RR estimated from the radar/disdrometer (Sect. 5.2.2) and to the rain extinction coefficient derived from the slope method using ceilometer measurements of total and background atmospheric extinction (Sect. 5.2.3, Eq. 5.15). As mentioned in Sect. 5.2.1, these products are retrieved with a temporal resolution of one bin ($\Delta T = 80\ s$). In Sect. 5.3.2 and Sect. 5.4 the estimated extinction coefficient will be related to the retrieved RRs and discussed in the context of further error sources.

The uncertainty related to the mean RR in a time bin is computed as the random-error standard deviation of the mean RR in the time bin as

$$\sigma_{\mathrm{j}}^{RR\_x} = \frac{\sigma_{\Delta T,j}^{RR\_x}}{\sqrt{M}}, \quad j = 1..J, \qquad [5.18]$$

where j is the time-bin number ($P = 132$ bins in Fig. 5.1), x stands for the instrument (radar/disdrometer), $\sigma_{\Delta T,j}^{RR\_x}$ is the radar/disdrometer RR standard deviation for the $j - th$ bin computed from the 16 s samples ($\Delta T_{master} = 16\ s$, Sect. 5.2.1) in the bin, and M is the temporal-averaging ratio ($M = 5,\ i.e., 80/16$)).

In the case of the rain-extinction coefficient (Eq. 5.15), the random-error standard deviation associated to the $j - th$ binis computed as

$$\sigma_j^{\propto\_rain} = \sqrt{\left(\sigma_j^{\propto}\right)^2 + \left(\sigma_j^{\propto\_no\_rain}\right)^2}, \quad j = 1..J, \qquad [5.19]$$

where $\sigma_j^{\propto}$ is the error standard deviation of the total extinction coefficient for the $j - th$ bin (Eq. 5.14 and Fig. 5.4c, red circles) and $\sigma_{u,j}^{\propto\_no\_rain}$ is the error standard deviation of the background extinction coefficient for the $j - th$ bin. In practice, because the background extinction is estimated shortly “before” and “after” the rain event (Figs. 5.4b Fig. 5.4c, purple and green traces, respectively), the background extinction for each bin in the rain interval is estimated by linear interpolation of the before- and after-rain extinction estimates as,

$$\alpha_j^{\propto\_no\_rain} = \frac{\alpha_{after}^{\propto\_no\_rain} - \alpha_{before}^{\propto\_no\_rain}}{J-1}(j-1) + \alpha_{before}^{\propto\_no\_rain}. \qquad [5.20]$$

Analogously, background-extinction root-mean-square error $RMSE_j^{\propto\_no\_rain}$ is computed in each bin by linear interpolation of the before- and after-rain root-mean-square errors, $RMSE_{before}^{\propto\_no\_rain}$ and $RMSE_{after}^{\propto\_no\_rain}$. Error standard deviations $\sigma_j^{\propto}$ and $\sigma_j^{\propto\_no\_rain}$ in Eq. 5.19 are assimilated to the respective extinction RMSEs,

$$\sigma_j^{\propto} = RMSE_j^{\propto}, \quad \sigma_j^{\propto\_no\_rain} = RMSE_j^{\propto\_no\_rain}. \qquad [5.21]$$

This Eq. 5.21 is based on the fact that for an unbiased estimator, which is the case of the slope method for SNRs > 5 (almost of all the cases shown here have SNR above this threshold) over the entire inversion range, the mean squared error and the variance (equivalently, the RMSE and the standard deviation) of the estimator coincide [Rocadenbosch et al., 1998]. Almost all of the cases used in this Chapter have SNR above this threshold

Finally, it is worth noting that the slope method, by itself, is ambiguous since it leads to the conjecture, $\frac{1}{\beta(R)}\left|\frac{d\beta(R)}{dR}\right| \ll 2\alpha$ over small range intervals. Since, a homogeneous atmosphere is associated to a virtually nil RMSE in the slope-method linear fit, usage of the RMSE as a quantitative indicator of atmospheric homogeneity must be interpreted with caution and by resorting to cooperative instrumentation (Sect. 5.3.2), because due to cloud reflections or haze, where the combination of an inhomogeneous atmospheric extinction-coefficient profile, $\alpha(R)$, with an inhomogeneous backscatter-coefficient profile, $\beta(R)$, in differential lidar equation (Eq. 5.12) cannot be distinguished from a pair of homogeneous profiles, $\alpha(R) = \alpha$ and $\beta(R) = \beta$ [Kunz, 1992]. Thus, although a homogeneous atmosphere is associated to virtually zero RMSE in the slope-method linear fit, the reverse is not always true. Therefore, the use of the RMSE as a quantitative indicator of atmospheric homogeneity must be interpreted with caution and is best evaluated with additional collocated instumentation.

5.3.2 RR-TO-EXTINCTION INTERCOMPARISON

Fig. 5.6 shows comparison results for the ceilometer-radar and ceilometer-disdrometer pairs according to the *RR*-α model,

$$RR = a + b\alpha_{rain}, \tag{5.22}$$

where a and b stand for the fitting parameters. To compute Eq. 5.22, first an outlier rejection criteria is applied and, second, the fitting parameters above are solved by using York's fitting method [York et al., 2004], which assimilates errors in both x- and y-variables (α_{rain} and RR, respectively).

5.3.2.1 OUTLIER REJECTION CRITERIA

Two main type of outliers are indentified. The first type is due to time variation in the rainfall character, for instance due to the horizontal wind shear which causes sudden changes in the slope of the diagonal signature of the rain curtain (e.g., 00:27 UTC – 00:42 UTC, Figs. 5.1a and 5.1d) and, in addition, temporal inhomogeneities in the rain intensity (e.g., intermittent rain, 00:42 UTC – 00:54 UTC). As a consequence, rain is swept from adjacent time bin to the current bin being analyzed causing that some column extinctions values are associated to very different RR values, thus, in Fig. 5.6 can be observed a large span of extinction values associated with a particular RR bin (se for instance 2-3 $mm \cdot h^{-1}$).

The second type accounts for the case in which the slope-method retrieves an extinction coefficient value, in the current time bin, with a much lower RMSE than the adjacent extinction coefficients (the current time bin results in a fit that is comparatively poorer than other time bin), due to the failure of the atmospheric homogeneity hypothesis in the height-fitting interval (Sect. 5.2.3). This is a limitation of the semi-automated fitting procedure, which uses the same starting/end fitting ranges over predefined time sub-intervals (chosen manually) instead of individualized starting/end fitting ranges for each time bin.

Fig. 5.6a shows the histogram of the radar RRs (i.e., the ordinates of the points therein; the statistical sample consists of 132 points) and Figs. 5.6b and 5.6c show the histogram of the rain-extinction coefficients for two examples (2-3 $mm \cdot h^{-1}$ and 4-5 $mm \cdot h^{-1}$) of Fig. 5.6a RR histogram. Thus, Fig. 5.6c plots the rain extinction associated to the 4-to-5 $mm \cdot h^{-1}$ points in Fig. 5.7a. The shape of the distribution of the rain extinction in the different RR bins is similar to the one shown in Fig. 5.6b with slight bi-modality for the 2-3 $mm \cdot h^{-1}$ bin. Table 5.2 shows 16th and 84th percentiles of the extinction for each RR bin.

To reject outliers is limited the spread of both the RR and the extinction distributions by excluding the points that fall out of the acceptance interval,

$$\left[\mu_{RR/\alpha} - n_{RR/\alpha} \cdot \sigma_{RR/\alpha},\ \ \mu_{RR/\alpha} + n_{RR/\alpha} \cdot \sigma_{RR/\alpha}\right], \tag{5.23}$$

where μ is the mean of the distribution, n is the standard-deviation factor, and subscripts RR and α refer to rain rate and extinction, respectively. Eq. 5.23 is applied first to the overall RR distribution (first outlier type, Fig. 5.6a) and second to the rain-extinction distribution associated to each successive 1 $mm \cdot h^{-1}$ bin of the RR distribution (second outlier type, Figs. 5.6b and 5.6c).

The RR histogram shown in Fig. 5.6a depicts a slightly skewed distribution, which is often the case for precipitation log-normal, [Sauvageot, 1994], but which is not far from the shape of a Gaussian distribution. This Gaussian-like distribution may be a consequence of the fact that the distribution merges into a single body not only the precipitation distribution itself but also that of the many different additive error sources. The sum distribution, on account of the central limit theorem, approaches the Gaussian when the number of sources tends to infinity [Barlow, 1989]. For an approximately normal data set, the values within one standard deviation of the mean ($\mu \pm 1\sigma$) account for about 68% of the set, or, equivalently, to the population between 16th (exactly, 15.9) and 84th (84.1) percentiles ($\mu - 1\sigma$ and $\mu + 1\sigma$, respectively). Table 5.2 corroborates the goodness of the Gaussian approximation within the approximate $\pm 1\sigma$ limits of the accepted extinction samples by showing virtually coincident percentiles between the normal and the measured distribution. For highly skewed distributions, the split-histogram method [McNicholas and Turner, 2014] is a good alternative.

Table 5.2. Comparison between 16th and 84th percentiles of the Gaussian distribution, computed as $\mu - 1\sigma$ and $\mu + 1\sigma$ respectively, and those of the measured rain-extinction distribution for each rain-rate bin (radar case). μ denotes the mean and σ denotes the standard deviation. μ and $\mu \pm 1\sigma$ values shown for the 4-5 $mm \cdot h^{-1}$ bin correspond to the vertical lines plotted in Fig. 5.6.

			Gaussian		**Measured**	
RR bin $(\boldsymbol{mm \cdot h^{-1}})$	**Number of** $\boldsymbol{\alpha}$ **bins**	$\boldsymbol{\mu\ (km^{-1})}$	$\boldsymbol{\mu - 1\sigma}$ $\boldsymbol{(km^{-1})}$	$\boldsymbol{\mu + 1\sigma}$ $\boldsymbol{(km^{-1})}$	**16th pc** $\boldsymbol{(km^{-1})}$	**84th pc** $\boldsymbol{(km^{-1})}$
0-1	3	0.17	0.07	0.27	0.06	0.26
1-2	7	0.17	0.15	0.20	0.14	0.20
2-3	23	0.20	0.06	0.33	0.05	0.34
3-4	24	0.24	0.11	0.37	0.11	0.36
4-5	28	0.39	0.29	0.49	0.32	0.48
5-6	18	0.40	0.30	0.51	0.31	0.53
6-7	17	0.49	0.34	0.65	0.31	0.61
7-8	3	0.61	0.52	0.70	0.51	0.69
8-9	5	0.46	0.41	0.50	0.41	0.51
9-10	1	0.56	0.56	0.56	0.56	0.56
10-11	1	0.69	0.69	0.69	0.69	0.69

When rejecting outliers of the first type, standard-deviation factors between $n_{RR} = 1 - 1.5$ (Eq. 5.23) presented similar model-fitting results while keeping the central bins of the distribution. With the choice, $n_{RR} = 1.5$, 19 samples are rejected (14 % of the population), keeping as valid data the large amount of samples between 2-3 $mm \cdot h^{-1}$ and 6-7 $mm \cdot h^{-1}$. Concerning outliers of the second type, extinction histograms computed for each 1 $mm \cdot h^{-1}$ bin (Figs. 5.6b and 5.6c) contain a much lower number of samples, which cause that the shape of the distribution is not well reproduced. By choosing the factor $n_\alpha = 1$ most of the tallest bins are accepted (approximately, full width half height of the distribution) while for $n_\alpha \geq 2$ all the bins are accepted, therefore, providing no filtering at all. After manual inspection of a set of 20 rejected samples (15% of the population), the percentage of wrongly rejected samples is below 10% (2 samples).

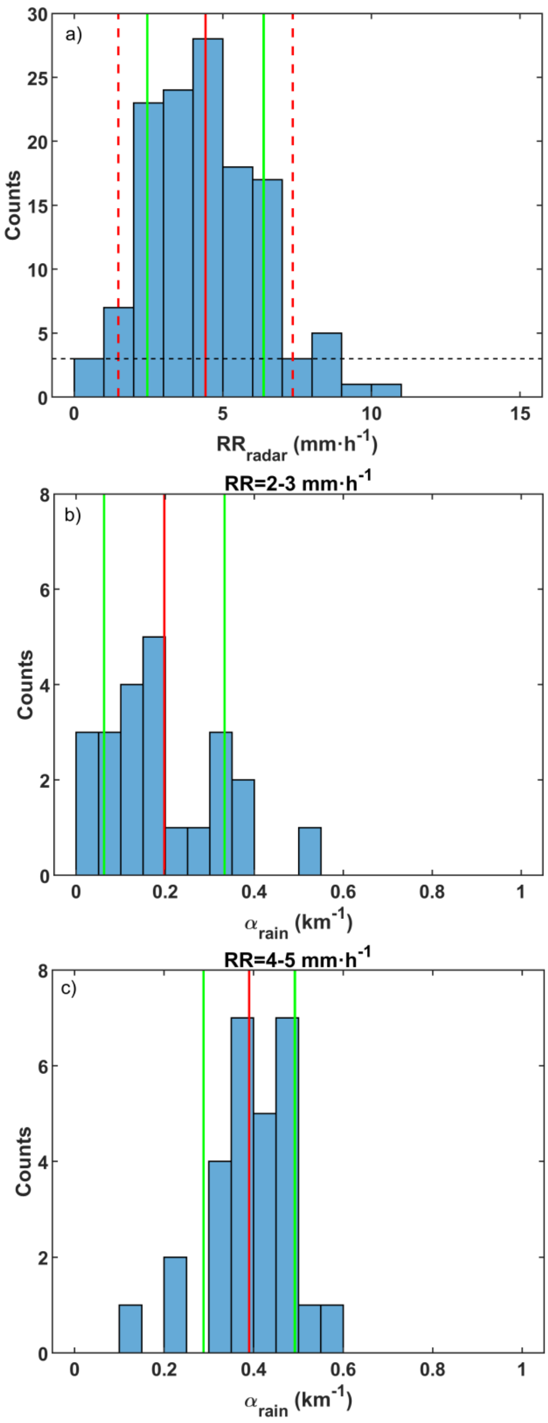

Fig. 5.6. Radar RR and extinction histograms (29-30 April 2016). (a) Radar-RR histogram. Bin-width is $1\ mm \cdot h^{-1}$. Red solid line indicates the mean rain rate (μ_{RR}), green solid lines delimit the acceptance interval at 1σ (i.e., $n_{RR} = 1$) and red dashed lines at 1.5σ. Horizontal black dashed line is set at 3 counts. (b-c) Histograms of the rain-extinction coefficient for 2-3 $mm \cdot h^{-1}$ and 4-5 $mm \cdot h^{-1}$ RR bins in (a). Bin-width is 0.05 km^{-1}. Red solid line indicates the mean value (μ_{α}), green solid lines delimit the acceptance interval at 1σ (i.e., $n_{\alpha} = 1$).

5.3.2.2 YORK'S FITTING METHOD

York's method [York et al., 2004] is a covariance-weighted method of fitting used to compute the best straight line fit to data points having normally distributed errors on both x and y components. The algorithm assigns weights to both the x- and y-variables (bivariate method) and uses a recursive procedure to estimate the fitted slope and their associated uncertainties under a maximum likelihood estimation criterion. A further output of the algorithm is the so-called weighted-RMSE of deviations from the best-fit line computed, which can be considered a goodness of fit parameter [Cantrell, 2008].

The input errors to York's method (rain-extinction and RR errors) have been computed according to Eqs. 5.18-5.21 above. The estimated model parameters (Eq. 5.22) in the ceilometer-radar case (Fig. 5.7a) are

$a = -0.45 \pm 0.29$ and $b = 13.49 \pm 0.79$, and in the ceilometer-disdrometer case (Fig. 5.7b) are $a = -0.80 \pm 0.25$, $b = 12.80 \pm 0.67$. The ceilometer-disdrometer case shows, comparatively lower uncertainties for the RR-α model. Similarly, the weighted RMSEs for the radar and disdrometer fits are 1.6 $mm \cdot h^{-1}$ and 1.1 $mm \cdot h^{-1}$, respectively. This behavior can be explained by the fact that the temporal variability of the RR, due to the effects of the horizontal and vertical wind components, is higher at the radar reference height (500 m) than at ground level. Fig. 5.7 also shows slightly lower RRs for the disdrometer than for the radar. Thus, for rain extinctions between 0.3-0.4 km^{-1} the mean radar RR value is 4.8 $mm \cdot h^{-1}$ (Fig. 5.7a) while the mean disdrometer RR value is 3.7 $mm \cdot h^{-1}$, about a 23% lower. A plausible explanation lies on the very different measurement snesitivities of the radar (which is sensitive to the sixth moment of the size distribution) and the disdrometer (which is sensitive to the volume of the rain, third moment of the size distribution). Overall, the RR-α correlation coefficients for the 132 bin dataset of Fig. 5.7 are $\rho_{RR\_radar}^{(\alpha)}$=0.78 (0.68 without outlier rejection) and $\rho_{RR\_disdro}^{(\alpha)}$ = 0.91 (0.71 without outlier rejection).

Following the discussion at the end os Sect. 5.2.4.2, depending on the RR, a 50% reduction in the aerosol extinction is present ($\alpha_{before}^{\propto\_no\_rain} = 0.09 \pm 0.02\ km^{-1}$, $\alpha_{after}^{\propto\_no\_rain} = 0.02 \pm 0.05\ km^{-1}$, Fig. 5.4c). The resulting impact in the derived RR of e.g., a 0.05 km^{-1} overestimation error in the aerosol extinction ($\Delta\alpha_{no\_rain} = \widehat{\alpha}_{after}^{\propto\_no\_rain} - \alpha_{after}^{\propto no_{rain}} = 0.05\ km^{-1}$, the "hat" means estimated value) is a systematic error $\Delta RR = -b \cdot \Delta\alpha_{no_{rain}} \approx -0.7\ mm \cdot h^{-1}$ (Eqs. 5.15 and 5.22)), which is particularly significant for small RRs. Graphically, this bias is equivalent to shifting the fitted line of Fig. 7a and Fig. 7b slightly to the right.

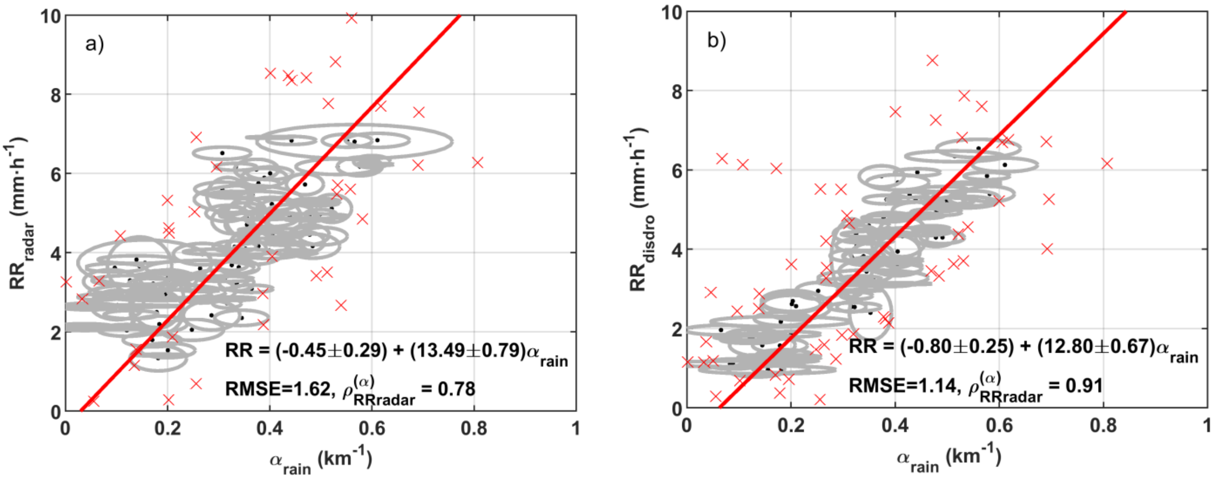

Fig. 5.7. RR-α model results (29-30 April 2016). (a) Radar RR versus extinction estimates (radar reference height, $R = 500\ m$). (b) Disdrometer RR versus extinction estimates. Red crosses indicate points rejected as outliers following the criteria exposed above. Gray ellipses delimit the 1σ-uncertainty locus in each variable.

5.4 MODEL VERIFICATION: 31 MARCH RAIN EVENT INTERCOMPARISON

The methodology presented in Sects. 5.2 and 5.3 has been applied to a different rain event, which took place during 31 March 2016, which is introduced in Fig. 5.8. During this event, the disdrometer was not deployed at Belle Mina, so only the radar RR-α model is evaluated during this event. The event is subdivided in two time intervals, one in the morning (10:22 UTC – 11:41 UTC, in what follows the morning case) and one in the afternoon (15:09 UTC – 16:52 UTC, afternoon case). The time interval (12:51 UTC – 14:48 UTC) between these two intervals above is not considered because the rain intensity is comparatively so high (16.2 $mm \cdot h^{-1}$

and 27.6 dBZ) that the ceilometer signal becomes fully extinguished in a very short distance (300-800 m), this situation does not allow successful application of the slope method (see Sect. 5.2.3).

In comparison to Fig. 5.1, the rain curtain is fairly uniform from 3 km downwards, pointing out either that the horizontal wind may be weaker than in the 29-30 April case, or that the source region for the precipitation is more uniform over a larger area. This observation is supported by very similar radar RR time series versus height in the selected morning and afternoon periods (Fig. 5.8c). In the central time interval (12:51 UTC – 14:48 UTC) the mean RR (Z) is about 16.2 $mm \cdot h^{-1}$ (27.6 dBZ) while in the selected morning and afternoon periods, the mean RR (radar reflectivity factor) is 4.4 $mm \cdot h^{-1}$ (20.2 dBZ) and 4.1 $mm \cdot h^{-1}$ (19.6 dBZ) respectively, similar to the values found in the previous case (29-30 April 2016; Sect. 5.2.4). Following analogous cross-covariance analysis (Fig. 5.5b), the chosen radar reference height is 500 m.

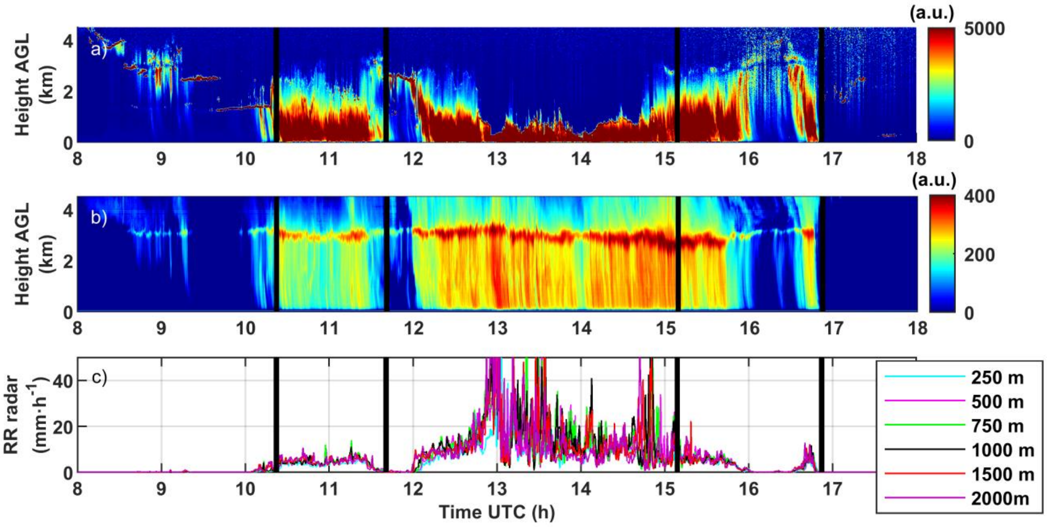

Fig. 5.8. Overview of 31 March 2016 rain episode. (a) Ceilometer range-corrected lidar signal (arbitrary units, (a.u.)) versus time. (b) Radar reflectivity factor (dBZ) computed after Eq. 5.11. (c) RR $(\mathrm{mm} \cdot \mathrm{h}^{-1})$ time series measured by the radar at different heights, from 250 m up to 2000 m. Temporal resolution (panels a-c) is 16 s. Spatial (height) resolution (panels a-c), see Table 5.1. Vertical lines delimit the morning and afternoon time intervals discussed in Sect. 5.2.1.

Fig. 5.9 shows, as Fig. 5.4c, the profile of the rain-extinction coefficient during the morning and afternoon rain periods. The average extinction coefficient during the morning event is $\alpha_{rain} = 0.34 \pm 0.05\ \mathrm{km}^{-1}$ ($I_1 = [0.5, 2.5]\ km$) and $\alpha_{rain} = 0.29 \pm 0.06\ km^{-1}$ ($I_2 = [0.3, 2.5]\ km$) during the afternoon (I_1 and I_2 indicate the slope-method fitting range intervals used). The estimated background extinction coefficients before and after the rain episode are: $\alpha_{before}^{\propto\_no\_rain} = 0.11 \pm 0.02\ km^{-1}$ (08:24 UTC – 08:26 UTC; $I_{before} = [0.3, 1.0]\ km$) and $\alpha_{after}^{\propto\_no\_rain} = 0.02 \pm 0.06\ km^{-1}$ (17:10 UTC – 17:34 UTC; $I_{after} = [0.3, 1.3]\ km$). These background-extinction values are similar to the ones obtained for the 29-30 April event (Sect. 5.2.4) and again substantially lower than the average rain-extinction coefficients above, which suggests that the aerosol is being removed (scavenged) by the precipitation.

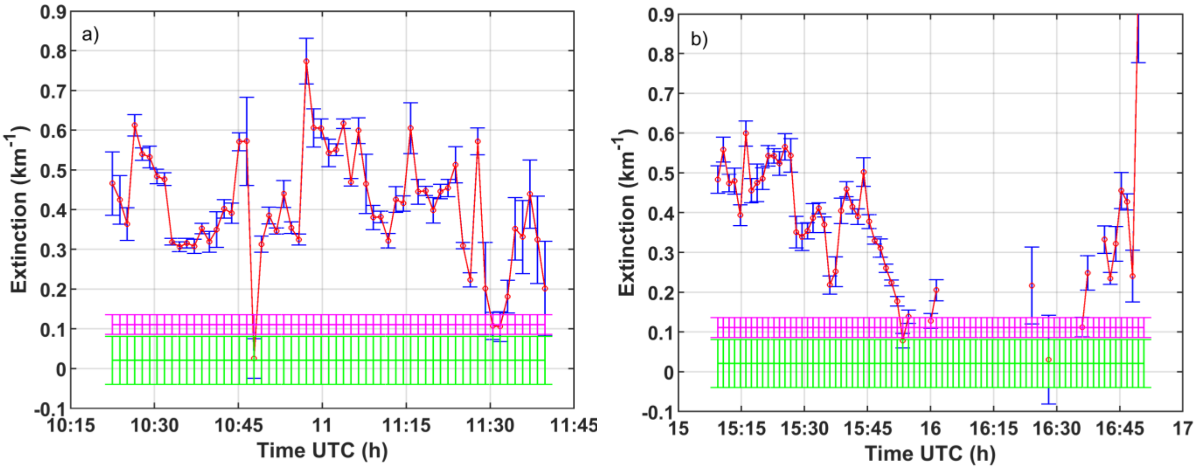

Fig. 5.9. Slope-method results (Belle Mina, AL, 31 March 2016). Time resolution 80 s, spatial resolution 200 m. (a) Morning rain interval, 10:22-11:41 UTC. 59 time bins. Same as Fig. 5.4c. (b) Afternoon rain interval, 15:09-16:52 UTC. 46 bins.

5.4.1 RR-TO-EXTINCTION MODEL

The methodology in Sect. 5.3.2 is used to estimate Eq. 5.22 *RR*-α model, considering three different dataset when deriving the fit parameters: (i) the morning dataset (see selected time period above), (ii) the afternoon dataset, and (iii) a dataset composed by joining the morning and afternoon datasets. York's linear-fitting results are shown in Fig. 5.10. The uncertainties of the fit for the morning case (Fig. 5.10a) are larger than for afternoon case (Fig. 5.10b) as shown by higher uncertainties in the estimated slope and intercept point, and higher RMSE (York's weighted $\mathrm{RMSE} = 1.49$). The low correlation coefficient obtained during the morning case, $\rho_{RRradar}^{(\alpha)} = 0.54$, which would be 0.51 without excluding outliers, is a consequence of the relatively narrow span of RR figures experienced during the morning period, mostly of the points are gathered between 3 and 6 $mm \cdot h^{-1}$, 10:22 UTC – 11:41 UTC in Fig. 5.8c). The situation in the afternoon is different because the afternoon period includes the final part of the rain event (15:09 UTC – 16:52 UTC), thus, in the selected time interval the decay of the rain intensity is well represented. As a result, although with fewer measurements (46 samples in the afternoon case as compared to 59 in the morning), a wider span of RR estimates is available. The RMSE is lower than in the morning dataset, decreases to 1.39, and the correlation coefficient increases to $\rho_{RRradar}^{(\alpha)} = 0.75$.

Fig. 5.10c shows that even though the uncertainties are larger in the morning, the data are still useful. By combining morning and afternoon datasets, the *RR*-α model benefits from a larger statistical sample (102) of RRs. The results show similar *RR*-α model parameters but with much lower uncertainties. The RMSE also decreases to 1.2, pointing out a higher goodness of fit.

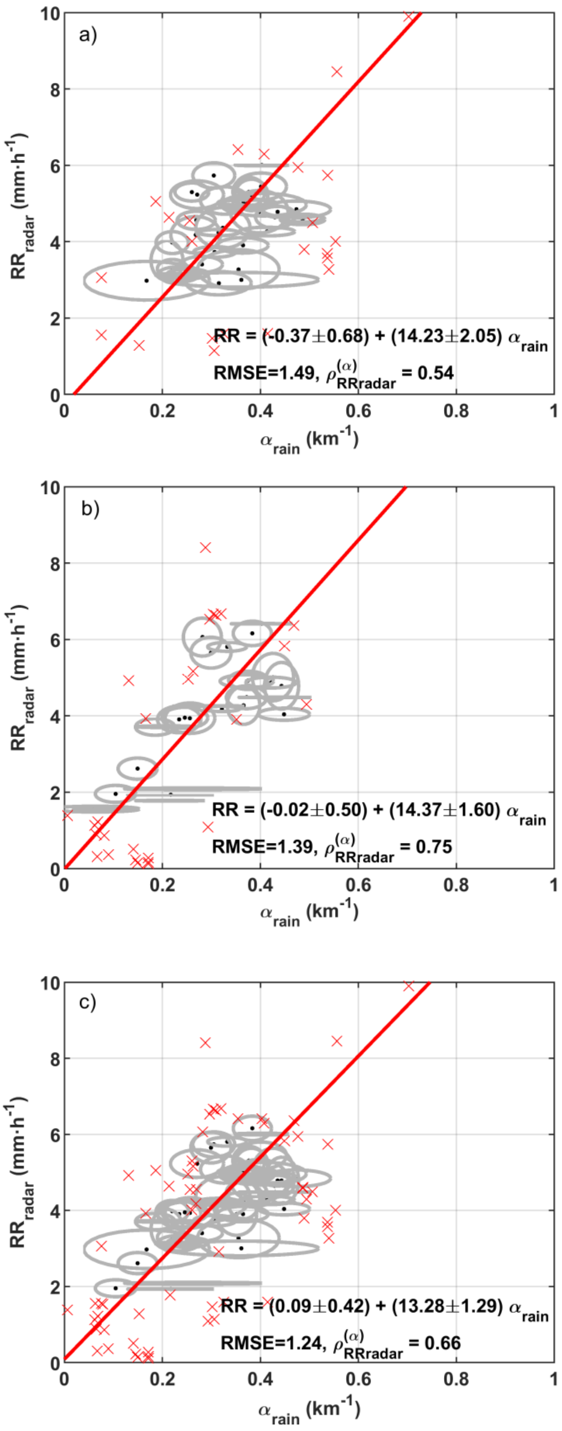

Fig. 5.10. RR-α model results (Belle Mina, AL, 31 March 2016). (a) Radar RR versus extinction estimates (radar reference height, h=500 m), morning case. (b) Afternoon case. (c) Shows the results with the morning and afternoon cases combined together. (All panels) Red crosses indicate rejected samples (outliers). (Solid red line) Linear fit with estimated errors. RMSE is the York-weighted Root Mean Square Error. $\rho^{(\propto)}_{RR\_radar}$ is the rain-rate-to-rain-extinction correlation coefficient. Gray ellipses delimit the 1σ-uncertainty locus in each variable.

Finally, Fig. 5.11 compares the RR-α models obtained for the cases 29-30 April (Sect. 5.2.1) and 31 March. The uncertainty locus due to slope and intercept-point uncertainties in York's fitting has been drawn as a shaded area. For the radar-ceilometer pair, the uncertainty locus of 29-30 April model virtually overlaps that of 31 March, which evidences that the method is consistent across these two cases. Besides, the fact that 29-30 April uncertainty region falls inside that of 31 March makes evident that model uncertainties are lower for the 29-30 April case. When the disdrometer-ceilometer pair is considered (available for April-29 case only), the disdrometer RR-α model (dashed red lines) also overlaps the radar RR-α model (both days) although slightly down-biased in RR (-0.5 to -1.5 $mm \cdot h^{-1}$ approximately). It is worth noting that some combination of systematic errors is preventing a closer match between RRs, possibly including the different sensitivities on what the different techniques measure, differential rain sedimentation and size sorting and variations in horizontal wind speed and direction during the passage of the storm.

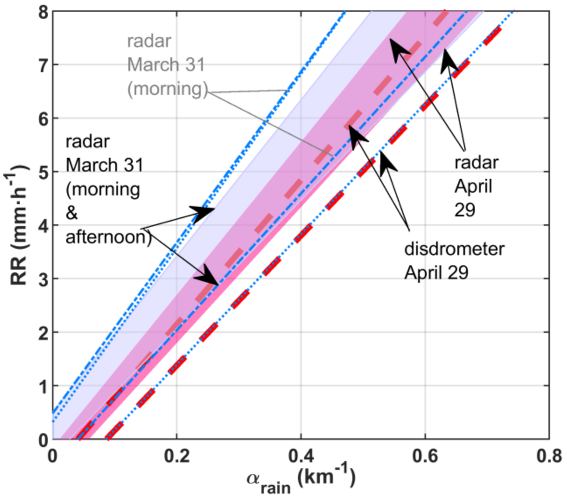

Fig. 5.11. Comparison between 29-30 April and 31 March *RR*-α models. 29-30 April case: Purple and dashed-red lines. Purple patch represents the uncertainty locus associated to the linear fit parameters of the radar *RR*-α model of Fig. 5.7a. Dashed-red lines delimit the uncertainty locus associated to the disdrometer *RR*-α model of Fig. 5.7b. 31 March case: Grey patch represents the uncertainty locus associated to the radar *RR*-α model of Fig. 5.10c (morning + afternoon). The morning case (Fig. 5.10a) is delimited by thin blue dotted lines and the afternoon case (Fig. 5.10b) by blue dash-dotted lines.

5.5 SUMMARY AND CONCLUSIONS

Vertically-pointed, 905-nm wavelength, ceilometer measurements of the optical extinction coefficient under low-to-moderate rain conditions (0.5-9.5 $mm \cdot h^{-1}$) have successfully been compared against S-band radar and ceilometer RR measurements considering two different test days from VORTEX-SE field campaign (29-30 April (Sect. 5.3) and 31 March (Sect. 5.4) 2016). The weighted RMSEs (York's weighted square root of the variance of the residuals) after fitting a linear *RR*-α model (Eq. 5.20) to the ceilometer-extinction and RR data are 1.6 $mm \cdot h^{-1}$ (radar RR) and 1.1 $mm \cdot h^{-1}$ (disdrometer RR) for the 29 April case (Sect. 5.3.2.2), and 1.2 $mm \cdot h^{-1}$ (radar RR) for the 31 March case (Sect. 5.4.1). A summary of the model uncertainty locus versus RR is shown in Fig. 5.11. A wide span of measured RR values is beneficial for regression analysis.

The rain extinction coefficient has been retrieved by using a differential formulation of the slope method [Kunz and de Leeuw, 1993] in which the height-averaged extinction is computed by subtracting the no-rain background extionction from the measured extinction under raining conditions (Sect. 5.2.3). The time-series of the layer extinction coefficient (Fig. 5.4c and Fig. 5.9) has been estimated by successive application of the method over adjacent time bins of width the smoothed temporal resolution (80 s).

The different instruments and temporal and spatial resolutions of the three involved instruments constitute an intercomparison difficulty (Sect. 5.2). Thus, while the ceilometer provides height-resolved attenuated-backscatter information, the slope-method retrieved extinction is a height-averaged product under the assumption of atmospheric homogeneity. Although there are many different error sources affecting both the measured ceilometer rain-extinction and the radar/disdrometer measured RRs, an attempt to quantify the most important ones has been made. The first error source analyzed is the uncertainty in the estimated rain-extinction coefficient; this error source is estimated by error-propagating the uncertainties in the slope used to derive the total extinction under rain conditions and the background extinction from the ceilometer attenuated backscatter measurements.

The second error source is related to the assumption that the aerosol extinction is unaffected by the precipitation. This error source is addressed by estimating the background extinction in closely spaced measurements before and after the rain event. York's method is used to estimate significant uncertainties associated with the linear regression coefficients in the empirical *RR*-α model used to derive the RR from extinction measurements. The uncertainty in the background aerosol extinction has the largest impact when the RR is small, for instance an overestimation of 0.05 km^{-1} translated into a systematic error of -0.7

$mm \cdot h^{-1}$. For higher RRs the impact of this error source is small to negligible. At higher RR values, RR estimation from ceilometer measurements is essentially limited by optical thicknesses around 1.8, which dramatically reduced the maximum measurement height to a few hundred of meters and impeded application of the slope method.

Third, is the assumption of a homogeneous atmosphere, or equivalently, a homogeneous rain curtain, which may be hampered by many different mechanisms as sudden changes in the wind horizontal speed (shear) and direction advecting the raindrops at different levels, rain streaks moving in and out of the probing column or microphysical processes. Such mechanisms can be responsible for irregular signatures and contraction and dilation of the rain curtain, contributing to decouple the column extinction estimated by the ceilometer with respect to the RR measured by the radar at the reference height, 500 m (Sect. 5.2.4.2).

Furthermore, RR estimation from ceilometer measurements is essentially limited by an optical thicknesses value around 1.8, which dramatically reduced the maximum measurement height to a few hundred of meters, hence hampering the application of the slope method. Finally, by using a manual process, based on a minimum RMSE criterion, to select the height interval over which the slope method is derived, might be causing slightly higher extinction errorbars over time intervals with larger inhomogeneities, for instance at the beginning and at the end of the rain episode, or close to the cloud base.

CHAPTER 6

Conclusions and Future Lines

This Chapter gives concluding remarks and future research lines mainly derived from Chaps. 2-5 of this Ph. D. thesis.

6.1 CONCLUSIONS

On implementation of a second depolarization channel in the CommSensLab multi-spectral lidar system.- A new depolarization sensing subsystem has been implemented to the CommSensLab 6-channel elastic/Raman lidar system (see Chapter 2), in order to enhance the capabilities of the Barcelona EARLINET station. The majority of the currently working systems use a single telescope and either a polarizing beam-splitter that separate the parallel and perpendicular polarization components of the light collected by the telescope or a non-polarizing beamsplitter plus a polarizer in one of its outputs [de Tomasi and Perrone, 2014; Engelmann et al, 2016; Freudenthaler, 2016]. These approaches present the issue of needing a very precise characterization of the crosstalk parameters of the beam-splitters. The main innovation of the system described in Sect. 2.2.6 is the use of an additional telescope (in fact, a telephoto lens) to measure the cross-polarized return signal without altering the original system.

The mechanical instability in the mutual alignment between the laser and the depolarization channel receiving telescope, has been solved and, thus, the result of the calibrations are now ranging in a medium-height value around 4, showing a deviation lower than 10% and staying stable after successive realignment procedures; while the initial calibrations show a deviation exceeding 30%. In spite of this good result, regular calibrations are still needed to decrease even more the deviation. The results of these calibrations are used in measurements performed during different aerosol load situations: dust and fire smoke (Sect. 2.2.6.3); and volume and particle depolarization ratios are compared to the ones retrieved by a collocated single-wavelength, polarization-sensitive elastic MPL system, showing a good agreement and, therefore, demonstrating the reliability of the new depolarization channel of the CommSensLab multi-wavelength lidar.

On the importance of the spectral resolution in radiative transfer models. - The importance of the correct spectral parameterization of a RTM has been presented in Chapter 3 to expand the knowledge about the effect of different parameterizations in the estimated radiative fluxes and ARE. To study different spectral parameterization, GAME and Two-Stream SW and LW radiative fluxes estimates are first compared to the fluxes measured by pyranometers and pyrgeometers (Sect. 3.3). A good agreement between the modeled SW and LW radiative fluxes and the experimental ones is found, the differences found among the analyzed data being within the experimental uncertainties (Sect. 3.3.2). Therefore, the lower spectral resolution of Two-Stream, compared to the one of GAME, and the different method used to solve the RT equation are not causing significant errors on the calculation of the fluxes.

Focusing on the SW-AREs (Sect. 3.3.3) at the TOA and at the BOA estimated by both RTMs, these AREs are in good agreement. As far as the LW spectral range is concerned, the LW-ARE at the TOA and at the BOA estimated by Two-Stream overestimates the AREs estimated by GAME on the days significantly affected by desert dust (AOD > 0.22 during 22 June), putting in evidence that this overestimation is caused by the low spectral resolution of Two-Stream in the LW spectral range and that a correct spectral parameterization of a RTM is mandatory in order to obtain reliable ARE. By means of an “optimization” procedure of the water vapor absorption coefficients and the *n* and *k* values of the refractive index, this overestimation is solved, decreasing the differences between the LW-AREs by about 80%, both at the BOA and at the TOA.

On the importance of the parameterization of the vertically-resolved properties in radiative transfer calculations. - In Sect. 3.4 GAME is fed by three different datasets composed by data from different sources (Sect. 3.4.2) in order to assess how different parameterizations affect the estimation of radiative fluxes and AREs. In terms of radiative fluxes the differences between the results obtained with the three aerosol input datasets are less than 1%. The evaluation of GAME SW and LW radiative fluxes against the fluxes measured by the aircraft, shows differences below 7%, therefore, it can be concluded that the three datasets used in Sect. 3.4 to feed GAME, bring a good performance. The variability in the SW- and LW-AREs is greater than the differences observed in the fluxes, reaching up to 33% and 26%, respectively depending on the input parameterization used. These differences are caused mostly by variations in the AOD (Sect. 3.4.3) which are slightly different for each dataset. According to the results presented in Sect. 3.4, the use of an accurate vertically-resolved aerosol properties database is crucial to feed a RTM, in order to reduce the uncertainties related to the ARE estimation.

Finally, it has been shown that, on average, the LW-ARE represents a 20% of the SW-ARE at the surface, pointing out that global models have to consider both spectral ranges to avoid overestimations on mineral dust cooling effect (negative AREs), by means of a combination of advance remote sensing data and studies on the optical and microphysical properties from aircraft measurements.

On the evolution of the aerosol optical properties during its transport over the WMB. - Chapter 4 presents, in Sect. 4.2, a study of the temporal evolution of the aerosol properties in order to identify gradients or behaviors characteristic of the WMB. Concretely, the AOD and especially its coarse-mode, presents a N-S (Ersa-Palma) increasing gradient, on a yearly basis, because of the African dust. This statement is supported by the NE-SW increasing gradient observed during the moderate event detected by the EARLINET stations participing in the SOP-1a and caused by the transport of the mineral dust over the WMB. The mineral dust outbreaks in the South (North) have a higher frequency in summer (spring). The presence of aerosols from the European continent (AOD^{f}_{440} increases) is more frequent in the North than in the South. Besides, the comparison between the three sites shows an increasing number of events with large AOD and with larger particles from North to South during the analyzed period. On the contrary, the asymmetry factor (g_{440}) ranges between similar values for mineral dust (0.71-0.73) and for pollution (0.69-0.70) causing very little inter-season and inter-site variations.

Focusing on the absorption properties, these are quite variable in the WMB because of the influence of the anthropogenic particles, except in summer in the South, where the strong influence of the mineral dust outbreaks causes a decrease in the effect of those absorption properties.

As a result, the radiative properties are also affected. AREs estimated in the WMB present the same gradient as the coarse-mode, while FE (more dependent on absorption) has no marked gradient. The presence of continental aerosols in spring in the North causes, at the BOA, a greater cooling effect at Ersa (almost double) with respect to Palma. However, at the TOA, because of the anthropogenic influence, no clear gradient is observed in the radiative properties.

On the spatio-temporal evolution of a Saharan dust event. - Sect. 4.3 is focused on the mineral dust event detected during June 2013 and gives light to the evolution of a mineral dust outbreak over the WMB. Firstly, the NE-SW increasing gradient in the AOD_{440} and in the coarse mode (decreasing gradient in the $AE_{440-870}$), commented above, is also observed during this mineral dust outbreak and it is caused by the loss of coarse mode particles during the transport of the dust plume over the WMB. This loss is mainly responsible of the rising of the dust plume base, being the dust plume detected at higher altitudes in the Italian stations than in the Spanish stations. During 22 June, the AOD_{440} and the coarse mode values in the Italian stations increase, reaching values similar to the ones retrieved in the Spanish stations, confirming the multi-intrusion aspect of the analyzed Saharan dust event. This hypothesis is supported by a detailed analysis made by means of back-trajectories and CALIPSO and airborne lidar observations.

In total, 18 SW- and LW-AREs are calculated during the studied Saharan dust event, being most of them in agreement with the literature. However, 5 cases of SW-ARE present an opposite sign (positive sign, heating effect, while the SW-AREs present negative sign in the literature) at the TOA associated with low values of SZA and to SSA values lower than 0.90, which are produced by presence of mineral dust mixed with anthropogenic particles in the atmosphere. As commented above, the anthropogenic particles increase the absorption properties of the atmospheric aerosols. Last but not least, the radiative properties are also an indicator of the multi-intrusion aspect of the Saharan dust event: the dust radiative effect in Granada on 16 June is practically the same as in Lecce on 22 June, pointing out a coarse mode reload caused by the entry of a secondary mineral dust event over southern Italy.

On the rain extinction coefficient estimation and its error sources. – RR estimation from vertically-pointed, 905 nm wavelength ceilometer measurements under moderate-to-low rain conditions (0.5-9.5 $mm \cdot h^{-1}$) has been presented in Chapter 5. In Sect. 5.2, a differential formulation of the well-known slope-method [Kunz and de Leeuw, 1993] to estimate column--averaged rain-extinction coefficients from the ceilometer attenuated backscatter profiles has been used. The rain-extinction coefficient is computed by subtracting the background (no-rain) extinction coefficient to the atmospheric total extinction coefficient computed by the slope-method. However, application of this method is limited by optical thicknesses of approximately 1.8, which causes total attenuation of the ceilometer signal and severe reduction of the maximum sounding range.

The methodology presented has considered three main error sources:

First, the uncertainty in the rain-extinction coefficient retrieved by means of the slope-method, which has been estimated by error propagating the uncertainties in the estimation of the rain-extinction and background-extinction coefficients under a RMSE criterion.

Second, the assumption that the aerosol background extinction is unaffected by precipitation. To solve this issue, the background extinction has been estimated by using closely-spaced measurements, before and after the rain event. It has been shown that errors are large for low RRs, and negligible for high RRs. As mentioned, in the latter type of situations RR estimation from ceilometer measurements is limited by optical thicknesses around 1.8.

Third, the assumption of a homogeneous atmosphere, which is hampered by many different mechanisms including wind shear (both in speed and direction), differential rain sedimentation and rain strikes coming in and out of the vertical measurement column of the remote sensing instruments. These mechanisms tend to decouple and incorrelate the column extinction measured by the ceilometer from the RR measured by the radar (at the reference height) and the disdrometer (at ground level) (Sect. 5.2.4.2).

On the *RR*-α model computation. – Accurate model relationships between (i) the ceilometer-measured rain extinction and the radar RR, and (ii) the ceilometer extinction and the disdrometer RR have successfully been estimated in Sects. 5.2-5.4. The advantage of these RR-α models is that they allow to estimate the RR from the ceilometer observations in similar situations that do not have a collocated radar or disdrometer. For the purpose of deriving the RR-α models discussed a two-step procedure has been used: (i) a histogrammed outlier-rejection step, and (ii) a covariance-weighted linear-fit step using bivariate-weighted errors (i.e., simultaneous errors in both in x and y variables). The 29-30 April, 2016 case (Sect. 5.3) has yielded RR residuals around 1.6 $mm \cdot h^{-1}$ and 1.1 $mm \cdot h^{-1}$ for the radar and the disdrometer RR-α models, respectively. Both models exhibit good correlation between the RR and rain-extinction values ($\rho^{(\alpha)}_{RR\_radar}$=0.78 and $\rho^{(\alpha)}_{RR\_disdro}$ =

0.91). These good results point out that departing from a one-off RR calibration to derive the RR-α model, the model can subsequently be used to estimate RR values directly from rain-extinction-coefficient measurements in similar situations. Sect. 5.4 has validated this methodology (Sect. 5.3) by successfully comparing the RR-α model from two different cases (31 March, 2016, early morning and late morning) to the 29-30-April case (Fig. 5.11). The estimated RR-α model residuals (ceilometer-radar) for the early-morning and late-morning 31 March cases are 1.5 $mm \cdot h^{-1}$ and 1.4 $mm \cdot h^{-1}$, respectively. The comparatively larger residuals as compated to the 29-30-April case makes evident that a larger span of RRs in the statistical sample used to build up the RR-α model is beneficial to reduce model residuals. When both datasets (early and later morning) are combined, residuals reduce to 1.2 $mm \cdot h^{-1}$ and $\rho_{RR\_radar}^{(\alpha)}$=0.66. Although not conclusive from just one single test day (April 29-30) the RR-α radar model has shown lower correlation than the disdrometer model. This may be attributable to irregular rain signatures in the downfall path caused by the combination of factors discussed above, mainly horizontal shear, at the radar reference height (500 m).

6.2 FUTURE LINES

Future research will be necessary in order to continue with the advancement in the aspects developed in this thesis, making emphasis in some topics:

(1) It has been shown that the 532 nm polarization channel has been installed in the CommSensLab lidar system with excellent results. Thus, after solving the mechanical instability, the depolarization system function presents a low deviation. Besides, this channel shows an excellent SNR because of it works without the presence of a fiber bundle, i.e., the PMT is installed directly in the optical chain. The excellent SNR allows detecting different plumes of aerosol at the same time. Within this framework, two main future research lines arise:

- Improve the stability of the mechanical parts of the channel in order to decrease, even more, the deviation of the depolarization channel system function, as of today the deviation is lower than 10%.
- Design and implementation of a 355 nm polarization channel based on the mechanical and optical design used successfully in the 532 nm polarization channel.

(2) The use of RTM models are widely spread in the WMB lidar stations, however Chapters 3 and 4 show that some atmospheric situations can invert the radiative effect, from cooling to heating effect and vice versa. Because of that, it is recommended to continue exploiting GAME RTM to obtain radiative fluxes in as much as possible atmospheric situations. Feeding RTMs with satellite data will provide radiative fluxes in areas without a lidar station and an AERONET sun-photometer.

(3) It is recommended to strengthen exploitation of the synergy among the many different VORTEX instruments (e.g., ceilometer-radar, ceilometer-disdrometer, radar-disdrometer) in the same way that lidar, sun-photometer, and radiosonde data is systematically exploited within the EARLINET stations. Analysis of VORTEX-2017 data is to be carried out in order to characterize new, interesting rain events, and to better evaluate performance and usefulness of the methodology presented in Chapter 5 with a larger statistical sample of rain events.

(4) Last but not least, the use of advanced lidar systems, for instance MPLs, which exhibit higher SNRs than ceilometers, will allow the use of the Klett-Fernald-Sasano method as well as advanced multi-wavelength extinction-retrieval methods to improve the methodologies and collaborative measurements outlined in Chapter 5.

APPENDIX A

LIST OF PUBLICATIONS

A.1. JOURNALS

1. Rocadenbosch, F., **Barragan, R.**, Frasier, S., Waldinger, J., Turner, D., Tanamachi, R., Dawson, D.: Ceilometer-based rainfall rate estimation, a case-study: comparison with S-band radar and disdrometer retrievals in the context of VORTEX-SE, submitted to *IEEE TGRS*. 2019.

2. Granados-Muñoz, M.J., Sicard, M., Román, R., Benavent-Oltra, J.A., **Barragan, R.**, Brogniez, G., Denjean, C., Mallet, M., Formenti, P., Torres, B., and Alados-Arboledas, L.: Impact of mineral dust on shortwave and longwave radiation: evaluation of different vertically-resolved parameterizations in 1-D radiative transfer computations, *Atmos. Chem. Phys.*, 19, 523-542, https://doi.org/10.5194/acp-2018-700. 2019.

3. Muñoz-Porcar, C., Comerón, A., Sicard, M., **Barragan, R.**, Garcia-Vizcaino, D., Rodríguez-Gómez, A., Rocadenbosch, F., Granados-Muñoz, M.J.: Calibration of raman lidar water vapor mixing ratio measurements using zenithal measurements of diffuse sunlight and a radiative transfer model, *IEEE TGRS*, 56 (12), doi: 10.1109/TGRS.2018.2851064. 2018.

4. Lolli, S., D'Adderio, L., Campbell, J.R., Sicard, M., Welton, E.J., Binci, A., Rea, A., Tokay, A., Comerón, A., **Barragan, R.**, Baldasano, J.M., Gonzàlez, S., Bech, J., Afflitto, N., Lewis, J.R., Madonna, F.: Vertically resolved precipitation intensity retrieved through a synergy between the ground-based NASA MPLNET Lidar network measurements, surface disdrometer datasets and an analytical model solution. *Remote Sens.*, 10, 1102. 2018.

5. Comerón, A., Rodríguez-Gómez, A., Sicard, M., **Barragan, R.**, Muñoz-Porcar, C., Rocadenbosch, F., Granados-Muñoz, M.J.: Considerations about the Determination of the Depolarization Calibration Profile of, a Two-Telescope Lidar and Its Implications for Volume Depolarization Ratio Retrieval, *Sensors*, 18, 1807, doi:10.3390/s18061807. 2018.

6. Rodríguez-Gómez, A., Sicard, M., Granados-Muñoz, M.J., Chahed, E.B., Muñoz-Porcar, C., **Barragan**, **R.**, Comerón, A., Rocadenbosch, F., Vidal, E.: An Architecture Providing Depolarization Ratio Capability for a Multi-Wavelength Raman Lidar: Implementation and First Measurements, *Sensors*, 17, 2957. doi:10.3390/s17122957. 2017.

7. Mandija, F., Sicard, M., Comerón, A., Alados-Arboledas, L., Guerrero-Rascado, J.L., **Barragan**, **R.**, Bravo-Aranda, J.A., Granados-Muñoz, M.J., Lyamani, H., Muñoz Porcar, C., Rocadenbosch, F., Rodríguez-Gomez, A., Valenzuela, A., García-Vizcaíno, D.: Origin and pathways of the mineral dust transport to two Spanish EARLINET sites: Effect on the observed columnar and range-resolved dust optical properties. *J. Atmos. Research*, 187, 69-83, doi: 10.1016/j.atmosres.2016.12.002. 2016.

8. **Barragan**, **R.**, Sicard, M., Totems, J., Léon, J.-F., Dulac, F., Mallet, M., Pelon, J., Alados-Arboledas, L., Amodeo, A., Augustin, P., Boselli, A., Bravo-Aranda, J.A., Burlizzi, P., Chazette, P., Comerón, A., D'Amico, G., Dubuisson, P., Granados-Muñoz, M.J., Leto, G., Guerrero-Rascado, J.L., Madonna, F., Mona, L., Muñoz-

Porcar, C., Pappalardo, G., Perrone, M.R., Pont, V., Rocadenbosch, F., Rodriguez-Gomez, A., Scollo, S., Spinelli, N., Titos, G., Wang, X., Zanmar Sanchez, R.: Spatio-temporal monitoring by ground-based and air- and space-borne lidars of a moderate Saharan dust event affecting southern Europe in June 2013 in the framework of the ADRIMED/ChArMEx campaign. *Air Qual Atmos Health*, 10: 261. https://doi.org/10.1007/s11869-016-0447-7. 2017.

9. Sicard, M., **Barragan**, **R.**, Muñoz-Porcar, C., Comerón, A., Mallet, M., Dulac, F., Pelon, J., Alados-Arboledas, L., Amodeo, A., Boselli, A., Bravo-Aranda, J.A., D'Amico, G., Granados-Muñoz, M.J., Leto, G., Guerrero-Rascado, J.L., Madonna, F., Mona, L., Pappalardo, G., Perrone, M.R., Burlizzi, P., Rocadenbosch, F., Rodriguez-Gomez, A., Scollo, S., Spinelli, N., Titos, G., Wang, X., Zanmar Sanchez, R.: Contribution of EARLINET/ACTRIS to the summer 2013 Special Observing Period of the ChArMEx Project. *International Journal of Remote Sensing*, 37:19, 4698-4711, doi: 10.1080/01431161.2016.1222102. 2016.

10. **Barragan**, **R.**, Romano, S., Sicard, M., Burlizzi, P., Perrone, M.R., Comeron, A.: Estimation of mineral dust direct radiative forcing at the European Aerosol Research Lidar NETwork site of Lecce, Italy, during the ChArMEx/ADRIMED summer 2013 campaign: Impact of radiative transfer model spectral resolutions. *J. Geophys. Res. Atmos.*, 121, doi:10.1002/2016JD025016. 2016.

11. Sicard, M., **Barragan**, **R.**, Dulac, F., Alados-Arboledas, L., Mallet. M.: Aerosol optical, microphysical and radiative properties at regional background insular sites in the western Mediterranean. *Atmos. Chem. Phys.* 16(18):12177-12203 doi: 10.5194/acp-16-12177-2016. 2016.

A.2. INTERNATIONAL CONFERENCES

1. **Barragan, R.**, Rocadenbosch, F., Waldinger, J., Frasier, S., Turner, D., Tanamachi, R., Dawson, D.: Rain-rate estimation from ceilometer measurements: a comparative case study using S-band radar and disdrometer retrievals. “ERAD2018: 10th European Conference on Radar in Meteorology and Hydrology: Ede-Wageningen, The Netherlands: July 1-6, 2018”. Abstracts book, p.267-268. (https://www.erad2018.nl/book-of-abstracts/).

2. Muñoz, C., Comerón, A., Sicard, M., **Barragan, R.**, García, D., Rodríguez-Gómez, A., Rocadenbosch, F.: Diffuse sunlight based calibration of the water vapor channel in the UPC Raman lidar. A: International Laser Radar Conference. "The 28th International Laser Radar Conference (ILRC 28): Bucharest, Romania, June 25-30, 2017". EDP Sciences, 2017, p. 1-4.

3. Rodríguez-Gómez, A., Sicard, M., Muñoz, C., **Barragan, R.**, Comerón, A., Rocadenbosch, F., Vidal, E.: Depolarization channel for barcelona lidar. Implementation and preliminary measurements. A: International Laser Radar Conference. "The 28th International Laser Radar Conference (ILRC 28): Bucharest, Romania, June 25-30, 2017". EDP Sciences, 2018. https://doi.org/10.1051/epjconf/201817601029.

4. **Barragan, R.**, Rocadenbosch, F., Waldinger, J., Frasier, S., Turner, D., Dawson, D., Tanamachi, R.: Rain-rate estimation from ceilometer measurements: a comparative case study using S-band radar and disdrometer retrievals. “European Geosciences Union General Assembly 2017”. Geophysical Research Abstracts, 2017, Vol. 19, EGU2017-7079, (http://meetingorganizer.copernicus.org/EGU2017/EGU2017-7079.pdf).

5. **Barragan, R.**, Sicard, M., Totems, J., Leon, J., Dulac, F., Mallet, M., Pelon, J., Alados, L., Amodeo, A., Augustin, P., Boselli, A., Bravo, J., Burlizzi, P., Chazette, P., Comeron, A., D'Amico, G., Granados, M.J., Leto, G., Guerrero Rascado, J., Madonna, F., Mona, L., Muñoz, C., Pappalardo, G., Perrone, M-R., Pont, V., Rocadenbosch, F., Rodriguez-Gomez, A., Scollo, Spinelli, N., Titos, G., Wang, X., Zanmar, R.: Spatio-temporal monitoring of a Saharan dust event affecting southern Europe by a synergy of several ground-based and air- and space-borne lidars and passive remote sensing instruments. " 8th International workshop on sand/duststorms and associated dustfall: 1-4 May 2016: Lisbon, Portugal" Book of abstracts, p.19.

6. Saeed, U., **Barragan, R.**, Rocadenbosch, F.: Enhanced signal-to-noise ratio estimation for tropospheric lidar channels. "European Geosciences Union General Assembly 2016". Geophysical research abstracts, 2016, Vol. 18, EGU2016-16946. (http://meetingorganizer.copernicus.org/EGU2016/EGU2016-16715.pdf).

7. **Barragan**, **R.,** Sicard, M., Totems, J., Léon, J.F., Dulac, F., Mallet, M., Pelon, J., Alados-Arboledas, L., Amodeo, A., Augustin, P., Boselli, A., Bravo-Aranda, J.A., Burlizzi, P., Chazette, P., Comerón, A., D'Amico, G., Granados-Muñoz, M.J., Leto, G., Guerrero-Rascado, J.L., Madonna, F., Mona, L., Muñoz-Porcar, C., Pappalardo, G., Perrone, M.R., Pont, V., Rocadenbosch, F., Rodriguez-Gomez, A., Scollo, S., Spinelli, N., Titos, G., Wang, X., Zanmar-Sanchez, R.: Spatio-temporal monitoring of a Saharan dust event affecting southern Europe by a synergy of several ground-based and air- and space-borne lidars and passive remote sensing instruments. "2nd ACTRIS-2 General Meeting, Frascati (Rome), Italy, 29 February – 4 March 2016". (http://actris2.nilu.no/Documentation/ACTRIS2IAinH2020(20152019)/Meetingdocuments.aspx).

8. **Barragan, R.**, Sicard, M., Totems, J., Comeron, A., Muñoz, C., Pappalardo, G., Rocadenbosch, F., Rodriguez-Gomez, A.: Characterization of Saharan dust ageing over the western Mediterranean Basin during a multi-intrusion event in June 2013 in the framework of the ADRIMED/ChArMEx campaign. "IEEE Young Professionals Conference on Remote Sensing 2015, Barcelona, Spain (3-4 Dec., 2015)". P.25. (http://ieee.uniparthenope.it/chapter/gold15.html)

9. **Barragan, R.**, Romano, S., Sicard, M., Burlizzi, P., Perrone, M.R., Comerón, A.: Estimation of aerosol direct radiative forcing in Barcelona and Lecce during the 2013 ADRIMED campaign. SPIE Remote Sensing 2015, 21-24 September 2015. (https://spie.org/conferences-and-exhibitions/past-conferences-and-exhibitions/remote-sensing-2015).

10. Comerón, A., Sicard, M., Vidal, E., **Barragan, R.**, Muñoz, C., Rodríguez-Gómez, A., Tiana, J., Rocadenbosch, F., Garcia, D.: Concept design of a multiwavelength aerosol lidar system with mitigated diattenuation effects and depolarization-measurement capability. A: International Laser Radar Conference. "27th International Laser Radar Conference: program booklet". New York: 2015, p. 37. (http://hdl.handle.net/2117/86013).

11. Sicard, M., Muñoz, C., Comerón, A., Rodríguez-Gómez, A., Rocadenbosch, F., **Barragan, R.**: Direct, longwave radiative forcing of mineral dust: improvement of its estimation by means of tools recently developed by the EARLINET community. A: International Laser Radar Conference. "27th International Laser Radar Conference: program booklet". New York: 2015, p. 35. (http://hdl.handle.net/2117/86011).

12. **Barragan, R.**, Sicard, M., Totems, J., Muñoz, C., Rocadenbosch, F., Rodríguez-Gómez, A., Comerón, A.: Characterization of Saharan dust ageing over the western Mediterranean Basin during a multi-intrusion event in June 2013 in the framework of the ADRIMED/ChArMEx campaign. "European Geosciences Union General Assembly 2015". Geophysical Research Abstracts Vol. 17, EGU2015-2789-1, 2015. (http://meetingorganizer.copernicus.org/EGU2015/orals/17085).

13. Sicard, M., Totems, J., **Barragan, R.**, Dulac, F., Mallet, M., Comerón, A., Alados-Arboledas, L., Augustin, P., Chazette, P., Leon, J., Olmo, F., Renard, J., Rocadenbosch, F.: Variability of Mediterranean aerosols properties at three regional background sites in the western Mediterranean Basin. A: Remote Sensing of Clouds and the Atmosphere. "Proceedings of SPIE 9242, Remote Sensing of Clouds and the Atmosphere XIX; and Optics in Atmospheric Propagation and Adaptive Systems XVII, 924201 (November 25, 2014)". Amsterdam: International Society for Photo-Optical Instrumentation Engineers (SPIE), 2014, p. 1-14. (https://doi.org/10.1117/12.2068694).

A.3. NATIONAL CONFERENCES

1. Muñoz, C., Comerón, A., Sicard, M., **Barragan, R.**, García, D., Rodríguez-Gómez, A., Rocadenbosch, F.: Diffuse sunlight based calibration of the water vapor channel in the UPC Raman lidar. “RICTA 2017: 5th Iberian Meeting on Aerosol Science and Technology: Barcelona, 4-6 July 2017”. (http://www.ricta2017.org/).

2. Rodríguez-Gómez, A., Sicard, M., Muñoz, C., **Barragan, R.**, Comerón, A., Rocadenbosch, F.: First particle depolarization ratio measurements at the Barcelona (Spain) EARLINET/ACTRIS station: developments, implementation and first results. “RICTA 2016: 4th Iberian Meeting on Aerosol Science and Technology: Aveiro: 29 June-1 July”. (http://ricta2016.web.ua.pt/)

3. Rodríguez-Gómez, A., Rocadenbosch, F., Sicard, M., Lange, D., **Barragan, R.**, Batet, O., Comerón, A., López-Márquez, M.A., Muñoz, C., Tiana, J., Tomás, S.: Multi-wavelength aerosol LIDAR signal pre-processing: practical considerations. A: Iberian Meeting on Aerosol Science and Technology. "IOP Conference Series: Earth and Environmental Science, 2015, vol.28". Elche: Institute of Physics (IOP), 2015, p. 1-7. (http://hdl.handle.net/2117/83843).

REFERENCES

AERONET: AERONET Version 2 Inversion Product Descriptions: http://aeronet.gsfc.nasa.gov/new_web/Documents/Inversion_products_V2.pdf, last access: 11 April 2016.

Ahmed, R., Siqueira, P., and Hensley, S.: Analyzing the Uncertainty of Biomass Estimates From L-Band Radar Backscatter Over the Harvard and Howland Forests, Geoscience and Remote Sensing, *IEEE Transactions on*, PP(99), 119, doi: 10.1109/TGRS.2013.2273738, 2013.

Althausen, D., Müller, D., Ansmann, A., Wandinger, U., Hube, H., Clauder, E., Zörner, S., Scanning 6-Wavelength 11-Channel Aerosol Lidar. *J. Atmos. Ocean. Technol*, *17*, 1469–1482. 2000.

Anderson, G.P., Clough, S. A., Kneizys, F. X., Chetwynd, J. H., Shettle, E. P.: AFGL atmospheric constituent profiles (0–120 km), Rep. AFGLTR- 86-0110, Air Force Geophys. Lab., Hanscom Air Force Base, Mass. 1986.

Angevine, W. M., S. K. Avery, and G. L. Kok, Virtual Heat Flux Measurements from a Boundary- Layer Profiler-RASS Compared to Aircraft Measurements, *Journal of Applied Meteorology*, 32 (12), 1901_1907, doi: 10.1175/1520 0450(1993)032<1901:VHFMFA>2.0.CO;2, 1993.

Angevine, W. M., Errors in Mean Vertical Velocities Measured by Boundary Layer Wind Profilers, *Journal of Atmospheric and Oceanic Technology*, 14 (3), 565_569, doi: 10.1175/1520-0426(1997) 014<0565:EIMVVM>2.0.CO;2, 1997.

Ansmann, A., Riebesell, M., Weitkamp, C.: Measurement of Atmospheric Aerosol Extinction Profiles with a Raman Lidar. *Optical Letters* 15 (13): 746–748. doi:10.1364/ OL.15.000746, 1990.

Ansmann, A., Bösenberg, J., Chaikovsky, A.P., Comerón, A., Eixmann, R., Freudenthaler, V., Ginoux, P., Konguem, L., Linné, H., Márquez, M.Á.L., Manoj, S., Matthias, V., Mattis, I., Mitev, V., Müller, D., Nickovic, S., Pelon, J., Sauvage, L., Sobolewsky, P., Stohl, A., Torres, O., Vaughan, G., Wandinger, U., Wiegner, M.: Long-range transport of Saharan dust to northern Europe: The 11-16 October 2001 outbreak with EARLINET, *Journal of Geophysical Research*, 108 (D24), 4783, doi:10.1029/2003JD00375, 2003.

Antón, M., A. Valenzuela, A. Cazorla, J.E. Gil, J. Fernández-Gálvez, H. Lyamani, I. Foyo-Moreno, F.J. Olmo, L. Alados-Arboledas, Global and diffuse shortwave irradiance during a strong desert dust episode at Granada (Spain), Atmospheric Research, 118, 232-239, doi: 10.1016/j.atmosres.2012.07.007, 2012.

Antón, M., A. Valenzuela, D. Mateos, I. Alados, I. Foyo-Moreno, F.J. Olmo, L. Alados-Arboledas, Longwave aerosol radiative effects during an extreme desert dust event in southeastern Spain, Atmospheric Research, 149, 18-23, doi: 10.1016/j.atmosres.2014.05.022, 2014.

Ansmann, A.; Riebesell, M.; Weitkamp, C. Measurement of atmospheric aerosol extinction profiles with a Raman lidar. *Opt. Lett.*, *15*, 746–748. 1990.

Ansmann, A., Wandinger, U., Riebesell, M., Weitkamp, C., Michaelis, W., Independent measurement of extinction and backscatter profiles in cirrus clouds by using a combined Raman elastic-backscatter lidar, *Appl. Opt.*, 31 (33), 7113-7131, 1992.

Atlas, D., Srivastava, R.C., Sekhon, R.S.: Doppler radar characteristics of precipitation at vertical incidence. *Reviews of Geophysics*, 11(1), pp.1–35. 1973.

Barlow, R.J.: Statistics: A Guide to the Use of Statistical Methods in the Physical Sciences. In D. J. Sandiford, F. Mandl, & A. C. Phillips, eds. Chichester (England): Wiley, pp. 48–67. 1989.

Barnaba, F. and Gobbi, G. P.: Aerosol seasonal variability over the Mediterranean region and relative impact of maritime, continental and Saharan dust particles over the basin from MODIS data in the year 2001, *Atmos. Chem. Phys.*, 4, 2367–2391, doi:10.5194/acp-4-2367-2004, 2004.

Barragan, R., Romano, S., Sicard, M., Burlizzi, P., Perrone, M.R., Comeron, A.: Estimation of mineral dust direct radiative forcing at the European Aerosol Research Lidar NETwork site of Lecce, Italy, during the ChArMEx/ADRIMED summer 2013 campaign: Impact of radiative transfer model spectral resolutions, *J. Geophys. Res. Atmos.*, 121, 10,237–10,261, doi:10.1002/2016JD025016. 2016.

Barragan, R., Sicard, M., Totems, J., Léon, J. F., Dulac, F., Mallet, M., Pelon, J., Alados-Arboledas, L., Amodeo, A., Augustin, P., Boselli, A., Bravo-Aranda, J. A., Burlizzi, P., Chazette, P., Comerón, A., D'Amico, G., Dubuisson, P., Granados-Muñoz, M. J., Leto, G., Guerrero-Rascado, J. L., Madonna, F., Mona, L., Muñoz-Porcar, C., Pappalardo, G., Perrone, M. R., Pont, V., Rocadenbosch, F., Rodriguez-Gomez, A., Scollo, S., Spinelli, N., Titos, G., Wang, X. and Sanchez, R. Z.: Spatio-temporal monitoring by ground-based and air- and space-borne lidars of a moderate Saharan dust event affecting southern Europe in June 2013 in the framework of the ADRIMED/ChArMEx campaign, *Air Qual. Atmos. Heal.*, 10(3), 261–285, doi:10.1007/s11869-016-0447-7, 2017.

Basart, S., Pérez, C., Cuevas, E., Baldasano, J. M., Gobbi, G. P.: Aerosol characterization in Northern Africa, Northeastern Atlantic, Mediterranean Basin and Middle East from direct-sun AERONET observations, *Atmos. Chem. Phys.*, 9, 8265–8282, doi:10.5194/acp-9-8265-2009, 2009.

Basart, S., Pérez, C., Nickovic, S., Cuevas, E., Baldasano, J.M.: Development and evaluation of the BSC-DREAM8b dust regional model over Northern Africa, the Mediterranean and the Middle East. *Tellus B* 64:1–23, 2012.

Battan, L.J.: *Radar Observations of the Atmosphere*, Univ. of Chicago Press. 1973.

Beer, A., Determination of the absorption of red light in colored liquids, *Ann. Phys*, 86, 78-88, 1852.

Behrendt, A., Nakamura, T.: Calculation of the calibration constant of polarization lidar and its dependency on atmospheric temperature. *Opt. Expres*, 10, 805–817. 2002.

Belegante, L.; Bravo-Aranda, J.A.; Freudenthaler, V.; Nicolae, D.; Nemuc, A.; Alados-Arboledas, L.; Amodeo, A.; Pappalardo, G.; D'Amico, G.; Engelmann, R., et al.: Experimental assessment of the lidar polarizing sensitivity. *Atmos. Meas. Tech. Discuss*. 1–44. 2016.

Benavent-oltra, J. A., Román, R., Granados-muñoz, M. J., Pérez-Ramírez, D., Ortiz-amezcua, P., Denjean, C., Lopatin, A., Lyamani, H., Guerrero-rascado, J. L., Fuertes, D., Dubovik, O., Chaikovsky, A., Olmo, F. J., Mallet, M. and Alados-arboledas, L.: Comparative assessment of GRASP algorithm for a dust event over Granada (Spain) during ChArMEx-ADRIMED 2013 campaign ., *Atmos. Meas. Tech.*, (July), 1–29, 2017.

Bergstrom, R. W., Pilewskie, P., Russell, P. B., Redemann, J., Bond, T. C., Quinn, P. K., Sierau, B.: Spectral absorption properties of atmospheric aerosols, *Atmos. Chem. Phys.*, 7, 5937–5943, doi:10.5194/acp-7-5937-2007, 2007.

Berk, A., Anderson, G.P., Acharya, P.K., Bernstein, L.S., Muratov, L., Lee, J., Fox, M., Adler-Golden, S.M., Chetwynd, J.H., Hoke, M.L., Lockwood, R.B., Gardner, J.A., Cooley, T.W., Borel, C.C., Lewis, P.E., Shettle, E.P., MODTRAN5: 2006 update. *Proc SPIE* 6233:62331F. 2006.

Bilbao, J., Román, R., Yousif, C., Mateos, D., De Miguel, A., Total ozone column, water vapour and aerosols effects on erythemal and global solar irradiance in Marsaxlokk, Malta, *Atmos. Environ.*, 99, 508–518. 2014.

Bioucas-Dias, J., Plaza, A., Dobigeon, N., Parente, M., Du, Q., Gader, P., Chanussot, J.: Hyperspectral unmixing overview: Geometrical, statistical, and sparse regression-based approaches, Selected Topics in Applied Earth Observations and Remote Sensing, IEEE Journal of, 5 (2), 354-379, doi: 10.1109/JSTARS.2012.2194696, 2012.

Böckmann, C., Wandinger, U., Ansmann, A., Bösenberg, J., Amiridis, V., Boselli, A., Delaval, A., Tomasi, F. D., Frioud, M., Grigorov, I. V., Hågård, A., Horvat, M., Iarlori, M., Komguem, L., Kreipl, S., Larchevêque, G., Matthias, V., Papayannis, A., Pappalardo, G., Rocadenbosch, F., Rodriguez, J.A., Schneider, J., Shcherbakov, V., Wiegner, M.: Aerosol Lidar Intercomparison in the Framework of the EARLINET Project. 2. Aerosol Backscatter Algorithms, *Appl. Opt.*, 43(4), 977–989, 2004.

Böckmann, C., Müller, D., Osterloh, L., Pornsawad, P., Papayannis, A., From EARLINET-ASOS Raman-Lidar signals to microphysical aerosol properties via advances regularizing software, pp. (II-422)-(II-425), *IEEE International Geoscience and Remote Sensing Symposium*, 2008.

Bodhaine, B.A., Wood, N.B., Dutton, E.G., Slusser, J.R., On Rayleigh Optical Depth Calculations, *Atmos. and Ocean. Technol.*, 16 (11), 1854_1861, 1999.

Boselli, A., Armenante, M., D'Avino, L., Pisani, G., Spinelli, N., Wang, X.: Characterization of atmospheric aerosol in the urban area of Napoli in the framework of EARLINET Project. *Proc. SPIE 5235*, Remote Sensing of Clouds and the Atmosphere VIII, 643 (February 16, 2004); doi:10.1117/12.514247, 2004.

Bösenberg, J., Hoff, R., Ansmann, A., Mïller, D., Antuna, J. C., Whitemann, D., Sugimoto, N., Apituley, A., Hardesty, M., Welton, J., Eloranta, E., Arshinov, Y., Kinne, S., Freudenthaler, V.: Plan for the implementation of the GAW Aerosol Lidar Observation Network (GALION), *WMO Report 1443*, World Meteorological Organization (WMO)-Global Atmosphere Watch (GAW), Hamburg, Germany (27-29 March 2007). 2007.

Bösenberg, J., Hoff, R.: Plan for the implementation of the GAW Aerosol Lidar Observation Network (GALION), *Tech. rep.*, World Meteorological Organization, Hamburg, Germany, GAW Report no. 178, WMO/TD-No. 1443, 2007.

Bösenberg, J., Matthias, V.: EARLINET: A European Aerosol Research Lidar Network to Establish an Aerosol Climatology, *Final report* (2000-2003) 191, Max-Planck Institut für Meteorologie, Hamburg (Germany), 2003.

Boucher, O. and Tanré, D.: Estimation of the aerosol perturbation to the Earth’s radiative budget over oceans using POLDER satellite aerosol retrievals, *Geophys. Res. Lett.*, 27, 1103–1106, doi:10.1029/1999GL010963, 2000.

Bravo-Aranda, J.A., de ArrudaMoreira, G., Navas-Guzmán, F., Granados-Muñoz, M.J., Guerrero-Rascado, J.L., Pozo-Vázquez, D., Arbizu-Barrena, C., Reyes, F.J.O., Mallet, M., Arboledas, L.A.: A new methodology for PBL height estimations based on lidar depolarization measurements: Analysis and comparison against MWR and WRF model-based results. *Atmos. Chem. Phys.*, 17, 6839–6851, 2017.

Browning, K.A., Wexler, R.: The determination of kinematic properties of a wind field using Doppler radar. *J. Appl. Meteor.*, 7, 105-113, doi:doi:10.1175/1520-0450(1968)007<0105:TDOKPO>2.0.CO;2., 1968.

Burton, S.P., Ferrare, R.A., Hostetler, C.A., Hair, J.W., Rogers, R.R., Obland, M.D., Butler, C.F., Cook, A.L., Harper, D.B., Froyd, K.D.: Aerosol classification using airborne High Spectral Resolution Lidar measurements-methodology and examples. *Atmos. Meas. Tech.* 5, 73–98. 2012.

Burton, S.P., Hair, J.W., Kahnert, M., Ferrare, R.A., Hostetler, C.A., Cook, A.L., Harper, D.B., Berkoff, T.A., Seaman, S.T., Collins, J.E., et al.: Observations of the spectral dependence of linear particle depolarization ratio of aerosols using NASA Langley airborne High Spectral Resolution Lidar. *Atmos. Chem. Phys*. 15, 13453–13473. 2015.

Cachorro, V. E., Toledano, C., Prats, N., Sorribas, M., Mogo, S., Berjón, A., Torres, B., Rodrigo, R., de la Rosa, J., de Frutos, A. M.: The strongest desert dust intrusion mixed with smoke over the Iberian Peninsula registered with Sun photometry, *J. Geophys. Res.*, 113, D14S04, doi:10.1029/2007JD009582. 2008.

Cantrell, C.A.: Technical Note: Review of methods for linear least-squares fitting of data and application to atmospheric chemistry problems. *Atmospheric Chemistry and Physics*, 8(17), pp.5477–5487. 2008.

Chaikovsky, A., Dubovik, O., Holben, B., Bril, A., Goloub, P., Tanré, D., Pappalardo, G., Wandinger, U., Chaikovskaya, L., Denisov, S., et al.: Lidar-Radiometer Inversion Code (LIRIC) for the retrieval of vertical aerosol properties from combined lidar/radiometer data: Development and distribution in EARLINET. *Atmos. Meas. Tech.* 9, 1181–1205. 2016.

Chazette. P., Totems, J., Ancellet, G., Pelon, J., Sicard, M.: Temporal consistency of lidar observations during aerosol transport event in the framework of the ChArMEx/ADRIMED campaign at Minorca in June 2013. *Atmos. Chem. Phys.* 16:2862–2875. doi:10.5194/acp16-2863-2016, 2016.

Chen, C., Dubovik, O., Henze, D. K., Lapyonak, T., Chin, M., Ducos, F., Litvinov, P., Huang, X., Li, L.: Retrieval of Desert Dust and Carbonaceous Aerosol Emissions over Africa from POLDER/PARASOL Products Generated by GRASP Algorithm, *Atmos. Chem. Phys. Discuss.*, https://doi.org/10.5194/acp-2018-35, in review, 2018.

Chou, C., Formenti, P., Maille, M., Ausset, P., Helas, G., Harrison, M., Osborne, S.: Size distribution, shape, and composition of mineral dust aerosols collected during the African Monsoon Multidisciplinary Analysis Special Observation Period 0: Dust and Biomass-Burning Experiment field campaign in Niger, January 2006, *J. Geophys. Res.*, 113, D00C10, doi:10.1029/2008JD009897. 2008.

CERES: CERES Terra Edition2B SSF TOA Fluxes – Accuracy and Validation: available at: https://eosweb.larc.nasa.gov/sites/ default/files/project/ceres/quality_summaries/ssf_toa_terra_ ed2B.pdf, last access: 11 April 2016.

Collis, R.T.H.; Russell, P.B. *Lidar measurements of Particles and Gases by Elastic Backscattering and Differential Absorption. In Laser Monitoring of the Atmosphere*; Hinkley, E., Ed.; Springer: New York, NY, USA, 1976; pp. 71–151.

Comerón, A., Rocadenbosch, F., Rodriguez, A., Lopez, M.A., Munoz, C., Garcia-Vizcaino, D., Sicard, M., Lidar techniques for remote sensing of the atmosphere (invited *paper), Proceedings Volume 5830, 13th International School on Quantum Electronics: Laser Physics and Applications,* Event: 13th International School on Quantum Electronics: Laser Physics and Applications, 2004, Bourgas, Bulgaria pp. 296-306, doi: 10.1117/12.618854, 2005.

Comerón, A.; Sicard, M.; Kumar, D.; Rocadenbosch, F. Use of a field lens for improving the overlap function of a lidar system employing an optical fiber in the receiver assembly. *Appl. Opt.*, 50, 5538–5544. 2011.

Comerón, A.; Sicard, M.; Vidal, E.; Barragan, R.; Muñoz, C.; Rodríguez, A.; Tiana-Alsina, J.; Rocadenbosch, F.; García-Vizcaíno, D. Concept Design of a Multiwavelength Aerosol Lidar System with Mitigated Diattenuation Effects and Depolarization-Measurement Capability. *In Proceedings of the 27th International Laser Radar Conference*, EPJ Web of Conferences. Volume 119. Article Number 23003; New York, NY, USA, 5–10 July 2015.

Contreras, R. F., Frasier, S., High-Resolution Observations of Insects in the Atmospheric Boundary Layer, *J. Atmos. Oceanic Technol.*, 25, 2176-2187, doi:10.1175/2008JTECHA1059.1, 2008.

Costa, M.J., Guerrero-Rascado, J., Sicard, M., Gómez-Amo, J.L., Ortíz-Amezcua, P., Bortoli, D., Comerón, A., Marcos, C., Bedoya, A.E., Muñoz-Porcar, C., et al.: Main features of an outstanding desert dust transport over

Iberia. *In Proceedings of the 5th Iberian Meeting on Aerosol Science and Technology (RICTA)*, Barcelona, Spain, 3–6 July 2017.

Coulter, R.L. A Comparison of Three Methods for Measuring Mixing-Layer Height. *J. Appl. Meteorol., 18*, 1495–1499. 1979.

Dawson, D.T., Bozell, J., Buckingham, J., Downing, W.L., Chavas, D.R., Mallison, H.M., Biggerstaff, M.I., Waugh, S.: Overview of Purdue's mobile disdrometer observations during VORTEX-SE. 28th *Conf. on Severe Local Storms*, Portland, Oregon, American Meteorological Society, 16A.12, https://ams.confex.com/ams/28SLS/webprogram/Paper301887.html. 2016.

De Tomasi, F.; Perrone, M.R. Multiwavelengths lidar to detect atmospheric aerosol properties. *IET Sci. Meas. Technol.*, 8, 143–149. 2014.

Deirmendjian, D., Scattering and Polarization Properties of Water Clouds and Hazes in the Visible and Infrared, *Appl. Opt.*, 3 (2), 187-196, doi: 10.1364/AO.3.000187, 1964.

Deirmendjian, D., Electromagnetic Scattering on Spherical Polydispersions, RAND Corporation, 1969.

Denjean, C., Cassola, F., Mazzino, A., Triquet, S., Chevaillier, S., Grand, N., Bourrianne, T., Momboisse, G., Sellegri, K., Schwarzenbock, A., Freney, E., Mallet, M., Formenti, P.: Size distribution and optical properties of mineral dust aerosols transported in the western Mediterranean, *Atmos. Chem. Phys., 16*(2), 1081–1104, doi:10.5194/acp-16-1081-2016, 2016.

Derimian, Y., Léon, J.-F., Dubovik, O., Chiapello, I., Tanré, D., Sinyuk, A., Auriol, F., Podvin, T., Brogniez, G., Holben, B. N.: Radiative properties of aerosol mixture observed during the dry season 2006 over M'Bour, Senegal (African Monsoon Multidisciplinary Analysis campaign), *J. Geophys. Res.*, 113, D00C09, doi:10.1029/2008JD009904, 2008.

Di Biagio, C., di Sarra, A., Meloni, D., Monteleone, F., Piacentino, S., Sferlazzo, D.: Measurements of Mediterranean aerosol radiative forcing and influence of the single scattering albedo, *J. Geophys. Res.*, 114, D06211, doi:10.1029/2008JD011037, 2009.

Di Biagio, C., Formenti, P., Balkanski, Y., Caponi, L., Cazaunau, M., Pangui, E., Journet, E., Nowak, S., Caquineau, S., Andreae O, M., Kandler, K., Saeed, T., Piketh, S., Seibert, D., Williams, E., Doussin, J. F. C.: Global scale variability of the mineral dust long-wave refractive index: A new dataset of in situ measurements for climate modeling and remote sensing, *Atmos. Chem. Phys., 17*(3), 1901–1929, doi:10.5194/acp-17-1901-2017, 2017.

di Sarra, A., Pace, G., Meloni, D., De Silvestri, L., Piacentino, S., Monteleone, F.: Surface shortwave radiative forcing of different aerosol types in the Mediterranean, *Geophys. Res. Lett.*, 35, L02714, doi:10.1029/2007GL032395, 2008.

di Sarra, A., Di Biagio, C., Meloni, D., Monteleone, F., Pace, G., Pugnaghi, S., Sferlazzo, D.: Shortwave and longwave radiative effects of the intense Saharan dust event of 25-26 March 2010 at Lampedusa (Mediterranean Sea), *J. Geophys. Res. Atmos., 116*(D23), n/a-n/a, doi:10.1029/2011JD016238, 2011.

Doviak, J.R., Zrnić, D.S.: *Doppler radar and weather observations* 2nd ed., Mineola (New York): Dover Publications. 2006.

Dubovik, O., King, M. D.: A flexible inversion algorithm for retrieval of aerosol optical properties from Sun and sky radiance measurements, *J. Geophys. Res. Atmos.*, 105(D16), 20673–20696, doi:10.1029/2000JD900282, 2000.

Dubovik, O., Smirnov, A., Holben, B.N., King, M.D., Kaufman, Y.J., Eck, T.F., Slutsker, I.: Accuracy assessment of aerosol optical properties retrieval from AERONET Sun and sky radiance measurements, *J. Geophys. Res.*, 105, 9791–9806, doi:10.1029/2000JD900040. 2000.

Dubovik, O., Holben, B. N., Lapyonok, T., Sinyuk, A., Mishchenko, M. I., Yang, P., Slutsker, I.: Non-spherical aerosol retrieval method employing light scattering by spheroids, *Geophys. Res. Lett., 29*(10), 54-1-54–4, doi:10.1029/2001GL014506, 2002a

Dubovik, O., Holben, B. N., Eck, T. F., Smirnov, A., Kaufman, Y. J., King, M. D., Tanré, D., Slutsker, I.: Variability of absorption and optical properties of key aerosol types observed in worldwide locations, *J. Atmos. Sci.*, 59, 590–608, 2002b..

Dubovik, O., Sinyuk, A., Lapyonok, T., Holben, B. N., Mishchenko, M., Yang, P., Eck, T. F., Volten, H., Muñoz, O., Veihelmann, B., van der Zande, W. J., Leon, J. F., Sorokin, M., Slutsker, I.: Application of spheroid models to account for aerosol particle nonsphericity in remote sensing of desert dust, *J. Geophys. Res. Atmos., 111*(11), D11208, doi:10.1029/2005JD006619, 2006.

Dubovik, O., Herman, M., Holdak, A., Lapyonok, T., Tanré, D., Deuzé, J. L., Ducos, F., Sinyuk, A., Lopatin, A.: Statistically optimized inversion algorithm for enhanced retrieval of aerosol properties from spectral multi-angle polarimetric satellite observations, *Atmos. Meas. Tech., 4*(5), 975–1018, doi:10.5194/amt-4-975-2011, 2011.

Dubovik, O., et al. "GRASP: a versatile algorithm for characterizing the atmosphere." SPIE Newsroom 25, 2014.

Dubuisson, P., Buriez, J. C., Fouquart, Y., High spectral resolution solar radiative transfer in absorbing and scattering media: Application to the satellite simulation, *J. Quant. Spectrosc. Radiat. Transfer*, 55, 103–126. 1996.

Dubuisson, P., Dessailly, D., Vesperini, M., Frouin, R. Water vapor retrieval over ocean using near-infrared radiometry. *J Geophys Res*., 109:D19106. doi:10.1029/2004JD004516. 2004.

Dubuisson, P., Giraud, V., Chomette, O., Chepfer, H., Pelon, J.: Fast radiative transfer modeling for infrared imaging radiometry, *J. Quant. Spectrosc. Radiat. Transf., 95*(2), 201–220, doi:10.1016/j.jqsrt.2004.09.034, 2005.

Dubuisson, P., Roger, J., Mallet, M., Dubovik, O., A Code to Compute the Direct Solar Radiative Forcing: Application to Anthropogenic Aerosols during the Escompte Experiment. In: Fischer H, Sohn BJ, Deepak A (eds). *Proc. International Radiation Symposium (IRS 2004) on Current Problems in Atmospheric Radiation*. Hampton, pp 127–130, 23–28 August 2004, Busan, Korea. 2006.

Dulac, F., Agacayak, T., Alados Arboledas, L., Alastuey, A., Ameur, Z., Ancellet, G., Assamoi, E.-M., et al.: An Update on Charmex (The Chemistry-Aerosol Mediterranean Experiment) Activities and Plans for Aerosol Studies in the Mediterranean Region. Paper presented at the European Aerosol Conference, Granada, September 2–7, 2012.

Dulac, F.: An overview of the Chemistry-Aerosol Mediterranean Experiment (ChArMEx), European Geosciences Union General Assembly, *Geophys. Res. Abstracts*, 16, EGU2014-11441, Vienna (Austria), 27 April–2 May 2014.

EARLINET, https://www.earlinet.org/, (accessed, February 2018), 2017.

Eaton, F.D., McLaughlin, S.A., Hines, J.R., A new frequency-modulated continuous wave radar for studying planetary boundary layer morphology, *Radio Science*, 30 (1), 75-88, doi: 10.1029/94RS01937, 1995.

Eck, T. F., Holben, B. N., Reid, J. S., Dubovik, O., Smirnov, A., O'Neill, N. T., Slutsker, I., Kinne, S.: Wavelength dependence of the optical depth of biomass burning, urban, and desert dust aerosols, *J. Geophys. Res. Atmos., 104*(D24), 31333–31349, doi:10.1029/1999JD900923, 1999.

Emeis, S., Schäfer, K., Münkel, C., Surface-based remote sensing of the mixing layer height; a review, *Meteorologische Zeitschrift*, 17 (5), 621-630, doi: doi:10.1127/0941-2948/2008/0312, 2008.

Engelmann, R., Kanitz, T., Baars, H., Heese, B., Althausen, D., Skupin, A., Wandinger, U., Komppula, M., Stachlewska, I.S., Amiridis, V., et al. The automated multiwavelength Raman polarization and water-vapor lidar PollyXT: The neXT generation. *Atmos. Meas. Tech.*, *9*, 1767–1784. 2016.

Escudero, M., Querol, X., Ávila, A., Cuevas, E.: Origin of the exceedances of the European daily PM limit value in regional background areas of Spain, *Atmos. Environ.*, 41, 730–744, doi:10.1016/j.atmosenv.2006.09.014, 2007.

Espinosa, W.R., Remer, L.A., Dubovik, O., Ziemba, L., Beyersdorf, A., Orozco, D., Schuster, G., Lapyonok, T., Fuertes, D., Martins, J.V.: Retrievals of aerosol optical and microphysical properties from imaging polar nephelometer scattering measurements. *Atmos. Meas. Tech.* 10, 811–824, 2017.

Esselborn, M., Wirth, M., Fix, A., Weinzierl, B., Rasp, K., Tesche, M., Petzold, A., Spatial distribution and optical properties of Saharan dust observed by airborne high spectral resolution lidar during SAMUM 2006. *Tellus Ser. B Chem. Phys. Meteorol.*, *61*, 131–143. 2009.

Fabry, F., Zawadzki, I.: Long-term radar observations of the melting layer of precipitation and their interpretation. *J. Atmos. Sci.*, 52, 838-851, doi:10.1175/1520-0469(1995)052<0838:LTROOT>2.0.CO;2. 1995.

Fernald, F.G., Hemran, B.M., Reagan, J.A., Determination of aerosol height distribution by lidar. *J. Appl. Meteorol., 11*, 482-489. 1972.

Fernald, F.G. Analysis of atmospheric lidar observations: Some comments. *Appl. Opt.* , *23*, 652–653. 1984.

Fiocco, G., Smullin, L., Detection of scattering layers in the upper atmosphere by optical radar, *Nature*, 199, 1275{1276, 1963.

Foote, G.B., Du Toit, P.S.: Terminal Velocity of Raindrops Aloft. *Journal of Applied Meteorology*, 8(2), pp.249–253. 1969.

Formenti, P., et al., STAAARTE-MED 1998 summer airborne measurements over the Aegean Sea, 2, Aerosol scattering and absorption, and radiative calculations, *J. Geophys. Res.*, 107 (D21), 4451, doi:10.1029/2001JD001536, 2002.

Forster, P., Ramaswamy, V., Artaxo, P., Berntsen, T., Betts, R., Fahey, D.W., Haywood, J., Lean, J., Lowe, D. C., Myhre, G., Nganga, J., Prinn, R., Raga, G., Schulz, M., Van Dor land, R., Changes in atmospheric constituents and in radiative forcing, in: Climate Change 2007, *The Physical Science Basis, Contribution of Working Group I to the Fourth Assessment Report of the Intergovernmental Panel on Climate Change*, edited by: Solomon, S., Qin, D., Manning, M., Chen, Z., Marquis, M., Averyt, K. B., Tignor, M., and Miller, H. L., Cambridge Univ. Press, Cambridge, UK, 129–234, 2007.

Franke, K., Ansmann, A., Müller, D., Althausen, D., Wagner, F., Scheele, R.: One-year observations of particle lidar ratio over the tropical Indian Ocean with Raman lidar, *Geophys. Res. Lett., 28*(24), 4559–4562, doi:10.1029/2001GL013671, 2001.

Freudenthaler, V.,Esselborn, M., Wiegner, M., Heese, B., Tesche, M., Ansmann, A., Müller, D., Althausen, D., Wirth, M., Fix, A., Ehret, G., Knippertz, P., Toledano, C., Gasteiger, J., Garhammer, M., Seefeldner, M.: Depolarization Calibration- Methods, EARLINET-ASOS, NA3QA, 5th workshop, Thessaloniki, 24 – 31 Feb 2008.

Freudenthaler, V., Esselborn, M., Wiegner, M., Heese, B., Tesche, M., Ansmann, A., Müller, D., Althausen, D., Wirth, M., Fix, A., et al. Depolarization ratio profiling at several wavelengths in pure Saharan dust during SAMUM 2006. *Tellus Ser. B Chem. Phys. Meteorol.*, *61*, 165–179. 2009.

Freudenthaler, V. About the effects of polarising optics on lidar signals and the Δ90 calibration. *Atmos. Meas. Tech.*, *9*, 4181–4255. 2016.

García, O. E., Díaz, A. M., Expósito, F. J., Díaz, J. P., Dubovik, O., Dubuisson, P., Roger, J.-C., Eck, T. F., Sinyuk, A., Derimian, Y., Dutton, E. G., Schafer, J. S., Holben, B. N., García, C. A.: Validation of AERONET estimates of atmospheric solar fluxes and aerosol radiative forcing by groundbased broadband measurements, *J. Geophys. Res.*, 113, D21207, doi:10.1029/2008JD010211, 2008.

García, O. E., Expósito, F. J., Díaz, J. P., Díaz, A. M.: Radiative forcing under aerosol mixed conditions, *J. Geophys. Res.*, 116, D01201, doi:10.1029/2009JD013625, 2011.

García, O. E., Díaz, J. P., Expósito, F. J., Díaz, A. M., Dubovik, O., Derimian, Y.: Aerosol Radiative Forcing: AERONET-Based Estimates, Climate Models, edited by: Druyan, L., ISBN-13: 978-953-51-0135-2, *InTech*, available at: http://www.intechopen.com/books/climate-models/ aerosol-radiative-forcing-aeronet-based-estimates (last access: 16 December 2015), 2012a.

García, O. E., Díaz, J. P., Expósito, F. J., Díaz, A. M., Dubovik, O., Derimian, Y., Dubuisson, P., Roger, J.-C.: Shortwave radiative forcing and efficiency of key aerosol types using AERONET data, *Atmos. Chem. Phys.*, 12, 5129–5145, doi:10.5194/acp-12- 5129-2012, 2012b.

Giorgi, F., Climate change Hot-spots. *Geophys. Res. Lett*. 33, L08707, 2006.

Gkikas, A., Houssos, E. E., Hatzianastassiou, N., Papadimas, C. D., Bartzokas, A.: Synoptic conditions favouring the occurrence of aerosol episodes over the broader Mediterranean basin, *Q. J. Roy. Meteor. Soc.*, 138, 932–949, doi:10.1002/qj.978, 2012.

Gkikas, A., Hatzianastassiou, N., Mihalopoulos, N., Katsoulis, V., Kazadzis, S., Pey, J., Querol, X., Torres, O.: The regime of intense desert dust episodes in the Mediterranean based on contemporary satellite observations and ground measurements, *Atmos. Chem. Phys., 13*(23), 12135–12154, doi:10.5194/acp-13-12135-2013, 2013.

Gkikas, A., Basart, S., Hatzianastassiou, N., Marinou, E., Amiridis, V., Kazadzis, S., Pey, J., Querol, X., Jorba, O., Gassó, S., Baldasano, J. M.: Mediterranean intense desert dust outbreaks and their vertical structure based on remote sensing data, *Atmos. Chem. Phys.*, 16, 8609–8642, doi:10.5194/acp-16-8609-2016, 2016.

Gobbi, G. P., Kaufman, Y. J., Koren, I., Eck, T. F.: Classification of aerosol properties derived from AERONET direct sun data, *Atmos. Chem. Phys.*, 7, 453–458, doi:10.5194/acp-7-453-2007, 2007.

Gómez-Amo, J.L., Pinti, V., Di Iorio, T., di Sarra, A., Meloni, D., Becagli, S., Bellantone, V., Cacciani, M., Fuà, D., Perrone, M.R.: The June 2007 Saharan dust event in the central Mediterranean: Observations and radiative effects in marine, urban, and sub-urban environments, *Atmospheric Environment 45*, 5385-5393, 2011.

Goodman, L.A.: On the Exact Variance of Products. J. Am. Stat. Assoc. 55, 708–713. 1960.

Gossard, E. E., *Radar research on the atmospheric boundary layer*, in Radar in Meteorology, edited by L. J. Battan, D. Atlas, and A. M. Society, chap. 5, pp. 477_527, American Meteorological Society, 1990.

Granados-Muñoz, M.J., Sicard, M., Román, R., Benavent-Oltra, J.A., Barragan, R., Brogniez, G., Denjean, C., Mallet, M., Formenti, P., Torres, B., and Alados-Arboledas, L.: Impact of mineral dust on shortwave and longwave radiation: evaluation of different vertically-resolved parameterizations in 1-D radiative transfer computations, *Atmos. Chem. Phys.*, 19, 523-542, https://doi.org/10.5194/acp-2018-700. 2019.

Groß, S., Gasteiger, J., Freudenthaler, V., Wiegner, M., Geiß, A., Schladitz, A., Toledano, C., Kandler, K., Tesche, M., Ansmann, A., et al.: Characterization of the planetary boundary layer during SAMUM-2 by means of lidar measurements. Tellus Ser. B *Chem. Phys. Meteorol*. 63, 695–705. 2011a.

Groß, S., Tesche, M., Freudenthaler, V., Toledano, C., Wiegner, M., Ansmann, A., Althausen, D., Seefeldner, M.: Characterization of Saharan dust, marine aerosols and mixtures of biomass-burning aerosols and dust by means of multi-wavelength depolarization and Raman lidar measurements during SAMUM 2. Tellus Ser. B *Chem. Phys. Meteorol.* 63, 706–724. 2011b.

Groß, S., Esselborn, M., Weinzierl, B., Wirth, M., Fix, A., Petzold, A.: Aerosol classification by airborne high spectral resolution lidar observations. *Atmos. Chem. Phys.* 13, 2487–2505. 2013.

Guan, H., Schmid, B., Bucholtz, A., Bergstrom, R.: Sensitivity of shortwave radiative flux density, forcing, and heating rate to the aerosol vertical profile, *Journal of Geophysical Research*, 115, D06209, doi:10.1029/2009JD012907, 2010.

Guerrero-Rascado, J. L., Ruiz, B., Alados-Arboledas, L.: Multi-spectral Lidar characterization of the vertical structure of Saharan dust aerosol over southern Spain. *Atmospheric Environment*, 42(11), 2668-2681, 2008.

Guleria, R.P., Kuniyal, J.C., Characteristics of atmospheric aerosol particles and their role in aerosol radiative forcing over the northwestern Indian Himalaya in particular and over India in general. *Air Qual. Atmos. Health* 9:795. doi:10.1007/s11869-015-0381-0. 2016.

Gunn, R., Kinzer, G.D.: The Terminal Velocity of Fall for Water Droplets in Stagnant Air. *Journal of Meteorology*, 6(4), pp.243–248. 1949.

Halldórsson, T., Langerholc, J., Geometrical form factors for the lidar function. *Appl. Opt.*, 17, 240–244. 1978.

Halthore, R. N., et al.: Intercomparison of shortwave radiative transfer codes and measurements, *J. Geophys. Res.*, 110, D11206, doi:10.1029/2004JD005293. 2005.

Hatzianastassiou, N., Matsoukas, C., Fotiadi, A., Stackhouse Jr., P.W., Koepke, P., Pavlakis, K.G., Vardavas, I.: Modelling the direct effect of aerosols in the solar near-infrared on a planetary scale, *Atmos. Chem. Phys.*, 7, 3211–3229. 2007.

H. C. van de Hulst: *Light scattering by small particles* 1st ed., New York: John Wiley & Sons, Ltd. 1957.

Heese, B., Freudenthaler, V., Seefeldner, M., Wiegner, M.: POLIS: a new portable system for ground-based and airborne measurements of aerosols and clouds. In: Lidar Remote Sensing in Atmospheric and Earth Sciences (eds. L. R. Bissonnette, G. Roy and G. Vallee). *Defence Research and Development*, Canada-Valcartier, Val-Belair, QU, Canada , 71–74, 2002.

Hess, M., Koepke, P., Schult, I.: Optical Properties of Aerosols and Clouds: The Software Package OPAC, Bull. *Am. Meteorol. Soc., 79*(5), 831–844, doi:10.1175/1520-0477(1998)079<0831:OPOAAC>2.0.CO;2, 1998.

Hoff, R. M., J. Bösenberg, Pappalardo, G.: The GAW Aerosol Lidar Observation Network (GALION), *IEEE International Geoscience and Remote Sensing Symposium*, Boston MA, USA, 2008.

Holben, B. N., Eck, T. F., Slutsker, I., Tanré, D., Buis, J. P., Setzer, A., Vermote, E., Reagan, J. A., Kaufman, Y. J., Nakajima, T., Lavenu, F., Jankowiak, I., Smirnov, A.: AERONET - A federated instrument network and data archive for aerosol characterization, *Remote Sens. Environ.,* 66(1), 1–16, doi:10.1016/S0034-4257(98)00031-5, 1998.

Holben, B. N., Tanré, D., Smirnov, A., Eck, T. F., Slutsker, I., Abuhassan, N., Newcomb, W. W., Schafer, J. S., Chatenet, B., Lavenu, F., Kaufman, Y. J., Castle, J. V., Setzer, A., Markham, B., Clark, D., Frouin, R., Halthore, R., Karneli, A., O'Neill, N. T., Pietras, C., Pinker, R. T., Voss, K., Zibordi, G.: An emerging ground-based aerosol climatology: Aerosol optical depth from AERONET, *J. Geophys. Res.*, 106, 12067–12097, doi:10.1029/2001JD900014, 2001.

Holben, B. N., Eck, T. F., Slutsker, I., Smirnov, A., Sinyuk, A., Schafer, J., Giles, D., Dubovik, O.: AERONET's Version 2.0 quality assurance criteria, in: Remote Sensing of the Atmosphere and Clouds, edited by: Tsay, S.-C., Nakajima, T., Ramesh P. S., and Sridharan, R., *Proc. of SPIE*, 6408, 64080Q, doi:10.1117/12.706524, 2006.

Huffaker, R.M., Hardesty, R.M., Remote sensing of atmospheric wind velocities using solid-state and CO2 coherent laser systems. *Proc. IEEE*, 84, 181–204. 1996.

Inaba, H., *Detection of Atoms and Molecules by Raman Scattering and Fluorescence*, in Laser Monitoring of the Atmosphere, edited by E. D. Hinkley, chap. 5, pp. 143-206, Springer-Verlag, New York, 1976.

İnce, T., Frasier, S.J., Muschinski, A., Pazmany, A.L., An S-band frequency-modulated continuous-wave boundary layer profiler: Description and initial results, *Radio Science*, 38 (4), doi: 10.1029/2002RS002753, 2003.

IPCC: *Climate Change 2013: The Physical Science Basis*, Contribution of Working Group I to the UN IPCC's Fifth Assessment Report, Cambridge University Press, New York (USA), 2013.

Israelevich, P., Ganor, E., Alpert, P., Kishcha, P., Stupp, A.: Predominant transport paths of Saharan dust over the Mediterranean Sea to Europe, *J. Geophys. Res. Atmos., 117*(2), n/a-n/a, doi:10.1029/2011JD016482, 2012.

Kahnert, M., Nousiainen, T., Räisänen, P.: Mie simulations as an error source in mineral aerosol radiative forcing calculations, *Q. J. R. Meteorol. Soc.*, 133, 299–307. 2007.

Karol, Y., Tanré, D., Goloub, P., Vervaerde, C., Balois, J. Y., Blarel, L., Podvin, T., Mortier, A., Chaikovsky, A.: Airborne sun photometer PLASMA: Concept, measurements, comparison of aerosol extinction vertical profile with lidar, *Atmos. Meas. Tech., 6*(9), 2383–2389, doi:10.5194/amt-6-2383-2013, 2013.

Kato, S. and Loeb, N. G.: Top-of-atmosphere shortwave broadband observed radiance and estimated irradiance over polar regions from Clouds and the Earth's Radiant Energy System (CERES) instruments on Terra, *J. Geophys. Res.*, 110, D07202, doi:10.1029/2004JD005308, 2005.

Kaufman, Y. J.: Aerosol optical thickness and atmospheric path radiance, *J. Geophys. Res.*, 98, 2677–2692, doi:10.1029/92JD02427, 1993.

Key, J., Schweiger, A.J., Tools for atmospheric radiative transfer: Streamer and FluxNet, *Comp. Geosci.*, 24, 443–451, doi:10.1016/ S0098-3004(97)00130-1. 1998.

Klett, J.D. Stable analytical inversion solution for processing lidar returns. *Appl Opt.*, *20*(2), 211–220. 1981.

Klett, J.D. Lidar inversion with Variable Bakcscatter Extinction Ratios. *Appl Opt., 24*(11), 1638-1643. 1985.

Koepke, P., Gasteiger, J., Hess, M., Technical note: optical properties of desert aerosol with non-spherical mineral particles: data incorporated to OPAC. *Atmos. Chem. Phys.* 15:5947–5956. doi:10.5194/acp-15-5947-2015. 2015.

Kokhanovsky, A.A., Macke, A.: Integral light-scattering and absorption characteristics of large, nonspherical particles. *Applied optics*, 36(33), pp.8785–8790. 1997.

Kokhanovsky, A.A., Davis, A.B., Cairns, B., Dubovik, O., Hasekamp, O.P., Sano, I., Mukai, S., Rozanov, V.V., Litvinov, P., Lapyonok, T., Kolomiets, I.S., Oberemok, Y.A., Savenkov, S., Martin, W., Wasilewski, A., Di Noia, A., Stap, F.A., Rietjens, J., Xu, F., Natraj, V., Duan, M., Cheng, T., Munro, R.: Space-based remote sensing of atmospheric aerosols: the multi-angle spectro-polarimetric frontier. *Earth Sci. Rev*. 145, 85–116, 2015.

Kokkalis, P.: Using paraxial approximation to describe the optical setup of a typical EARLINET lidar system. *Atmos. Meas. Tech.* 10, 3103–3115. 2017.

Komabayasi, M., Gonda, T., Isono, K.: Life Time of Water Drops before Breaking and Size Distribution of Fragment Droplets. *Journal of the Meteorological Society of Japan. Ser. II*, 42(5), pp.330–340. 1964.

Kotthaus, S., O'Connor, E., Münkel, C., Charlton-Perez, C., Haeffelin, M., Gabey, A. M., and Grimmond, C. S. B.: Recommendations for processing atmospheric attenuated backscatter profiles from Vaisala CL31 ceilometers, *Atmos. Meas. Tech.*, 9, 3769-3791, https://doi.org/10.5194/amt-9-3769-2016, 2016.

Kovalev, V.A., Eichinger, W.E.: Analytical Solutions of the Lidar Equation. In *Elastic Lidar. Theory, Practice, and Analysis Methods*. NJ: Wiley, pp. 105–142. 2004.

Kovalev, V. A.: *Fundamentals of the Lidar Technique*, in Elastic Lidar: Theory, Practice, and Analysis Methods, edited by V. A. Kovalev and W. E. Eichinger, chap. 3, pp. 53-104, John Wiley & Sons, Inc., USA, 2004.

Krajewski, W.F., Smith, J.A.: Radar hydrology: Rainfall estimation. *Advances in Water Resources,* 25(8–12), pp.1387–1394, 2002.

Krajewski, W.F., Kruger, A., Caracciolo, C., Golé, P., Barthes, L., Creutin, J.D., Delahaye, J.Y., Nikolopoulos, E.I., Ogden, F., Vinson, J.P.: DEVEX-disdrometer evaluation experiment: Basic results and implications for hydrologic studies. *Advances in Water Resources*, 29(2), pp.311–325, 2006.

Krekov, G.M., Models of atmospheric aerosols. In: Jennings SG (ed) Aerosol effects on climate. University of Arizona Press, Tucson, AZ, pp. 9–72. 1993.

Ku, H.H.: Notes on the use of propagation of error formulas. J. Res. Natl. Bur. Stand. Sect. C Eng. Instrum. 70C, 263. 1966.

Kumar, D., Sicard, M., Tomás, S., Muñoz, C., Rocadenbosch, F., Comerón, A.: Engineering of a water vapour, Raman, elastic-backscatter Lidar at the Technical University of Catalonia (Spain), 6367, pp. 63,670U/163,670U/12, *Proc. SPIE*, doi:10.1117/12.690701, 2006.

Kumar, D., Rocadenbosch, F., Sicard, M., Comerón, A., Muñoz, C., Lange, D., Tomás Martínez, S., Gregorio, E.: Six-channel polychromator design and implementation for the UPC elastic/Raman LIDAR. *In Proceedings of the SPIE International Symposium*—Remote Sensensing, Prague, Czech Republic, 19–20 September 2011; Volume 8182, pp. 81820W-1–81820W-10. 2011.

Kumar, D., Lange, D., Rocadenbosch, F., Tomás, S., Sicard, M., Muñoz, C., Comerón, A., Power budget and performance assessment for the RSLAB multispectral elastic/Raman lidar system, *IEEE International Geoscience and Remote Sensing Symposium*, Munich (Germany), 2012.

Kumar, D., Rocadenbosch, F. Determination of the overlap factor and its enhancement for medium-size tropospheric lidar systems: A ray-tracing approach. *J. Appl. Remote Sens*., 7, 1–15. 2013.

Kunz, G.J.: Remote Sensing of the Propagation Environment. In *AGARD Conference Proc. 502*. Neuilly sur Seine (France): AGARD, pp. 1–11. 1992.

Kunz, G.J. & de Leeuw, G.: Inversion of lidar signals with the slope method. *Applied Optics*, 32(18), pp.3249–3256. 1993.

Lack, D. A. and Cappa, C. D.: Impact of brown and clear carbon on light absorption enhancement, single scatter albedo and absorption wavelength dependence of black carbon, *Atmos. Chem. Phys.*, 10, 4207–4220, doi:10.5194/acp-10-4207-2010, 2010.

Lambert, D., Mallet, M., Ducrocq, V., Dulac, F., Gheusi, F., Kalthoff, N.: CORSiCA: a Mediterranean atmospheric and oceanographic observatory in Corsica within the framework of HyMeX and ChArMEx, *Adv. Geosci.*, 26, 125–131, doi:10.5194/adgeo-26-125-2011, 2011.

Lange, D., Kumar, D., Rocadenbosch, F.: Backscattered signal level and SNR validation methodology for tropospheric elastic lidars, *IEEE International Geoscience and Remote Sensing Symposium*, Munich (Germany), 2012.

Lange, D.: Lidar and S-band radar profiling of the atmosphere: Adaptive processing for Boundary-Layer monitoring, optical-parameter error estimation, and application cases, Ph.D. thesis, Dep. Signal Theory and Communications, Universitat Politècnica de Catalunya (UPC). https://upcommons.upc.edu/handle/2117/95440, 2014.

Landulfo, E., Papayannis, A., Artaxo, P., Castanho, A. D. A., De Freitas, A. Z., Souza, R. F., Vieira, N. D., Jorge, M. P. M. P., Sánchez-Ccoyllo, O. R., Moreira, D. S.: Synergetic measurements of aerosols over São Paulo, Brazil using LIDAR, sunphotometer and satellite data during the dry season, *Atmos. Chem. Phys., 3*(5), 1523–1539, doi:10.5194/acp-3-1523-2003, 2003.

Lee, Y.C., Wenig, M., Zhang, Z.: Dust episodes in Hong Kong (South China) and their relationship with the Sharav and Mongolian cyclones and jet stream. *Air Qual. Atmos. Health* 5:413–424. doi:10.1007/s11869-011-0134-7, 2012.

Lenoble, J., Mishchenko, M.I., Herman, M., *Absorption and scattering by molecules and particles*, in Aerosol Remote Sensing, edited by J. Lenoble, L. Remer, and D. Tanré, chap. 2, pp. 13-51, Springer-Verlag Berlin Heidelberg, 2013.

Leon, J.F., Augustin, P., Mallet, M., Bourrianne, T., Pont, V., Dulac, F., Fourmentin, M., Lambert, D., Sauvage, B.: Aerosol vertical distribution, optical properties and transport over Corsica (western Mediterranean). *Atmos. Chem. Phys. Discuss.* 15:9507–9540. doi:10.5194/acpd-15-9507-2015, 2015.

Leosphere, 2017. Windcube 100S/200S/400S. Available at: http://www.leosphere.com/products/3d-scanning/windcube-100s200s400s-turbulence-wind-lidar [Accessed November 17, 2017].

Leto, G., Zanmar-Sanchez, R., Bellassai, G., Bruno, P., Maccarone, M.C., Martinetti, E.: All Sky Camera, LIDAR and Electric Field Meter: Auxiliary instruments for the ASTRI SST-2M prototype. *AtmoHEAD 2014*, Padova, Italy, Edited by M. Doro; EPJ Web of Conferences, Volume 8 9, id. 02006, doi: 10.1051/epjconf/20158902006, 2015.

Lewandowski, P.A., Eichinger, E.W., Kruger, A., Krajewski, W.F.: Lidar-based estimation of small-scale rainfall: Empirical evidence. *Journal of Atmospheric and Oceanic Technology*, 26(3), pp.656–664, https://doi.org/10.1175/2008JTECHA1122.1. 2009.

Liao, H., Seinfeld, J.: Radiative forcing by mineral dust aerosols: Sensitivity to key variables, *J. Geophys. Res*., 103, 31,637–31,645, doi:10.1029/1998JD200036. 1998.

Lin, X., Hou, A.Y.: Estimation of rain intensity spectra over the continental United States using ground radar-gauge measurements. *Journal of Climate*, 25(6), pp.1901–1915. https://doi.org/10.1175/JCLI-D-11-00151.1 2012.

Loeb, N. G., Kato, S., Loukachine, K., Smith, N. M.: Angular distribution models for top-of-atmosphere radiative flux estimation from the Clouds and the Earth's Radiant Energy System instrument on the Terra satellite: Part I. Methodology, *J. Atmos. Ocean. Tech.*, 22, 338–351 https://doi.org/10.1175/JTECH1712.1., 2005.

Loeb, N. G., Kato, S., Loukachine, K., Manalo-Smith, N., Doelling, D. R.: Angular Distribution Models for Top-ofAtmosphere Radiative Flux Estimation from the Clouds and the Earth's Radiant Energy System Instrument on the Terra Satellite. Part II: Validation, *J. Atmos. Ocean. Tech.*, 24, 564–584, doi:10.1175/JTECH1983.1, 2007.

Lolli, S., Madonna, F., Rosoldi, M., Campbell, J. R., Welton, E. J., Lewis, J. R.: Impact of varying lidar measurement and data processing techniques in evaluating cirrus cloud and aerosol direct radiative effects, *Atmos. Meas. Tech.*, 11, 1639–1651, 2018.

Lopatin, A., Dubovik, O., Chaikovsky, A., Goloub, P., Lapyonok, T., Tanré, D., Litvinov, P.: Enhancement of aerosol characterization using synergy of lidar and sun-photometer coincident observations: The GARRLiC algorithm, *Atmos. Meas. Tech., 6*(8), 2065–2088, doi:10.5194/amt-6-2065-2013, 2013.

Lyamani, H., Olmo, F. J., Alcántara, A., Alados-Arboledas, L.: Atmospheric aerosols during the 2003 heat wave in southeastern Spain II: Microphysical columnar properties and radiative forcing, *Atmos. Environ.*, 40, 6465–6476, doi:10.1016/j.atmosenv.2006.04.047, 2006.

Lyamani, H., Valenzuela, A., Perez-Ramirez, D., Toledano, C., Granados-Muñoz, M. J., Olmo, F. J., Alados-Arboledas, L.: Aerosol properties over the western Mediterranean basin: temporal and spatial variability, *Atmos. Chem. Phys.*, 15, 2473–2486, doi:10.5194/acp-15-2473-2015, 2015.

Macke, A., Großklaus, M.: Light scattering by nonspherical raindrops. *Journal of Quantitative Spectroscopy and Radiative Transfer*, 60(3), pp.355–363. https://doi.org/10.1016/S0022-4073(98)00011-9. 1998.

Madonna, F., Amodeo, A., Boselli, A., Cornacchia, C., Cuomo, V., D'Amico, G., Giunta, A., Mona, L., Pappalardo, G.: CIAO: the CNR-IMAA advanced observatory for atmospheric research. *Atmos. Meas. Tech.* 4:1191–1208. doi:10.5194/amt-4-1191-2011, 2011.

Madonna, F.; Amato, F.; Hey, J.V.; Pappalardo, G. Ceilometer aerosol profiling versus Raman lidar in the frame of the INTERACT campaign of ACTRIS. *Atmos. Meas. Tech., 8*, 2207–2223. 2015.

Mahafza, B.R., Elsherbeni, A.Z., *Introduction to radar basics, in Matlab Simulations for Radar Systems Design*, edited by CRC-Press, chap. 1, pp. 1-71, CRC Press, Boca Raton, FL, USA, 2004.

Mahafza, B.R., *Linear FM (LFM) CW Radar* in Radar Systems Analysis and Design Using Matlab, edited by CRC-Pess, chap. 3, pp. 126-129, CRC Press, Boca Raton, FL, USA, 2005.

Mallet, M., Dubovik, O., Nabat, P., Dulac, F., Kahn, R., Sciare, J., Paronis, D., Lén, J. F.: Absorption properties of Mediterranean aerosols obtained from multi-year ground-based remote sensing observations, *Atmos. Chem. Phys.*, 13, 9195–9210, doi:10.5194/acp-13-9195-2013, 2013.

Mallet, M., Dulac, F., Formenti, P., Nabat, P., Sciare, J., Roberts, G., Pelon, J., Ancellet, G., Tanré, D., Parol, F., Denjean, C., Brogniez, G., di Sarra, A., Alados-Arboledas, L., Arndt, J., Auriol, F., Blarel, L., Bourrianne, T., Chazette, P., Chevaillier, S., Claeys, M., D' Anna, B., Derimian, Y., Desboeufs, K., Di Iorio, T., Doussin, J.-F., Durand, P., Féron, A., Freney, E., Gaimoz, C., Goloub, P., Gómez-Amo, J. L., Granados-Muñoz, M. J., Grand, N., Hamonou, E., Jankowiak, I., Jeannot, M., Léon, J.-F., Maillé, M., Mailler, S., Meloni, D., Menut, L., Momboisse, G., Nicolas, J., Podvin, T., Pont, V., Rea, G., Renard, J.-B., Roblou, L., Schepanski, K., Schwarzenboeck, A., Sellegri, K., Sicard, M., Solmon, F., Somot, S., Torres, B., Totems, J., Triquet, S., VErdier, N., Verwaerde, C., Waquet, F., Wenger, J., Zapf, P., Overview of the Chemistry-Aerosol Mediterranean Experiment/Aerosol Direct Radiative Forcing on the Mediterranean Climate (ChArMEx/ADRIMED) summer 2013 campaign, *Atmos. Chem. Phys.*, 16, 455-504, doi:10.5194/acp-16-455-2016, 2016.

Mamouri, R.E., Nisantzi, A., Ansmann, A., Hadjimitsis, D.G.: Extreme dust storm over the eastern Mediterranean in September 2015: Lidar vertical profiling of desert dust at Limassol, Cyprus. *Atmos. Chem. Phys. Discuss.*, doi:10.5194/acp-2016-354, 2016.

Manninen, T., Riihelä, A., de Leeuw, G.: Atmospheric effect on the ground-based measurements of broadband surface albedo, *Atmos. Meas. Tech.*, 5, 2675–2688, doi:10.5194/amt-5-2675-2012. 2012.

Marshall, J.S., Hitschfeld, W., Gunn, K.L.S.: Advances in radar weather. *Adv. Geophys.*, 2, pp.1–56. 1955.

Marshall, J.S., Palmer, W.M.: The size distribution of raindrops. *Journal of Me*, 5, pp.165–166. 1948.

Martner, B.E., Yuter, S.E., White, A.B., Matrosov, S.Y., Kingsmill, D.E., Ralph, F.M.: Raindrop Size Distributions and Rain Characteristics in California Coastal Rainfall for Periods with and without a Radar Bright Band. *Journal of Hydrometeorology*, 9(3), pp.408–425. Available at: http://journals.ametsoc.org/doi/abs/10.1175/2007JHM924.1. 2008.

Matthias, V., Balis, D., Bösenberg, J., Eixmann, R., Iarlori, M., Komguem, L., Mattis, I., Papayannis, A., Pappalardo, G., Perrone, M. R., Wang, X.: Vertical aerosol distribution over Europe: Statistical analysis of Raman lidar data from 10 European Aerosol Research Lidar Network (EARLINET) stations, *J. Geophys. Res.*, 109 (D18201), doi:10.1029/2004JD004638, 2004.

Mattis, I., Siefert, P., Müller, D., Tesche, M., Hiebsch, A., Kanitz, T., Schmidt, J., Finger, F., Wandinger, U., Ansmann, A.: Volcanic aerosol layers observed with multiwavelength Raman lidar over central Europe in 2008-2009, *J. Geophys. Res.: Atmospheres*, 115 (D2), n/an/a, doi: 10.1029/2009JD013472, 2010.

Mayer, B., Kylling, A., Technical note: The libRadtran software package for radiative transfer calculations – Description and examples of use, *Atmos. Chem. Phys.*, 5, 1855–1877, doi: 10.5194/acp-5-1855-2005. 2005.

McCormick, M. P., Leavor, K.R., *Active lidar remote sensing*, in Aerosol Remote Sensing, edited by J. Lenoble, L. Remer, and D. Tanré, chap. 10, pp. 283_313, Springer-Verlag Berlin Heidelberg, 2013.

McNicholas, C., Turner, D.D.: Characterizing the convective boundary layer turbulence with a High Spectral Resolution Lidar. *Journal of Geophysical Research: Atmospheres*, 119(22), p.12,910-12,927. Available at: https://agupubs.onlinelibrary.wiley.com/doi/full/10.1002/2014JD021867. 2014.

Meador, W. E., Weaver, W. R.: Two-stream approximation to radiative transfer in planetary atmospheres: A unified description of existing methods and new improvement, *J. Atmos. Sci.*, 37, 630–643. 1980.

Measures, R. M., *Interaction and Propagation of Radiation*, in Laser Remote Sensing: Fundamentals and Applications, chap. 4, pp. 138-145, Krieger, Malabar, Fla., 1992a.

Measures, R. M., *Laser Systems as Remote Sensors*, in Laser Remote Sensing: Fundamentals and Applications, chap. 6, pp. 226-233, Krieger, Malabar, Fla., 1992b

Measures, R. M., *Laser-Remote Sensor Equations*, in Laser Remote Sensing: Fundamentals and Applications, chap. 7, pp. 237-280, Krieger, Malabar, FL USA, 1992c.

Meloni, D., Di Sarra, A., DeLuisi, J., Di Iorio, T., Fiocco, G., Junkermann, W., Pace, G., Tropospheric aerosols in the Mediterranean: 2. Radiative effects through model simulations and measurements. *J. Geophys. Res.,* 108:4317. doi:10.1029/2002JD002807. 2003.

Meloni, D., Di Sarra, A., Di Iorio, T., Fiocco, G.: Direct radiative forcing of Saharan dust in the Mediterranean from measurements at Lampedusa Island and MISR space-borne observations. *J. Geophys. Res.* 109:D08206. doi:10.1029/2003JD003960, 2004.

Meloni, D., Di Sarra, A., Di Iorio, T., Fiocco G.: Influence of the vertical profile of Saharan dust on the visible direct radiative forcing, *J. Quant. Spectrosc. Ra.*, 93, 397–413, doi:10.1016/j.jqsrt.2004.08.035, 2005.

Meloni, D., Di Sarra, A., Monteleone, F., Pace, G., Piacention, S., Sferlazzo, D.M.: Seasonal transport patterns of intense dust events at the Mediterranean island of Lampedusa. *Atmos. Res.* 88:134–148. doi:10.1016/j.atmosres.2007.10.007, 2008.

Meloni, D., Junkermann, W., di Sarra, A., Cacciani, M., De Silvestri, L., Di Iorio, T., Estellés, V., Gómez-Amo, J.L., Pace, G., Sferlazzo, D.M., Altitude-resolved shortwave and longwave radiative effects of desert dust in the Mediterranean during the GAMARF campaign: Indications of a net daily cooling in the dust layer, *J. Geophys. Res. Atmos.*, 120, 3386–3407, doi:10.1002/2014JD022312. 2015.

Meloni, D., di Sarra, A., Brogniez, G., Denjean, C., De Silvestri, L., Di Iorio, T., Formenti, P., Gómez-Amo, J. L., Gröbner, J., Kouremeti, N., Liuzzi, G., Mallet, M., Pace, G., Sferlazzo, D. M.: Determining the infrared radiative effects of Saharan dust: A radiative transfer modelling study based on vertically resolved measurements at Lampedusa, *Atmos. Chem. Phys., 18*(6), 4377–4401, doi:10.5194/acp-18-4377-2018, 2018.

Merritt, D. A., A Statistical Averaging Method for Wind Profiler Doppler Spectra, *Journal of Atmospheric and Oceanic Technology*, 12 (5), 985_995, doi: 10.1175/1520 0426(1995)012<0985:ASAMFW>2.0.CO;2, 1995.

METEK (Meteorologische Messtechnik GmbH), 2009. *MRR Physical Basics*, Available at: http://www.metek.de.

Minnis, P., Young, D., Sun-Mack, S., W. Heck, P., Doelling, D. R., Trepte, Q. Z.: CERES cloud property retrievals from imagers on TRMM, Terra, and Aqua, paper presented at 10th International Symposium on Remote Sensing, Conference on Remote Sensing of Clouds and the Atmosphere VII, Soc. of Photo-Opt. *Instrum. Eng.* (SPIE), Barcelona, Spain, 8–12 September 2003.

Mishra, A. K., Klingmueller, K., Fredj, E., Lelieveld, J., Rudich, Y., Koren, I.: Radiative signature of absorbing aerosol over the eastern Mediterranean basin, *Atmos. Chem. Phys.*, 14, 7213– 7231, doi:10.5194/acp-14-7213-2014, 2014.

Mona, L., Amodeo, A., Pandol, M., Pappalardo, G.: Saharan dust intrusions in the Mediterranean area: Three years of Raman lidar measurements, *J. Geophys. Res.*, 111 (D16203), doi:10.1029/2005JD006569, 2006.

Mona, L., Liu, Z., Müller, D., Omar, A., Papayannis, A., Pappalardo, G., Sugimoto, N., Vaughan, M.: Lidar measurements for desert dust characterization: an overview. *Adv. Meteorol.* 2012:356265, 2012

Moosmüller, H., Chakrabarty, R. K., Arnott, W. P.: Aerosol light absorption and its measurement: A review, *J. Quant. Spectrosc. Ra.*, 110, 844–878, doi:10.1016/j.jqsrt.2009.02.035, 2009.

Moulin, C., Lambert, C.E., Dayan, U., Masson, V, Ramonet, M., Bousquet, P., Legrand, M., Balkanski, Y. J., Guelle, W., Marticorena, B., Bergametti, G., Dulac, F.: Satellite climatology of African dust transport in the Mediterranean atmosphere, *J. Geophys. Res.*, 103, 13137-13144, doi:10.1029/98JD00171, 1998.

Murayama, T., Müller, D., Wada, K., Shimizu, A., Sekiguchi, M., Tsukamoto, T.: Characterization of Asian dust and Siberian smoke with multi-wavelength Raman lidar over Tokyo, Japan in Spring 2003. *Geophys. Res. Lett*, 31. 2004.

Müller, D., Ansmann, A., Mattis, I., Tesche, M., Wandinger, U., Althausen, D., Pisani, G.: Aerosol type-dependent lidar ratio observed with Raman lidar, *J. Geophys. Res.*, 112, D16,202, doi:10.1029/2006JD008292, 2007.

Müller, D., Veselovskii, I., Kolgotin, A., Tesche, M., Ansmann, A., Dubovik, O.: Vertical profiles of pure dust and mixed smoke–dust plumes inferred from inversion of multiwavelength Raman/polarization lidar data and comparison to AERONET retrievals and in situ observations. *Appl. Opt*. 52, 3178–3202. 2013.

Nabat, P., Somot, S., Mallet, M., Michou, M., Sevault, F., Driouech, F., Meloni, D., di Sarra, A., Di Biagio, C., Formenti, P., Sicard, M., Léon, J.-F., Bouin, M.-N.: Dust aerosol radiative effects during summer 2012 simulated with a coupled regional aerosol–atmosphere–ocean model over the Mediterranean, *Atmos. Chem. Phys.*, 15, 3303-3326, doi:10.5194/acp-15-3303-2015, 2015.

Nikolopoulos, E.I., Kruger, A., Krajewski, W.F., Williams, C.R., Gage, K.S.: Comparative rainfall data analysis from two vertically pointing radars, an optical disdrometer, and a rain gauge. *Nonlinear Processes in Geophysics*, 15(6), pp.987–997, doi: 10.5194/npg-15-987-2008. 2008.

O'Connor, E.J., Illinworth, A.J., Hogan, R.J.: A Technique for Autocalibration of Cloud Lidar. *Journal of Atmospheric and Oceanic Technology*, 21(5), pp.777–786. https://doi.org/10.1175/1520-0426(2004)021<0777:ATFAOC>2.0.CO;2. 2004.

Olmo, F.J., Quirantes, A., Lara, V., Lyamani, H., Alados-Arboledas, L.: Aerosol optical properties assessed by an inversion method using the solar principal plane for non-spherical particles. *J. Quant. Spectrosc. Radiat. Transf.* 109, 1504–1516. 2008.

Omar, A. H., Won, J. G., Winker, D. M., Yoon, S. C., Dubovik, O., McCormick, M. P.: Development of global aerosol models using cluster analysis of Aerosol Robotic Network (AERONET) measurements, *J. Geophys. Res.*, 110, D10S14, doi:10.1029/2004JD004874, 2005.

Osada, K., Ura, S., Kagawa, M., Mikami, M., Tanaka, T.Y., Matoba, S., Aoki, K., Shinoda, M., Kurosaki, Y., Hayashi, M., Shimizu, A., Uematsu, M.: Wet and dry deposition of mineral dust particles in Japan: factors related to temporal variation and spatial distribution. *Atmos. Chem. Phys.* 14:1107–1121. doi:10.5194/acp-14-1107-2014, 2014.

OTT Messtechnik, 2004. *Operating instructions*, Available at: http://www.ott.com/en-us/products/meteorological-sensors/ott-parsivel2/ [Accessed December 21, 2017].

Ottersten, H., Atmospheric Structure and Radar Backscattering in Clear Air, *Radio Science*, 4 (12), 1179_1193, doi: 10.1029/RS004i012p01179, 1969.

Pal, S.R., Carswell, A.I.: Polarization properties of lidar backscattering from clouds. *Appl. Opt.* 12, 1530–1535. 1973.

Pandolfi, M., Gonzalez-Castanedo, Y., Alastuey, A., de la Rosa, J. D., Mantilla, E., Sanchez de la Campa, A., Querol, X., Pey, J., Amato, F., Moreno, T.: Source apportionment of PM10 and PM2.5 at multiple sites in the strait of Gibraltar by PMF: impact of shipping emissions, *Environ. Sci. Pollut. Res.*, 18, 260–269, doi:10.1007/s11356-010-0373-4, 2011.

Papadimas, C. D., Hatzianastassiou, N., Matsoukas, C., Kanakidou, M., Mihalopoulos, N., Vardavas, I.: The direct effect of aerosols on solar radiation over the broader Mediterranean basin, *Atmos. Chem. Phys., 12*(15), 7165–7185, doi:10.5194/acp-12-7165-2012, 2012.

Papayannis, A., Amiridis, V., Mona, L., Tsaknakis, G., Balis, D., Bösenberg, J., Chaikovski, A., Tomasi, F. D., Grigorov, I., Mattis, I., Mitev, V., Müller, D., Nickovic, S., Pérez, C., Pietruczuk, A., Pisani, G., Ravetta, F., Rizi, V., Sicard, M., Trickl, T., Wiegner, M., Gerding, M., Mamoury, R., D’Amico, G., Pappalardo, G.: Systematic lidar observations of Saharan dust over Europe in the frame of EARLINET (2000-2002), *J. Geophys. Res.*, 113 (D10204), doi:10.1029/2007JD009028, 2008.

Papayannis, A., Mamouri, R.E., Amiridis, V., Kazadzis, S., Pérez, C., Tsaknakis, G., Kokkalis, P., Baldasano, J.M.: Systematic lidar observations of Saharan dust layers over Athens, Greece in the frame of EARLINET project (2004-2006). *Ann. Geophys.* 27:3611–3620, 2009.

Pappalardo, G., Amodeo, A., Mona, L., Pandol, M., Pergola, N., Cuomo, V.: Raman lidar observations of aerosol emitted during the 2002 Etna eruption, *Geophys. Res. Lett.*, 31, 2004a.

Pappalardo, G. , Amodeo, A., Pandolfi, M., Wandinger, U., Ansmann, A., Bösenberg, J., Matthias, V., Amoiridis, V., Tomasi, F. D., Frioud, M., Iarlori, M., Komguem, L., Papayannis, A., Rocadenbosch, F., Wang, X.: Aerosol Lidar Intercomparison in the Framework of the EARLINET Project. 3. Raman Lidar Algorithm for Aerosol Extinction, Backscatter, and Lidar Ratio” *Appl. Opt.*, 43(28), 5370–5385, 2004b.

Pappalardo, G., Mona, L., D'Amico, G., Wandinger, U., Adam, M., Amodeo, A., Ansmann, A., Apituley, A., Alados Arboledas, L., Balis, D., Boselli, A., Bravo-Aranda, J. A., Chaikovsky, A., Comeron, A., Cuesta, J., De Tomasi, F., Freudenthaler, V., Gausa, M., Giannakaki, E., Giehl, H., Giunta, A., Grigorov, I., Groβ, S., Haeffelin, M., Hiebsch, A., Iarlori, M., Lange, D., Linné, H., Madonna, F., Mattis, I., Mamouri, R.-E., McAuliffe, M. A. P., Mitev, V., Molero, F., Navas-Guzman, F., Nicolae, D., Papayannis, A., Perrone, M. R., Pietras, C., Pietruczuk, A., Pisani, G., Preiÿler, J., Pujadas, M., Rizi, V., Ruth, A. A., Schmidt, J., Schnell, F., Seifert, P., Serikov, I., Sicard, M., Simeonov, V., Spinelli, N., Stebel, K., Tesche, M., Trickl, T., Wang, X., Wagner, F., Wiegner, M.. and Wilson, K. M. Four-dimensional distribution of the 2010 Eyjafjallajökull volcanic cloud over Europe observed by EARLINET, Atmospheric Chemistry and Physics, 13 (8), 44294450, doi: 10.5194/acp-13-4429-2013, 2013.

Pappalardo, G., Amodeo, A., Apituley, A., Comeron, A., Freudenthaler, V., Linné, H., Ansmann, A., Bösenberg, J., D’Amico, G., Mattis, I., Mona, L., Wandinger, U., Amiridis, V., Alados-Arboledas, L., Nicolae, D., Wiegner, M.: EARLINET: towards an advanced sustainable European aerosol lidar network, *Atmos. Meas. Tech.*, 7, 2389–2409, doi:10.5194/amt-7-389-2014, 2014.

Pelon, J., Flamant, C., Chazette, P., Leon, J.F., Tanre, D., Sicard, M., Satheesh, SK.: Characterization of aerosol spatial distribution and optical properties over the Indian Ocean from airborne LIDAR and radiometry during INDOEX’99. *J Geophys Res-Atmos* 107:8029. doi:10.1029/2001JD000402, 2002.

Pérez, C., Nickovic, S., Baldasano, J.M., Sicard, M., Rocadenbosch, F., Cachorro, V.E.: A long Saharan dust event over the western Mediterranean: Lidar, Sun photometer observations, and regional dust modeling. *J. Geophys. Res.* 111:D15214. doi:10.1029/2005JD006579, 2006a.

Pérez, C., Nickovic, S., Pejanovic, G., Baldasano, J.M., Özsoy, E.: Interactive dust-radiation modeling: a step to improve weather forecasts. *J. Geophys. Res.* 111:D16206. doi:10.1029/2005JD006717, 2006b.

Peris-Ferrús, C., Gómez-Amo, J.L., Marcos, C., Freile-Aranda, M.D., Utrillas, M.P., Martínez-Lozano, J.A.: Heating rate profiles and radiative forcing due to a dust storm in the Western Mediterranean using satellite observations, *Atmospheric Environment* 160, 142-153, 2017.

Perrone, M.R., Bergamo, A.: Direct radiative forcing during Sahara dust intrusions at a site in the Central Mediterranean: Anthropogenic particle contribution, *Atmos. Res., 101*(3), 783–798, doi:10.1016/j.atmosres.2011.05.011, 2011.

Perrone, M.R., Tafuro, A.M., Kinne, S.: Dust layer effects on the atmospheric radiative budget and heating rate profiles, *Atmos. Environ.*, 59, 344–354, doi:10.1016/J.ATMOSENV.2012.06.012, 2012.

Perrone, M. R., De Tomasi, F., Gobbi, G. P.: Vertically resolved aerosol properties by multi-wavelength lidar measurements, *Atmos. Chem. Phys.*, 14, 1185–1204, doi:10.5194/acp-14-1185- 2014, 2014.

Petzold, A., Rasp, K., Weinzierl, B., Esselborn, M., Hamburger, T., Dörnbrack, A., Kandler, K., Schütz, L., Knippertz, P., Fiebig, M., Virkkula, A.: Saharan dust absorption and refractive index from aircraft-based observations during SAMUM 2006, *Tellus*, 61B, 118–130, doi:10.1111/j.1600-0889.2008.00383.x, 2009.

Pollard, B.D., Khanna, S., Frasier, S.J., Wyngaard, J.C., Thomson, D.W. McIntosh, R.E.: Local structure of the convective boundary layer from a volume-imaging radar, *J. Atmos. Sci.*, 57, 22812296, doi: 10.1175/1520-0469(2000)0572.0.CO;2, 2000.

Proakis, J.G., Manolakis, D.G.: Design of Digital Filters. In *Digital Signal Processing. Principles, Algorithms and Applications*. NJ: Pearson, Prentice-Hall, pp. 654–749. 2007.

Pruppacher, H.R., Beard, K. V.: A wind tunnel investigation of the internal circulation and shape of water drops falling at terminal velocity in air. *Quarterly Journal of the Royal Meteorological Society*, 96(408), pp.247–256. https://doi.org/10.1002/qj.49709640807. 1970.

Pruppacher, H.R., Pitter, R.L.: A Semi-Empirical Determination of the Shape of Cloud and Rain Drops. *Journal of the Atmospheric Sciences*, 28(1), pp.86–94. https://doi.org/10.1175/1520-0469(1971)028<0086:ASEDOT>2.0.CO;2. 1971.

Ralph, F.M.: Using radar-measured radial vertical velocities to distinguish precipitation scattering from clear-air scattering. *J. Atmos. Oceanic Technol.*, 12, 257-267, doi:10.1175/1520-0426(1995)012<0257:URMRVV>2.0.CO;2. 1995.

Rasmussen, E.N., Koch, S.: VORTEX-SE: Lessons learned and early results. 28th Conf. on Severe Local Storms, Portland, Oregon, American Meteorological Society, 3.2, https://ams.confex.com/ams/28SLS/webprogram/Paper301782.html. 2016.

Reba, M.N.M., Rocadenbosch, F., Sicard, M., Muñoz, C., Tomas, S.: Piece-wise variance method for signal-to-noise ratio estimation in elastic/Raman lidar signals. *International Geoscience and Remote Sensing Symposium (IGARSS)*, pp.3158–3161. doi: 10.1109/IGARSS.2007.4423515. 2007.

Reba, M.N.M., Rocadenbosch, F., Sicard, M., Kumar, D., Tomás, S., On the lidar ratio estimation from the synergy between aeronet sun-photometer data and elastic lidar inversion, pp. 883_886, *Proc. 25th International Laser Radar Conference*, St. Petersburg (Russia), ISBN: 978-5-94458-109-9, 2010.

Redemann, J., Turco, R. P., Liou, K. N., Russell, P. B., Bergstrom, R. W., Schmid, B., Livingston, J. M., Hobbs, P. V., Hartley, W. S., Ismail, S., Ferrare, R. A., Browell, E. V.: Retrieving the vertical structure of the effective aerosol complex index of refraction from a combination of aerosol in situ and remote sensing measurements during TARFOX, *J. Geophys. Res.*, 105, 9949–9970, doi:10.1029/1999JD901044, 2000.

Remote Sensing Laboratory (RSLAB), Universitat Politècnica de Catalunya (UPC), "Optical Remote Sensing Group," http://www.tsc.upc.edu/ors/. Accessed on Feb 1, 2018.

Rensch, D.B., Long, R.K.: Comparative Studies of Extinction and Backscattering by Aerosols, Fog, and Rain at 10.6 micro and 0.63 micro. *Applied optics*, 9(7), pp.1563–73. doi: 10.1364/AO.9.001563. 1970.

Ricchiazzi, P., Yang, S., Gautier, C., Sowle, D., SBDART: a research and teaching software tool for plane-parallel radiative transfer in the Earth's atmosphere. *B. Am. Meteor. Soc.* 79: 2101–2114. doi:10.1175/1520-0477(1998), 1998.

Richter, J. H., High resolution tropospheric radar sounding, *Radio Science*, 4 (12), 1261_1268, doi: 10.1029/RS004i012p01261, 1969.

Riley, J. , Radar cross section of insects, *Proc. IEEE*, vol. 73, no. 2, pp. 228–232, Feb. 1985.

Rocadenbosch, F.: Lidar Sensing of the Atmosphere: Receiver Design and Inversion Algorithms for an Elastic System, Ph.D. thesis, Dep. Signal Theory and Communications, Universitat Politècnica de Catalunya (UPC). http://www.grss-ieee.org/education/ phd-theses/ , 1996.

Rocadenbosch, F., Comerón, A., Pineda, D.: Assessment of Lidar Inversion Errors for Homogeneous Atmospheres. *Applied Optics*, 37(12), p.2199. https://doi.org/10.1364/AO.37.002199. 1998.

Rocadenbosch, F., *Lidar-Wind, Raman and Other Sensing*, in Encyclopedia of Optical Engineering, edited by D. D. Driggers, pp. 1114_1127, Marcel Dekker, New York, ISSN 0.8247-0939-X (print format), ISSN 0-8247-0940-3 (electronic format), 2003a

Rocadenbosch, F., *Lidar - Aerosol Sensing*, in Encyclopaedia of Optical Engineering, edited by R. G. Driggers, pp. 1090_1102, Marcel Dekker, USA, 2003b.

Rocadenbosch, F., Reba, M.N.M., Sicard, M., Comerón, A., Practical analytical backscatter error bars for elastic one-component lidar inversion algorithm, *Appl. Opt.*, 49 (17), 3380-3393, 2010a.

Rocadenbosch, F., Frasier, S., Kumar, D., Lange, D., Gregorio, E., Sicard, M., Backscatter Error Bounds for the Elastic Lidar Two-Component Inversion Algorithm, *Geoscience and Remote Sensing*, IEEE Transactions on, 50 (11), 4791_4803, doi: 10.1109/TGRS.2012.2194501, 2012.

Rodríguez, S., Alastuey, A., Alonso-Pérez, S., Querol, X., Cuevas, E., Abreu-Afonso, J., Viana, M., Pérez, N., Pandolfi, M., de la Rosa, J.: Transport of desert dust mixed with North African industrial pollutants in the subtropical Saharan Air Layer, *Atmos. Chem. Phys.*, 11, 6663–6685, doi:10.5194/acp-11-6663- 2011, 2011.

Rodríguez-Gómez, A., Sicard, M., Granados-Muñoz, M.J., Ben CHahed, E., Muñoz-Porcar, C., Barragán, R., Comerón, A., Rocadenbosch, F., Vidal, E., An Architecture Providing Depolarization Ratio Capability for a Multi-Wavelength Raman Lidar: Implementation and First Measurements. *Sensors*, 17, 2957; doi: 10.3390/s17122957, 2017.

Roger, J. C., Mallet, M., Dubuisson, P., Cachier, H., Vermote, E., Dubovik, O., Despiau, S., A synergetic approach for estimating the local direct aerosol forcing: Application to an urban zone during the Experience sur Site pour Contraindre les Modèles de Pollution et de Transport d'Emission (ESCOMPTE) experiment, *J. Geophys. Res.*, 111, D13208, doi:10.1029/2005JD006361. 2006.

Rogers, R.R.: A review of multiparameter radar observations of precipitation. *Radio Science*, 19(1), pp.23–36. https://doi.org/10.1029/RS019i001p00023. 1984.

Román, R., Antón, M., Valenzuela, A., Gil, J.E., Lyamani, H., de Miguel, A., Olmo, F. J., Bilbao, J., Alados-Arboledas, L., Evaluation of the desert dust effects on global, direct and diffuse spectral ultraviolet irradiance, *Tellus B*, 65, 19578, doi:10.3402/tellusb.v65i0.19578. 2013.

Román, R., Torres, B., Fuertes, D., Cachorro, V.E., Dubovik, O., Toledano, C., Cazorla, A., Barreto, A., Bosch, J.L., Lapyonok, T., González, R., Goloub, P., Perrone, M.R., Olmo, F.J., Alados-Arboledas, L.: Remote sensing of lunar aureole with a sky camera: Adding infomration in the nocturnal retreival of aerosol properties with GRASP code, *Remote Sens. Environ.*, 196, 238-252, http://dx.doi.org/10.1016/j.rse.2017.05.013, 2017.

Román, R., Benavent-Oltra, J.A., Casquero-Vera, J.A., Lopatin, A., Cazorla, A., Lyamani, H., Denjean, C., Fuertes, D., Pérez-Ramírez, D., Torres, B., Toledano, C., Dubovik, O., Cachorro, V.E., de Frutos, A.M., Olmo, F.J., Alados-Arboledas, L.: Retrieval of aerosol profiles combining sunphotometer and ceilometer measurements in GRASP code, *Atmos. Res.*, 204, 161-177, https://doi.org/10.1016/j.atmosres.2018.01.021, 2018.

Romano, S., Burlizzi, P., Perrone, M.R., Experimental determination of short- and long-wave dust radiative effects in the central Mediterranean and comparison with model results, *Atmos. Res.*, 171, 5–20, doi:10.1016/j.atmosres.2015.11.019. 2016.

Roy, G., Bissonnette, L.R.: Strong dependence of rain-induced lidar depolarization on the illumination angle: experimental evidence and geometrical-optics interpretation. *Applied optics*, 40, pp.4770–4789. https://doi.org/10.1364/AO.40.004770. 2001.

Russell, P.B., Bergstrom, R.W., Shinozuka, Y., Clarke, A.D., De-Carlo, P.F., Jimenez, J.L., Livingston, J. M., Redemann, J., Dubovik, O., Strawa, A.: Absorption Angstrom exponent in AERONET and related data as an indicator of aerosol composition, Atmos. Chem. Phys., 10, 1155–1169, doi:10.5194/acp-10-1155-2010. 2010.

Saeed, U., Rocadenbosch, F., Crewell, S.: Adaptive Estimation of the Stable Boundary Layer Height Using Combined Lidar and Microwave Radiometer Observations. *IEEE Transactions on Geoscience and Remote Sensing*, 54(12), pp.6895–6906. doi: 10.1109/TGRS.2016.2586298. 2016.

Sasano, Y., Nakane, H. significance of the extinction backscatter ratio and the boundary-value term in the solution for the 2-component lidar equation. *Appl Opt, 23* (1), 11-13. 1984.

Sassen, K., Hsueh, C.: Contrail properties derived from high-resolution lidar studies during SUCCESS *Geophys. Res. Lett*. 25, 1165–1168. 1998.

Sassen, K. Polarization in Lidar. In *Lidar*; Weitkamp, C., Ed.; Springer: New York, NY, USA,; pp. 19–42 2005.

Saunders, R. W., Brogniez, G., Buriez, J. C., Meerkotter, R., Wendling, P.: A comparison of measured and modeled broadband fluxes from aircraft data during the ICE ’89 field experiment, *J. Atmos. \& Ocean. Technol., 9*(4), 391–406, doi:10.1175/1520-0426(1992)009<0391:ACOMAM>2.0.CO;2, 1992.

Sauvageot, H., *Radar meteorology*, 374 pp., Artech House, 1992a.

Sauvageot, H., *Basic concepts of radar*, in Radar meteorology, chap. 1, pp. 1-68, Artech House, Norwood, MA, USA, 1992b.

Sauvageot, H.: The Probability Density Function of Rain Rate and the Estimation of Rainfall by Area Integrals. *Journal of Applied Meteorology*, 33(NOVEMBER), pp.1255–1262. https://doi.org/10.1175/1520-0450(1994)033<1255:TPDFOR>2.0.CO;2. 1994.

Sawamura, P., Vernier, J., Barnes, J., Berkoff, T., Welton, E., Alados-Arboledas, L., Navas-Guzmán, F., Pappalardo, G., Mona, L., Madonna, F., Lange, D., Sicard, M., Godin-Beekmann, S., Payen, G., Wang, Z., Hu, S., Tripathi, S., Córdoba-Jabonero, C., Hoff, R.: Stratospheric AOD after the 2011 eruption of Nabro volcano measured by lidars over the Northern Hemisphere, *Environmental Research Letters*, 7 (3), 034,013, 2012.

Schotland, R.M., Sassen, K., Stone, R.: Observations by Lidar of Linear Depolarization Ratios for Hydrometeors. *J. Appl. Meteorol*. 10, 1011–1017. 1971.

Schuster, G. L., Dubovik, O., Holben, B. N.: Angstrom exponent and bimodal aerosol size distributions, *J. Geophys. Res.*, 111, D07207, doi:10.1029/2005JD006328, 2006.

Sciare, J., Dulac, F., Feron, A., Crenn, V., Sarda Esteve, R., Baisnee, D., Bonnaire, N., Hamonou, E., Mallet, M., Lambert, D., Nicolas, J. B., Bourrianne, T., Petit, J.E., Favez, O., Canonaco, F., Prevot, A., Mocnik, G., Drinovec, L., Marpillat, A., Serrie, W.: Carbonaceous aerosols in the Western Mediterranean during summertime and their contribution to the aerosol optical properties at ground level: First results of the ChArMExADRIMED 2013 intensive campaign in Corsica, European Geosciences Union General Assembly, *Geophys. Res. Abstracts*, 16, EGU2014-2358, Vienna (Austria), 27 April–2 May 2014.

Seibert, P., Beyrich, F., Gryning, S.-E., Jo-re, S., Rasmussen, A., Tercier, P., Review and intercomparison of operational methods for the determination of the mixing height, *Atmospheric Environment*, 34 (7), 1001 - 1027, doi: http://dx.doi.org/10.1016/S1352-2310(99)00349-0, 2000.

Seinfeld, J.H., Pandis, S. N.: Atmospheric Chemistry and Physics: From Air Pollution to Climate Change, 1st ed., John Wiley, New York. 1998.

Sekhon, R.S., Srivastava, R.C.: Doppler Radar Observations of Drop-Size Distributions in a Thunderstorm. *Journal of the Atmospheric Sciences*, 28(6), pp.983–994. https://doi.org/10.1175/1520-0469(1971)028<0983:DROODS>2.0.CO;2. 1971.

Sicard, M., Chazette, P., Pelon, J., Won, J. G., Yoon, S.-C., Variational method for the retrieval of the optical thickness and the backscatter coefficient from multiangular lidar profiles, *Appl. Opt.*, 41, 493 – 502, 2002.

Sicard, M., Reba, M.N.M., Rocadenbosch, F., Gregorio, E., Kumar, D., Tomás, S., Comerón, A., Molero, F., Pujadas, M., Guerrero-Rascado, J. L., Pedros, R., Martinez, J. A.: Intercomparison of Spanish advanced lidars in the framework of EARLINET, in Proc. IEEE International Geoscience and Remote Sensing Symposium (*IGARSS*), Barcelona, Spain, 23-28 July 2007, pp. 2763–2766 (2007).

Sicard, M., Molero, F., Guerrero-Rascado, J. L., Pedrós, R., Expósito, F. J., Córdoba-Jabonero, C., Bolarín, J. M., Comerón, A., Rocadenbosch, F., Pujadas, M., Alados-Arboledas, L., Martinez-Lozano, J.A., Díaz, J.P., Gil, M., Requena, A., Navas-Guzmán, F., Moreno, J.M.: Aerosol lidar intercomparison in the framework of SPALINET the SPAnish LIdar NETwork: methodology and results, *IEEE Trans. Geosci. Remote Sens.*, 47, 35473559, 2009.

Sicard, M., Mallet, M., García-Vizcaíno, D., Comerón, A., Rocadenbosch, F., Dubuisson, P., Muñoz-Porcar, C., Intense dust and extremely fresh biomass burning in Barcelona, Spain: Characterization of their optical properties and estimation of their radiative forcing, *Environ. Res. Lett.*, 7, 034016, doi:10.1088/1748-9326/7/3/034016. 2012.

Sicard, M., Bertolín, S., Mallet, M., Dubuisson, P., Comerón, A.: Estimation of mineral dust long-wave radiative forcing: Sensitivity study to particle properties and application to real cases in the region of Barcelona, *Atmos. Chem. Phys., 14*(17), 9213–9231, doi:10.5194/acp-14-9213-2014, 2014a.

Sicard, M., Bertolín, S., Muñoz, C., Rodríguez, A., Rocadenbosch, F., Comerõn, A.: Separation of aerosol fine- and coarse-mode radiative properties: Effect on the mineral dust longwave, direct radiative forcing, *Geophys. Res. Lett.*, 41(19), 6978–6985, doi:10.1002/2014GL060946, 2014b.

Sicard, M., Barragan, R., Muñoz-Porcar, C., Comerón, A., Mallet, M., Dulac, F., Pelon, J., Alados Arboledas, L., Amodeo, A., Boselli, A., Bravo-Aranda, J.A., D'amico, G., Granados-Muñoz, M.J., Leto, G., Guerrero-Rascado, J.L., Madonna, F., Mona, L., Pappalardo, G., Perrone, M.R., Burlizzi, P., Rocadenbosch, F., Rodríguez-Gómez, A., Scollo, S., Spinelli, N., Titos, G., Wang, X., Zanmar Sanchez, R.: Contribution of EARLINET/ACTRIS to the summer 2013 Special Observing Period of the ChArMEx project: monitoring of a Saharan dust event over the western and central Mediterranean, *International Journal of Remote Sensing*, 37:19, 4698-4711. doi: 10.1080 /01431161.2016.1222102, 2016a

Sicard, M., Barragan, R., Dulac, F., Alados-Arboledas, L., Mallet, M.: Aerosol optical, microphysical and radiative properties at regional background insular sites in the western Mediterranean, *Atmos. Chem. Phys., 16*(18), 12177–12203, doi:10.5194/acp-16-12177-2016, 2016b.

SigmaSpace. Micro Pulse Lidar Type 4, Instruction Manual; SigmaSpace Corporation: Lanham, MD, USA, 2012.

Skolnik, M. I., *Introduction to Radar systems*, McGraw Hill, New York, 2001.

Smirnov, A., Holben, B. N., Eck, T. F., Dubovik, O., Slutsker, I.: Clouds creening and quality control algorithms for the AERONET database, *Remote Sens. Environ.*, 73, 337–349, doi:10.1016/S0034-4257(00)00109-7, 2000.

Smirnov, A., Holben, B. N., Kaufman, Y. J., Dubovik, O., Eck, T. F., Slutsker, I., Pietras, C., Halthore, R. N.: Optical properties of atmospheric aerosol in maritime environments, *J. Atmos. Sci.*, 59, 501–523, doi:10.1175/1520-0469(2002)0592.0.CO;2, 2002.

Sokolik, I. N. and Toon, O. B.: Incorporation of mineralogical composition into models of the radiative properties of mineral aerosol, *J. Geophys. Res.*, 104, 9423–9444, doi:10.1029/1998JD200048, 1999.

SPALINET, http://www.lidar.es/spalinet/, (accessed, February 2018), 2007.

Stamnes, K., Tsay, S.C., Nakajima, T., Computation of eigenvalues and eigenvectors for discrete ordinate and matrix operator method radiative transfer, *J. Quant. Spectrosc. Radiat. Transfer*, 39:415–419. 1988.

Stein, A.F., Draxler, R.R., Rolph, G.D., Stunder, B.J.B., Cohen, M.D. : NOAA’s HYSPLIT atmospheric transport and dispersion modelling system. *Am. Meteorol. Soc.*, doi:10.1175/BAMS-D-14-00110.1, 2015.

Stelmaszczyk, K., Dell’Aglio, M., Chudzy ´nski, S., Stacewicz, T., Wöste, L., Analytical function for lidar geometrical compression form-factor calculations. *Appl. Opt.*, 44, 1323–1331. 2005.

Strauch, R. G., W. C. Campbell, R. B. Chadwick, and K. P. Moran, Microwave FM-CW Doppler radar for boundary layer probing, Geophysical Research Letters, 3 (3), 193_196, doi: 10.1029/ GL003i003p00193, 1976.

Stull, R.B., *Mean Boundary layer characteristics*, in An Introduction to Boundary Layer Meteorology, chap. 1, pp. 1-28, Kluwer Academic Publishers, 1988a.

Sugiyama, G., Nasstrom, J.S., *Methods for Determining the Height of the Atmospheric Boundary Layer*, Tech. Rep. UCRL-ID.133200, Lawrence Livermore National Laboratory, 1999.

Tafuro, A.M., Barnaba, F., De Tomasi, F., Perrone, M.R., Gobbi, G.P.: Saharan dust particle properties over the central Mediterranean. *Atmos. Res.* 81, 67–93. 2006.

Tafuro, A.M., Kinne, S., De Tomasi, F., Perrone, M.R.: Annual cycle of aerosol direct radiative effect over southeast Italy and sensitivity studies, *J. Geophys. Res.*, 112, D20202, doi:10.1029/2006JD008265. 2007.

Tanamachi, R., Frasier, S.J., Heberling, W., Waldinger, J., Seedor, M., Bozell, J.: Purdue-UMass Mobile Radar Observations Collected during VORTEX-Southeast 2016. In *Results from the VORTEX-SE Field Program, Session*

3 in 28th Conference on Severe Local Storms. Portland: American Meteorological Society, p. Paper 3.6. Available at: https://ams.confex.com/ams/28SLS/webprogram/Paper301419.html. 2016.

Tatarski'i, V., *Wave Propagation in a Turbulent Medium*. New York, NY, USA: McGraw-Hill, 1961.

Tegen, I. and Lacis, A. A.: Modeling of particle size distribution and its influence on the radiative properties of mineral dust aerosol, *J. Geophys. Res.*, 101, 19237–19244, doi:10.1029/95JD03610, 1996.

Telford, J.W.: A New Aspect of Coalescence Theory. *Journal of Meteorology*, 12, pp.436–444. https://doi.org/10.1175/1520-0469(1955)012<0436:ANAOCT>2.0.CO;2 1955.

Tesche, M., Ansmann, A., Müller, D., Althausen, D., Mattis, I.N.A., Heese, B., Freudenthaler, V., Wiegner, M., Esselborn, M., Pisani, G., et al. Vertical profiling of Saharan dust with Raman lidars and airborne HSRL in southern Morocco during SAMUM. *Tellus Ser. B Chem. Phys. Meteorol.*, *61*, 144–164. 2009.

The National Severe Storms Laboratory (NSSL), Research tools: CLAMPS. Available at: https://www.nssl.noaa.gov/tools/clamps/ [Accessed January 30, 2018].

Thieuleux, F., Moulin, C., Bréon, F.M., Maignan, F., Poitou, J., Tanré, D.: Remote sensing of aerosols over the oceans using MSG/SEVIRI imagery. *Ann Geophys* 23:3561–3568. doi:10.5194/angeo-23- 3561-2005, 2005.

Tokay, A., Short, D.A.: Evidence from Tropical Raindrop Spectra of the Origin of Rain from Stratiform versus Convective Clouds. *Journal of Applied Meteorology*, 35(3), pp.355–371. https://doi.org/10.1175/1520-0450(1996)035<0355:EFTRSO>2.0.CO;2 1996.

Tokay, A., Hartmann, P., Battaglia, A., Gage, K.S., Clark, W., Williams, C.R.: A field study of reflectivity and Z-R relations using vertically pointing radars and disdrometers. *Journal of Atmospheric and Oceanic Technology*, 26(6), pp.1120–1134. doi: 10.1175/2008JTECHA1163.1. 2009.

Toledano, C., Cachorro, V. E., Berjon, A., de Frutos, A. M., Sorribas, M., de la Morena, B. A., Goloub, P.: Aerosol optical depth and Ångström exponent climatology at El Arenosillo AERONET site (Huelva, Spain), *Q. J. Roy. Meteor. Soc.*, 133, 795–807, doi:10.1002/qj.54, 2007.

Torres, B., Dubovik, O., Fuertes, D., Schuster, G., Cachorro, V. E., Lapyonok, T., Goloub, P., Blarel, L., Barreto, A., Mallet, M., Toledano, C., Tanré, D.: Advanced characterisation of aerosol size properties from measurements of spectral optical depth using the GRASP algorithm, *Atmos. Meas. Tech.*, 10, 3743-3781, https://doi.org/10.5194/amt-10-3743-2017, 2017.

Totems, J., Chazette, P.: Calibration of a water vapour Raman lidar with a kite-based humidity sensor, *Atmos. Meas. Tech.*, 9, 1083-1094, https://doi.org/10.5194/amt-9-1083-2016, 2016.

Trabal, J., Colom-Ustariz, J., Cruz-Pol, S., Pablos-Vega, G., McLaughlin, D.: Remote Sensing of Weather Hazards Using a Low-Cost and Minimal Infrastructure O-the-Grid Weather Radar Network, Geoscience and Remote Sensing, *IEEE Transactions on*, 51 (5), 25412555, doi: 10. 1109/TGRS.2012.2214227, 2013.

Ulbrich, C.W., Atlas, D.: Assessment of the contribution of differential polarization to improved rainfall measurements. *Radio Science*, 19(1), pp.49–57. https://doi.org/10.1029/RS019i001p00049. 1984.

Vaisala, Vaisala Ceilometer CL-31, http://www.vaisala.com/en/products/ceilometers/Pages/ CL31.aspx, Last accessed in February, 2014.

Valenzuela, A., Olmo, F. J., Lyamani, H., Antón, M., Quirantes, A., Alados-Arboledas, L.: Aerosol radiative forcing during African desert dust events (2005-2010) over Southeastern Spain, *Atmos. Chem. Phys., 12*(21), 10331–10351, doi:10.5194/acp-12-10331-2012, 2012.

Valenzuela, A., Olmo, F. J., Lyamani, H., Granados-Muñoz, M. J., Antón, M., Guerrero-Rascado, J. L., Quirantes, A., Toledano, C., Pérez-Ramírez, D., Alados-Arboledas, L.: Aerosol transport over the western Mediterranean basin: Evidence of the contribution of fine particles to desert dust plumes over Alborán Island, *J. Geophys. Res.-Atmos.*, 119, 14028–14044, doi:10.1002/2014JD022044, 2015.

Vasseur, H., Gibbins, C.J.: Prediction of apparent extinction for optical transmission through rain. *Applied Optics*, 35(36), pp.7144–7150. https://doi.org/10.1364/AO.35.007144. 1996.

Vaughn, C., Birds and insects as radar targets: A review, *Proc. IEEE*, vol. 73, no. 2, pp. 205–227, Feb. 1985.

Veselovskii, I., Goloub, P., Podvin, T., Bovchaliuk, V., Derimian, Y., Augustin, P., Fourmentin, M., Tanre, D., Korenskiy, M., Whiteman, D.N., et al.: Retrieval of optical and physical properties of African dust from multiwavelength Raman lidar measurements during the SHADOW campaign in Senegal. *Atmos. Chem. Phys.* 16, 7013–7028. 2016.

Vidal, E. Disseny D'un Canal de Despolarització a 532 nm per al Lidar d'EARLINET de la UPC. BarcelonaTech. 2013. Available online: http://hdl.handle.net/2099.1/18273 (accessed on 15 September 2018).

Vieux, B.E., Bedient, P.B.: Estimation of Rainfall for Flood Prediction from WSR-88D Reflectivity: A Case Study, 17–18 October 1994. *Weather and Forecasting*, 13(2), pp.407–415. https://doi.org/10.1175/1520-0434(1998)013<0407:EORFFP>2.0.CO;2. 1998.

VORTEX-SE, VORTEX-SE. *The National Severe Storms Laboratory (NSSL)*. Available at: http://www.nssl.noaa.gov/projects/vortexse/ [Accessed November 23, 2017].

Wagner, W., Pruß, A.: The IAPWS formulation 1995 for the thermodynamic properties of ordinary water substance for general and scientific use, *J. Phys. Chem.* Ref. Data, 31, 387–535, doi:10.1063/1.1461829. 2002.

Wagner, J.T., Klein, P.M., Turner, D.: A New Generation of Ground-Based Mobile Platforms for Active and Passive Profiling of the Boundary Layer. *BAMS*, pp.137-152. doi:10.1175/BAMS-D-17-0165.1. 2019.

Wan, Z.: New refinements and validation of the collection-6 MODIS land-surface temperature/emissivity product, *Remote Sens. Environ.*, 140, 36–45, doi:10.1016/j.rse.2013.08.027, 2014.

Wandinger, U., *Introduction to lidar*, in Lidar, Range-Resolved Optical Remote Sensing of the Atmosphere, edited by C. Weitkamp, chap. 1, pp. 1_18, Springer, Singapore, 2005.

Wandinger, U., Ansmann, A., Mattis, I., Müller, D., Pappalardo, G.: Calipso and beyond: Long-term ground-based support of space-borne aerosols and cloud lidar missions. *In Proceedings of the 24th International Laser Radar Conference*, Boulder, CO, USA, 23–27 June 2008; pp. 715–718. 2008.

Wang, K., Wan, Z., Wang, P., Sparrow, M., Liu, J., Zhou, X., Haginoya, S.: Estimation of surface long wave radiation and broadband emissivity using Moderate Resolution Imaging Spectroradiometer (MODIS) land surface temperature/emissivity products, *J. Geophys. Res.*, 110, D11109, doi:10.1029/2004JD005566. 2005.

Wang, X., A. Boselli, L. D'Avino, G. Pisani, N. Spinelli, A. Amodeo, A. Chaikovsky, M. Wiegner, S. Nickovic, A. Papayannis, M.R. Perrone, V. Rizi, L. Sauvage, Stohl, A.: Volcanic dust characterization by EARLINET during Etna eruptions in 2001-2002, *J. Atmos. Environ.*, 42, 893905, 2008.

Welton, E.J., Campbell, J.R., Spinhirne, J.D., Scott III, V.S.: Global monitoring of clouds and aerosols using a network of micropulse lidar systems, pp. 151158, doi: 10.1117/12.417040, 2001.

Westbrook, C.D., Hogan, R., O'Connor, E.J., Illingworth, A.J.: Estimating drizzle drop size and precipitation rate using two-colour lidar measurements. *Atmospheric Measurement Techniques*, 3(3), pp.671–681. doi: 10.5194/amtd-3-891-2010. 2010.

Wiegner, M.; Madonna, F.; Binietoglou, I.; Forkel, R.; Gasteiger, J.; Geiß, A.; Pappalardo, G.; Schäfer, K.; Thomas, W. What is the benefit of ceilometers for aerosol remote sensing? An answer from EARLINET. *Atmos. Meas. Tech.*, 7, 1979–1997. 2014.

Williams, C.R.: Vertical air motion retrieved from dual-frequency profiler observations. *Journal of Atmospheric and Oceanic Technology*, 29(10), pp.1471–1480. https://doi.org/10.1175/JTECH-D-11-00176.1. 2012.

Williams, C.R., Gage, K.S.: Raindrop size distribution variability estimated using ensemble statistics. *Annales Geophysicae*, 27, pp.555–567. Available at: http://www.ann-geophys.net/27/555/2009/angeo-27-555-2009.html. 2009.

Willis, P.T., Tattelman, P.: Drop-Size Distributions Associated with Intense Rainfall. *Journal of Applied Meteorology*, 28, pp.3–15. https://doi.org/10.1175/1520-0450(1989)028<0003:DSDAWI>2.0.CO;2. 1989.

Winker, D.M.; Osborn, M.T. Airborne lidar observations of the Pinatubo volcanic plume. *Geophys. Res. Lett.* 19, 167–170. 1992.

Winker, D., Pelon, J., McCormick, P., Initial Results from CALIPSO, pp. 991-994, *23rd International Laser Radar Conference*, Tokyo Metropolitan Univ., Tokyo, 2006.

York, D., Evensen, N.M.: Unified equations for the slope, intercept, and standard errors of the best straight line. *American Journal of Physics*, 72(3), pp.367–375. Available at: http://aapt.scitation.org/doi/10.1119/1.1632486. 2004.